ATLAS : Search for Supersymmetry and optimization of the High Granularity timing detector

Corentin Allaire

université PARIS-SACLAY

NNT : 2019SACLS316

Thèse de doctorat

UNIVERSITÉ PARIS SUD

Comprendre le monde, construire l'avenir

ATLAS : Search for Supersymmetry and optimization of the High Granularity timing detector

Thèse de doctorat de l'Université Paris-Saclay
préparée à l'Université Paris-Sud

École doctorale n°576 Particules, Hadrons, Énergie, Noyau, Instrumentation, Imagerie, Cosmos et Simulation (PHENIICS)
Spécialité de doctorat : Physique des particules

Thèse présentée et soutenue à Orsay, le 27-09-2019, par

CORENTIN ALLAIRE

Composition du Jury :

Fabien CAVALIER LAL, Orsay	Président
Anne-Catherine LE BIHAN IPHC, Strasbourg	Rapporteur
Tilman PLEHN ITP, Heidelberg University	Rapporteur
Ana Maria HENRIQUES CORREIA CERN	Examinatrice
Dirk ZERWAS LAL, Orsay	Directeur de thèse

Laboratoire de l'Accélérateur Linéaire n°LAL 19-012

List of Abbreviations

SM	**S**tandard **M**odel
QFT	**Q**uantum **F**ield **T**heory
QED	**Q**uantum **E**lectro**d**ynamic
QCD	**Q**uantum **C**hromo**d**ynamic
BSM	**B**eyond the **S**tandard **M**odel
GUT	**G**rand **U**nification **T**heory
CP	**C**harge **P**arity
SUSY	**Su**per**sy**mmetry
LSP	**L**ightest **S**upersymmetric **P**article
MSSM	**M**inimal **S**upersymmetric **S**tandard **M**odel
pMSSM	**p**henomenological **M**inimal **S**upersymmetric **S**tandard **M**odel
MRSSM	**M**inimal R-symmetric **S**upersymmetric **S**tandard **M**odel
LO	**L**eading **O**rder
NLO	**N**ext to **L**eading **O**rder
CL	**C**onfidence **L**evel
EFT	**E**ffective **F**ield **T**eory
RPV	**R**-**P**arity **V**iolation
SR	**S**ignal **R**egion
ATLAS	**A** **T**oroidal **L**HC **A**pparatu**S**
CMS	**C**ompact **M**uon **S**olenoid
LHC	**L**arge **H**adron **C**ollider
HL-LHC	**H**igh **L**uminosity-LHC
ITk	**I**nner **Tr**acker
LAr	**L**iquid **Ar**gon Calorimeter
HGTD	**H**igh **G**ranularity **T**iming **D**etector
LGAD	**L**ow **G**ain **A**valanche **D**etector
ASIC	**A**pplication-**S**pecific **I**ntegrated **C**ircuit
MIP	**M**inimum **I**onizing **P**article
CFD	**C**onstant **F**raction **D**iscriminator
ToA	**T**ime **o**f **A**rrival
ToT	**T**ime **o**ver **T**hreshold

Remerciements

Dans un premier temps, je souhaite remercier Dirk Zerwas pour l'encadrement ma thèse. Grâce à toi j'ai eu l'opportunité de travailler sur des sujets extrêmement intéressants tout en conservant une grande liberté dans mon travail. J'ai beaucoup apprécié nos discussions, qu'elles touchent à la physique des particules ou pas, c'était toujours pour moi un plaisir de passer à ton bureau. Je tiens également à te remercier de m'avoir invité à tous les GDR Terascale, j'ai eu l'occasion d'y rencontrer des personnes très intéressantes, d'y écouter des présentations qui l'étaient tout autant (quand je les comprenais) et le plus important de participer à des dîners aussi bons les uns que les autres. En résumé j'ai extrêmement apprécié ces trois années à travailler avec toi et je pense sincèrement que je n'aurais pu espérer de meilleur directeur.

Je tiens à remercier les rapporteurs et examinateurs : Anne-Catherine Le Bihan, Tilman Plehn et Ana Maria Henriques Correia pour avoir fait le déplacement jusqu'à Orsay et pour avoir pris le temps de lire mon manuscrit malgré les nombreuses typos et fautes de grammaires qu'il contenait.

Je remercie également Achille Stocchi pour m'avoir accueilli au laboratoire en stage de L3 et durant ma thèse ainsi que Fabien Cavalier pour avoir dégagé du temps dans son agenda que j'imagine surchargé pour présider mon jury.

Je remercie tous les membres du groupe HGTD au LAL : Laurent Serin avec qui il était toujours très intéressant de discuter qui m'a très gentiment rappelé jour après jour qu'il fallait que je rédige ma thèse. Nikola Makovec avec qui j'ai partagé le bureau pendant deux ans avant qu'il ne parte vers d'autres horizons à l'autre bout du couloir. Aboud Fallou dont j'ai beaucoup aimé l'enthousiasme quand nous discutions de la mécanique et du cooling. Sabrina Sacerdoti avec qui j'ai beaucoup apprécié nos longues discussions sur le layout et la position des modules même si je suis bien heureux de ne plus avoir à m'en préoccuper ! Et finalement Christina Agapopoulou, à qui je souhaite beaucoup de courage pour la rédaction de sa thèse et la continuation du travail sur le design du HGTD.

Je souhaite également remercier tous les autres membres du HGTD qu'il soient au LPNHE, à Omega au CERN ou autre. Ça a été un plaisir de travailler et interagir avec vous et je suis extrêmement heureux d'avoir fait partie de cette communauté. Petite pensée à Alexander Leopold dont la dédicacions aux performances et au Hit-to-track matching inspire le respect, pour ton info, je le note ici : les pads font $1.3\,\mathrm{mm} \times 1.3\,\mathrm{mm}$.

Parmi mes collaborateurs je souhaite finalement remercier Simone Amoroso avec qui j'ai travaillé sur l'analyse et qui a pris de son temps malgré un emploi du temps très chargé pour interagir avec moi.

De manière plus générale je remercie tous les membres du groupe ATLAS du LAL qui ont toujours été très sympathiques et en particulier les permanents qui m'ont accueilli durant leur pause café quand il n'y avait plus d'étudiants dans le couloir. Un grand merci au personnel administratif du LAL qui a toujours été très patient avec moi et en particulier à Geneviève Gilbert et Catherine Nizery pour avoir toujours été présentes quand l'on avait besoin de vous.

Sincères remerciements à toute l'équipe de science ACO pour avoir été très accueillant avec moi. Ça a été pour moi très enrichissant de pouvoir discuter avec chacun d'entre vous. Je pense que ce que vous faites tous est très important et j'espère que vous allez pouvoir continuer à faire vivre ce lieu pendant encore de nombreuse années.

Un grand merci à tous les doctorants et post-doc avec qui j'ai passé du temps ces trois dernières années. En particulier je remercie : Steven Calvez pour avoir étendu mon répertoire de blagues (ce qui n'est sans doute pas une bonne chose) et pour avoir acheté une chaise afin que je puisse m'asseoir quand je lui ai rendu visite à Chicago. Christophe Goudet pour avoir été l'instigateur des soirées film que j'ai continué à organiser ces deux dernières années. Baptiste Abbeloos pour la bonne humeur qu'il apportait au labo. Charles Delporte pour nos parties de Civilisations et pour avoir contribué à la large diaspora bretonne du laboratoire. Merci à Antoine Laudrain pour toujours avoir été prêt à discuter quand j'avais du temps à perdre et merci à Antinéa Guerguichon pour avoir été là quand j'avais besoin de me plaindre. Bon courage à Tobias Fitschen et Anastasia Kotsokechagia pour le reste de leurs thèses et merci d'avoir apporté du sang neuf aux pauses cafés. Et finalement merci à Konie Al Khoury pour m'avoir fait sortir de chez moi le weekend et m'avoir suivi au japonais tous les jeudis, ça va me manquer !

Merci à tous les membres des soirées films, j'attendais toujours avec impatience les lundi (puis mardi) pour passer du temps avec vous. Julien Ripoche et Mathieu Ehrhart, après avoir passé 3 mois au CERN en tant qu'étudiant d'été avec vous je suis heureux qu'on se soit retrouvés au même endroit pour nos thèses. Merci à Victor pour avoir toujours été là aux soirées prêt à râler à propos de tout et n'importe quoi. Bon courage à Noe Roy et Cloé Girard-Carillo pour l'avenir, je vous confie les soirées, puissiez-vous les maintenir sous une forme ou une autre dans le futur.

Finalement je remercie ma famille en Bretagne pour avoir toujours été la, c'est toujours un plaisir de revenir vous voir. En particulier je remercie ma grand-mère Suzanne Lebreton qui nous a quitté il y a deux ans et qui à toujours été pour moi un exemple à suivre. Et Finalement mes parents Catherine et Yannick Allaire pour m'avoir soutenu pendant ces 26 dernières années, sans vous je n'aurais jamais pu arriver jusqu'où j'en suis aujourd'hui.

Table des matières

Chapitre 1

Introduction

In 2012, ATLAS and CMS discovered the Higgs boson in pp collisions with a center of mass energy of $\sqrt{s} = 7 - 8\,\mathrm{TeV}$ at the LHC, completing the particle content of standard model. Nevertheless, there are still open questions that are left unanswered by the standard model. These issue include, the unification of the three forces, the hierarchy problem, the absence of a dark matter candidate, the observation of neutrino oscillations, the matter-antimatter asymmetry, and the absence of gravitation in the model. Many models beyond the Standard model try to provide a framework to solve some of these problems, resulting in the prediction of new particles that might be observable at the LHC. To find such particles many searches have been performed at the LHC. Among these searches, searching for new colored particles have been central to the physics program of the LHC. The new particles are predicted by many models, for example Supersymmetry with the superpartner of the quark or gluons. The search benefits from an increase energy in the center of mass energy, as this result in an increase production cross section for colored particles. Combined with the increased luminosity at the LHC, this will improve the capability to probe higher mass ranges in search of new particles. The different searches can be classified by their final state, such as for example the number of leptons and jets in the final state, the flavor of the jets or the presence or not of missing transverse energy. In this thesis, the pair production of new particles have been searched for, where each of these particles then decay into two jets. This results in a final state with four jets in the detector with no missing transverse energy. Three different channels have been studied, one inclusive with four jets regardless of their flavor, one with two b-jets in the final state and one with four b-jets in the final state.

To be able to continue extending the masse range probed by the LHC as well as to continue to probe with more precision the parameters of the Standard model it is necessary to increase the luminosity delivered at the LHC. This is the purpose of the High Luminosity LHC, this upgrade of the accelerator is scheduled for 2026 and will deliver an integrated luminosity of up to $4000\,\mathrm{fb}^{-1}$. To achieve this goal, the instantaneous luminosity will be increased by a factor 5, up to $7.5 \times 10^{34}\,\mathrm{cm}^{-2}\,\mathrm{s}^{-1}$. To cope with these new conditions, the sub-detectors of the ATLAS experiment has to be upgraded. Indeed, at the HL-LHC due to the large instantaneous luminosity, the number of interactions per bunch crossing will become extremely large, leading to high radiation damages and an increased complexity for the reconstruction of the events. To improve the reconstruction, a new detector is being design for the forward region of the ATLAS detector. This detector, called the High Granularity Timing Detector (HGTD) will be able to provided information on charged particles in both time and space. This additional information will improve the reconstruction of the particles in the forward region by differentiating the objects coming from the signal and the background via the use of the timing.

The chapters of this thesis are divided in two parts, the first three chapters will present the theoretical and experimental context of this thesis. The second half, composed of chapter four to six present my contribution to physics analysis and detector development.

The first chapter will provide the theoretical and phenomenological context to the search of new pair produced colored particles. The standard model of particle physics as well as its limitation will be discussed. Supersymmetry and the different model that can lead to a four jets signature in the ATLAS detector will then be presented.

The experimental apparatus used to perform the analysis will be presented in the second chapter. This includes the accelerator complex, the ATLAS detector and the reconstruction techniques used for the different particles. In addition, this section will also present the HL-LHC upgrades plan as well as the motivations for the upgrades. The evolution of the collision scheme at the HL-LHC and the consequences on the beam parameters will also be explained. The upgrades of the different sub-detectors of ATLAS will also be detailed.

The last part of general presentation will be on the High Granularity Timing Detector. In this part the motivation for this detector as well as its latest design will be presented. To better explain the constraints on the detector layout that will be discussed in Chapter 7, the different components of this detector are also presented in this section. Finally, the performance in terms of object reconstruction and physics analysis will also be presented.

The search of new pair produced colored particles in ATLAS using data from the years 2016, 2017 and 2018 will be presented in Chapter 5. For this analysis, I evaluated the difference between sgluon simulated at LO and NLO. To determine how to reconstruct the signal and how to separate it from the background, I studied the topology of the events. The analysis strategy and the background estimation method will be presented. Finally, prospect for the full Run 2 analysis will be shown.

In Chapter 6, studies that I did on the Higgs coupling measurement prospect at the HL-LHC will be presented. The studies were performed using the SFitter framework. I have determined the precision with which the couplings can be extracted from the expected measurements in the framework of coupling modifiers and effective field theory.

My work on the High Granularity Timing Detector will be presented in the last chapter. This work included the development of the simulation that was used as an input to derive most of the object performance study that were presented in Chapter 4. Using this simulation, I optimized the layout of the detector while taking into account the constraints from the different component of the HGTD. Finally, using this simulation I performed several studies that will be presented in this section, both on the timing performance of the detector and the improvement on electrons reconstruction using the HGTD.

Chapitre 2

Phenomenology

The Standard Model of Particle Physics (SM) has been extremely successful in describing the elementary particles and their interactions. Nevertheless, several questions are not answered by this model motivating the construction of models beyond the SM. In a first time, the chapter will present general consideration of the SM of particle physic and its particle content. In a second time, physics Beyond the Standard Model (BSM) and in particular Supersymmetry will be presented. Different supersymmetric model that can lead to the pair produced resonances decaying into four jets will be detailed.

2.1 The Standard Model of particle physics

The Standard Model (SM) of particle physics [1] was developed during the second half of the 20th century. This theory is a Quantum Field Theory (QFT) [2], describing all elementary particles and their interactions. It has been thoroughly tested experimentally during the last decades and has successfully managed to explain the data obtained at these experiments. The last missing particle predicted in this model, the Higgs Boson, has been observed at the LHC by the ATLAS [3] and CMS [3] experiment in 2012 roughly 60 years after its prediction. The SM can describe three out of the four fundamental interactions :

- The electromagnetic interaction, responsible for the interaction between charged particles.
- The weak interaction, related to the neutron decay and the neutral currents.
- The strong interaction, acting on the quark and confining them together to form hadrons.

2.1.1 Particle content of the Standard Model

The particles of the SM can be separated into two different categories, the fermions which have a half-integer spin and the bosons with an integer-spin. All these particles are presented in Figure 2.1, the different boxes correspond to their interactions. All of these elementary particles have an anti-particles with same mass and spin but opposite charge, Lepton and Baryon number.

Fermions are the building block of matter, they can be split into two categories, the quarks that carry a color charge and the leptons that do not. Leptons and quarks can be grouped into three generations. The first generations is composed of the lightest stable particles while the third is composed of the heaviest particles.

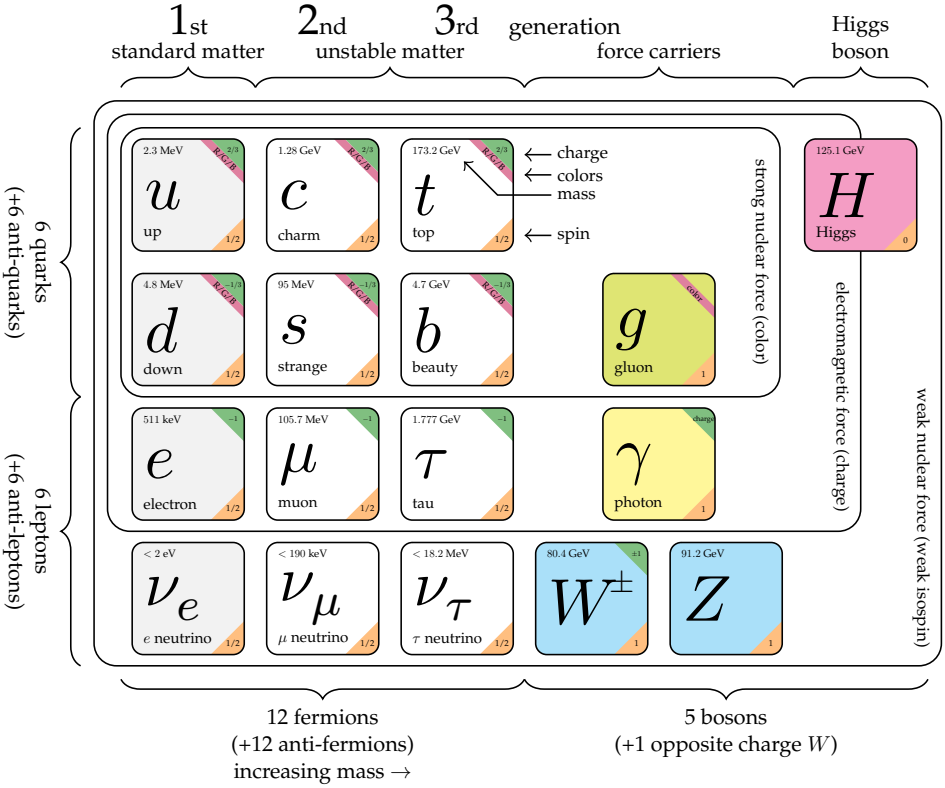

FIGURE 2.1 – The particle content of the Standard Model.

Leptons have a Lepton number of one and a Baryon number of zero. Each lepton generation is composed of a pair of a particle with a charge -1 and its associated neutrino, which is electrically neutral. The first generation is composed of the electron and the electron neutrino, the second of the muon and the muon neutrino and finally the third one of the tau and the tau neutrino. Since none of the leptons have a color charge they don't interact via the strong interaction, moreover due to its neutral charge the neutrino cannot interact via electromagnetic interaction and thus can only interact via weak interaction.

Quarks have a Baryon number of one third and a Lepton number of 0. In the quark sector, each generation is composed of a pair of quarks, one with a charge $+\frac{2}{3}$ and one with a charge $-\frac{1}{3}$. The first generation contains the quarks up and down, the second the quarks charm and strange and the last one the quarks top and bottom (sometime called beauty). The quarks interact via all the interactions of the standard model. Because of confinement the quarks cannot observe individually and will always combine with other quarks to create colorless objects called hadron. Hadrons can be mesons which are quark-anti-quark systems or baryons which are three quark states. States such as Tetra- and Pentaquarks exist, but are rare.

The second type of particles are the bosons, which are the mediators of fundamental interactions. In the SM the interaction between two particles can be seen as an exchange of a boson. There are two types of bosons, the gauge bosons, with a spin equal to one and the scalar boson with a spin equal to zero. Each fundamental force has its own corresponding gauge boson. The electromagnetic force is carried by the photon, the weak interaction is carried by the Z and $W^{\pm}$ bosons and the strong interaction is carried by the gluons. Currently, only one scalar boson has been observed the Higgs boson.

The SM is a gauge theory in which the SM Lagrangian is invariant with respect to the local symmetries of the group $G_{SM} = SU(3)_C \times SU(2)_I \times U(1)_Y$, in which the QCD color charge

C, weak isospin I and hypercharge Y are conserved respectively. In the Lagrangian expression, fermion fields are written in the form of Dirac spinors ψ, the bosons correspond to the gauge fields.

To explain how these symmetries operate, let's look at the invariance of gauge transformation under local U(1) (which correspond to the quantum electrodynamics (QED)). The Lagrangian for a free propagating particle with spin $1/2$, mass m is :

$$\mathcal{L} = \bar{\psi}(i\gamma^\mu \partial_\mu - m)\psi \tag{2.1}$$

where ψ denotes the Dirac spinor of the particle's field. Now consider the U(1) local gauge transformation, a change of phase :

$$\psi(x) \longrightarrow e^{i\alpha(x)}\psi(x) \tag{2.2}$$

where $\alpha(x)$ can be any arbitrary real function of x. Our initial Lagrangian is not invariant under this transformation and it becomes :

$$\mathcal{L} = \bar{\psi}(i\gamma^\mu \partial_\mu - m)\psi - \bar{\psi}\gamma^\mu \partial_\mu \alpha(x)\psi \tag{2.3}$$

To recover the invariance, the partial derivative ∂_μ is replaced by the covariant derivative D_μ, with :

$$D_\mu = \partial_\mu - ieA_\mu \tag{2.4}$$

where A_μ is a vector field that transform as :

$$A_\mu \longrightarrow A_\mu + \frac{1}{q_e}\partial_\mu \alpha(x) \tag{2.5}$$

We can then verify that the new modify Lagrangian is invariant under U(1) :

$$\begin{aligned} \bar{\psi}(i\gamma^\mu \partial_\mu - m)\psi &\longrightarrow \bar{\psi}(i\gamma^\mu D_\mu - m)\psi, \\ &= \bar{\psi}(i\gamma^\mu \partial_\mu - m)\psi + e\bar{\psi}\gamma^\mu \psi A_\mu, \\ &= \mathcal{L}_{\bar{\psi}\psi} + \mathcal{L}_{\bar{\psi}\psi A} \end{aligned} \tag{2.6}$$

This new Lagrangian is composed of two terms the first one corresponds to the free propagation of particles with spin $1/2$, while the second corresponds to the interaction of particles with photons. A_μ will thus be considered in the context of QED as the gauge field for the electromagnetic interaction with interaction strength e.

Beyond the QED, the Electroweak model unifies the electromagnetic and weak interaction as a gauge theory [4] [5] with respect to the local symmetries of the group $SU(2)_I \times U(1)_Y$. Instead of a single gauge field A_μ, four are necessary : $W_\mu^{1,2,3}$ and B_μ. The new covariant derivative can then be written :

$$D_\mu = \partial_\mu - i[gW_\mu^a \frac{\tau^a}{2} + g' B_\mu \frac{Y}{2}] \tag{2.7}$$

where, g and g' are coupling constants, $\tau^{1,2,3}$ (Pauli matrices) and Y are the group generators of respectively $SU(2)_I$ and $U(1)_Y$. By writing the corresponding Lagrangian and splitting it into

its neutral and charged components, one can write the 4 bosons carrying the interaction :

$$\begin{aligned} W_\mu^+ &= \frac{1}{\sqrt{2}}(W_\mu^1 - iW_\mu^2), \\ W_\mu^- &= \frac{1}{\sqrt{2}}(W_\mu^1 + iW_\mu^2), \\ Z_\mu &= cos(\theta_W)W_\mu^3 - sin(\theta_W)B_\mu \\ A_\mu &= sin(\theta_W)W_\mu^3 + cos(\theta_W)B_\mu \end{aligned} \tag{2.8}$$

In this expression, the weak mixing angle $\theta_W = tan^{-1}(g'/g)$ appears. This angle which rotates the W_μ^3 and B_μ fields to generate Z and γ bosons. This rotation is necessary to prevent the photon to couple with the neutrinos. The resulting Lagrangian for the EW theory is thus :

$$\mathcal{L}_{EW} = i\overline{\psi}_R^i \gamma^\mu D_\mu \psi_R^i - \frac{1}{4}W_{\mu\nu}^a W_a^{\mu\nu} - \frac{1}{4}B_{\mu\nu}^a B_a^{\mu\nu} \tag{2.9}$$

Finally, the last gauge theory used to build the standard model is the Quantum Chromodynamic (QCD). This theory describes the strong interaction and its mediator the gluon field G_μ in the $SU(3)_C$ formalism with three color charges. This results in 8 generators of this group which are the Gell-Mann matrices λ^a, this allows us to express the covariant derivative as :

$$D_\mu = \partial_\mu - ig_S G_\mu^a \frac{\lambda^a}{2} \tag{2.10}$$

where g_S is coupling constant of the strong interaction. The Lagrangian of the QCD can be written as :

$$\mathcal{L}_{QCD} = i\overline{\psi}\gamma^\mu D_\mu \psi - m\overline{\psi}\psi - \frac{1}{4}G_{\mu\nu}^a G_a^{\mu\nu} \tag{2.11}$$

The consequence of the description of the strong interaction with SU(3) are on one hand confinement, the force is strong so that no free elementary colored particles can be observed. On the other hand it is asymptotic freedom, i.e., the quarks in a baryon can be treated as free particles. The coupling constant of QCD is small at large momentum transfer (asymptotic freedom) and large at small momentum transfer (confinement) when radiative corrections are calculated.

2.1.2 The Higgs Boson

The Brout-Englert-Higgs Mechanism

In the model that was described in Section 2.1.1 all the particles are massless. Indeed, if one tries to add a mass term for one of the boson, for example for the photon in the QED case, this would result in the following term in the Lagrangian :

$$\mathcal{L}_\gamma = \frac{1}{2}m^2 A^\mu A_\mu \tag{2.12}$$

This additional term will break the gauge invariance :

$$A^\mu A_\mu \longrightarrow (A^\mu - \frac{1}{e}\partial^\mu \alpha(x))(A_\mu - \frac{1}{e}\partial_\mu \alpha(x)) \neq A^\mu A_\mu \tag{2.13}$$

This can be generalized to all particles in the SM which are thus massless in this theory.

This is in disagreement with the experimental results that have shown that the $W^{\pm}$ and the Z bosons are massive while the photon and the gluons are indeed massless particles. To explain the masses in the SM, the Brout-Englert-Higgs [6] [7] mechanism was introduced. This solution involves an additional ψ field. The Higgs field is parameterized as a weak isospin doublet of complex fields with unit hypercharge value. Its Lagrangian can be written as :

$$\mathcal{L}_{Higgs} = (D_\mu \phi)^\dagger (D^\mu \phi) - V(\phi) \quad \text{with} \quad V(\phi) = \mu^2 \phi^\dagger \phi + \lambda (\phi^\dagger \phi)^2 \tag{2.14}$$

where the first term represent the kinetic and gauge coupling term and the second one the Higgs potential.

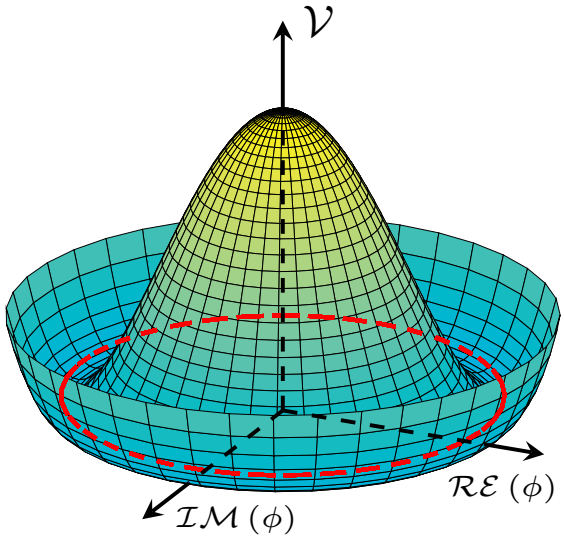

FIGURE 2.2 – Illustration of the Higgs potential in the SM. The spontaneous symmetry breaking arise from the vacuum value at the minimum of the potential, which occurs for $\phi \neq 0$ along the red line.

If we assume that $\lambda < 0$ and $\mu^2 > 0$, then the Higgs potential has a Vacuum Expectation Value (VEV) different from 0 and equal to $v = \sqrt{-\mu^2/\lambda}$. This potential is illustrated in Fig. 2.2. The expression of the Higgs field can then be developed around the ground state to obtain the following expression :

$$\phi_0 = \frac{1}{\sqrt{2}} \begin{pmatrix} 0 \\ v \end{pmatrix} \quad \longrightarrow \quad \phi(x) = \frac{1}{\sqrt{2}} \begin{pmatrix} 0 \\ v + h(x) \end{pmatrix} \tag{2.15}$$

Thus the symmetry is spontaneously broken. which then lead to the following Lagrangian :

$$\mathcal{L}_{Higgs} = \frac{1}{2}(\partial_\mu H)(\partial^\mu H) + \frac{g^2}{4}(v+H)^2 (W_\mu^+ W^{\mu-}) + \frac{1}{8}(g^2+g'^2) Z_\mu Z^\mu (v+H)^2 + \frac{\mu^2}{2}(v+H)^2 - \frac{\lambda}{4}(v+H)^4 \tag{2.16}$$

In this Lagrangian mass term appear for the Z, W and Higgs bosons, these masses are :

$$\begin{aligned} m_W &= \frac{1}{2} g\nu, \\ m_Z &= \frac{1}{2}\sqrt{g^2 + g'^2}\nu = \frac{m_W}{cos(\theta_W)}, \\ m_{Higgs} &= \sqrt{-2\lambda\nu^2} \end{aligned} \tag{2.17}$$

In the absence of the rotation of W,B into photon and Z boson, the photon (B) would have become massive.

Production modes

The Higgs Boson is produced in the interaction of quarks and gluons during the protons collisions. The main process are illustrated at leading order in Figure 2.3. For a Higgs boson with a mass of $125\,\mathrm{GeV}$ produced in collisions at a center of mass energy of $\sqrt{s}$ = 13 TeV [8], the four dominant processes are :

- **Gluon fusion (ggF) :** Dominant production mode at the LHC with a production cross section of σ_{ggF} = $48.61\,\mathrm{pb}$. For this process two gluons interact via a quark loop. This loop is dominated by loop with heavy quarks (bottom and top) as the coupling of the Higgs boson to quarks is directly proportional to their masses.
- **Vector Boson Fusion (VBF) :** In this process two quarks radiate heavy bosons (W or Z) that combine to create a Higgs boson. The final state of such interaction is two hard jets emitted in the forward region of the detector. This process is the second most likely for the production of Higgs with a cross section of σ_{VBFH} = $3.766\,\mathrm{pb}$, which is more than ten times smaller that ggF.
- **Vector Boson associated production (VH) :** Associated production of the Higgs boson with either a W or Z boson. The final state of this process can be interesting due to the presence of lepton resulting from the decay of the Vector Boson which will help trigger on such event. Even if the cross section of such process is relatively small, σ_{WH} = $1.358\,\mathrm{pb}$ σ_{ZH} = $0.880\,\mathrm{pb}$, this production mode will leave a clear signature in the detector.
- **Top quark associated production (ttH) :** In this process two gluons top quarks are produced from which the Higgs boson is radiated. The signature of such process is one Higgs with two jets of quark top in the detector. This production mode is hard to measure due to the small cross section of σ_{ttH} = 0.612 pb but provide important information on the coupling of the Higgs boson to the top quark.

Decay modes

After its production, the Higgs will decay. As explained previously the coupling of the Higgs to the particles of the SM is directly proportional to their mass, therefore the more massive a particle is the more likely the Higgs is to decay into it. A summary of the SM Higgs boson decay branching ratios for a mass of the Higgs around $125\,\mathrm{GeV}$ [9] is shown in Figure 2.4. The study of the different decay channels at the LHC is imperative, as a precise measurement of the value of the cross section times branching ratio of the Higgs is needed to determine its coupling to the different particles of the SM.

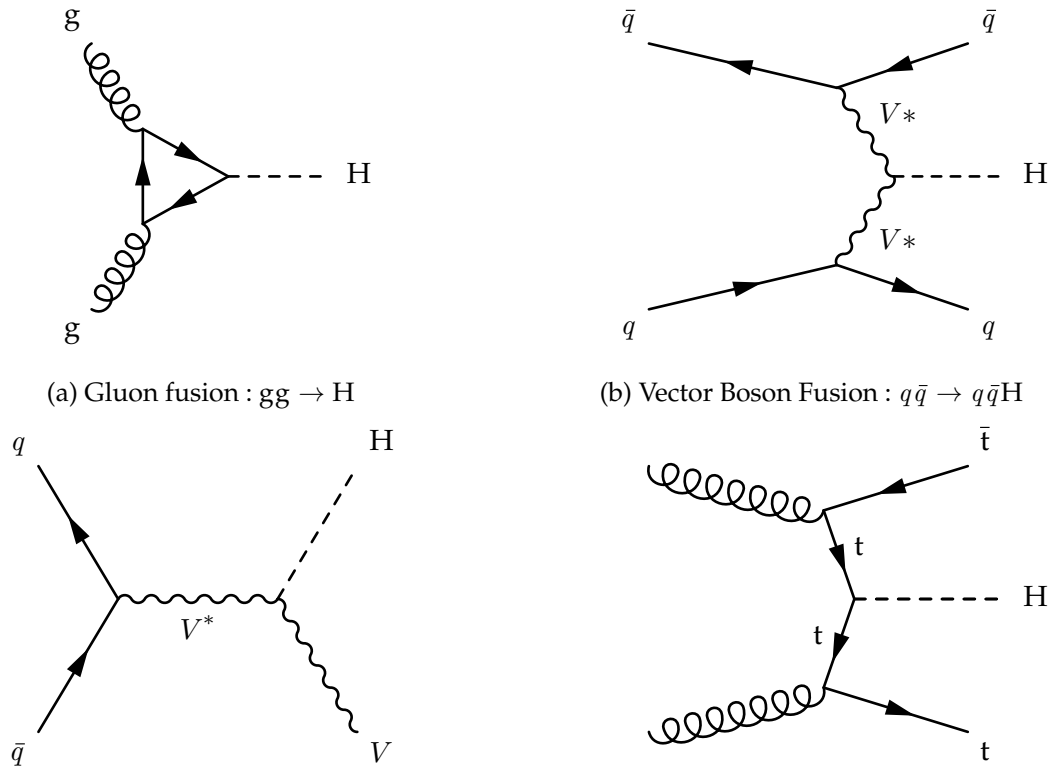

(a) Gluon fusion : gg → H

(b) Vector Boson Fusion : $q\bar{q} \rightarrow q\bar{q}$H

(c) VH : $q\bar{q} \rightarrow V$H

(d) ttH : gg → t$\bar{\text{t}}$H

FIGURE 2.3 – Feynman diagrams for the Higgs boson production processes.

The dominant decay modes of the Higgs boson are the ones to pairs of fermions (H → $f\bar{f}$). Since the coupling of the Higgs boson are proportional to the mass, the decay to a pair of b quark (H → b$\bar{\text{b}}$) and to a pair of tau lepton (H → $\tau^-\tau^+$) are dominant with respective branching ratio of 58% and 6.3%. Decays to lighter lepton can also be observed, for example the decay to pair of c quarks (H → c$\bar{\text{c}}$) or to pair of muons (H → $\mu^-\mu^+$), but since the branching ratio of such signal are small (respectively 2.3% and 0.2%) their measurement would require an increase in luminosity of the LHC and in the case of charm quarks effective c-tagging.

The Higgs boson can also decay to pairs of bosons. In the case of massive bosons the mass of the Higgs being smaller than twice their mass, the process need the emission of an off-shell boson. This decreases the branching ratio of such decay down to 22% for the W pair (H → WW*) and 2.7% for the Z pair (H → ZZ*). In addition, decays to massless boson are also possible via loop of heavy quarks or a W boson in a process similar to the ggF production mode. The decay have small cross section, 8.2% and 0.2% respectively for gluons (H → gg) and photons (H → $\gamma\gamma$).

Couplings

Since the discovery of the Higgs boson, the measurement of its coupling has become an important activity at the LHC. In addition to a precise understanding of the property of the Higgs boson the measurement of the coupling can also provide a way to probe new physics. Indeed, if new particles exist and couple to the Higgs boson they might contribute to its decay and production modes and thus modify its couplings.

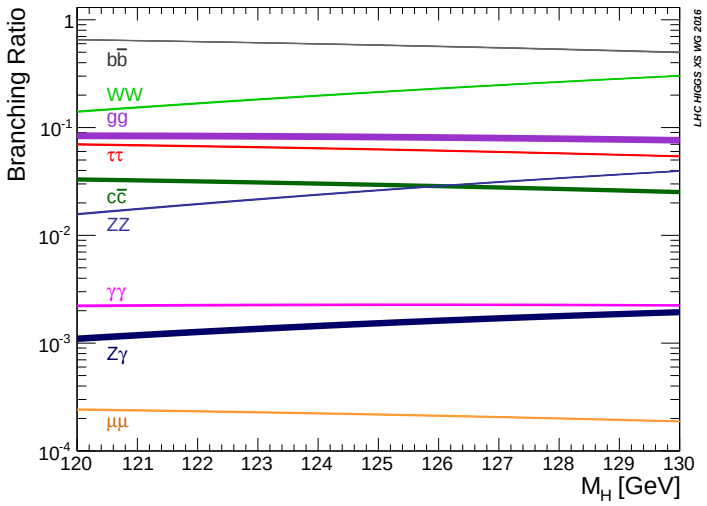

FIGURE 2.4 – The Standard Model Higgs boson decay branching ratios as a function of its mass.

To study the couplings, multiple approaches can be used, two of these that will be used later in Chapter 6 will be presented here. The first one is what is call the Delta framework : In this framework a coupling modifier [10] [11] called kappa is defined for each coupling of the Higgs boson as follows :

$$g_{xxH} \equiv g_x = \kappa_x g_x^{SM} = (1 + \Delta_x) g_x^{SM} \tag{2.18}$$

Using this formalism one can determine the value of Δ combining the result of the different LHC experiments. Figure 2.5 (a) shows an evaluation of the Δ using a combination of analysis from ATLAS and CMS. These analysis were performed using part of the dataset of Run 1 of the LHC. The uncertainty of the value of Δ are shown for a confidence level (CL) of 68%.

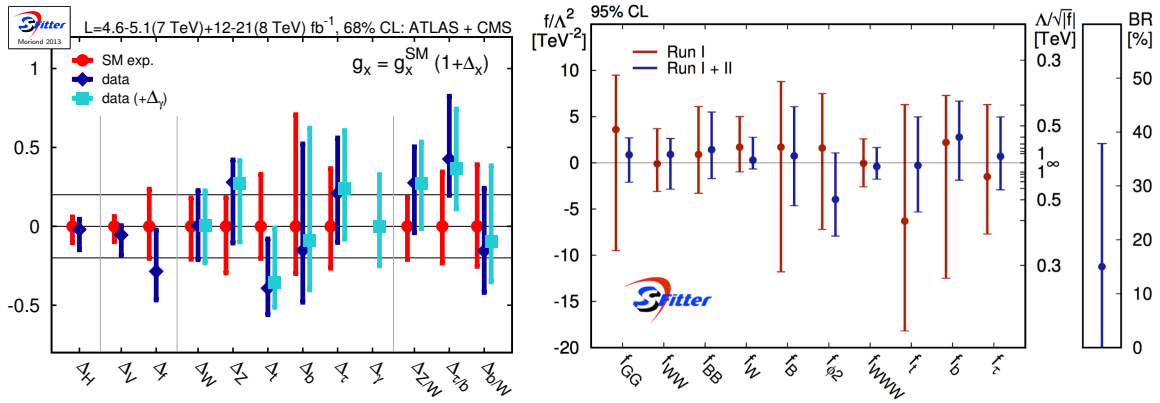

(a) (b)

FIGURE 2.5 – (a) Higgs coupling extraction using the Δ method based on all ATLAS and CMS results presented until the Winter conferences 2013 in Moriond and Aspen[12]. (b) Limits on the Wilson coefficient in an effective Lagrangian description of the Higgs couplings for Run 1 (in red) and Run 1 + Run 2 (blue) [13].

The other approach to study the deviation of the couplings is to use an Effective Field Theory (EFT) [14]. Let's assume that the new state that could affect the coupling of the Higgs belong to

$SU(2)$, the new state can be taken into account via an EFT, which should be valid as long as the scale of such new physics (noted Λ later) is not kinetically accessible at the LHC. The resulting effective Lagrangian combine the SM Lagrangian with an $SU(2)_I \times U(1)_Y$ invariant dimension 6 Lagrangian [15] :

$$\mathcal{L}_{eff} = \mathcal{L}_{SM} + \sum_x \frac{f_x}{\Lambda^2}\mathcal{O}_x + ... \tag{2.19}$$

where $\mathcal{O}_x$ is the operator, Λ the new physics scale and f is the coupling constant also called Wilson coefficients. There exist a total of 59 independent dimension 6 operators, by imposing C and P invariance [16] and neglecting all the operator that are not constrained by the Higgs measurement at the LHC we can derive the following effective Lagrangian :

$$\begin{aligned} Lagr_{eff} = & \frac{-\alpha_s}{8\pi}\frac{f_{GG}}{\Lambda^2}\mathcal{O}_{GG} + \frac{f_{BB}}{\Lambda^2}\mathcal{O}_{BB} + \frac{f_{WW}}{\Lambda^2}\mathcal{O}_{WW} + \frac{f_B}{\Lambda^2}\mathcal{O}_B + \frac{f_{WWW}}{\Lambda^2}\mathcal{O}_{WWW} \\ & + \frac{f_{\phi 2}}{\Lambda^2}\mathcal{O}_{\phi 2} + \frac{f_{\phi 3}}{\Lambda^2}\mathcal{O}_{\phi 3} + \frac{f_\tau m_\tau}{\nu\Lambda^2}\mathcal{O}_{e\phi,33} + \frac{f_b m_b}{\nu\Lambda^2}\mathcal{O}_{d\phi,33} + \frac{f_t m_t}{\nu\Lambda^2}\mathcal{O}_{u\phi,33} \\ & + invisible\ decay \end{aligned} \tag{2.20}$$

with the operator defined as followed :

$$\begin{aligned} \mathcal{O}_{GG} &= \phi^\dagger\phi G^a_{\mu\nu}G^{a\mu\nu} & \mathcal{O}_{BB} &= \phi^\dagger\hat{B}_{\mu\nu}\hat{B}^{\mu\nu}\phi & \mathcal{O}_{WW} &= \phi^\dagger\hat{W}_{\mu\nu}\hat{W}^{\mu\nu}\phi \\ \mathcal{O}_B &= (D_\mu\phi)^\dagger\hat{B}^{\mu\nu}(D_\nu\phi) & \mathcal{O}_W &= (D_\mu\phi)^\dagger\hat{W}^{\mu\nu}(D_\nu\phi) & & \\ \mathcal{O}_{\phi 2} &= \frac{1}{2}\partial^\mu(\phi^\dagger\phi)\partial_\mu(\phi^\dagger\phi) & \mathcal{O}_{WWW} &= Tr(\hat{W}_{\mu\nu}\hat{W}^{\nu\rho}\hat{W}^\mu_\rho) & & \\ \mathcal{O}_{e\phi,33} &= \phi^\dagger\phi\overline{L_3}\phi_{e_{R3}} & \mathcal{O}_{d\phi,33} &= \phi^\dagger\phi\overline{Q_3}\phi_{d_{R3}} & \mathcal{O}_{u\phi,33} &= \phi^\dagger\phi\overline{Q_3}\phi_{u_{R3}} \end{aligned} \tag{2.21}$$

The results of the analysis of the Higgs coupling using this framework can be seen in Figure 2.5 (b) using data from both Run 1 and Run 2 with ATLAS and CMS [13]. Improvement on the limits are indeed observed between the Run 1 and Run 1+2 cases, by up to a factor two in the case of f_τ, f_b and f_t. All the result are compatible with the SM with limits ranging around $\Lambda/\sqrt{f} = 400 - 800\,\text{GeV}$.

2.1.3 Limitations of the Standard Model

The standard model of particle physics can provide precise and accurate predictions for many physical process. Yet, some observations cannot be explained using the formalism of the SM therefor other separate models are needed to understand them. Due to these limitations search for physics Beyond the Standard Model (BSM) is an active field of research at the LHC.

The Unification of the Forces

The standard model is based on the direct product of three gauge group : $SU(3)_C \times SU(2)_I \times U(1)_Y$ with different coupling in each sub-group. The model thus has in total 19 free parameters that cannot be predicted by the theory and need to be measure experimentally :

- Fermion masses ($m_{e,\mu,\tau}$ and $m_{d,u,s,c,b,t}$) ;
- CKM mixing angles (θ_{12}, θ_{23}, θ_{13}) and CP violation phase δ ;
- $U(1)_Y, SU(2)_I$ and $SU(3)$ gauge couplings (g, g' and g_S) ;

- QCD vacuum angle θ_{QCD} ;
- Higgs vacuum expectation value v ;
- Higgs boson mass m_H.

One could thus expect the existence of a more general theory with a smaller number of free parameters that would unify the strong and electroweak interaction at high scale, the Grand Unification (GUT) scale. The non-identical values of the coupling constants at the electroweak scale are the consequence of the running of the couplings as function of the energy scale. Technically this is achieved by solving the renormalization group equations for the three coupling constants starting at a common value at the GUT scale.

The hierarchy problem

The hierarchy problem is a problem is related to the large difference the weak interaction and the gravitational interaction (the weak interaction is of the order of 10^{24} times stronger than gravity). In the SM this inconsistency lead to problem related to the Higgs mass. When one compute the quantum correction to the Higgs mass, quadratic divergence proportional to the scale of the cut-off Λ (scale at which the theory stops to be applicable) appear. The correction to the Higgs mass to obtain the measured mass can thus be written :

$$m_{\mathrm{H}}^2 = m_0^2 - \frac{|\lambda_f|^2}{8\pi^2}\Lambda^2 + ... \tag{2.22}$$

where λ_f is the Yukawa coupling of a given fermion (which is directly proportional to its mass). If one wants to extend to SM to higher energy scales such as the Planck scale or the GUT scale the correction that has to be applied to the Higgs mass would become 30 order of magnitude larger than the measured mass of the Higgs. This implies that the scale Λ needs to be of the same order of magnitude as the Higgs mass or that an extreme fine-tuning is necessary for the mass of the Higgs m_0 and the correction to exactly compensate each other.

Dark matter

Discrepancy between cosmological observation from experiment such as Plank and theoretical prediction using the general relativity has led to the prediction of the existence of so called dark matter (DM). As a particle, dark matter does not interact electromagnetically (and thus cannot be observed in astrophysical/cosmological experiments). The effect of DM has been observed through its gravitational effect on galaxies and lensing effect. It has been predicted to constitute 26.8% of the energy in the universe, while SM particles would only contribute to 4.9%.

The standard model does not provide any candidate for dark matter since the only possible candidate, the neutrinos, have a mass too small to be able to contribute to the observed gravitational effect. The extension of the standard model could provide candidate for dark matter that could be produced in collider and detected as missing transverse energy in the final state of such event.

Matter-antimatter asymmetry

In the theory of the Big Bang, the universe should contain an equal amount of matter and antimatter [17]. Most observation tend to show the universe is almost entirely made of with matter.

In the standard model the baryon number is conserved, the only possible mechanism to transform matter into antimatter is the CP-violation in weak-interaction but the predicted asymmetry from this mechanism is too small compared to the one observed. BSM models might thus be necessary to explain the observed asymmetry.

2.2 Physics beyond the Standard Model

To find solution to the limitations presented in the previous section, BSM models have been developed. This section will present a particularly attractive model : Supersymmetry.

2.2.1 Supersymmetry

Supersymmetry (SUSY) [18] is a theory beyond the standard model based on a symmetry between bosons and fermions. The generators $\mathcal{Q}$ of such symmetry has to be an anti-commutating Weyl spinor such as :

$$\mathcal{Q}\,|Boson\rangle = |Fermion\rangle\,, \qquad \mathcal{Q}\,|Fermion\rangle = |Boson\rangle \tag{2.23}$$

Within this model a fermion can be associated to each boson via the action of $\mathcal{Q}$ and vice versa, the new particles obtained via this transformation are called superpartners. Together a particle and its superpartner form a supermultiplet. The generator $\mathcal{Q}$ being a Weyl spinor implied that they carry spin angular momentum $1/2$, since the spin is a geometrical property this means that Supersymmetry is a spacetime symmetry. $\mathcal{Q}$ commutes with the spacetime translation operator, for which the eigenvalues are the mass states, the particles and their superpartners should thus have the same masses. Similarly, $\mathcal{Q}$ commutes with the generators of gauge transformations, the particles and their superpartners should thus have the same quantum numbers : same hypercharge, same weak isospin and same color.

In this initial form SUSY implies an equal number of bosons and fermions, with the particles within the same supermultiplet having the same mass. This is in contradiction with the experimental result that did not observe any superpartners. Therefore, SUSY needs to be broken. To avoid the naturalness problem and avoid fine-tuning of the parameters, the mass differences should be kept small and of the order of the TeV.

Motivation

The radiative correction to the Higgs mass diverge quadratically with the scale of the cut-off. This can be solved with the addition of new particles. The contribution to the radiative corrections are positive for the bosons and negative for the fermion. With the addition of the superpartner, which have the same coupling to the Higgs as their SM equivalent, both contributions are going to cancel each other. This would solve the hierarchy problem as no radiative correction would have to be applied to the mass of the Higgs.

In the case of a broken supersymmetry additional term proportional to $\log(\Lambda)$ and to the mass differences of the particles in the same supermultiplets remain. This remaining radiative corrections that are proportional to $\log(\Lambda)$ [19] and can be written as :

$$m_{\mathrm{H}}^2 = m_0^2 - \frac{N_f|\lambda_f|^2}{4\pi^2}\left[(m_S^2 - m_f^2)\log\left(\frac{\Lambda}{m_S}\right) + 3m_f^2\log\left(\frac{m_S}{m_f}\right)\right] + ... \tag{2.24}$$

where m_S is the mass of the boson and m_f the mass of the fermion for one given supermultiplet. As long as the difference of mass stays small enough, for example of the order of the TeV, the correction can be kept small and no large fine-tuning is necessary.

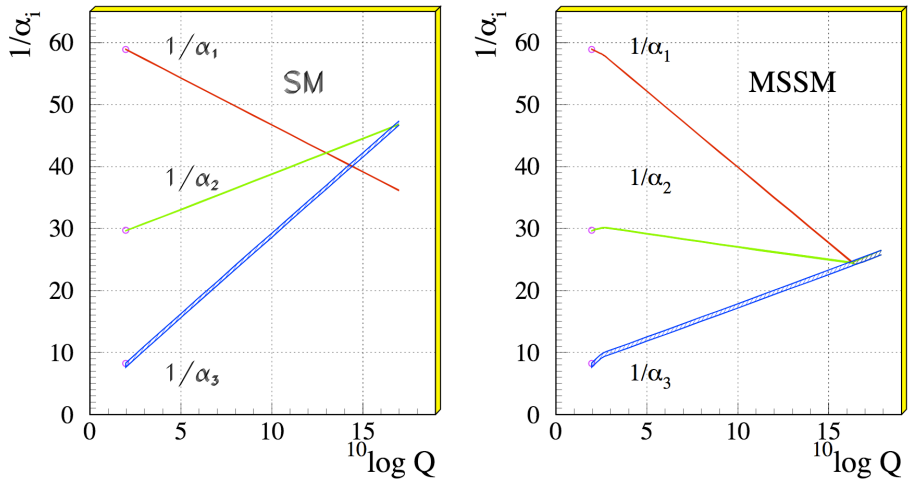

FIGURE 2.6 – Evolution of the coupling constant as a function of the energy scale (log scale). On the left, the coupling constants of the SM do not converge. On the right, coupling constants of the MSSM can be unified at the Grand Unification scale [20]

Another motivation for SUSY is that it can unify the coupling of all three interactions. Taking into account the radiative corrections, one can compute the running of the coupling constants with the scale. Figure 2.6, show the running of the coupling constant of the electromagnetism ($U(1)$), weak interaction ($SU(2)$) and strong interaction ($SU(3)$) for the SM (on the left) and the MSSM (on the right) for mass of the order of the TeV. The addition of the additional SUSY particles leads to a modification of the running of the coupling constants that result in a unification of the different coupling constant at large energy of the order of 10^{16} GeV.

R-Parity

In the standard model, due to gauge invariance both the Lepton number (L) and the Baryon number (B) are automatically conserved. In Supersymmetry couplings that violate such conservation can be found. If both L and B are violated this could result in a decay of the proton as shown in Figure 2.7. On the other hand the proton lifetime has been measured to be larger than $10^{29} - 10^{33}$ years in different experiments (depending on if a model dependent or independent approached is used). The proton can thus be expected to be stable and interactions that would lead to its decay thus have to be removed from the theory. This can be achieved by adding an additional symmetry to SUSY called R-parity [21]. This new quantum number is defined for each particle as : $R = (-1)^{3(B-L)+2s}$ where s is the spin of the particle. For a SM particle this number will be equal to 1 and for a sparticle it will be equal to -1.

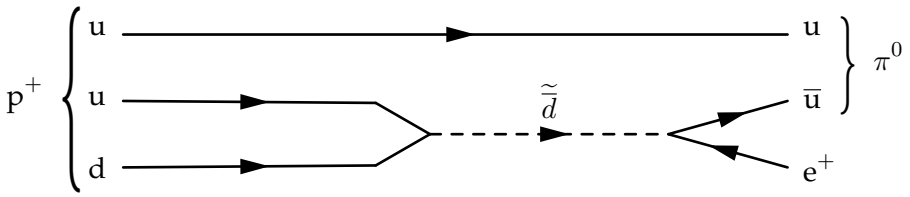

FIGURE 2.7 – Feynman diagrams for the decay of the proton in the absence of R-parity.

The addition of this additional symmetry has different consequences on the SUSY phenomenology :

- When sparticles are produced from SM particles they are always pair produced.
- A decaying sparticle can only decay into an impair number of particles.
- There must be at least one stable sparticle. This corresponds to the lightest sparticle, called the LSP (lightest supersymmetric particle).

If the LSP is neutral and only interacts weakly, like a neutrino, its direct detection in the detector will not be possible. The signature for such particle would rely on the presence of missing transverse energy in the event that would help identify events where sparticles were produced. If this LSP exists it would also be a good candidate for Dark matter as its properties would make it almost impossible to detect and its mass would be large enough to account for the observed cosmological effect.

Search of sparticle in the context of SUSY without R-parity are also ongoing. Such scenario would not be impossible if only B or L are violated or if the coupling violating the second one is infinitely small. In such scenario no stable LSP exist, which results in no dark matter candidate, and sparticles can decay into SM particles. This open up the possibility of direct observation of sparticle resonances.

MSSM

Starting from the standard model, one can construct its minimal supersymmetric extension (MSSM) [22]. In this theory superpartners of the standard models particles, generally called sparticles, are introduced. The list of the sparticles of the MSSM is shown in Table 2.1.

The superpartners of the quarks in this new model are called the squarks, those of the leptons, the sleptons and those of the gauge bosons gauginos. In the MSSM up and down type fermions cannot couple to the same Higgs doublet (holomorphism of the superpotential [18]). Therefore, at least two $SU(2)$ Higgs doublets are necessary. The superpartners of the Higgs fields are called higgsinos. Since right and left fermion don't have the same quantum number they need to be placed into different supermultiplet, for example the superpartner of the right top (t_R) will be the right stop ($\widetilde{t}_R$), for the sparticle right and left does not refer to the helicity of the particle but to the helicity of its partner. In this model the neutral electroweak gauginos ($\widetilde{W}^3$ and $\widetilde{B}_\mu$) and the neutral higgsinos ($\widetilde{H}_u^0$ and $\widetilde{H}_d^0$) mix to create four neutralinos : $\widetilde{\chi}_1^0$, $\widetilde{\chi}_2^0$, $\widetilde{\chi}_3^0$ and $\widetilde{\chi}_4^0$ with $\widetilde{\chi}_1^0$ the lightest one and $\widetilde{\chi}_4^0$ the heaviest one. Similarly, the charged electroweak gaugino ($\widetilde{W}^\pm$) and the charged higgsino ($\widetilde{H}_u^+$ and $\widetilde{H}_d^-$) mix to create two charginos : $\widetilde{\chi}_1^\pm$, $\widetilde{\chi}_2^\pm$.

Names	SM field	superpartner	SU(3)	SU(2)	U(1)
quark, squarks, (3 families)	$(u_L d_L)$	$(\widetilde{u}_L \widetilde{d}_L)$	3	2	$\frac{1}{6}$
	u_R	$\widetilde{u}_R$	$\overline{3}$	1	$-\frac{2}{3}$
	d_R	$\widetilde{d}_R$	$\overline{3}$	1	$\frac{1}{3}$
leptons, slepton, (3 families)	$(\nu_L e_L)$	$(\widetilde{\nu}_L \widetilde{e}_L)$	1	2	$-\frac{1}{2}$
	e_R	$\widetilde{e}_R$	1	1	1
higgs, higgsino	$(H_u^+ H_u^0)$	$(\widetilde{H}_u^+ \widetilde{H}_u^0)$	1	2	$\frac{1}{2}$
	$(H_d^0 H_d^-)$	$(\widetilde{H}_d^0 \widetilde{H}_d^-)$	1	2	$-\frac{1}{2}$
gluons, gluinos	g	$\widetilde{g}$	8	1	0
W boson, winos	$W^{\pm}, W^3$	$\widetilde{W}^{\pm}, \widetilde{W}^3$	0	3	0
B boson, bino	B_μ	$\widetilde{B}_\mu$	0	1	0

TABLE 2.1 – Particle content of the MSSM

In total the MSSM has 124 free parameters, due to this extremely large number of parameters scanning the MSSM in an analysis is extremely complicated. Additionally, some of the degree of freedom can lead to phenomenological inconsistency with what have been observed so far in particle physics experiment. To solve these problems, most of the analysis use the framework of the pMSSM (phenomenological MSSM) [23]. In this model, one can reduce the total number of parameters to 19 by imposing three extra phenomenological conditions on the MSSM :

- No additional source of CP violation.
- No flavor changing neutral current.
- Universality of the first two family of squarks and sleptons.

In this model 8 of the 19 remaining parameters correspond to the squarks masses breaking, 2 to the sleptons masses soft breaking, 3 to the gauginos masses soft breaking, 1 to the higgsino mass parameter, one to the ratio of the VEV of the two Higgs, one to the Higgs mass and finally three to the trilinear coupling of the third generation.

2.2.2 Sgluons

As explain in the previous section the MSSM encounter phenomenological problem related to the flavor violating process. Different extensions this model have thus been developed to try to solve this problem. One of these solution consist in extending the concept of R-parity to a $U(1)_R$ continuous symmetry called R-symmetry. The addition of this symmetry to the MSSM form the minimal R-symmetric supersymmetric Standard Model (MRSSM) [24]. In this model the R-symmetry is used to forbid the flavor violating terms and force the mass terms of the gauginos to be Dirac masses. This would also reduce the flavor-violating process amplitude as the running terms in the loop are proportional to $1/m_{\widetilde{g}}$ for Majorana masses and $1/m_{\widetilde{g}}^2$ for Dirac masses.

Having Dirac gauginos also result in other interesting consequences, for example let's consider a Dirac gluino. In that case the two degree of freedom from the gluons are not enough to construct a Dirac particle with four degree of freedom. The two additional degree of freedom can be recovered by adding a scalar partner to the gluino called the sgluon [25]. The resulting supermultiplet is thus composed of the gluon, the gluino and the sgluon.

The phenomenology of such scalar field is quite interesting, its R-charge is null like the other SM particles, it can thus decay into pairs of quarks or gluons via the mediation of sparticles. The different possible decay of the sgluon are shown in Figure 2.8.

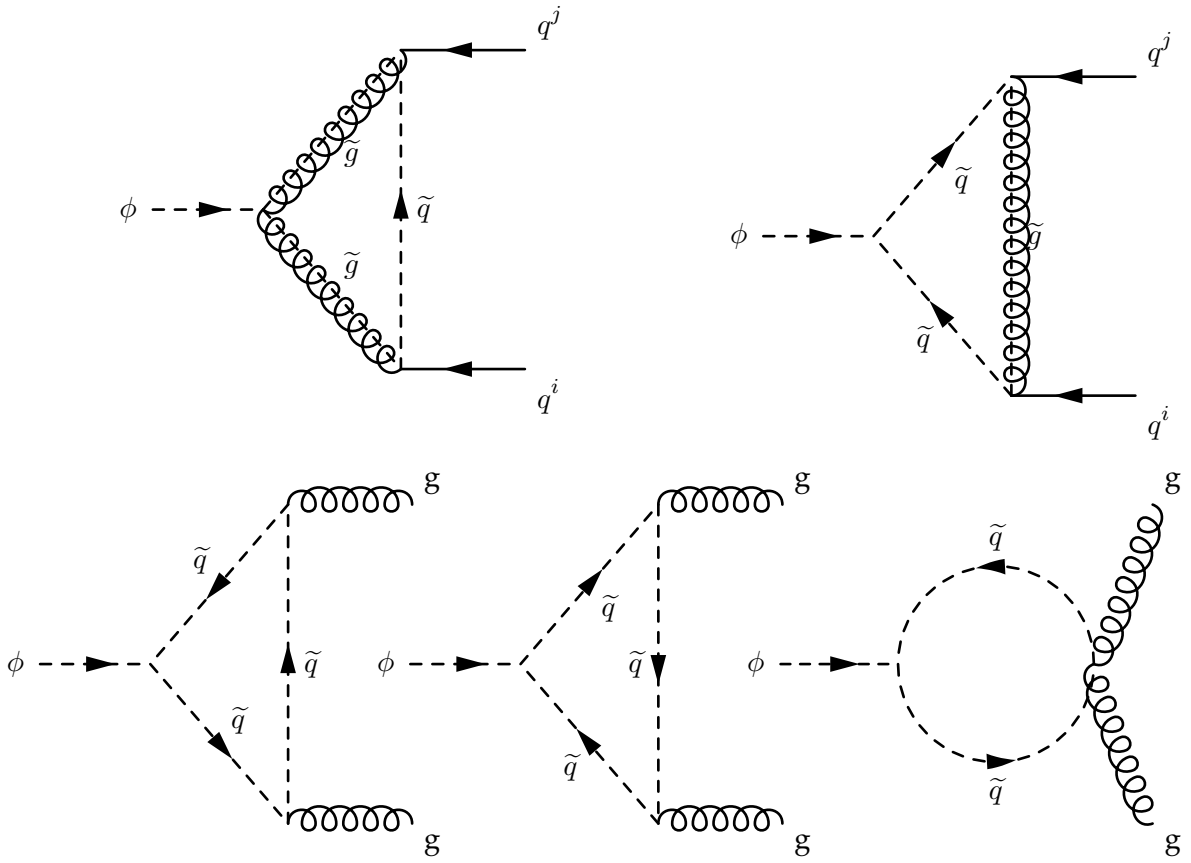

FIGURE 2.8 – Feynman diagrams for sgluon into a pair of quark or gluons.

Other model could lead to such scalar gluon, for example the N=1/N=2 hybrid supersymmetric model[26]. N refers to the number of time the generator of supersymmetry are included in the model. Most standard SUSY model are build with N=1. The hybrid model expand to N=2 in the gaugino sector. This lead to an additional gluino/sgluon super-multiplet in addition to the N=1 gluon/gluino super-multiplet. In that case if the gluino for both super-multiplet have the same masses they can also be combined to create a Dirac field.

2.2.3 4 Jets signature at the LHC

At the LHC, search for new phenomena in fully hadronic final states without missing transverse energy or leptons, is experimentally challenging due to the very large multijet production cross-section. It is thus important to probe this part of phase space for new physics as it is not usually explored in standard SUSY analysis. This section will focus on a signature with four jets in the final state forming two resonances.

Sgluon

Sgluons are scalar partner to Dirac gluino in the context of the MRSSM. These particles couple to quarks via loops of gluinos and squarks and they couple to gluons via loops of squarks as shown in Figure 2.8.

At the LHC, the sgluon can be pair produced. Each of the sgluons will then decay to either a pair of quarks or a pair of gluons, leading to a total of 4 jets. Since the sgluon carries a R-charge is null like the other SM particles the LSP is not involved in its decay chain leading to a final state with no missing energy. To identify such events one can use the fact that the four jets can be paired back into two resonances of the same mass corresponding the two sgluons.

Finally, as shown in the Figure 2.8, the sgluon can also couple to a pair of gluons, this mean that at the LHC production of single sgluon is possible and could be observed as a dijet resonances. This will not be studied in this document as the production cross section is model dependent and the continuum standard model background is large.

R-Parity violating stop

Four jets signature can also be found in SUSY without adding additional particles. If R-Parity is violated [27], some SUSY model would allow supersymmetric interaction of the form :

$$W_{RPV} = \frac{1}{2}\lambda_{ijk}L_iL_jE_k^c + \lambda'_{ijk}L_i\overline{Q}_j\overline{D}_k + \frac{1}{2}\lambda''_{ijk}\overline{U}_i\overline{D}_j\overline{D}_k + \mu_iH_uL_i \tag{2.25}$$

where λ_{ijk}, λ'_{ijk}, λ''_{ijk} are Yukawa couplings, and i, j, k are quark and lepton generation indices following the summation convention. The doublet of left-handed superfields of the lepton and quark are denoted by L_i and Q_i, respectively, while the E_i, U_i and D_j represent the singlet right-handed superfields of the lepton, up-type and down-type quarks, respectively. Finally, the Higgs superfield is denoted by H_u and couples to up-type quarks. We will consider here only a model in which one of the λ''_{ijk}, which allows vertices of a sfermion interacting with two fermions, are non zero.

In most model λ''_{ijk} are non null for $j \neq k$, the sparticle will therefore decay in two different quarks. Indirect experimental constraint of λ''_{ijk} already exist but are primarily valid for low squark mass and first and second generation coupling[28]. For this reason, we will in Chapter 5 focus on scenarios in which the stop is the lightest sparticle and can decay via the λ''_{ijk} coupling into pairs of quarks, resulting in the process : $\widetilde{t} \longrightarrow \overline{q}_j\overline{q}_k$.

At the LHC, stops can be pair produced during the collision. The stops can then decay via RPV coupling into pairs of quarks. In particular two type of decay will be considered, the decay to a b-quark and a strange quark with the coupling λ''_{323} and the decay into a strange quark and a down quark with the coupling λ''_{312}. The Feynman diagram corresponding to the interactions is shown in Figure 2.9. The decay into b-quarks are particularly interesting as the b-tagging

capability of the detector, will provide additional information to differentiate the signal and the background.

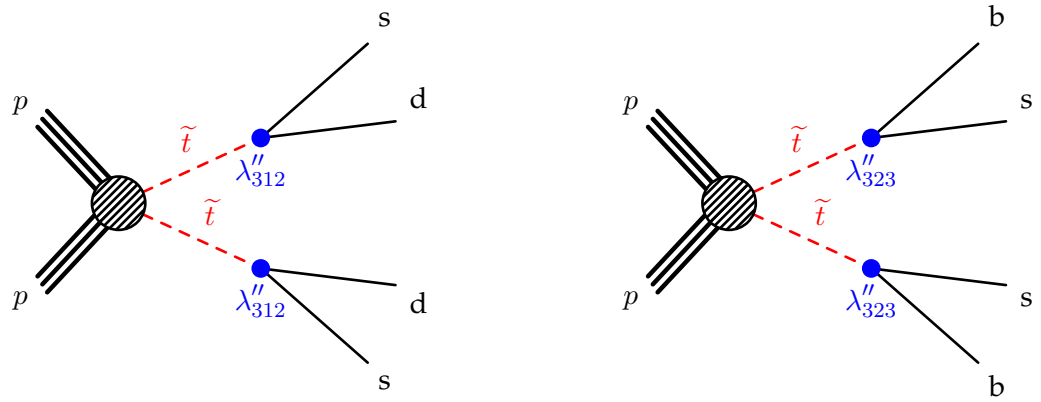

(a) $\widetilde{t}\widetilde{t} \to (\mathrm{sd})(\mathrm{sd})$ (b) $\widetilde{t}\widetilde{t} \to (\mathrm{bs})(\mathrm{bs})$

FIGURE 2.9 – Diagrams depicting the direct production of stop quark pairs decaying into s and an d quark or to a b and an s quark through the RPV λ'' coupling.

Search of such signature have already been performed in ATLAS and CMS. For ATLAS a search using data from 2015 and 2016 (corresponding to $37.14\,\mathrm{fb}^{-1}$). Stop with a mass lower than $410\,\mathrm{GeV}$ decaying into two light jet have excluded with a 95% Confidence Level (CL) while stop decaying a b-quark and a light quark have been excluded up to a mass of $650\,\mathrm{GeV}$[29]. CMS also performed a similar search using data from 2016 (corresponding to $35.8\,\mathrm{fb}^{-1}$) and exclude stop mass lower than $520\,\mathrm{GeV}$ [30].

Chapitre 3

The ATLAS Detector and the HL-LHC upgrades

This chapter will present first the LHC and the ATLAS detector. Then, the upgrade of the LHC to the HL-LHC [31] as well as the upgrade of the ATLAS detector to accommodate the increased luminosity will be shown. Finally, the reconstruction of an event in ATLAS will be explained.

3.1 The Large Hadron Collider

The Large Hadron Collider (LHC) is a circular collider with a 27 km circumference. The collider was designed to record pp collisions with a center of mass energy of $\sqrt{s} = 14\,\mathrm{TeV}$, additionally lead-lead and proton-lead collisions were also recorded to study the quark-gluon plasma. After the project was approved in 1994, its construction started in 2000 at CERN in the tunnel of the Large Electron Positron (LEP) accelerator. Since early 2010 the LHC has been taking data, the objectives of its program include, the discovery of the Higgs bosons which was achieved in 2012, the study of its properties and the search for BSM physics as well as precise measurements of the SM.

3.1.1 The Accelerator Complex

The LHC is the last step of the CERN acceleration chain, shown in Figure 3.1. First the protons are obtained via the ionization of hydrogen gas. The protons then first go through the Linac 2, a $30\,\mathrm{m}$ long linear accelerator which accelerates the protons up to an energy of $50\,\mathrm{MeV}$. After leaving the Linac, the protons goes through the Proton Synchrotron Booster (PSB), a series of four superimposed synchrotron rings with a $157\,\mathrm{m}$ circumference, which brings the energy of protons to $1.4\,\mathrm{GeV}$. This increase in energy allows for an improved injection rate in the next accelerator the Proton Synchrotron (PS) since the low energy of $50\,\mathrm{MeV}$ used to limit the amount of protons the PS could accept. The PS is a circular accelerator with a $638\,\mathrm{m}$ circumference, it increases the energy of the protons up to $25\,\mathrm{GeV}$. The protons then go through the Super Proton Synchrotron (SPS), a $6\,\mathrm{km}$ accelerator that brings the protons energy up to $450\,\mathrm{GeV}$ before being injected into the LHC. In addition to providing protons for the LHC, it also provides particles for other CERN based experiment such as AWAKE, NA61, NA62 and also provide particles to the test beam area used by the teams from the LHC experiments to test the detectors that will be used for the future upgrades.

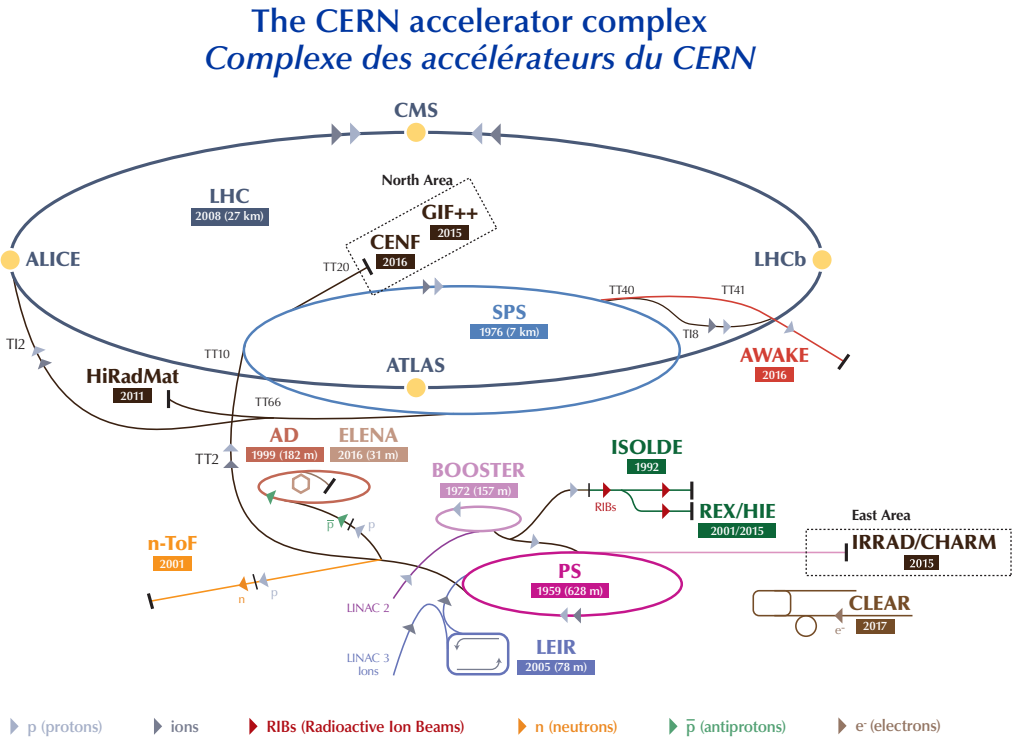

FIGURE 3.1 – The LHC accelerator chain[32].

The protons in this acceleration chain are grouped into bunches, each bunch containing 1.15×10^{11} protons. All bunches are separated by $25\,\mathrm{ns}$, the time period of the collisions. It takes approximately two hours to fully fill the LHC as it requires to fully fill multiple times the smaller accelerators of the complex to fill the LHC. Due to the large amount of protons in each bunch, the probability of having two protons interact with each other during a bunch crossing can be high enough to observe more than one interaction per bunch crossing. This is known as the pile up, additional collisions happening at the same time as the one of interest. This will affect the reconstruction of the events in the detector.

3.1.2 Principle of the Accelerator

The LHC follow the same basic design as most of the circular accelerator, a magnetic field is used to keep particles on a circular orbit, on this orbit the particles encounter an electric field that will result in their acceleration. Since the LHC collide protons with protons, the design is a bit more complex than in the more classical particle-antiparticle colliders. Indeed, in that case two beam-pipes are necessary one for the proton going in one direction and another for the proton going in the other. To generate a magnetic field in each of the ring, two-in-one superconductive dipole magnets are used. The magnets operate at a temperature of $1.9\,\mathrm{K}$ and produce a magnetic field of $8.3\,\mathrm{T}$. In total 1232 of the $15\,\mathrm{m}$ long magnets are installed on the LHC. In addition to the dipoles, the LHC is also equipped with 392 quadrupoles. These are used to focus the beam before the collision in order to increase the resulting interaction rate.

While the magnetic system allows the transport of the particles along the ring, an electric field is necessary to accelerate the particles. This is provided by the Radio Frequency (RF) Accelerating system (ACS), 16 of such cavities are installed at the LHC (8 for each ring). Each of these cavities are equipped with a klystron and a waveguide, the klystron uses an electron beam to generate an electric wave with a frequency of $400\,\mathrm{MHz}$, this wave is then transferred

to the cavity via the waveguide where it will accelerate the protons. Each cavity creates an accelerating voltage of the order of $2\,\mathrm{MV}$ for a total of $16\,\mathrm{MV}$ per ring. It takes approximately 20 minutes to accelerate the proton from $450\,\mathrm{GeV}$ to $6.5\,\mathrm{TeV}$.

With this accelerating system an energy in the center of mass of the order of $\sqrt{s} = 13\,\mathrm{TeV}$ can be achieved. Achieving a large $\sqrt{s}$ is important as the larger this value the heavier the particles produced in the collision can be, which enable us to probe higher energy scales for discovery or to constrain physics models.

3.1.3 Luminosity and Pile-up

One of the most important parameters [33] when observing particle collisions in an accelerator is the luminosity. This quantity which can be express as events per time per area is directly proportional to the number of event that can be observed at the LHC via the following formula :

$$\mathcal{L} = \frac{1}{\sigma}\frac{dN}{dt} \tag{3.1}$$

where σ correspond to the cross section of a given physical process and N the number of time this process occur. Nowadays many physics analysis result are still statistically dominated, which means that what limits their precision is the lack of statistics. A larger luminosity would lead to a larger number of events observed in the same amount of time and would result in an improved precisions for such an analysis. Additionally, if a signal has a small cross section σ, it might remain unobserved at the LHC. Increasing the luminosity would make such signal accessible.

The luminosity is directly related to the parameters of the beams and the quality of the beam crossing :

$$\mathcal{L} = \frac{n_1 n_2 f \mathrm{N}_b \mathrm{F}}{4\pi\sigma_x\sigma_y} \tag{3.2}$$

where n_1 and n_2 are the number of protons in the two colliding bunches, N_b is the number of bunches per beam, f is the revolution frequency of the bunches, F is a geometrical factor accounting for the collision angle of the beam and σ_x and σ_y correspond to the transverse size of the beam at the collision point. A summary of the nominal value of these parameters can be found in Table 3.1. Those parameters only correspond to the average value, the real value can vary bunch to bunch and with time.

For many analyses, it is also important to know precisely the value of the integrated luminosity, for example if one want to measure precisely the cross section of a specific physic process. As shown in Equation 3.1, by dividing the number of time the process was observed by integrated the luminosity on the data taking period, one can directly calculate the cross section of the process. In that case, any uncertainty on the luminosity would result in an uncertainty on the cross section. To measure precisely the luminosity specific detector, called luminometers, have been installed in the different experiments.

As the luminosity increases, the number of interactions per bunch crossing also increases. During a bunch crossing one interaction, called hard-scatter interaction, will correspond to a signal of interest. The presence of the additional pile-up will result in a decrease of the performance of the detector as the particles originating from the interactions can contaminate hard scatter events, resulting in a worst reconstruction of the objects. The evolution of the number

pile-up interactions per bunch crossing can be expressed with the following formula :

$$\mu = \frac{\mathcal{L} \times \sigma_{inel}}{\mathrm{N}_b f} \tag{3.3}$$

were σ_{inel} corresponds to the total inelastic cross section ($\sim 70\,\mathrm{mb}$).

The LHC has been operating since 2010. The data taking period from 2011 to 2012 is referred to as Run 1 while the period between 2015 and 2018 is referred to as Run 2, the period following the next re-start of the LHC in 2021 will be Run 3. Between the different periods of data taking are long shutdowns (LS) of a few years, the purpose of these shutdowns is to allow time to upgrade the accelerator to reach higher energy and luminosity as well as to upgrade the detectors to improve their performance and enable them to maintain good performance with the new collision conditions.

Figure 3.2 (a) shows the integrated luminosity collected by the ATLAS experiment during the years of the Run 1. During Run 1 an integrated luminosity of $\mathcal{L} \sim 25\,\mathrm{fb}^{-1}$ was recorded at an energy of 7 and $8\,\mathrm{TeV}$ (a bit more than half of the nominal energy of the LHC). The pile-up for this run can also be seen in Figure 3.2 (b), its average value is of 20 interactions per bunch crossing.

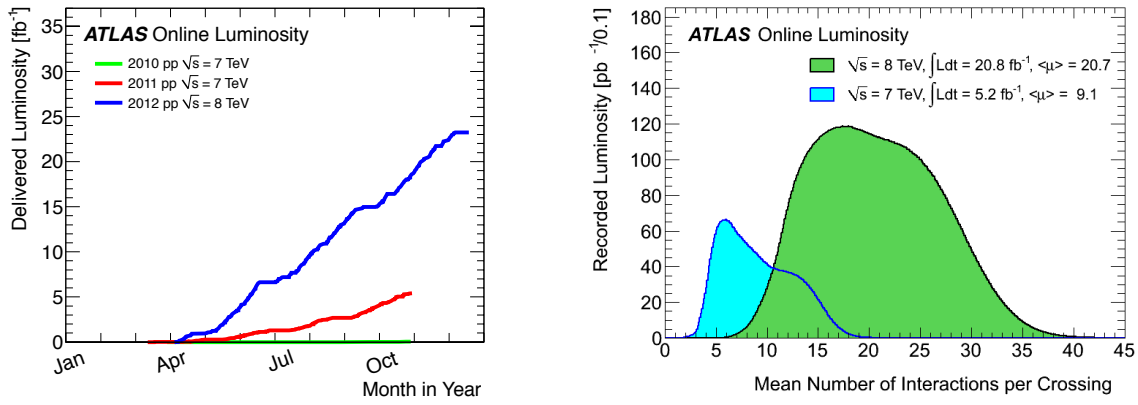

(a) (b)

FIGURE 3.2 – Profile of integrated luminosity and average number of interactions per bunch crossing in Run 1[34].

Figure 3.3 presents the same information for Run 2. During the Run 2 the energy was increased up to $13\,\mathrm{TeV}$ (just below the nominal energy of the LHC) and a total integrated luminosity of $\mathcal{L} = 146.9\,\mathrm{fb}^{-1}$ was registered, almost six times more than during Run 1. For this run the pile-up was increased to an average of 34, but the main pile-up related challenge during Run 2 was the increase of the maximum $\langle\mu\rangle$ from 40 in Run 1 up to 70. In these condition the operation and calibration of the detectors became challenging.

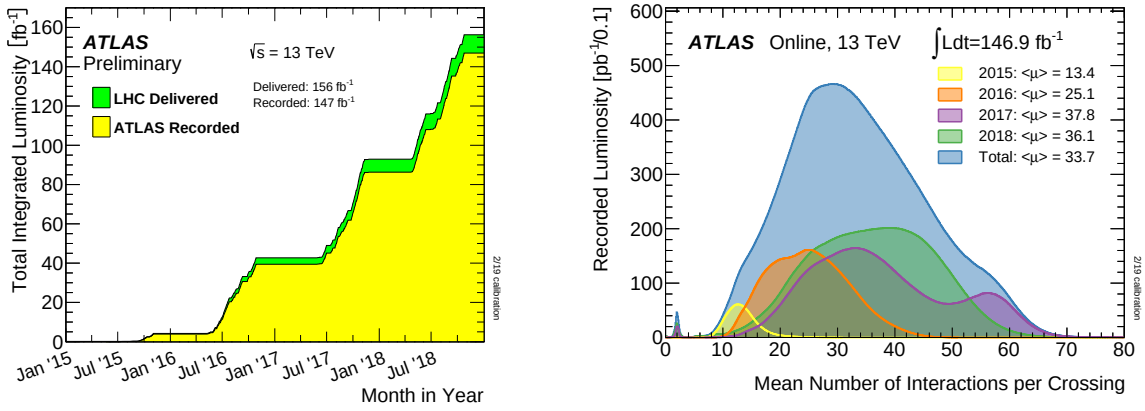

(a) (b)

FIGURE 3.3 – Profile of integrated luminosity and average number of interactions per bunch crossing in Run 2[35].

3.2 The ATLAS Detector

To exploit the collisions produced at the LHC seven experiments have been built, each focusing on different aspect of high energy physics :

- ATLAS [36] (A Thoroidal LHC Apparatus) is general purpose experiment with physics programs oriented toward the measurement of the Higgs boson properties, new physics searches, and study of the Standard Model.
- CMS [37] (Compact Muon Solenoid) follows the same physics program as ATLAS, having two similar experiments with different technology ensure the repeatability of the measurements made by these two experiments.
- LHCb [38] is a precision measurement experiment dedicated to the study of B-physics, looking for example at CP violation.
- ALICE [39] (A Large Ion Collider Experiment) is an experiment motivated by the study of quark-gluon plasma produced in heavy ions collisions.
- LHCf [40] (LHC forward) is a forward physics (close to LHC beams) program aiming at the study of the origin of ultra-high energy cosmic rays.
- TOTEM [41] (TOTal Elastic and diffractive cross section Measurement) is an experiment installed on both side of CMS that measure low angle particle, it aims at measuring the total cross-section, elastic scattering, and diffractive processes in proton-proton collisions.
- MoEDAL [42] (Monopole and Exotics Detector at the LHC) is an experiment installed on both side of LHCb that also measure low angle particle, it aims at discovering magnetic monopole and other long-lived exotic particle that could be produced in the forward region.

The position of these experiments on the LHC can be seen in Figure 3.1. In the rest of this section, the ATLAS detector will be presented.

The ATLAS detector consists of sub-detectors as illustrated in Figure 3.4 :

- The Inner Detector. Composed of several high granularity tracking detectors, it is used reconstructs the trajectory and the momentum of the charged particles using the curvature of the trajectory in the magnetic field. It is also used to identify the primary and secondary vertices and separate pile vertices from the hard-scatter one.
- The Calorimeters. Use a combination of active material and absorber to induce showering, for the measurement of the energy of the particles.
- The Muon Spectrometer. Detector placed at the periphery of the ATLAS detector, used to identify muons and complement the information of the Inner Detector for their reconstruction.

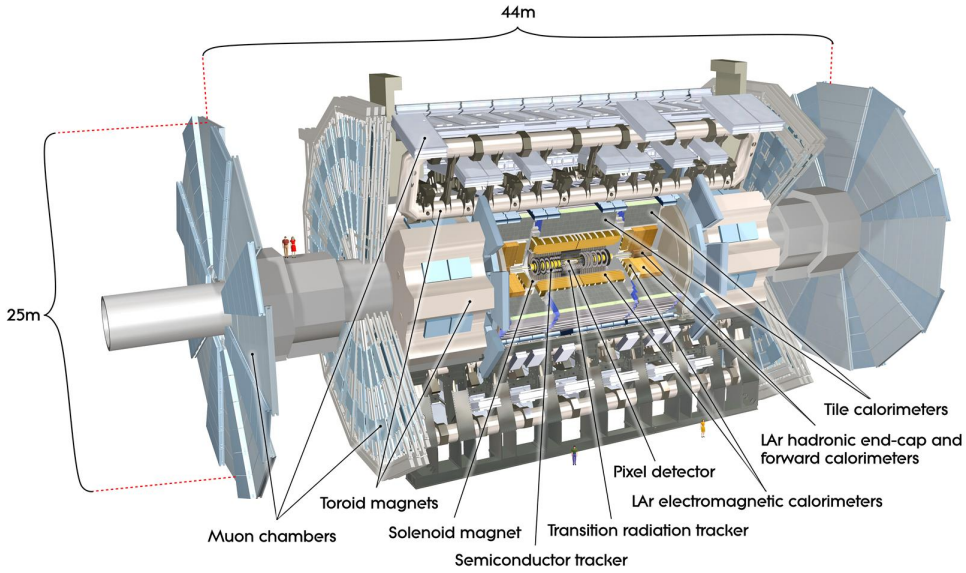

FIGURE 3.4 – Schematic view of the ATLAS detector.

During the bunch crossing the particle that are colliding are the partons inside protons and not the protons themselves. It is thus impossible to precisely to know the momentum of the colliding particles along the beam axis. On the other hand, since the beam are traveling along the beam axis their momentum in the transverse plane is close to 0. The sum of the transverse momentum ($p_{\mathrm{T}}^2 = p_x^2 + p_y^2$) of the particles produce during the collision should be 0, this can be used reconstruct objects that are not leaving energy in the detector such as neutrinos.

Cylindrical coordinate (θ, ϕ, z) are used in the ATLAS experiment. In this coordinate system, z is the direction of the beam axis. The angle ϕ is defined in the transverse plane as the angle with the horizontal plane ($-\pi < \phi < \pi$, with positive π corresponding to the top half of the detector). The angle θ is the angle with the beam axis, it can sometime also be replaced with r which correspond to the distance to the beam axis at the position z. The angle θ is often replace with the pseudo-rapidity η, it is defined as :

$$\eta = -ln(\tan\frac{\theta}{2}) \tag{3.4}$$

A pseudo-rapidity $\eta = 0$ corresponds to the center of the detector while $\eta \to \infty$ corresponds to the beam axis. The central part of the ATLAS detector correspond to the region for which $|\eta| < 2.5$ while the forward region correspond to $|\eta| > 2.5$. Using θ and ϕ it is then possible to

go from the transverse momentum to the momentum in the Cartesian coordinate :

$$\begin{aligned} p_x &= p_{\mathrm{T}} \cos\phi \\ p_y &= p_{\mathrm{T}} \sin\phi \\ p_z &= p_{\mathrm{T}} \sinh\eta \\ |\vec{p}| &= p_{\mathrm{T}} \cosh\eta \end{aligned} \tag{3.5}$$

In this cylindrical coordinate system the distance between two point will be expressed as :

$$\Delta R = \sqrt{\Delta\eta^2 + \Delta\phi^2} \tag{3.6}$$

In addition to cylindrical coordinates, Cartesian ones (x, y, z) can occasionally be used, for example when considering a detector that is only in the transverse plane. In that case, x correspond to the horizontal coordinate in the transverse plane and points toward the center of the LHC, y correspond to the vertical axis pointing upward and finally z correspond to the direction of the beam-pipe as such as this basis is right-handed.

3.2.1 Inner detector

The Inner Detector (ID) [43] consists of a succession of different layers of silicon sensors immersed in a $2\,\mathrm{T}$ magnetic field and has a coverage up to $|\eta| < 2.5$. An overview of the inner detector is shown in Figure 3.5.

When a charged particle interacts with the material of the ID they generate a hit, along its trajectory in the ID the particle will thus create many hits in each of the different layers. These hits can then be combined to reconstruct the trajectory (tracks) of the particles. The expected resolution as function of the p_{T} of the particle can be express as :

$$\frac{\sigma_{p_T}}{p_T} = 0,05\%\ p_T\ [GeV] \oplus 1\% \tag{3.7}$$

These tracks can then be used to reconstruct the interaction vertices at which the particle were produced. This precise reconstruction of the primary and secondaries vertices is essential to many physics analysis as it allows to minimize the effect of pile-up and ensure a good reconstruction of the events.

The ID is itself composed of four different detectors utilizing different technologies :

Insertable B-Layer

The Insertable B-Layer (IBL) [44] is the most central part of the ID, it was installed during the first long shutdown between the Run 1 and 2. It was inserted below the Pixels to compensate the degradation of the ID due to irradiation and to improve the track reconstruction precision. It is particularly useful for event containing B-hadrons for which the tracks might appear to originate from a secondary vertex due their long lifetime. For this reason the IBL has an important role in $b-tagging$ algorithm, improving its performance by 10%. To be able to operate in this high radiation environment the IBL use 3D sensors and CMOS technology.

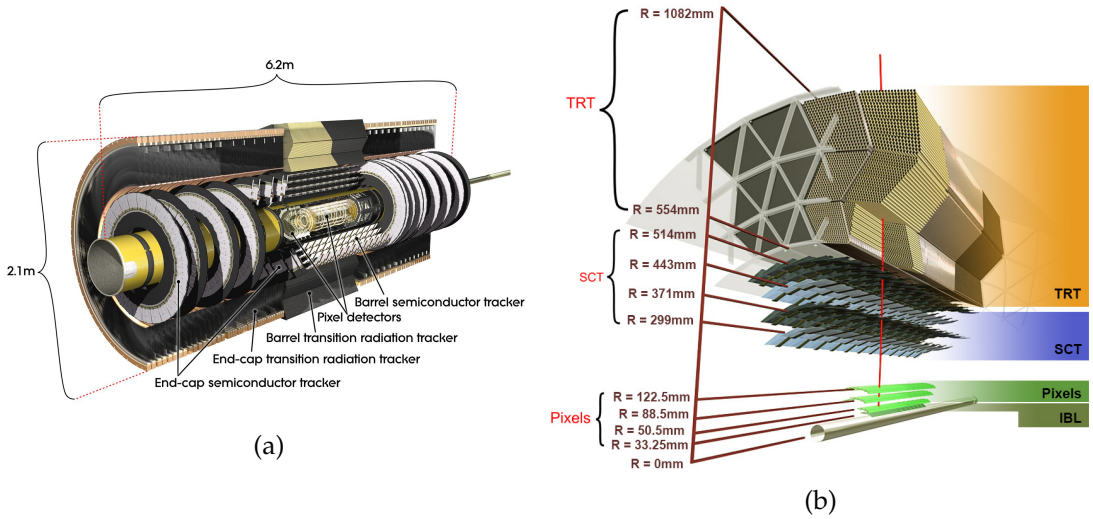

FIGURE 3.5 – Overview of the ATLAS Inner Detector.

Pixel detector

The second detector of the ID is the Pixel detector, it surrounds the IBL and is composed of 3 layers of pixels with extra disc place in the forward region around beam-pipe to improve the coverage up to $|\eta| = 2.5$. The different layers are place at respectively $50.5\,\mathrm{mm}$, $88.5\,\mathrm{mm}$ and $122.5\,\mathrm{mm}$ from the center of the beam pipe. The layers are composed of silicon pixel modules that are segmented in R and z with a minimum active size of $50\,\mu\mathrm{m} \times 400\,\mu\mathrm{m}$. This small granularity allows for an excellent resolution of $12\,\mu\mathrm{m}$ in R and $50\,\mu\mathrm{m}$ in z.

The silicon pixels are made of p-n junction on which a bias voltage is applied that create an electric field. Once a particle cross the pixel it creates pair of electrons and holes along its trajectory, under the effect of the field the electrons and holes will start to drift in the junction toward the cathode and anode respectively. This drift will induce an electric current that will be output as the signal.

SemiConductor Tracker

The next layer is called the SemiConductor Tracker (SCT), it operates with the same silicon technology as the pixel detector using strips instead of pixels. It is also divided, like the pixel, into a central part and forward disk providing a coverage up to $|\eta| = 2.5$. It is composed of 4 layers respectively at radii of $299\,\mathrm{mm}$, $371\,\mathrm{mm}$, $443\,\mathrm{mm}$ and $514\,\mathrm{mm}$. The strip are have a width $80\,\mu\mathrm{m}$ and a length of $64\,\mathrm{mm}$, they thus provided an extremely good resolution in R ($17\,\mu\mathrm{m}$) but a poor one in z ($558\,\mu\mathrm{m}$).

Transition Radiation Tracker

The final component of the tracker is the Transition Radiation Tracker (TRT). It surrounds the rest of the ID and provide a coverage up to $|\eta| = 2$. This detector is composed of a superposition of drift tubes layers disposed parallel to the beam axis. The drift tube are filled with a gaseous mix of 70 Xenon, 20 % methane and 10 % CO2, a charged particle propagating though the gas will ionize it resulting in the emission of electrons. These drifting electrons are then collected

by a string at the center of the tube acting as an anode, similar to the silicon detector this drift will result in an electric current that correspond to the output signal.

The TRT has the worst resolution of all the detectors in the ID but can provide up to 36 measurements per tracks which help the track, momentum and particle reconstruction. In addition, it can also be used to discriminate between electron and pion tracks. When a charged particle go through the transition between two materials with different dielectric constants, a transition photon is emitted. This phenomenon, called transition radiation will depend on the mass of the particles, by measuring the radiation emitted when particle enters the gas inside the drift tube it is possible differentiate between electrons and pions.

3.2.2 Calorimeters

The Calorimeters are placed surrounding the ID and are used to measure the energy of the photons, electrons and hadrons. This detector has been designed to be deep enough to contain the entire particle shower, its coverage goes up to $|\eta| = 4.9$ to ensure that all the energy of the event can be measured. The calorimeter system of ATLAS is composed of three different calorimeters :

- The Electromagnetic Calorimeter, provide precision measurements of electrons and photons, as well as their identification.
- The Hadronic Calorimeter, reconstruct and measure the energy of jets of hadrons, it is also used to contain the showers before they reach the muons spectrometer.
- The Forward Calorimeter, with a coverage of $3.2 < |\eta| < 4.9$ it measures the energy in the forward region completing the coverage of the calorimeter.

The different detectors can be seen in Figure 3.6.

The calorimeters in ATLAS are sampling calorimeter, they are built of a succession of active layers and absorber layers. In calorimeters the absorbers are used to develop the shower while the active materials are used to measure the signal. The advantages of the calorimeters is that they can be segmented, helping the particle reconstruction and identification, and can contain all type of shower in a reasonable size. Their main disadvantage is that since some of the energy of the particles are deposited in the absorber the stochastic term of the calorimeter energy resolution is degraded.

The energy resolution of a calorimeter can always be express as follow :

$$\frac{\sigma_E}{E} = \frac{a}{\sqrt{E}} \oplus \frac{b}{E} \oplus c \tag{3.8}$$

where :

- σ_E is the energy resolution.
- E is the reconstructed energy.
- a is the stochastic term. This corresponds to the statistical fluctuation of the shower, the quantum fluctuation of the signal and the effect of the sampling.
- b is the noise term. This corresponds to the electronic noise and the effect of the pile-up.
- c is the constant term. This corresponds to the effect of the calibration, the geometry, the loss of energy before the calorimeter and the particle escaping the calorimeter.

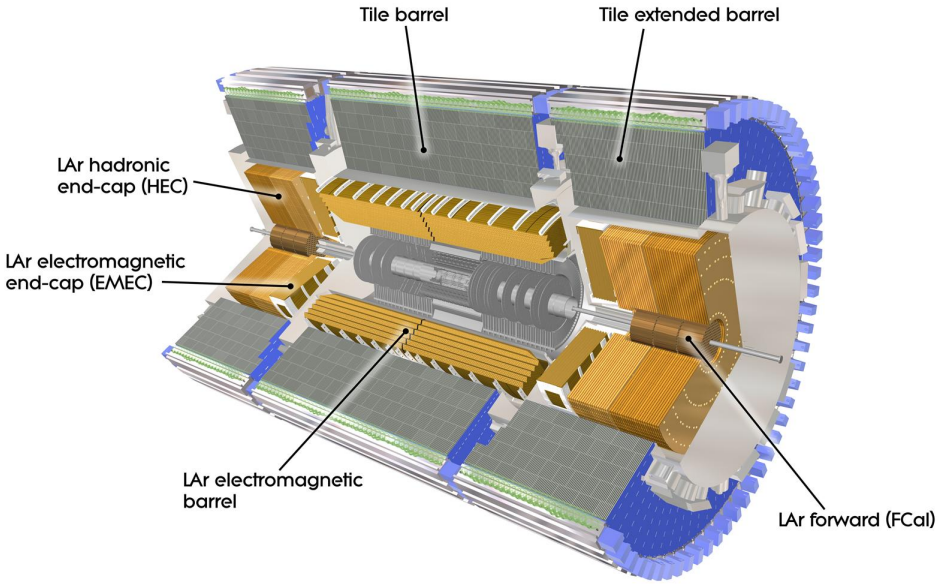

FIGURE 3.6 – Schematic view of the ATLAS Calorimeter system.

Electromagnetic calorimeter

The ATLAS electromagnetic calorimeter (ECAL), is a Liquid Argon Calorimeter (LAr) [45] composed of two parts, the barrel one that cover everything up to $|\eta| = 1.475$ and the end-cap one $1.375 < |\eta| < 3.2$. Both of these parts use liquid argon for active material and lead for absorber. The electrons and the photons will initiate electromagnetic shower as they go through the lead absorber. The liquid argon will be ionized by the shower, the resulting charges will then drift toward the electrodes and create a signal.

The barrel of the LAr is composed of 3 layers with different granularity, as the showers develop the granularity decreases. This design lead to a fine granularity in the first layer allowing good pointing capability. This fine granularity also allows particle identification, for example it can be used to separate isolated photons from photons originating from pions decay. Each of these layers is disposed in accordion structure, which enables a full ϕ coverage without azimuthal cracks.

For the electromagnetic calorimeter barrel, the resolution is [45] :

$$\frac{\sigma_E}{E} = \frac{10.7\%}{\sqrt{E}} \oplus 0.5\% \tag{3.9}$$

the noise term is neglected in this equation, it is dominant at low energy and is of the order of $270\,\mathrm{MeV}$. These are testbeam results, in ATLAS the resolution is also affected by the material of the inner detector in front of the calorimeter.

Hadronic calorimeter

The hadronic calorimeter [46], is placed around the LAr it is composed of three different parts, the central barrel part for $|\eta| < 1$, the extended barrel for $0.8 < |\eta| < 1.7$ and the end-cap part for $1.7 < |\eta| < 3.2$. The hadronic calorimeter is used to detect hadrons, which interact

via strong and electromagnetic interactions (in contract to electrons and photons which only interact via electromagnetic interaction). The barrel part use steel as absorber and scintillating tiles as active region, while the end-cap part use copper as absorber and liquid argon as active material.

The resolution of this detector can be written as :

$$\frac{\sigma_E}{E} = \frac{50\%}{\sqrt{E}} \oplus 3\% \tag{3.10}$$

The interactions of hadrons with matter are more complex than the ones of electrons and photons. Some of the hadrons energy is therefore not measured in the calorimeter resulting in a larger stochastic term. The noise of the hadronic calorimeter is estimated to be of the order of $150\,\mathrm{MeV}$.

Forward calorimeter

The last element of the calorimeter system is The Forward Calorimeter (FCal). It is installed in the forward region ($3.1 < |\eta| < 4.9$), its main purpose is to enhance the coverage of the ATLAS detector. It is segmented into three disk layers, all of them use liquid argon as active material. The first layer use copper as absorber which allows a good reconstruction of the electromagnetic shower while the next two use tungsten to reconstruct more precisely the hadronic shower.

The detector allows the reconstruction of jet of particles at small angles, while the jets might not always be directly important for the analysis they are necessary to compute the total energy of the event and thus be able to reconstruct the Missing Transverse Energy corresponding to particles that were not detected in ATLAS.

3.2.3 Muon spectrometer

The muons are the only particles that can go through the ID and the Calorimeter system without being absorbed. To detect them and to precisely measure their momentum a specific detector need to be installed. The Muons Spectrometer (MS) [47] is installed as the outermost layer of ATLAS with a coverage up to $|\eta| < 2.7$, Figure 3.7 show a schematic view of the MS. In total the MS utilize four different types of detectors, two precision chambers used to measure precisely the position of the muons and two trigger chambers used by the triggering system :

- The Monitored Drift Tubes (MDTs), installed both in the barrel and the end-caps. They provide a precise measurement of tracks coordinates in most of the $|\eta|$ range ($|\eta| < 2.7$).
- The Cathode Strip Chambers (CSCs), installed in the end-caps. These multiwire proportional chambers are used to improve the reconstruction of the muon in forward regions ($2 < |\eta| < 2.7$), in which the event rate is too high for the MDTs.
- The Resistive Plate Chambers (RPCs), installed in the barrel, has a coarser granularity compare the MDTs but can be read at the trigger level as part of the muon triggering system.
- The Thin Gap Chambers (TGCs), serve a similar purpose to the RPCs but in the endcaps.

The trigger chambers can also be used to measure the track coordinate in the direction orthogonal to that measured by precision chambers (orthogonal to the bending direction).

To reconstruct the momentum of the muons a strong magnetic field has to be applied to the MS, as it was the case for the ID. It is respectively of $1\,\mathrm{T}$ and $0.5\,\mathrm{T}$ in the barrel and endcaps, with this a resolution of the order of 10 % can be achieved for muons of $1\,\mathrm{TeV}$ and a resolution of 3 % can be achieved for muons of $300\,\mathrm{GeV}$. The information from the MS can also be combined with the momentum measurement in ID to improve this resolution.

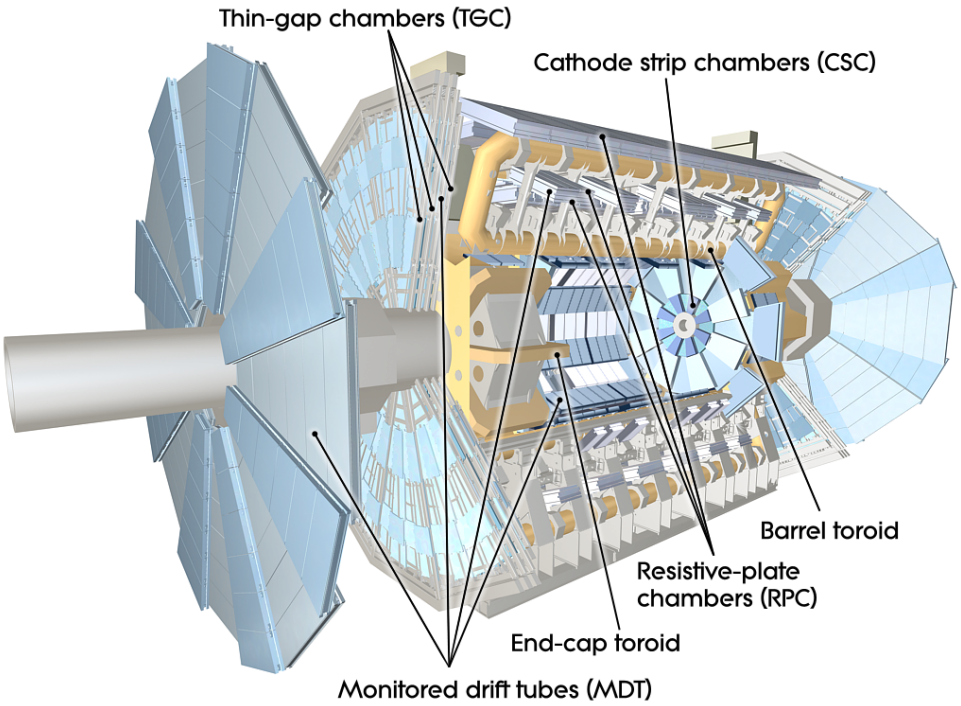

FIGURE 3.7 – Schematic view of the muon spectrometer system.

3.2.4 Trigger

The collision rate in ATLAS is of the order of $40\,\mathrm{MHz}$. This frequency is extremely large compared to the event recording frequency of the ATLAS detector which is, in nominal condition of the order of $1\,\mathrm{kHz}$. To ensure that most of the events useful for physics analysis are kept while rejecting the uninteresting events, a trigger system [48] is used. The layout of this trigger system can be seen in Figure 3.8. The trigger system operate in two time, first the Level 1 trigger (L1) and the High Level Trigger (HLT).

The L1 trigger is a hardware based trigger, it is used to identify region of interests (RoIs) in the calorimeter and the MS, if no RoIs were identified the event is then discarded. At this level the calorimeter is read with a coarser granularity and the longitudinal segmentation is ignored to increase the speed at which this trigger takes a decision. This allows to reduce the event rate from $40\,\mathrm{MHz}$ down to $100\,\mathrm{kHz}$. This operation is performed in $2.5\,\mu\mathrm{s}$, afterwards the identified RoIs are sent to the HLT.

The HLT use more complex algorithm to reconstruct the object in the different RoIs using the information of the full ATLAS detector in the RoIs. At this level more complex objects can be reconstructed such as tracks, electrons, muons and jets. After this step only the events with a topology interesting for physics are kept. The events are then associated with different trigger menus corresponding to the physics topologies associated to the event. Examples for these menus include : N jets with a minimum p_{T} of Y, one muon with a p_{T} of at least $50\,\mathrm{GeV}$, 2

electrons of at least 20 GeV, ... After applying the HLT the event rate is decrease to 1 kHz, events are recorded on disk for further offline reconstruction and analysis.

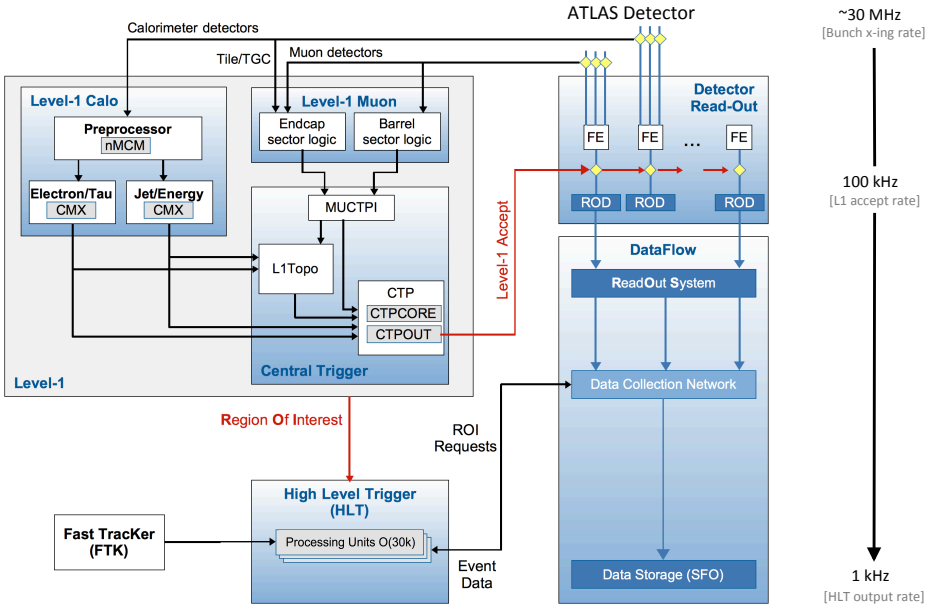

FIGURE 3.8 – Schematic layout of the Run-2 ATLAS trigger and data acquisition system.

3.3 The HL-LHC Upgrades

The High Luminosity Large Hadron Collider (HL-LHC) [31] is the second phase of the LHC program, it is scheduled to start in 2026. The main goal of the HL-LHC is to increase the instantaneous luminosity up to $7.5 \times 10^{34} \mathrm{cm}^{-2}\,\mathrm{s}^{-1}$ with the goal of reaching up to $4000\,\mathrm{fb}^{-1}$ by the end of the HL-LHC program. A program of upgrades for the LHC and the experiments is ongoing, the planning of the upgrade for the LHC is presented in Figure 3.9.

The upgrades will be performed during the Long Shutdown of the LHC. First during LS1 some consolidation work on the superconductive magnets was performed, this allowed the energy in the center of mass to be raised from $\sqrt{s} = 8\,\mathrm{TeV}$ in run Run 1 to $\sqrt{s} = 13\,\mathrm{TeV}$. During LS2 which started beginning of 2019 the injectors of the LHC will be consolidated, this will allow an increase in beam brightness by increasing the number of protons per bunch as well as their density. Finally, LS3 will aim to finalize the installation of the HL-LHC and the upgrades of the detectors, the main upgrade from the LHC side will be the replacement of the magnets near the experiments used to focus the beams before the collisions. With all upgrades the HL-LHC could reach an instantaneous luminosity up to 20 times larger than the nominal LHC.

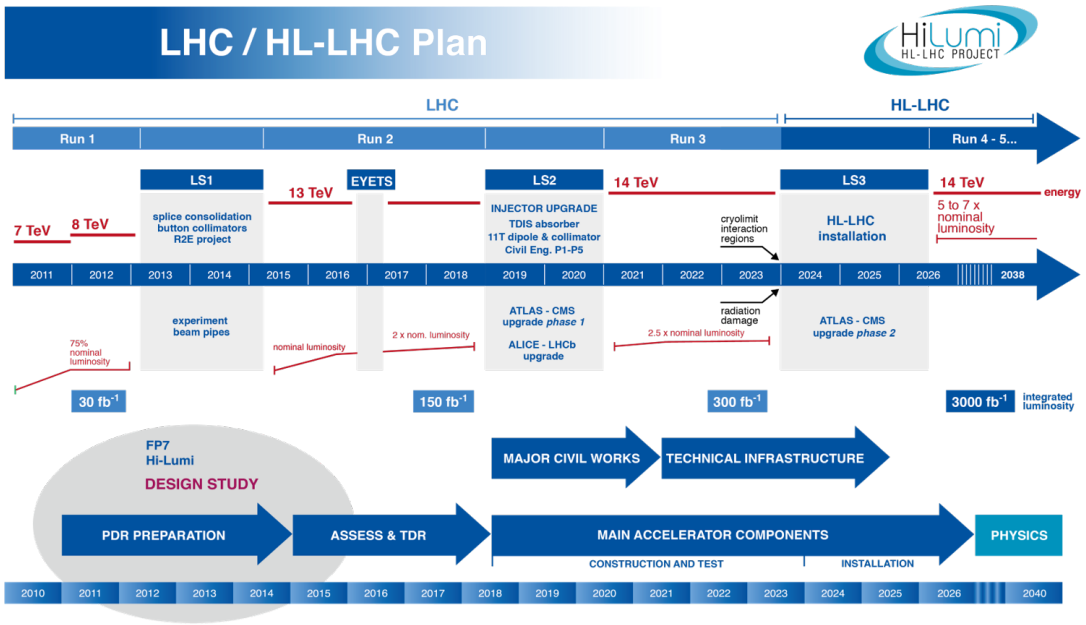

FIGURE 3.9 – Plan for the LHC upgrades toward the HL-LHC[49].

As the number of protons per bunch decrease, due to the lost of protons after each collisions the luminosity would also decrease, reaching a luminosity similar to the nominal LHC after 15 h. The large luminosity would result in an extremely large pile-up that could not be handled by the detectors. To avoid this the HL-LHC will be operated using luminosity leveling. The idea of luminosity leveling is to modify the beam parameters as time passes to compensate for the decrease of the number of protons in each bunch and maintain a constant luminosity for as long as possible. With this method a luminosity of the order of 5 times larger than the nominal LHC one can be maintained for up to 8 h and after 15 h the luminosity would still be 2.5 times larger than the nominal LHC. The luminosity profile with and without leveling is shown in Figure 3.10.

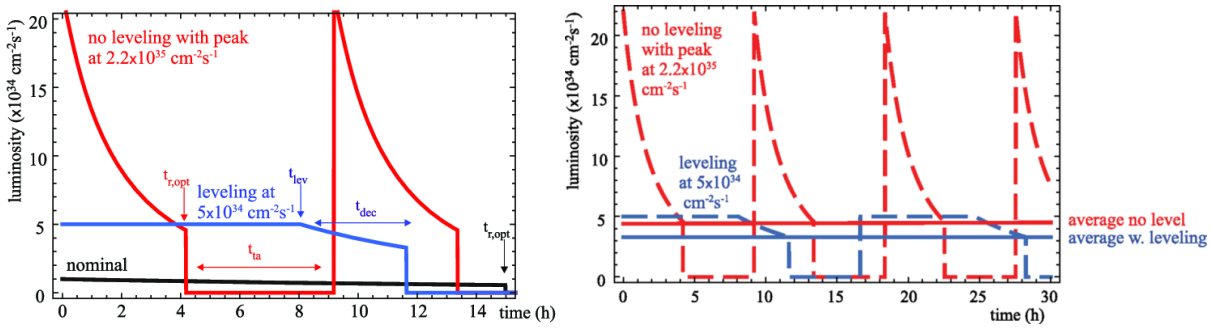

(a) (b)

FIGURE 3.10 – (a) Luminosity profile for a single long fill : starting at nominal peak luminosity (black line), with upgrade and without leveling (red line), with leveling (blue line). (b) Luminosity profile with optimized run time, without and with leveling (red and blue dashed lines), and average luminosity in both cases (solid lines)[31].

3.3.1 Physics

After Run 3, the statistical gain that could be expected in running the LHC without increasing its luminosity would be marginal and it would take more than ten years of operation to halve the statistical uncertainty on any measurement after 2020 [50]. Therefore, to continue the physic program of the LHC and fully exploit the LHC, a luminosity upgrade is necessary.

The main focus for the ATLAS and CMS experiments has been to measure the Higgs properties. This implies studying the different decay modes of the Higgs boson and computing it coupling with the different particles of the SM. So far the decay of the Higgs to b-quarks, τ lepton, W and Z bosons and photons have been observed and its coupling to the top measured. The increased luminosity would allow the study of other rarer decay modes, for example the decay of the Higgs to two muons. After the HL-LHC, a signal significance of the order of 9.4 σ is expected which would mean to the observation of this decay mode. The HL-LHC will also allow to start studying the self coupling of the Higgs boson by looking for Higgs-boson-pair production. The observation of such events at the HL-LHC is not expected for a luminosity of $3000\,\mathrm{fb}^{-1}$ as in that case the expected significance would be of 3.5 σ.

In addition to the measurement related to the Higgs boson, the precise measurement of different standard model parameters will be performed at the HL-LHC with the ATLAS detector. Among these measurements are the measure of the weak mixing angle, this is one of the fundamental parameter of the SM that has been measured at previous and current collider. The current world average is dominated by the combination of measurements at LEP and at SLD, however these two measurements differ by over 3σ. Due to the larger statistic and the improved detector a measurement of the same order of magnitude as these two previous one should be achievable at the HL-LHC. At the HL-LHC the measurement of the four top production will also achievable. This is an extremely rare process predicted by the standard model that has not been observed in ATLAS so far. Many BSM theory predict an enhancement of the cross section of such signal. The increased statistics at the HL-LHC will should provide a significance well above 5 σ (as this could be reached with $300\,\mathrm{fb}^{-1}$) as well as a precise measurement of the cross section with an uncertainty of the order of 11%.

Finally, the measurement from ATLAS at the HL-LHC will increase the limits on BSM models. Many BSM models predict new particles that should be observable at the LHC, the larger the mass of such particles the smaller their production cross-section will be. The large increase of luminosity at the HL-LHC should thus allow us to observe such particles even if they are at high masses.

3.3.2 LHC upgrades

To be able to reach a luminosity of $4000\,\mathrm{fb}^{-1}$ and an energy of $\sqrt{s} = 14\,\mathrm{TeV}$ several aspects of the LHC will need to be upgraded. Some of the subsystem of the LHC will need to be replaced to withstand the high radiation dose they will be exposed to. During the upgrade, systems will be replaced by with new more performant equipment instead of spare improving the performance of the LHC. A comparison of the beam parameters before and after the upgrades is shown in Table 3.1.

The main difference between the LHC and the HL-LHC parameters are an increase in the number of protons per bunches and a reduction of the size of the bunch. Combine together the evolution of the two parameters lead to an increase of the proton density in the bunches, which will result during the bunch crossing in an increase instantaneous luminosity.

Parameters	Nominal LHC	Standard HL-LHC
n, number of particles per bunch [10^{11}]	1.15	2.2
N_b, number of bunches per beam	2808	2748
f, revolution frequency of the bunches [kHz]	11.25	11.25
F, luminosity reduction factor without (with) crab-cavity	0.836 (0.981)	0.369 (0.715)
$\sigma_{x/y}$, transverse size of the beam [µm]	16.7	8.2
$\mathcal{L}$, peak luminosity without (with) crab-cavity [10^{34} cm^{-2} s^{-1}]	1.00 (1.18)	6.52 (12.6)

TABLE 3.1 – Relevant beam parameter for the LHC and HL-LHC to compute the luminosity [33] [31].

This improved particles density can be achieved via the replacement of the insertion magnet. These quadrupolar magnets placed on both side of both ATLAS and CMS are used to squeeze the bunches before the collisions to reach the required instantaneous luminosity. The new insertion magnet will use Nb_3Sn technology capable of creating magnetic field of up to 12 T, this will allow a reduction of the transverse size of the bunch and thus improve instantaneous luminosity.

The main downside of this reduction of the bunch width is the decrease of the geometrical luminosity reduction factor. This factor corresponds to the reduction in luminosity induced by the fact the 2 bunches are not colliding head to head but with a slight angle, the thinner the bunch the larger this effect. To compensate this effect and make the size reduction improve the luminosity new RF cavity are planned to be installed on both side of ATLAS and CMS [51]. These cavities, called crab cavities induce a tilt of the bunches increasing greatly the overlap of the two bunches in the crossing region resulting in an increase of the geometrical luminosity reduction factor. A schematic view of the effect of the crab cavities can be seen in Figure 3.11. This scheme will affect the distribution in time and position of the different interaction during the crossing.

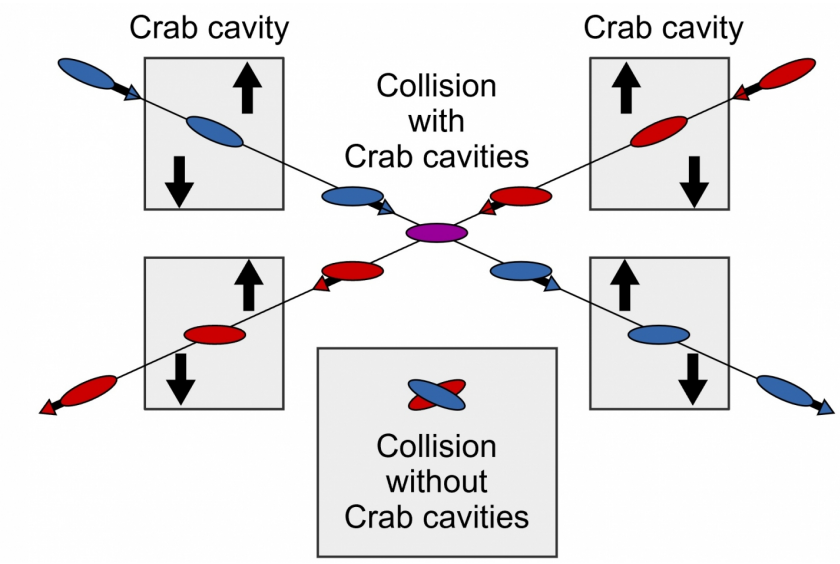

FIGURE 3.11 – Schematic view of the effect of the crab cavities on proton bunches.

After the HL-LHC upgrade an instantaneous luminosity of up to $7.5 \times 10^{34}\text{cm}^{-2}\,\text{s}^{-1}$ and an energy in the center of mass of $\sqrt{s} = 14\,\text{TeV}$. This will lead in the ATLAS detector to a pile-up of up to $\langle\mu\rangle = 200$. The ATLAS detector will need to be updated to operate under these

conditions, both to withstand the large dose resulting in the increase number of particles within the detectors and the larger pile that will increase the complexity of the object reconstruction.

3.4 ATLAS upgrades for the HL-LHC

The main goal of the upgrades of ATLAS is to maintain performance at least as good to the one obtain at the LHC and if possible to improve them. The main upgrade project for ATLAS is the replacement of the ID by the new Inner Tracker (ITk). At the same time the electronics the LAr calorimeter will be replaced and the Trigger scheme will be updated. Finally, to mitigate the pile-up and improve the performance in the ATLAS detector in the forward region a timing detector HGTD is being developed for the forward region.

3.4.1 The Inner Tracker

At the HL-LHC, due to the radiation level and high pile-up the ID will not be usable. The ID will thus be replaced by the ITk, an all silicon detector composed of both pixels and strips. A side view of the ITk is shown in Figure 3.12, in this picture the blue represent the strips and the red the pixels.

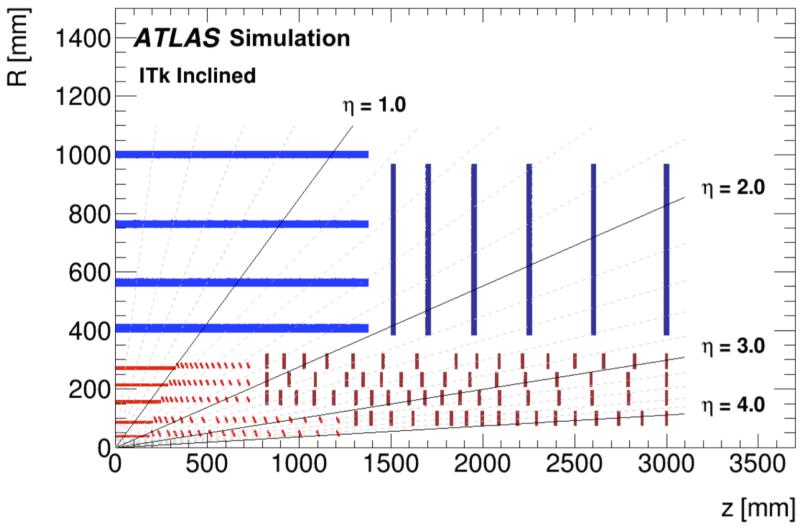

FIGURE 3.12 – Schematic layout of the ITk. The active elements of the barrel and end-cap Strip Detector are shown in blue, for the Pixel Detector the sensors are shown in red for the barrel layers and in dark red for the end-cap rings.

An all silicon design was chosen due to the good radiation resistance of this material. Due to the proximity to the beam-pipe of the inner layer of the ITk the fluence in this region will be extremely large. To maintain good performance a replacement of the modules after $2000\,\mathrm{fb}^{-1}$ is foreseen. A larger pile-up implies a larger number of particles going through the detector and thus a larger number of hits in the trackers. If the fraction of pixels receiving a hit per event (occupancy) becomes too important the reconstruction of the tracks is impacted as it will become almost impossible to merge hits together to construct tracks. To avoid this, a target occupancy of 1% has been fixed, this is achieved with the ITk by increasing the granularity by a factor 8 compared to the pixels of the ID.

Compared with the ID which has a coverage up to $|\eta| = 2.5$, the ITk will provide a coverage up to $|\eta| = 4$. This improved coverage approaches the one from the calorimeters, this will thus lead to a better reconstruction of the forward objects as they could be reconstructed using a combination of calorimeter clusters and tracks.

The Inner part of the ITk [52] will be composed of $50\,\mu\text{m} \times 50\,\mu\text{m}$ (or $25\,\mu\text{m} \times 100\,\mu\text{m}$) silicon pixels. This sub-detector is composed of 5 layers in the barrel and a succession of disks in the end-caps and offer a coverage up to $|\eta| = 4$. Due to its high granularity it allows for a good reconstruction of the position of the primary vertex of the order of $200\,\mu\text{m}$ in the barrel for low p_{T} tracks, this resolution increases at larger η up to a few mm.

Around the pixel detector, the Strip detector [53] will be installed, it is composed of four layers in the barrel of strip silicon detectors and six petal shape disks on both end-caps to provide a coverage up to $|\eta| = 2.7$. It is composed of two types of silicon strips, both of them with a pitch of $75.5\,\mu\text{m}$ and a length of either $24.10\,\text{mm}$ or $48.20\,\text{mm}$ depending on the local occupancy. The strips are radially distributed on stave in the barrel and petal in the end-caps and provide thus a good radial resolution. To maintain some resolution in the other direction the modules are tilted with a small stereo angle.

The layout of both the pixel has been optimized to provide a total of at least 13 hits for $|\eta| = 2.6$. This should allow the ITk to archive a better performance in the barrel region than the ID during Run 2, while providing a coverage with acceptable performance up to $|\eta| = 4$.

3.4.2 High Granularity Timing Detector

Pile-up interactions correspond to inelastic scattering, the resulting particles are thus mostly emitted in the forward region in which they will degrade the performance of the calorimeters and the ITk. To improve the performance in this region, a new detector, the HGTD [54] is being designed for the forward region, it expected coverage is of $2.4 < |\eta| < 4$. This detector will use Low Gain Avalanche Detector (LGAD), silicon sensors with an intrinsic gain, to measure precisely the time of the hits. The good granularity of this detector of $1.3\,\text{mm} \times 1.3\,\text{mm}$ was chosen to maintain an occupancy of less than 10%. With this occupancy it becomes possible to associate the information in the HGTD to the track reconstructed in the ITk.

Ultimately the goal is to associate times with a resolution of $30\,\text{ps}$ to the tracks in the ITk. Since all the interaction during a bunch crossing happen at different times with a time spread of around $180\,\text{ps}$, by associating a time to each tracks one should be able to separate pile-up tracks from signal tracks and thus reduce the contamination from pile-up of the physics object by up to a factor 6.

3.4.3 Calorimeter upgrades

The LAr colorimeters are expected to still perform well under the HL-LHC condition [55]. But the electronics used for these calorimeters will need to be replaced, indeed the current electronic is not radiation hard and are thus not adapted to the condition of the HL-LHC. Additionally, the upgrade of ATLAS will come with an upgrade of the Trigger system itself, the current readout electronic of the LAr will not be compatible with such system. For both of these reason the electronic of the LAr colorimeters will be changed in the context of the HL-LHC upgrade.

With the increase in $\langle\mu\rangle$ the contribution of the pile-up to the noise term (b in Equation 3.8) of the energy resolution will increase and will start to dominate. The implementation of a new

electronic for the LAr allows for new signal processing algorithm, with these new algorithms it is possible to reduce the effect of the pile-up on the energy resolution by up to 20%.

This improvement of the electronic combined with improvement of the different object reconstruction algorithm for photon, electrons and jet should allow the Calorimeter to reach similar performance at the HL-LHC as the one obtain in Run 2.

3.5 Object reconstruction in the ATLAS experiment

Once the signals from the different sub-detectors of ATLAS have been collected, algorithms are applied to reconstruct the different physics objects. Each particle type will produce some specific signals in the sub-detectors as it can be seen in Figure 3.13. This step is extremely important for the different physics analysis as they will base their separation of signal and background on the different variables corresponding to these objects.

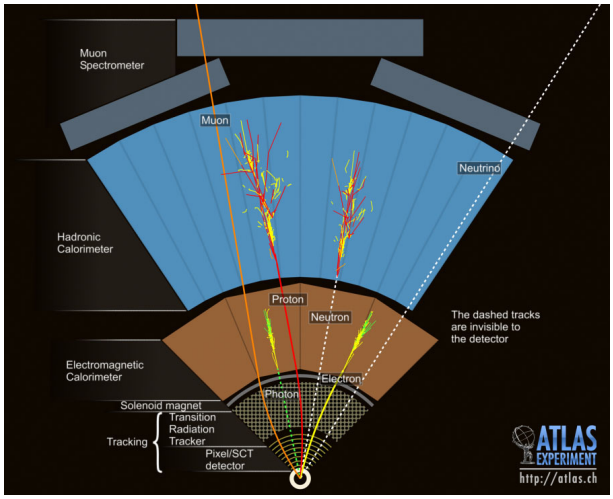

FIGURE 3.13 – Transverse view of the ATLAS detector with a representation the interaction of different particles types with the different sub-detector.

3.5.1 Tracks and Vertices

A track corresponds to the trajectory of a charged particle inside the ID [56]. The first step to reconstruct the tracks is to create clusters of measurements in the ID. These clusters are then transformed into 3D points corresponding to the path of the particle through the detector. Track seeds are then reconstructed out of these points, different criterion are applied on these seed to maximize their purity : momentum, impact parameters, detectors associated to the points, ... Once the seed have been selected, a combinatorial Kalman filter is applied to reconstruct the tracks candidates using the remaining points. To each of the reconstructed tracks a score based on the variables is associated, the largest the score the more probable the candidate is of actually being a genuine track. In case of ambiguity the hits can only be associated with up to two tracks, if it would be associated with more it is associated with the two tracks with the largest score. Finally, after the all the ambiguities have been resolved the remaining good tracks candidates are fitted with a high-resolution fit.

It is extremely important be able to separate signal tracks from tracks originating from pile-up, this can be achieved by reconstructing the primary hard scatter vertex [57] and only keep

the tracks associated to it. The reconstruction of the vertex is done through an iterative process, first a set of tracks with similar impact parameters are selected, from these a seed position of the vertex is determined. Then the tracks and the seed are used together with a fit an estimate the best possible position of the vertex, this is done iteratively, after each fit the weight of the tracks are recomputed depending on their proximity to the vertex. Once this process is finished and the optimal position of the vertex has been computed, the tracks which are too far away are removed from the vertex. The process can then be repeated with others tracks until all the vertex have been founded. In case more than one vertex is identified, the one with the highest sum of squared tracks p_{T} is selected as the primary vertex, it as been predicted using simulation that for $\langle\mu\rangle = 30$ the efficiency of finding the right primary vertex is larger than 99%. At the HL-LHC, due to the large number of pile-up vertices the efficiency of this method might drop as multiple close by pile-up vertices might get combined together into one vertex if they are too close.

3.5.2 Electrons and Photons

Electrons[58] and photons[59] are reconstructed by combining information from the calorimeter clusters with information from the tracks reconstructed in the ID. The energy deposit in the electromagnetic calorimeter are put together using a topological cell clustering algorithm to create clusters. The clusters can correspond to electrons or photons, specific algorithms are thus used to determine the origin of the cluster.

In the electron case, in addition to the calorimeter cluster a track associated with the cluster is also necessary. To ensure that the track correspond to the primary vertex and is not a pile-up track, it is required that the impact parameters of the track correspond to the primary vertex.

In parallel to the electron reconstruction, the photon reconstruction is performed. The photons can either be unconverted or converted. In the case of an unconverted photon, no track should be associated with the energy cluster to identify it as a photon. In the case of a converted photon, two tracks will be associated with the energy cluster, the two track are used to compute the conversion vertex. A conversion vertex is build from pairs of opposite charged particles. Additional constraint on the tracks associated with the vertex are then applied to ensure a good reconstruction efficiency. If the cluster is then matched with this conversion vertex the particle is identified as a photon.

For both the electrons and the photons different selections are defined, the tighter the selection the larger the reconstruction purity of the method but the looser the selection the larger the reconstruction efficiency. The electrons have three selections : Thigh (78% efficiency), Medium (88% efficiency) and Loose (95% efficiency) while the photon only have two : Tight (85% efficiency) and Loose (97% efficiency).

To ensure that the electron and photons are primary particles, many analyses require these particles to be isolated. There are two type of Isolation : the calorimetric isolation and the track isolation. The calorimetric isolation ensures that there are no energy deposits close to the calorimeter cluster in a window of $\Delta R < 0.2$, the energy cut on the sum of the energy of the cluster can be adapted depending on the efficiency required for the isolation. This is used for both electrons and photons. The track isolation ensure that there are no energetic tracks close to the primary electron in a window of $\Delta R < min(0.2, 10\,\mathrm{GeV}/E_T)$. As for the calorimetric isolation, the cut on the sum p_{T} of the nearby tracks can be adapted. This isolation is only used for the electrons.

3.5.3 Muons

Muons[60] are reconstructed using both the ID and the MS. They are first reconstructed separately as a track in each detector. In the MS, a χ^2 fit is performed to associate the hits to the track. In the ID the muon track are reconstructed similarly to the other charge particle tracks as explain in Section 3.5.1. The two tracks are then combine to reconstruct a muon.

Quality criteria are applied to the reconstructed muons to suppress the background, composed mainly of pion and kaon decays. These include, the number of hits in the MS, the value of the χ^2 used for the fit and isolation criteria similar to the one used for the electrons and photons. In total, 95% of the muons with at least $5\,\mathrm{GeV}$ pass the $Medium$ identification criteria while less than 0.4% of the background does.

3.5.4 Jets

In the hadronic calorimeter, particles are detected as jets of hadrons, they will leave energy through the electromagnetic and hadronic calorimeters. Once a cluster have been reconstructed in the calorimeters [61], they are combine together using the anti-kT algorithm [62], in the analysis presented in this thesis, a radius parameter of the jets of $\Delta R = 0.4$ is used.

The anti-kt algorithm is an iterative algorithm for jet reconstruction, it uses two main distances :

$$\begin{aligned} d_{ij} &= \min(\frac{1}{k_{ti}^2}, \frac{1}{k_{tj}^2})\frac{\Delta_{ij}}{R^2}, \\ d_{iB} &= \frac{1}{k_{ti}^2}, \end{aligned} \tag{3.11}$$

where $\Delta_{ij} = (y_i - y_j)^2 + (\phi_i - \phi_j)^2$ and k_{ti}, y_i and ϕ_i respectively are the transverse momentum, the rapidity and the azimuthal angle of the particle i. R is the radius of the jets. For every cluster in the calorimeter the distance d_{ij} between it and the other object is computed as well as the distance with the Beam (B) d_{iB}. The smallest distance is then identified, if it is a d_{ij} i and j are merged together and the process is repeated. If d_{iB} is the smallest the i is considered a jet and the algorithm restarts with another cluster. This is done until all the object have been processed. The value of d_{ij} is substantially larger between two soft particles that between a soft and a hard particle. Soft particles will therefore tend to cluster with hard ones before clustering among themselves. The resulting jet produced with this algorithm will tend to be circular centered on the hardest cluster as all the soft cluster get merged with the hard one. This facilitates the calibration of the detector as the shape of most jets are the same.

Some of these reconstructed jets might come from pile-up or noise, to ensure that only hard-scatter jets are used in the analysis, some cleaning is then applied. The cleaning can utilize information from various sources, first the pulse shape of the signal can be used to reduce the fake jets originating from the noise. Secondarily the energy ratio between the two calorimeters can be used. And finally the information from the tracks can be used.

Calibration

Once the jet have been reconstructed various correction based on simulation and data are applied to them. The calibration of the jets [63] is necessary to improve the performance of the detector and remove the systematic effect on the detector response.

The first correction applied on the jet is the origin correction. The four-momentum of the jet is recomputed to point toward the hard-scatter primary vertex rather than the center of the detector.

The second correction is the pile-up correction. First, the p_{T} of the jet is corrected base on the median pile-up p_{T} density at the position of the jet and the area jet. Additional correction are then applied based on the number of primary vertex in the event and the $\langle\mu\rangle$.

The next step is the absolute MC-based calibration. Correction factor to the values of the energy and the η of the jets as function of η are extracted from a comparison between the truth jet and the reconstructed jet in the simulation.

Additional correction on the jet energy scale are obtained via the global sequential correction. This method uses the topology of the energy deposits in the calorimeter and tracking information to take into account the fluctuations in the particle content of the shower development. This allows for an improved energy resolution and jet energy scale.

Finally, an in-situ correction is performed by comparing the jets in the data with the jet in the simulation.

b-jet Tagging

Once the jets have been reconstructed, additional algorithm can be applied to determine which type of particle is at the origin of the jets. The most commonly used of such algorithm is the b-tagging, the identification of jets originating from b quarks [64].

The main property used for the b-tagging identification is the long lifetime of the B hadrons ($1.5\,\mathrm{ps}$), this means that a B hadrons of at least $50\,\mathrm{GeV}$ will have an average flight length of $3\,\mathrm{mm}$ before decay. Due to this flight length, a displaced vertex will appear at a distance from the primary vertex. This information plus other discriminating information such as the large mass and hard fragmentation of the B-hadron are then used by three different algorithms to separate b jets from c and light jets :

- The impact parameter based algorithms (IP2D, IP3D), which use the track parameters of the tracks associated with the jet.
- The Secondary vertex finding algorithms (SV0, SV1), which use the secondary vertex and the flight length.
- Decay chain reconstruction algorithm (JetFitter), which reconstruct the full decay chain assuming it to be : Primary vertex $\rightarrow$ B-hadron $\rightarrow$ c-hadron.

To further enhance the discrimination the output of the three algorithms are combine together using a multivariate analysis based on a Boosted Decision Tree (BDT) called MV2. The result of MV2 is a single variable from -1 to 1, value close to 1 indicate that the jet is more b-like while value close to -1 correspond to jets that are more c or light like. A cut on this variable can then be applied to discriminate both cases, depending on the chosen value different b-jet efficiency and c/light jet rejection can be achieved. The typical working point for analysis is 77% efficiency for the b-jet reconstruction. This corresponds to a mis-tag rate of 13% for c-jet and of 0.7% for light flavor jet.

Chapitre 4

The High Granularity timing detector

In addition of the upgrade of the ATLAS sub-detector for the HL-LHC a timing detector is being design for the forward region, the HGTD[54]. This chapter will provide a general presentation of this detector to introduce the Chapter 7 which will detailed my contribution to the development and study of the HGTD. The design of the HGTD as of the time of writing of this thesis will be presented. This includes the layout of the detector, the Low Gain Avalanche detector used to detect the particles and the electronic capable of measuring a time using the sensors signal. Finally, some studies of the performance of the detector and of the possible improvement of physics analysis will be presented.

4.1 Introduction

One of the main challenge for the ATLAS detector at the HL-LHC is pile-up. In nominal operation, an average of 200 simultaneous pp interactions ($\langle\mu\rangle = 200$) will occur within the same bunch crossing. One of the major challenges for the tracking system in this environment is to efficiently reconstruct the trajectory of charged particles produced in the primary interaction and correctly assign the tracks to the corresponding vertex.

The HGTD has been design to operate in this high pile-up environment up to a total integrated luminosity of $4000\,\mathrm{fb}^{-1}$. The main purpose of this detector is to associate timing information to the particles, this information can then be used to complement the information provided by the tracker and calorimeter system to enhance the object reconstruction. The goal of the HGTD is to maintain the performance at a level comparable to the one currently achieved in ATLAS with a pile-up 4 time smaller.

Considering the space constraints in the ATLAS Detector, the HGTD will be located in the gap between the barrel and the end-cap calorimeters, at a distance of approximately $\pm 3.5\,\mathrm{m}$ from the interaction point. This region lies outside the ITk volume and is in front of the end-cap and the forward calorimeters in the space currently occupied by the Minimum-Bias Trigger Scintillators (MBTS), which will be removed. The position of the two vessels for the HGTD in the ATLAS detector is shown in Figure 4.1.

Due to the limited space and the high radiation level expected at the position of the HGTD, a silicon-based timing detector technology was chosen. Low Avalanche Gain Detector (LGAD) [65] pads of $1.3\,\mathrm{mm} \times 1.3\,\mathrm{mm}$ with an active thickness of $50\,\mu\mathrm{m}$ have been shown to fulfill these requirements.

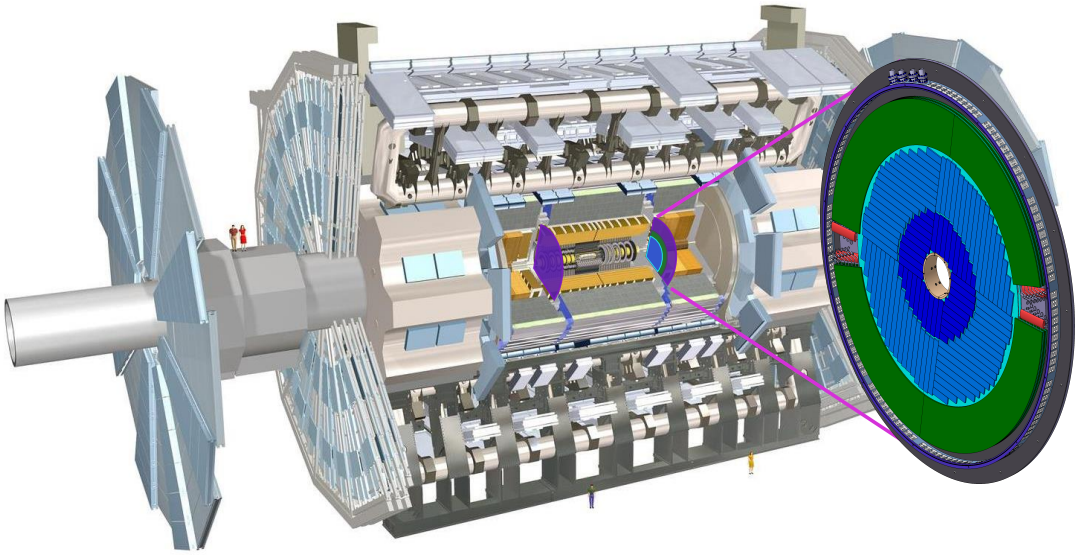

FIGURE 4.1 – Position of the HGTD within the ATLAS Detector. The HGTD acceptance is defined as the surface covered by the HGTD between a radius of $120\,\mathrm{mm}$ and $640\,\mathrm{mm}$ at a position of $z = \pm 3.5\,\mathrm{m}$ along the beamline, on both sides of the detector.

A custom Application-specific integrated circuit (ASIC) : the ALTIROC, which will be bump-bonded to the sensor, is being developed to meet the requirements on time resolution and radiation hardness of the readout electronics. The ASIC will also provide functionality to count the number of hits registered in the sensor and transmit this data at $40\,\mathrm{MHz}$ to allow unbiased, bunch-by-bunch measurement of the luminosity.

4.2 HGTD Design

The size of the bunch will stay the same between now and the HL-LHC while the number of interactions per bunch crossing increase. This means that the density of interactions will increase, up to a most probable value of $1.4\,\mathrm{vertices/mm}$. Figure 4.2 shows the comparison of two event displays, one obtain from data in 2016 with $\langle\mu\rangle = 25$ (a) and one simulated using $\langle\mu\rangle = 200$ (b). In the second case it becomes extremely difficult to assign each track to a unique interaction making the event reconstruction more complicated.

As pile-up vertices get closer to the hard scatter vertex, the probability of two vertices merging in the tracker increases. A track is associated to a vertex if its origin is geometrically compatible in z with the vertex position. The compatibility is determined by the resolution on the track z_0 impact parameter such that :

$$\frac{\left|z_0 - z_{\mathrm{vertex}}\right|}{\sigma_{z_0}} < 2, \tag{4.1}$$

where σ_{z_0} is the per-track resolution on the longitudinal impact parameter and depends primarily on the track η and p_{T}.

Figure 4.3 shows the resolution of the z_0 parameter for the tracks in the ITk as function of η. At low η this resolution allows to pinpoint precisely the position of most of the vertices. Larger η tracks are harder to associate correctly to a vertex, this mean that pile-up tracks can

be associated with a signal vertex which can change the topology of the event or affect the reconstruction of the objects. This figure was obtain using the performance of the version 2.2 of the ITk, the maximum observed for $\eta = 3.7$ and the decrease of the resolution for larger η appear because of the specific geometry of the detector and its services as well as the material in the forward region of the ATLAS detector. Since then version 3 of the ITk have been developed, it leads to a better z_0 resolution as well as the absence of a local maximum.

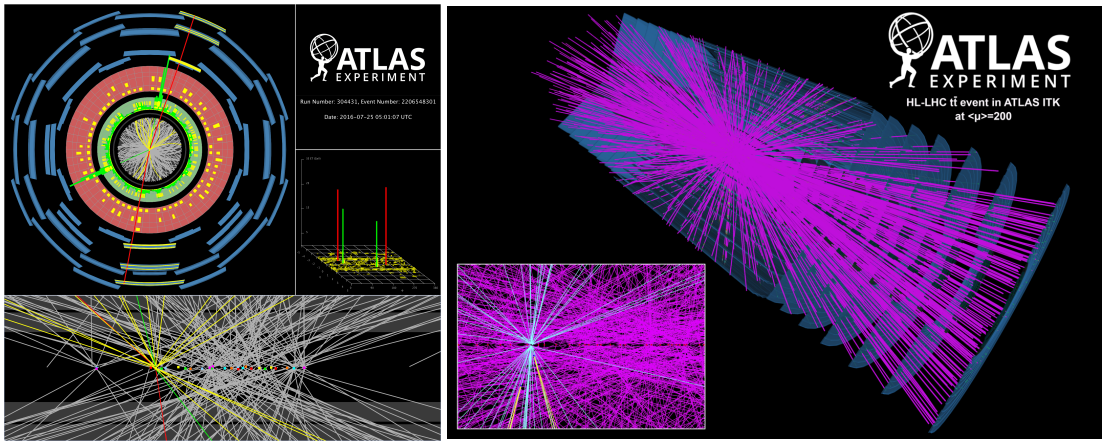

(a) (b)

FIGURE 4.2 – (a) Event display of a candidate Higgs boson decaying into two electrons and two muons recorded in 2016 in the ATLAS detector. 25 additional interaction were recorded in the same buch crossing. (b) Simulated $t\bar{t}$ event with an average pile-up of 200 collisions per bunch crossing.

The only handle for the forward tracker to address the challenge of pileup on track-to-vertex association in the forward region is to tighten the selection cuts used in Equation 4.1, reducing the track-to-vertex association efficiency. Timing information can supplement the tracker z_0 measurement in assigning tracks to vertices and mitigate the impact of a high vertex density while maintaining a good efficiency. The time and position of a vertex are uncorrelated, measuring the times can provide an additional and transverse information to separate tracks coming from two different vertices at the same position but different times, the following selection can thus be introduced :

$$\frac{|t - t_{\text{vertex}}|}{\sigma_t} < 2, \tag{4.2}$$

where t is the track time measured by the HGTD, and σ_t is the track time resolution.

The use of this 2-dimensional space-time track-to-vertex association, allows to maintain a high track selection efficiency while greatly reducing the contamination of pileup tracks within the z selection window. The use of timing information in the forward region, hence, can compensate for the worsening of the z_0 impact parameter resolution, allowing the tracker to maintain good track-to-vertex association performance for all η, mitigating the impact of the large pileup contamination in the forward region.

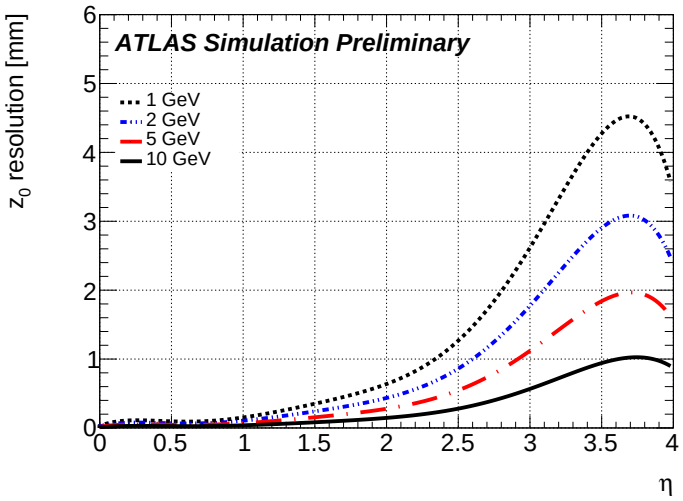

FIGURE 4.3 – Resolution of the z_0 parameter for the tracks in the ITk as function of η. z_0 is the position along the z axis of the intersection of the particle trajectory and the z axis.

4.2.1 HGTD Layout

The current layout of the HGTD is shown in Figures 4.4 and 4.7. The envelope of the detector vessel has a radial extent of 110 to 1100 mm, it contains the cooling system, the active sensors and the moderator.

The moderator is a $50\,\mathrm{mm}$ plate of borated polyethylene placed behind the HGTD that reduces the flux of back scattered neutron created in the end-cap/forward calorimeters, protecting both the ITk and the HGTD. This decreases the radiation damage to both the HGTD and ITk as well as the number of particles crossing both detectors making the object reconstruction easier.

The cooling is ensured by two cooling plates on which the silicon modules will be mounted on both sides. Within these plates pipes are running transporting the high pressure CO_2 used for the cooling. The cooling system is based on a 2 phased CO_2, the same cooling system used by the ITk and the tracking system of most LHC experiments after the upgrades. The CO_2 is initially pumped in liquid form from an external cold source, as it goes through the detector it absorbs the heat dissipated by the HGTD components and partially evaporate. Within each pipe, a small amount of CO2 flows at high pressure in the form of small drops, and enough space is left for the vapor to circulate. Due to the large latent heat needed for a high pressure liquid CO_2 to vaporize, this method is highly efficient in heat extraction. This cooling technique brings many advantages, the CO_2 is radiation hard, it is thus appropriate for the harsh environment in which the HGTD will operate. As a mix between liquid and vapor, it weights significantly less than other liquid mono-phase refrigerants. Because of the small pipe and small amount of CO_2 it does not increase by too much the material in the detector and thus minimizes the effect on the performance. The cooling pipes are connected to the cooling system of ATLAS at the level of the peripheral electronics as shown in Figure 4.4. This cooling system is then connected to the cooling plant that will be installed in a room next to the ATLAS cavern.

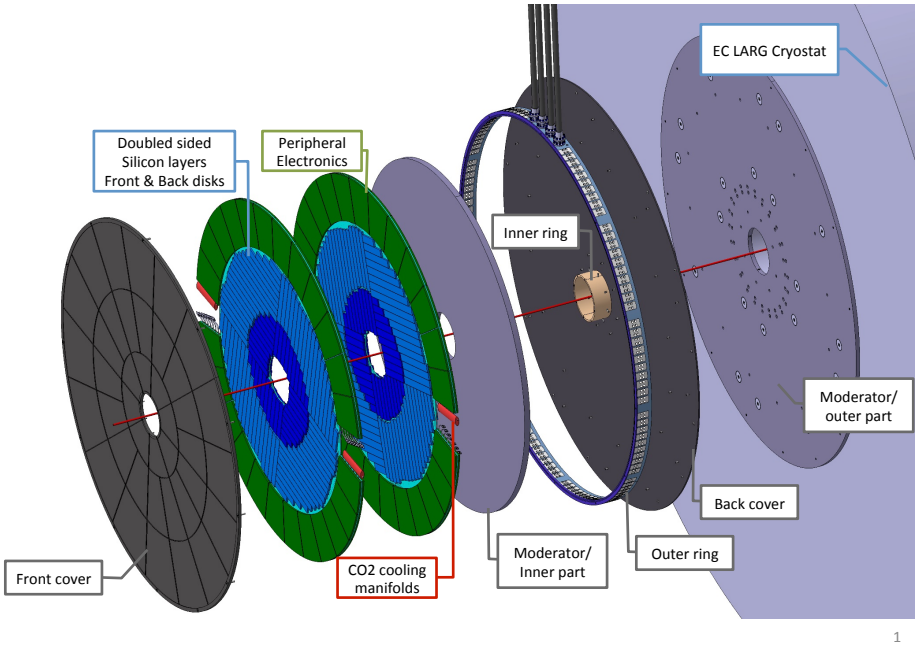

FIGURE 4.4 – Global view of the HGTD to be installed on each of two calorimeters extended barrels. The various components are shown : hermetic vessel (front and rear covers, inner and outer rings), two instrumented double-sided layers (mounted in two cooling disks), two moderator pieces placed inside and outside the hermetic vessel.

The active part of the detector is composed of silicon-based timing detectors mounted on both side of the cooling plates. Sensors are installed within a radius of $120\,\mathrm{mm}$ and $640\,\mathrm{mm}$, corresponding to a coverage of $2.4 < |\eta| < 4$. The size of the pads was optimized taken into account the efficiency, the occupancy of the detector and the cost. If the occupancy is too large, associating times to the tracks becomes extremely complicated, a maximum occupancy of 10% was imposed. Reducing the size of the pad decreases the occupancy but this has to be balanced with the efficiency and the cost. Indeed, for smaller pad the inactive area of the sensor becomes non negligible with respect to the active area, reducing the efficiency. Figure 4.5 show the occupancy of the detector, defined as the fraction of pad hit per event, as function of the radius for $1.3\,\mathrm{mm} \times 1.3\,\mathrm{mm}$ pads. With this pad size the occupancy stays below 10% while maintaining a good efficiency.

Each module consists of different elements, the silicon sensor, the readout chips and a connector to the flex cable. The sensor is composed of an array matrix of 15×30 pads with a $0.25\,\mathrm{mm}$ dead region around the active area, its total size is thus of $20.0\,\mathrm{mm} \times 39.5\,\mathrm{mm}$ as shown in Figure 4.6. The pad size of $1.3\,\mathrm{mm} \times 1.3\,\mathrm{mm}$ was optimized to maintain an occupancy below 10%. The readout of the pads is performed by two ASICs with a size of $21.7\,\mathrm{mm} \times 19.9\,\mathrm{mm}$ that can each read a matrix of 15×15 channels. The sensor and the ASICs will be bump-bonded. To connect the ASICs with the peripheral electronics a flex cable will be glued to the sensor, this flex cable will be wired bonded to the two ASICs.

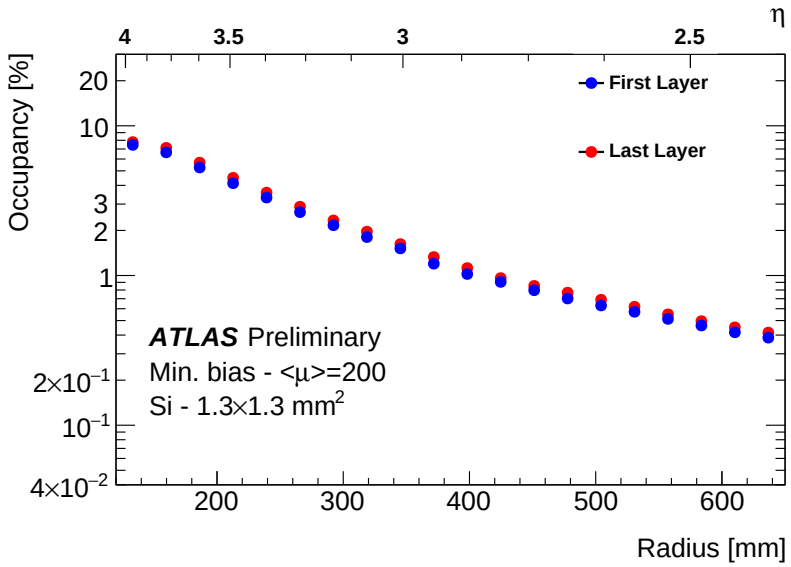

FIGURE 4.5 – The occupancy is shown as a function of the radius for a pad size $1.3\,\mathrm{mm} \times 1.3\,\mathrm{mm}$ at a pile-up of $\langle\mu\rangle = 200$[66].

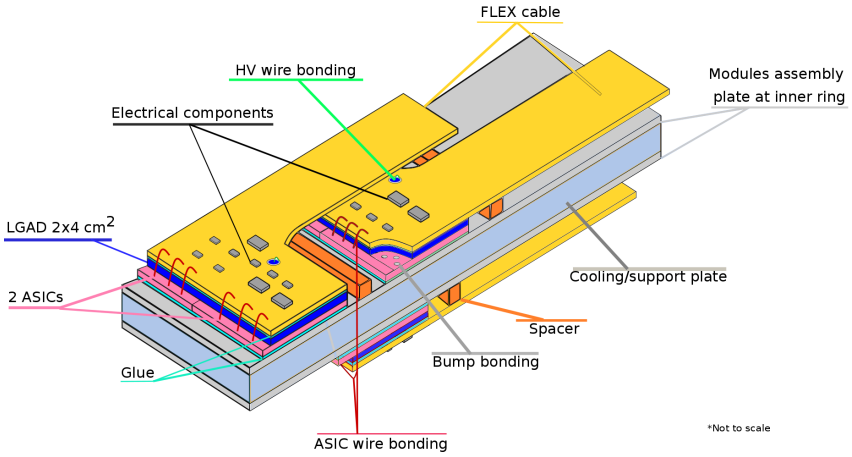

FIGURE 4.6 – Schematic drawing of two adjacent modules on the top side and one on the bottom side of the cooling plate ; the modules are mounted on thin support plates.

The modules are then assemble into staves to cover the full surface of the detector, the staves are rectangular structures with a width corresponding to the size of one module and varying length. Figure 4.7 shows the staves within a layer as blue rectangles. As shown in Figure 4.6 some space is necessary to properly connect the flex cables to the ASICs, due to this space the modules cannot be put continuously on one stave. To ensure a full coverage modules are installed on both sides of each cooling plate, with the modules on the back side placed to cover the gaps in the front side. The overlap of the front and back modules can be changed to increase in average the number of hits associated to the tracks and thus improve the performance at the cost of an increase of the cost and the number of flex cables need. My optimization of the design demonstrated that an 80% overlap in the inner region ($R < 320\,\mathrm{mm}$, represented in dark blue on Figure 4.7) and 20% overlap in the outer region ($R > 320\,\mathrm{mm}$, represented in blue on Figure 4.7) should be used. I optimized the overlaps such as at $R < 320\,\mathrm{mm}$ on average about three hits are obtained for a charged particle, whereas at $R > 320\,\mathrm{mm}$ an average of about two hits are expected to be associated to a track.

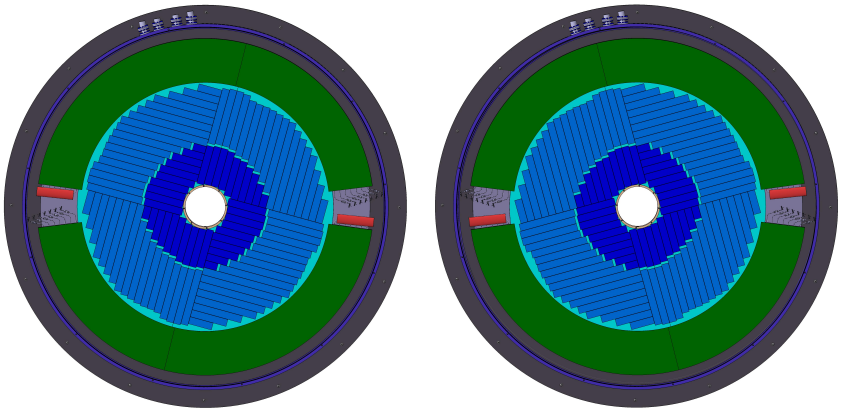

FIGURE 4.7 – View of the two double-sided layers that would be installed in one end-caps. Each layer is rotated in opposite directions by 15°. This angle of 30° improve the performance and help the installation.

The layout of staves in each endcap was defined by maximizing the coverage and minimizing the effect of non-instrumented regions due to mechanical tolerances. The active width of a module is $39\,\mathrm{mm}$ will limit how well the area near the circular opening at $120\,\mathrm{mm}$ can be covered. For $R > 150\,\mathrm{mm}$, the coverage is complete. The maximum length of the readout rows is limited by the manufacturing capabilities for the flexible circuits used for the data transmission. Due to guard ring and the mechanical assembly tolerances many small dead areas exist within each layer. To avoid the overlap of these regions between the two layers, creating completely inefficient regions, a mirror symmetry and a 30° rotation have been applied between the position of the staves in the first and second layers. This layout, called Helix 2 ensures a maximal efficiency and improves the homogeneity of the detector. In addition to optimizing the coverage the rotation frees sufficient room to install at $640\,\mathrm{mm}$ the cooling equipment between the peripheral electronics.

The performance of the sensors decreases with the irradiation up until a point at which the LGAD sensors cease to work. A replacement of the sensor at low radius $R < 320\,\mathrm{mm}$ is expected after half of the life of the detector. This corresponds to the replacement of the sensors with 80 % overlap (in dark blue in Figure 4.7).

4.3 HGTD Low Avalanche Gain Detector

To operate the HGTD, thin, radiation hard sensors with a good time resolution are necessary. LGAD sensor fulfill these requirements, they are based on a technology pioneered by the Centro Nacional de Microelectronica (CNM) Barcelona and developed in the last 5 years within the RD50 collaboration [67].

4.3.1 LGAD Sensors

LGADs are n-on-p silicon detectors containing an extra highly-doped p-layer below the n-p junction to create a high field which causes internal amplification as shown in Figure 4.8 (a) [68]. When a charged particle crosses the sensor it will create electron/hole pairs along its trajectory, with the number of pairs depending on the type of incoming particle, its energy and the sensor thickness. In the electric field induced by the bias voltage (voltage applied to the sensor) the electrons will drift toward the n+ layer and the holes toward the p+ layer, this drift will induce a current in the electrode.

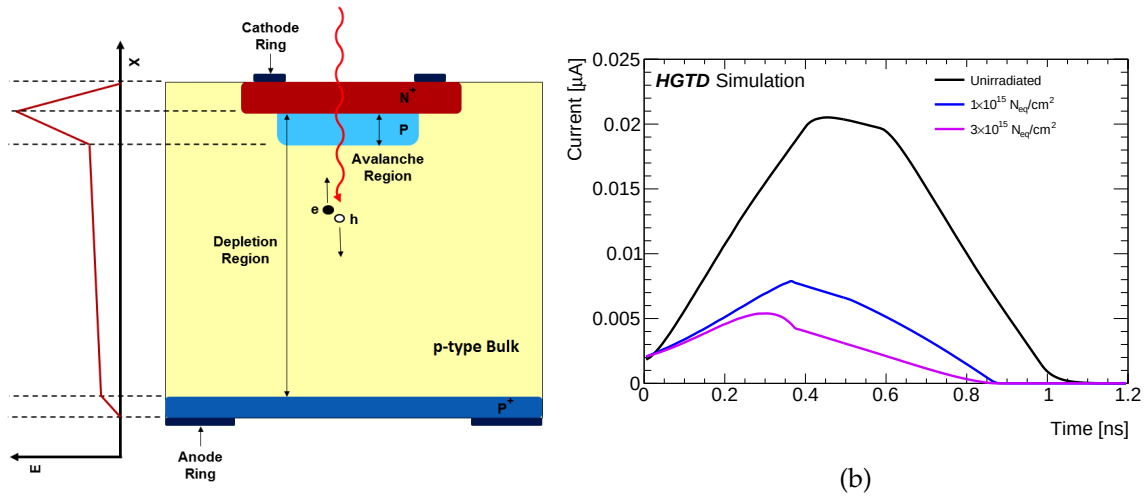

FIGURE 4.8 – Cross section of an LGAD[54] (a) and simulated signal current in LGADs for different irradiation levels (b)

When the electrons reach the amplification region an avalanche process is initiated due to the high electric field, resulting in the creation of additional electron/hole pairs. The additional gain electrons will be immediately collected by the cathode but the gain holes will drift through the sensor toward the anode. This will lead to an amplified current with a gain corresponding to the average number of gain electron/holes pairs produced per initial electron. This current, much larger than in a standard diode, is the key ingredient to the excellent time resolution for MIP particles.

For unirradiated sensors an initial gain of the order of 10-20 is expected. The expected currents for different irradiation levels are presented in Figure 4.8 (b). For large gain, the rise time is about 500 ps and the signal duration is approximately 1 ns. For large fluences, the charge is smaller and the rise time and the signal duration are shorter.

Three major effects determine the time resolution : time walk from amplitude variations, jitter from electronic noise and "Landau fluctuation" from the charge deposit non-uniformity

along the particle path. Time walk and noise jitter depend on the type of readout electronics chosen, they are illustrated in Figure 4.9.

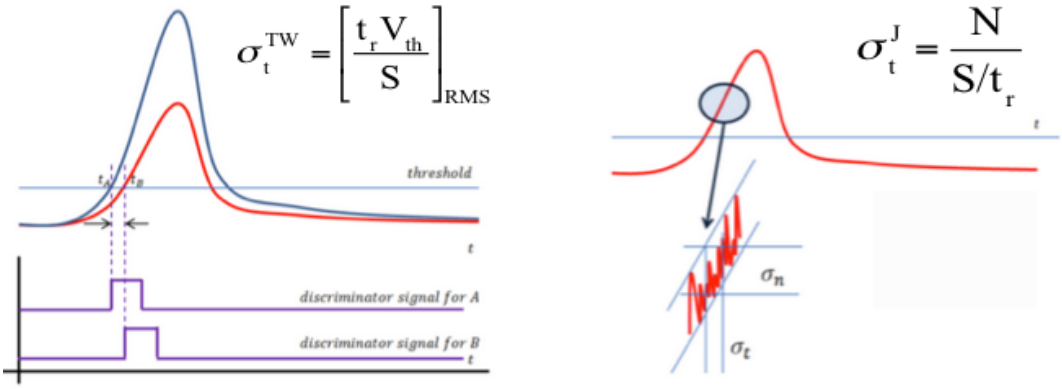

FIGURE 4.9 – Effect of the time walk (on the left) and jitter (on the right) on the reconstruction of the time.

Time walk corresponds to the variation of the reconstructed time as function of the energy when a fixed threshold is used, it can usually be corrected for by a large extent using time reconstruction algorithms such as constant-fraction discrimination (CFD) or amplitude or time-over-threshold (ToT) corrections. The time jitter is the variation of the reconstructed time due to the noise on the amplitude, if the noise is large enough it can cause the signal to pass the threshold too early or too late leading to an incorrect reconstructed time. This can be mitigated by a good signal over noise ratio. Both effects depend inversely on the signal slope (voltage slope at the output of the amplifier) dV/dt :

$$\sigma_{\text{TimeWalk}} = \left[\frac{V_{\text{th}}}{\frac{S}{t_{\text{rise}}}}\right]_{\text{RMS}}, \qquad \sigma_{\text{Jitter}} = \frac{N}{(dV/dt)} \simeq \frac{t_{\text{rise}}}{(S/N)}, \tag{4.3}$$

where S refers to the signal which is proportional to the gain, N to the noise, t_{rise} to the rise time and V_{th} to the threshold voltage. The lowest noise jitter and time walk are achieved with sensors with high signal-to-noise ratio (S/N) and small rise time, i.e. with thin sensors and large gain.

The third effect called "Landau fluctuation" is due to the non-uniform charge deposition along the particle path leading to time-of-arrival fluctuations. Its contribution depends on the thickness of the sensor (the thinner the sensor the lower the fluctuation) and the setting of the threshold. Adding the three contributions in quadrature yields the overall time resolution. After time-walk correction, the noise jitter is the dominating contribution for low S/N and the Landau term takes over for high S/N.

4.3.2 LGAD Performance

The time resolutions of sensors from different producers have been extensively studied in various beam tests and lab setup, result for HPK sensors are shown in Figure 4.10 (a). For single sensor it is shown that a timing resolution lower than 30 ps can be achieved before irradiation with a bias voltage lower than the breakdown. Above the breakdown voltage, the charge carriers in the sensor will start to move at high velocity due to the high electric field, creating an avalanche. This avalanche will result in a large current that will ultimately burn the sensor. The

main difference between the two sensor shown in Figure 4.10 (a) comes from their thickness, one being $30\,\mu\mathrm{m}$ thick while the other is $50\,\mu\mathrm{m}$ thick.

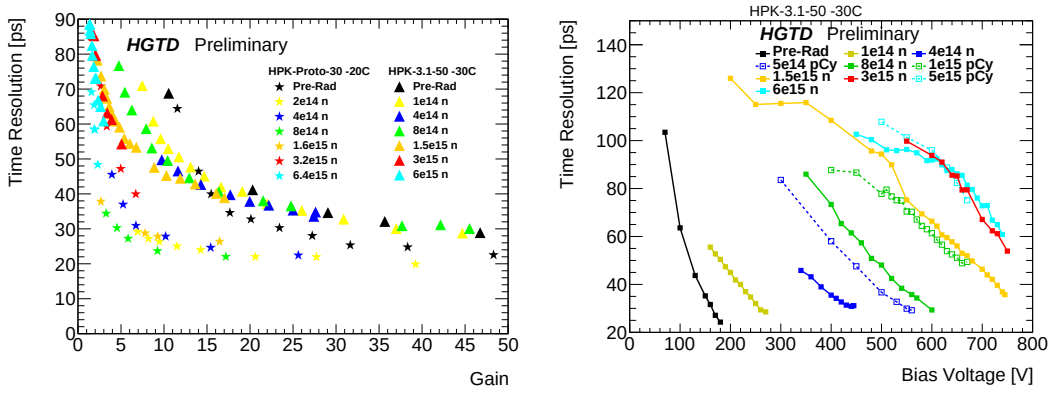

(a) (b)

FIGURE 4.10 – (a) Time resolution σ_t as a function of gain for two irradiated HPK LGADs of 50 and $30\,\mu\mathrm{m}$ thicknesses with time walk correction applied. (b) shows the Time resolution for these two sensors as function of the bias voltage at a temperature of $-30\,^{\circ}\mathrm{C}$.

Radiation damage in silicon mainly results in the change of the effective doping concentration, the introduction of trapping centers that reduce the mean free path of the charge carrier, and the increase of the leakage current. Within the HGTD at the end of the HL-LHC, fluence will vary from $6 \times 10^{15}\,\mathrm{n_{eq}\,cm^{-2}}$ at low radius down to $1 \times 10^{15}\,\mathrm{n_{eq}\,cm^{-2}}$ at large radius. This range heavily depend on the amount of material in front of the HGTD.

For LGAD the main effect is the loss of the effective doping concentration in the multiplication layer due to deactivation of initial boron as acceptors, this lead to a reduction in gain and thus an increase of the time resolution [69]. For fluence larger than $1 \times 10^{15}\,\mathrm{n_{eq}\,cm^{-2}}$, there is little difference between LGAD and simple PIN diode. Fortunately, at such high fluence a gain is observed for both PIN and LGAD devices since deep effective acceptors created by irradiation in combination with a higher breakdown voltage result in electric fields high enough for charge multiplication in the full sensor. This can be seen in Figures 4.10 (b), as the fluence increase the maximum bias voltage achievable increase. At large fluence the timing resolution can thus be maintained by increasing the bias voltage applied on the sensor.

In these conditions a gain of the order of 8 can be achieved, this allows for a timing resolution lower than $60\,\mathrm{ps}$ for a fluence of $1 \times 10^{16}\,\mathrm{n_{eq}\,cm^{-2}}$ as seen in Figure 4.11.

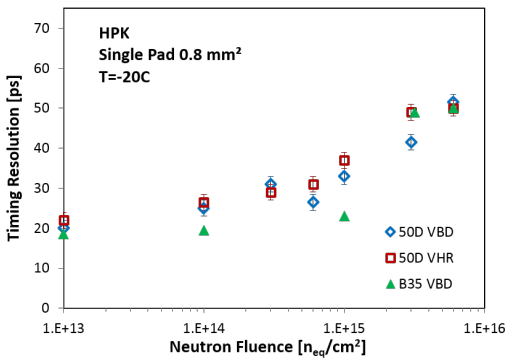

FIGURE 4.11 – Time resolution as a function of neutron fluence for different LGAD sensors at $-20\,^{\circ}\mathrm{C}$

Testbeam studies have shown [70] that the efficiency (fraction of pion creating a signal at least 3 time above the noise level) stays homogeneous in the central part of the sensor both before and after irradiation. In both case an efficiency of 99% in the center was achieved. The time resolution is also homogeneous within the pad before and after irradiation. Before irradiation a resolution of $39\,\mathrm{ps}$ is achieved on average, this resolution is degraded after irradiation. After irradiation the efficiency and timing resolution in the inter-pad region tend to increase as the gain in this region will increase leading to a greater efficiency and an improved resolution.

4.4 HGTD Electronics

The role of the electronics is to amplify and shape the pulses, extract the relevant information from these pulses, digitize the information and then send it though the flex cable toward the peripheral on-detector electronics located at $700\,\mathrm{mm} < R < 900\,\mathrm{mm}$.

The ASIC also need to be able to accommodate signal with a large dynamic range from 1 to 20 MIP. This range was determined using simulation of the electrons shower within the HGTD.

4.4.1 From pulse to time

To determine a time from a pulse, different step are necessary. First the output signal go through the preamplifier, its purpose it to further increase the amplitude of the pulse compared to the jitter and thus reduce σ_{jitter} as much as possible. The signal then go through a discriminator which will return a constant output as long as the signal is above a certain threshold. This output is then send to two Time to Digital Converter (TDC), one for the measurement of the Time of Arrival (TOA) and one for the Time Over Threshold (TOT).

The TDC operate with two input, one start and one stop, the start input is then delayed compare to the stop one by incrementation of $20\,\mathrm{ps}$, the number of delays necessary for the stop signal to be ahead of the start is then multiply by $20\,\mathrm{ps}$, this will correspond to the time between the start and the stop, that value is then outputted as a digital signal.

For the TOA measurement the start signal corresponds to the signal of the discriminator and the stop to the end of the measurement window, with this scheme the TDC will not receive any start signal if no hit was measure, reducing the power dissipation of the ASIC. In the case of the TOT a longer range is used (of the order of $20\,\mathrm{ns}$), in that case the start signal will also correspond to the discriminator output but the stop will this time correspond to the moment when the discriminator output goes back to 0.

4.4.2 Time walk correction

The time resolution of the electronic has to be smaller than the one of the LGAD. The contribution to the time resolution from the electronics is given by :

$$\sigma^2_{\mathrm{elec}} = \sigma^2_{\mathrm{jitter}} + \sigma^2_{\mathrm{TW}} + \sigma^2_{\mathrm{TDC}} \tag{4.4}$$

The σ_{TDC} corresponds to the effect of the TDC which converters time to digital information. For this conversion a quantization with a fixed binning is used, the bin size has to be smaller than the timing resolution. Bins of $20\,\mathrm{ps}$ are used, the resulting contribution to the resolution should be of the order of $5\,\mathrm{ps}$ and thus be negligible compare to the resolution of the sensor. The time offset of each individual channel will have to be calibrated in situ.

To minimize the effect of the time walk, techniques exist to make the measurement insensitive to the amplitude of the pulse. First one could use a Constant Fraction Discriminator instead of a fixed threshold. With this method the threshold is defined as a fraction of the maximal amplitude of the pulse, since the shape of the pulse does not depend on its amplitude this means that the time measured will be independent on the amplitude of the pulse. However, its implementation in an ASIC is quite complex, especially for the performance expected for the HGTD.

The second technique, which is the one used for the HGTD ASICs, consists of applying a correction of the TOA time based on the TOT. Since the time walk dispersion is correlated with the amplitude of the pulse, if one can measure this amplitude then it should be possible to correct the time. Instead of directly measuring the pulse amplitude the most common way to perform this correction in silicon detectors is to measure the pulse width, which is proportional to the amplitude. That way, only two TDCs are necessary (one for the TOA and one for TOT) instead of needing a TDC for the TOA and Analog to Digital Converter (ADC) for the amplitude. The measurement of the time of the rising edge of the discriminator pulse provides the TOA, while that of the falling edge, combined with the TOA, provides the TOT.

A residual σ_{TW} lower than $10\,\mathrm{ps}$ can be achieved after correction of the time walk using the TOT. The larger the amplitude the larger the value of the TOT becomes, for high energy hits, the value of the TOT could become larger than the $20\,\mathrm{ns}$ range used for the TOT measurement. In that case the only information for the correction of the TOA will be that the TOT is saturated. Fortunately for really large signal amplitude the dependency of the time walk with the amplitude decreases. The correction that would be applied for a TOT $20\,\mathrm{ns}$ can thus be applied to these events to partially correct the time walk.

4.5 HGTD Physics and Performance

The main goal of the HGTD is to improve the object reconstruction capability of the ATLAS detector with the use of additional timing information. In all the object-level performance studies shown in this section, full simulation and reconstruction of the tracker, calorimeters and muon system is combined with a fast simulation of the HGTD which smears the nominal tracks times with the expected per-track time resolution I computed. These results are based on studies performed for the HGTD Technical Proposal since the more recent studies haven't been made public yet [54].

4.5.1 Jets and Pileup

The HGTD can be used to mitigate the effect of the pile-up by associating times to tracks and jets. The association of times to jets is currently under study, two main method are being proposed, either combining together the times of all the tracks associated with the jet or using the times of all the hits in the HGTD that can be associated to the jet.

The key element to suppress pile-up in jets is the accurate association of jets with tracks and primary vertices. A simple but powerful discriminant is the $R_{p_{\mathrm{T}}}$ jet variable, defined as the scalar sum of the p_{T} of all tracks that are inside the jet cone and originate from the hard-scatter vertex PV_0, divided by the fully calibrated jet p_{T} , i.e.

$$R_{p_{\mathrm{T}}} = \frac{\Sigma p_{\mathrm{T}}^{\mathrm{trk}}(\mathrm{PV}_0)}{p_{\mathrm{T}}^{\mathrm{jet}}}.$$

The tracks used to calculate $R_{p_{\mathrm{T}}}$ fulfill the quality requirements defined in [56] and are required to have $p_{\mathrm{T}} > 1\,\mathrm{GeV}$, finally they are also required to satisfy Equation (4.1) [71]. Once this variable has been reconstructed, applying a simple cut on it can be used to separate the pile-up jets from the signal ones.

At moderate levels of pile-up, where track impact parameter measurements can be used to assign tracks to vertices with relatively little ambiguity, small values of $R_{p_{\mathrm{T}}}$ correspond to jets which have a small fraction of charged-particle p_{T} originating from the hard-scatter vertex. These jets are therefore likely to be pile-up jets, applying a simple cut on the value of the $R_{p_{\mathrm{T}}}$ can thus be used to separate the pile-up jets from the signal ones. However, at high pile-up conditions, and particularly in the forward region, the power of this discriminant is reduced. The effect can be mitigated by including timing information from the HGTD, removing tracks outside a $2\sigma_t$ window around the time of the hard-scatter vertex as explained in Section 4.2.

Hard-scatter and pile-up jets for simulated events are defined by their matching to truth jets, which are reconstructed from stable and interacting final state particles coming from the hard interaction. The matching criteria are defined in Reference [72]. Reconstructed hard-scatter jets are required to be within $\Delta R = \sqrt{(\Delta\eta)^2 + (\Delta\phi)^2} < 0.3$ of a truth jet with $p_{\mathrm{T}} > 10\,\mathrm{GeV}$. The pile-up jets must be at least $\Delta R > 0.6$ away from any truth jet with $p_{\mathrm{T}} > 4\,\mathrm{GeV}$.

The effect of the $R_{p_{\mathrm{T}}}$ and its improvement using timing information can is shown in Figure 4.12, showing the rejection of pile-up jets (defined as the inverse of the fraction of pile-up jet incorrectly reconstructed as hard scatter jet) as function of the efficiency for hard scatter jets (fraction of hard-scatter jet identify as hard-scatter). The efficiency and rejection curves (ROC) were computed using simulated samples of di-jets events with an $\langle\mu\rangle = 200$, the events were required to have the leading or sub-leading jet reconstructed in the HGTD acceptance.

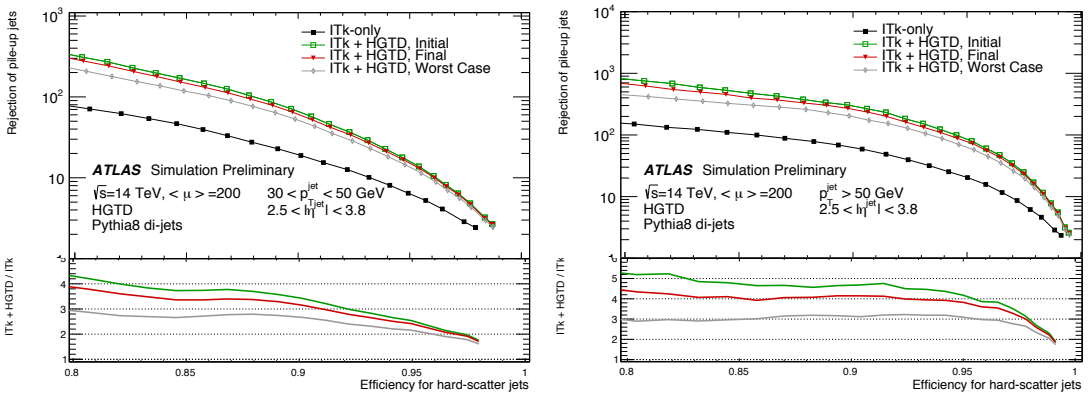

(a) Jets with $30 < p_{\mathrm{T}} < 50\,\mathrm{GeV}$.

(b) Jets with $p_{\mathrm{T}} > 50\,\mathrm{GeV}$.

FIGURE 4.12 – Pile-up jet rejection as a function of hard-scatter jet efficiency in the $2.4 < |\eta| < 4.0$ region, for the ITk-only and combined ITk + HGTD scenarios with different time resolutions.

Using the timing information, the pile-up rejection can be improved by a factor up to four for a constant hard scatter jets efficiency. Subsequent studies using the upgraded performance of the ITk and HGTD and a more realistic efficiency for the determination of the time of the primary vertex have shown that this improvement drop to a factor between 1.9 and 1.5.

In addition to improving the rejection of pile-up jets the timing measurement provided by the HGTD can also be used to improve the identification of b-jets in the forward region. The current algorithm use a multivariate technique with a neural network (called MV1) to estimate if a jet is more b-jet like or light jet like [64]. For this algorithm, many variables base on the

kinematics of the jet and their impact parameter are exploited. Due to the fact that the B-hadron have a long lifetime, the impact parameter of the b-jets may be large as the jet originate from the decay of a displaced vertex. This information can also be used in the b-tagging but this also mean that this technique is particularly sensitive to pileup-track contamination. Indeed, with a large z_0 window many pile-up track might get added to the b-jet, increasing greatly the rate of misidentified light-quark jets.

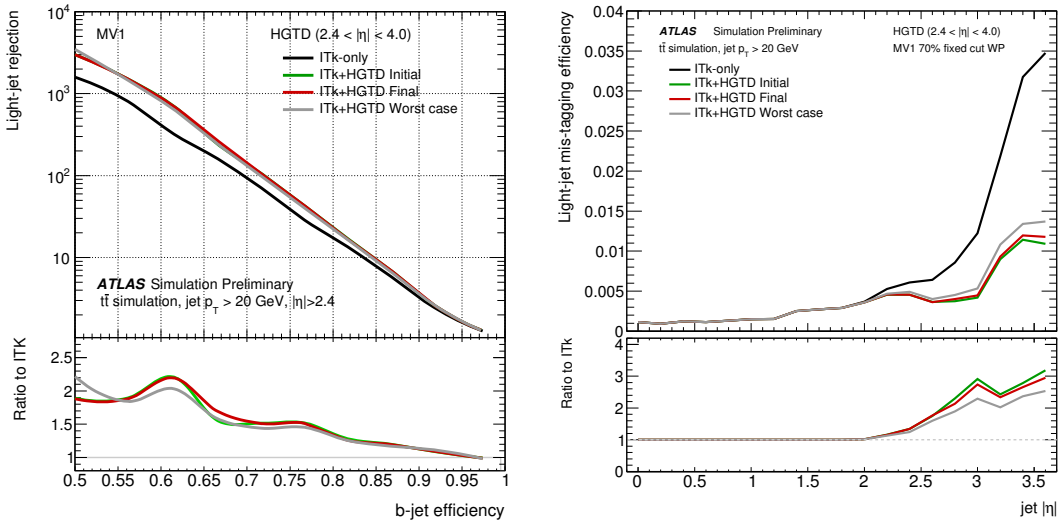

(a) (b)

FIGURE 4.13 – (a) Light-jet rejection versus b-tagging efficiency for the MV1 tagger and (b) Light-jet mis-tag efficiency for a 70% b-tagging efficiency working point as a function of jet $|\eta|$. The study uses $t\bar{t}$ events at $\langle\mu\rangle = 200$ and shows the achieved performance for different time resolution scenarios. The ratio plots at the bottom show the relative performance achieved with the HGTD with respect to the ITk-only scenario.

Figure 4.13 (a) shows the light-jet rejection versus b-tagging efficiency for the MV1 algorithm. The addition of the HGTD removes the majority of pileup tracks from the track selection. As a result, the performance of the b-tagger is significantly improved. For a b-tagging efficiency of 70% and 85%, the corresponding light-jet rejection for MV1 is increased by 1.4 and 1.2, respectively.

Figure 4.13 (b) shows the light-jet mis-tag rate for a 70% b-tagging efficiency working point as a function of jet $|\eta|$ for the timing scenarios. It can be seen from Figure 4.13 (b) that all timing scenarios yield significant improvements in the performance, even in the Worst Case scenario (defined at the time as a resolution of $65\,\mathrm{ps}$ for all the sensors). Importantly, significant improvements are observed also after the expected radiation damage during HL-LHC operation.

4.5.2 Physics

The physics performance improvements enabled by the HGTD can enhance the physics potential of ATLAS in several ways :

- The improved suppression of pileup jets is particularly important for searches or measurements of VBF processes, which produce forward dijet pairs with large invariant masses. Additional forward jets mimicking the VBF topology increase the background from processes like Z+jets. This improvement of the pileup jets rejection can also improve the sensibility of BSM search with multiples jets in the final state like the search presented in Section 5.
- The improved b-tagging performance in the forward region can benefit physics analyses with forward b-quarks, especially if the background originate from mis-tagged event. Additionally, improved b-tagging can increase the rejection of background event that should be b-tagged but are not like the $t\bar{t}$ background in measurements of and searches for Higgs bosons produced via VBF.
- The improved lepton efficiency can enhance the precision of important Standard Model measurements at high luminosity that require forward leptons, such as the measurement of the weak mixing angle.
- The capability of the HGTD to assign a time to nearly all vertices can enable the reconstruction of masses of long-lived particles that decay within the HGTD acceptance. For any new massive particle that lives long enough to reach the HGTD, estimates of the increased ionization energy loss and time-of-flight expected for a particle with $v < c$ could help identify them.

VBF $H \rightarrow WW^*$

VBF Higgs boson production can be computed with small theoretical uncertainties and is therefore a good channel for measuring the couplings between the Higgs boson and electroweak gauge bosons. The forward jet topology originating from the VBF is a distinct feature which can be used to separate signal processes from many backgrounds. The VBF $H \rightarrow WW^*$ process have been studied in ATLAS using Run 1 data at $\sqrt{s} = 7\,\text{TeV}$. The signal strength, defined as the ratio of the observed to the expected signal yield, was found to be of $\mu = 1.27^{+0.44}_{-0.40}(\text{stat.})^{+0.30}_{-0.21}(\text{syst.})$[73]. Increased pileup poses a challenge to the reconstruction of forward jets, and VBF final states are particularly sensitive to the precision with which jet-to-vertex association can be done in the forward region.

Detector scenario	N_{VBF}	N_{bkg}	N_{ggF}	N_{WW}	N_{VV}	$N_{t\bar{t}}$	N_t	$N_{Z/\gamma^*+\text{jets}}$	$N_{W+\text{jets}}$
ITk	80	65	19	15	0	21	0	10	0
ITk + HGTD	80	37	19	4	0	5	0	10	0

TABLE 4.1 – The signal and background yields are shown for the most sensitive BDT bin for different scenarios.

The signal and background yield is shown is for both ITk only and ITk+HGTD in the most sensitive bin of the BDT in Table 4.1. The addition of the HGTD is shown to reduce the background by 43%. This decrease affects two of the background categories, the WW background in which the pile-up can create additional forward jet and the $t\bar{t}$ category in which the decay of the t can create a forward b-jet that can be incorrectly tagged. For the WW the improved pile-up rejection led to a reduction of 73% of this background with the HGTD, for the $t\bar{t}$ the improved

b-tagging lead to a reduction of 76% of this background. Without the use of the HGTD, a $\Delta\mu$ of 0.096 is expected, the addition of the HGTD improves this value by 8 % down to 0.088.

tH production

A measurement of tH production is the only direct probe of the sign of the top-Yukawa coupling. The integrated luminosity produced by the LHC so far is not sensible to this parameter, but determining it is an important goal for the HL-LHC physics program. The diagrams contributing to tH are shown in Figure 4.14.

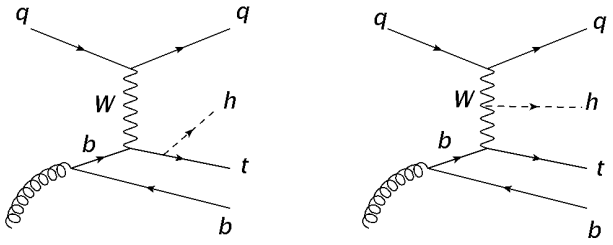

FIGURE 4.14 – Contributing diagrams to tH production with the top-Yukawa coupling (left) and the W to Higgs-boson coupling (right). In both cases, a forward jet is expected, with additionally a gluon splitting to $b\bar{b}$ pair producing a b-jet in the forward region in 25% of the events.

The use of the HGTD can help clean the forward region of pile-up jets and thus reducing the contamination from background with a central signal and a forward pile-up jet. Using a log-likelihood ratio binned in η of the light forward jet, the sensitivity to tH is improved by 11% as shown in Table 4.2.

Scenario	Signal significance
ITk	1.28σ
ITk + HGTD	1.42σ

TABLE 4.2 – Expected (statistical only) signal significance of $tH \to b\bar{b}$ using ITk or ITk + HGTD.

$\sin^2\theta_{\text{eff}}$

The weak mixing angle is one of the fundamental parameters of the SM. Several measurements of $\sin^2\theta_{\text{eff}}$ have been made at previous and current colliders, and the current world average is dominated by the combination of measurements at LEP and at SLD, which gives $\sin^2\theta_{\text{eff}} = 0.231530 \pm 16 \times 10^{-5}$. However, the two most precise measurements differ by over 3σ.

At HL-LHC, the best sensitivity to $\sin^2\theta_{\text{eff}}$ is at high Z rapidity when at least one lepton is present in the forward region [73]. Only Z bosons decaying to electrons are considered in this analysis since this final state provides the best experimental precision within the largest acceptance.

The contribution of jets misidentified as electrons is suppressed using a tight electron identification and a track isolation requirement. In the forward region, the timing information provided by the HGTD can be used to improve the isolation efficiency of the electrons while maintaining the same rejection for the un-isolated one. This is achieved by removing out of time

tracks close to the electrons that would make it appear un-isolated. The purity of the candidate sample is determined with simulation, and is found to be greater than 99% in the CC channel, between 90 and 98% in CF, and between 60 and 90% in the FF channel. The signal significance with HGTD is up to 20% higher with respect to the case of ITk only in the CF channel.

When considering only the experimental uncertainties, including the HGTD in the ATLAS forward region brings a 13% improvement on the $\sin^2\theta_{\text{eff}}$ sensitivity in the CF channel. Combining the three channels together, the expected sensitivity reaches a precision of $\Delta\sin^2\theta_{\text{eff}} = 18\times10^{-5} \pm 16\times10^{-5}$ (PDF) $\pm 9\times10^{-5}$ (exp.), which exceeds the precision achieved in all previous single-experiment results so far.

Monopole searches

Magnetic monopoles are elementary particles with a single pole magnetic charge, unlike dipoles that have both a north and south magnetic pole. These particles were first theorized by physicist Paul Dirac in 1931[74], they were also predicted as part of grand unified theories as described in [75] and several new electroweak models predicted monopoles with a mass that could be accessible at LHC [76] thus allowing the detection in LHC experiments. Until today, no direct evidence of the existence of magnetic monopoles was found.

The Bethe-Bloch formula for magnetic particles is different from the one for electrically charged particle. Electrons and protons have high ionization power at low energy and then stabilize to MIPs at high energy due to the $1/\beta^2$ term. For magnetic monopoles the ionization at high energy grows as a function of β^2, deviation significantly from the MIP signature. The resulting signature would consist of a long-lived particle that would deposit a high amount of energy via ionization when reaching the detector. This energy will be proportional to the Dirac (magnetic) charge of the particle and can as high as 100 times larger than the one deposited by a MIP.

Previous search in ATLAS have failed to find any monopoles [77] but such searches focused only on the barrel, the addition of the HGTD will provide a tool to measure such particles if they are emitted in the forward region. In the HGTD such particles would leave several low-energy hits and one or two hits with a very high-energy. This topology could be used by the electronic of the HGTD at the trigger level to save such event and make them available offline.

4.5.3 Luminosity

In addition to its capability as a timing detector the HGTD can also be employed as a luminosity detector (luminometer). Most luminometer operate under the same principle, they are used to measure a quantity that is hypothesized to be linearly related to the instantaneous luminosity (or related to the average number of interactions $\langle\mu\rangle$). For example some quantities that can be used are : the average number of charged track in the tracker [78] or the number of cluster in a pixel detector.

The luminometer are usually calibrated in a van der Meer run, in these run the parameter of the beam are precisely controlled such as the luminosity can be mathematically calculated. The position of the two beam are then slowly shifted as such as they are scanned through. The quantity measured by the luminometer is then compared with the distance between the two beams to calibrate the detector. As a fine control of the beam parameter is needed such runs are performed at low $\langle\mu\rangle$ between 1 and 10^{-3}, the luminometer therefore has to be able to operate linearly as function of the luminosity on the order of 5 orders of magnitudes between $\langle\mu\rangle \sim 10^{-3}$ and $\langle\mu\rangle \sim 200$.

The occupancy of the HGTD can be used to access the number of interactions and thus to reconstruct the luminosity. Compared to the information on the number of charged tracks, which is only available offline after reconstruction, the number of hits in the HGTD is an information that can be accessed both offline and online (i.e. for every bunch crossing). The measurement of the luminosity will not be performed on the full range of the detector, only for a range of $320\,\mathrm{mm} < R < 640\,\mathrm{mm}$ ($2.4 < |\eta| < 3.1$). This limited range was chosen to limit the amount of data send, avoid using sensor at low radius that are more affected by the irradiation (and would thus degrade quicker) and to only use sensor in the low occupancy region.

The presence of multi-hit pad in the detector would result in non-linearity on the measurement of the luminosity. Fortunately the occupancy the HGTD in the region used for the luminosity measurement is lower than 2% which lead to a multi-hit fraction of 0.04%. The cavern noise, also called afterglow, can also induce non-linearity as it increase after each bunch crossing. This effect can be removed using the timing resolution of the HGTD by comparing the occupancy during the bunch crossing to the occupancy before and after the bunch crossing.

Figure 4.15 shows the average number of hits per event registered in the first layer (both sides of the innermost cooling plate) of the HGTD as a function of the number of simultaneous pp interactions. This study was performed using the full simulation of the HGTD that I developed. The linear fit is performed in the hatched region and extended to the full luminosity range, for the region of $\langle\mu\rangle$ 200 this fit match the measured point with a precision of the order of the percent. This illustrates the linearity of the number of hits in the HGTD as function of the number of pp collision.

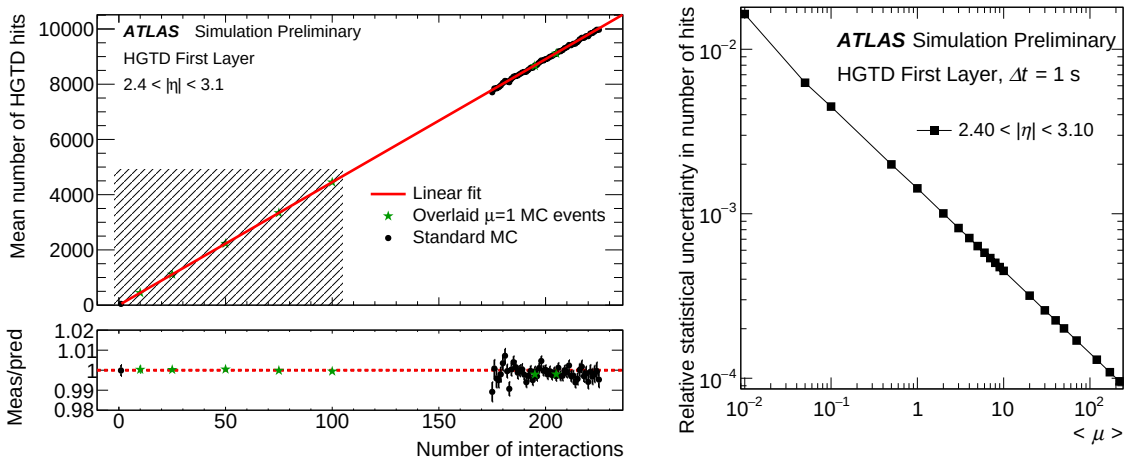

FIGURE 4.15 – (a) Linearity of $< n_{hits} >$ as a function of μ. (b) Statistical uncertainty as function of $< \mu >$.

From a physics point of view, the uncertainty on the measurement of the integrated luminosity affects the majority of physics analyses at the LHC. It is especially relevant for precision measurements, for which the total uncertainty is dominated by systematic effects such as the estimation luminosity. The luminosity has been measured in Run 1 and Run 2 with several detectors, currently the resulting uncertainty for the nominal proton-proton collision data are currently 2.1%, 2.2% and 2.4% for data from 2015, 2016, and 2017, respectively. The increase uncertainty with time is directly link to the increase of $\langle\mu\rangle$, for the HL-LHC if no upgrade were performed, the resulting uncertainty would be even larger.

Prospect on the cross-section measurement for different Higgs analysis have been performed for the HL-LHC [50]. Those prospect use an uncertainty on the luminosity of 1% which is really ambitious compared to the more realistic 2% obtain for the LHC. This value was chosen as to not dominate all other sources of uncertainty (which are all below 2%), with the help of the HGTD archiving such a performance should be possible. This would ultimately improve all the physics measurement at the HL-LHC by reducing their systematic uncertainty.

Chapitre 5

Search for pair produced color resonances

The search of fully hadronic final states at the LHC is extremely challenging. Such a signature might escape more traditional supersymmetric analyses based on missing transverse energy. In this chapter, a search for pair produced scalar particles in final states with four jets that I have performed is presented. In particular the search presented in this chapter will focus on the RPV stop but it can easily be extended to other scalar colored particles. The data have not been unblinded yet for this analysis, this section chapter will thus focus on the optimization of the Signal Region used for the analysis, study of the topology of the signal events and different algorithms to reconstruct the two pair produced particles from the four jets as well as the estimation of the background.

5.1 Signature Characterization

The final state consists of four jets forming two pairs (resonances). To reconstruct the signal, identifying these two pairs is critical. The pair of resonances is used to compute discriminating variables which will be useful in separating the signal from the background.

If the mass of the stop is small, the p_{T} of the stops will be large and the two jets in each pair will be close to each other. The sum of the distance of the two jets in each pair : $\Delta R_{min} = \sum_{i=1,2} |\Delta R_i - 1|$ can be used to determine the correct pair of resonances. ΔR_i is defined as the square root of the difference of the azimuthal angles and pseudorapidity squared : $\Delta R_i = \sqrt{(\Delta\eta)^2 + (\Delta\phi)^2}$.

The stops are pair produced so both jet pairs should have the same reconstructed mass corresponding to the stop mass. To exploit this information, the mass asymmetry : $A = \frac{m_1 - m_2}{m_1 + m_2}$ where m_1 and m_2 are the masses of the two reconstructed pairs, is used in the analysis.

After boosting the system formed by the resonance-pair into the center-of-mass frame we define the cosine of the angle with the beamline : $|\cos(\theta^*)|$. This variable is expected to be large for the multijet background.

To reconstruct the mass of the stop, the mass average of the two resonances is used : $m_{avg} = \frac{m_1 + m_2}{2}$.

5.2 Event Generation

The optimization of the analysis relies on the accurate simulation of the signal to optimize the separation between the background and the signal. A study of the generation of the signal was thus performed to understand how the simulation of the signal would affect the variables used in the analysis. The simulation in the analysis use production of sgluons at Leading Order (LO). The Next to Leading Order (NLO) increases the total cross section by about a factor 1.6 [79]. Additional jets produced at NLO might affect the variables used in the analysis. As this could lead to change of the efficiency and thus affect the results (limits), the sensitivity of the variables to the difference between LO and NLO has to be checked. To perform this study, Madgraph [80] was use for the simulation of the signal as it allows to generate both LO and NLO of the same signature.

Madgraph is a Monte Carlo (MC) event generator used for both SM and BSM phenomenology, it combines multiple tools to be able to start from a given process and model and go down to detector simulation. First, using the process and model, the different possible Feynman diagrams are computed, then the corresponding matrix elements are determined. Parton level (hard) events are generated using MC techniques, the events are hadronized using Pythia [81]. Finally, a detector simulation called Delphes is used, this will take into account first order effect that are expected from a hadron collider detector such as reconstruction, resolution and return variables similar to the one that are measured in a detector.

To understand the impact of the order of the simulation on the analysis. The efficiency of the signal selection, defined as : $\frac{N_{SR}}{N_{tot}}$, using an analysis strategy similar to the one that will be presented in Section 5.5.1 was used.

A Madgraph implementation of both the LO and the NLO production for the sgluons was used [82]. In total, 8 samples were produced, with 50000 events in each of those samples, for 4 different mass for the sgluons : $200\,\mathrm{GeV}$, $400\,\mathrm{GeV}$, $800\,\mathrm{GeV}$ and $1\,\mathrm{TeV}$ generated both at LO and NLO. A series of cuts, corresponding to the Signal Region (SR) of the analysis, are applied on the events generated by Madgraph :

1. At least 4 jets are required.
2. The four jets are required to have a p_{T} large enough. The value of this cut depend on the mass : $50\,\mathrm{GeV}$ for the mass of $200\,\mathrm{GeV}$, $100\,\mathrm{GeV}$ for the mass of $400\,\mathrm{GeV}$ and $120\,\mathrm{GeV}$ for the mass of $800\,\mathrm{GeV}$ and $1\,\mathrm{TeV}$.
3. Two sgluons have to be reconstructed from the 4 jets.
4. The sum of the distances between the two jet in each resonance is required to be :
   $\Delta R_{min} < -0.002 \times m_{avg} - 225 + 0.72$ for $m_{avg} < 225\,\mathrm{GeV}$ and
   $\Delta R_{min} < +0.0013 \times m_{avg} - 225 + 0.72$ for $m_{avg} > 225\,\mathrm{GeV}$.
5. The pair production angle has to be : $|\cos(\theta^*)| < 0.3$
6. The mass asymmetry between the two sgluons has to be : $A < 0.05$ where $A = \frac{m_1 - m_2}{m_1 + m_2}$

The result of this analysis can be seen in Table 5.1 for all the mass $\geqslant 400\,\mathrm{GeV}$. For each mass the first line is the efficiency of the cut while the second is the total efficient of up to that cut in the cut flow. For each cut the efficiency does vary between the LO and the NLO case and the difference between the two is of less than 5%.

Mass [GeV]	Jets > 4	p_T cut	2 sgluons reco	ΔR_{min}	$\lvert\cos(\theta^*)\rvert$	A
400	94.4%	40.8%	100%	25.3%	53.8%	17.0%
LO	94.4%	38.5%	38.5%	9.7%	5.2%	0.9%
400	94.2%	40.0%	100%	24.8%	53.8%	18.0%
NLO	94.2%	37.5%	37.5%	9.3%	5.2%	0.9%
800	98.1%	70.9%	100%	38.2%	50.3%	13.5%
LO	98.1%	69.5%	69.5%	26.5%	13.4%	1.8%
800	98.1%	70.9%	100%	37.1%	51.5%	14.3%
NLO	98.1%	69.5%	69.5%	25.8%	13.3%	1.9%
1000	98.6%	79.4%	100%	47.6%	49.8%	12.8%
LO	98.6%	78.3%	78.3%	37.1%	18.5%	2.4%
1000	98.7%	79.8%	100%	46.7%	49.8%	13.0%
NLO	98.7%	78.7%	78.7%	36.7%	18.3%	2.4%

TABLE 5.1 – Efficiency of the different cuts used in the analysis for the LO and NLO samples.

For a mass of 200 GeV the efficiency ratio is shown in Table 5.2 as function of the value of the p_T cut. For low value of the p_T cut the efficiency ratio is close to one but it decreases as the value of the cut increases. A similar effect can be observed for the other mass points if the p_T is increased to large values.

p_T cut [GeV]	Eff LO	p_T cut Eff LO	Eff NLO	p_T cut Eff NLO	Rato NLO/LO
10	1.5%	100%	1.4%	100%	92.8%
20	1.5%	100%	1.4%	100%	92.8%
30	1.5%	92.6%	1.4%	92.1%	92.0%
40	1.3%	74.9%	1.2%	73.8%	91.5%
50	1.1%	55.9%	1.0%	53.9%	90.3%
60	0.8%	38.3%	0.7%	35.8%	91.7%
70	0.6%	24.2%	0.5%	21,9%	88.0%
80	0.4%	14.6%	0.3%	12.3%	76.9%
90	0.3%	8.7%	0.2%	7.0%	68.7%
100	0.2%	5.3%	0.1%	4.2%	57.9%

TABLE 5.2 – Signal efficiency and p_T cut efficiency for 200 GeV sgluon for LO and NLO sample.

This effect of the p_T cut can also be observed in Figure 5.1. The distribution of the average mass of the two reconstructed sgluons is the same for LO and NLO as expected. However, the NLO corrections decrease the hardness of the produced signal jets.

At NLO the jet multiplicity in the final state can be increased with an additional gluon being emitted[79]. As the initial momentum stays the same this result in softer jets in the final state as shown in [79].

The analysis is not affected by these differences except for the low mass point that has already been excluded. Therefore, the LO simulation can be used with an adequate systematic error.

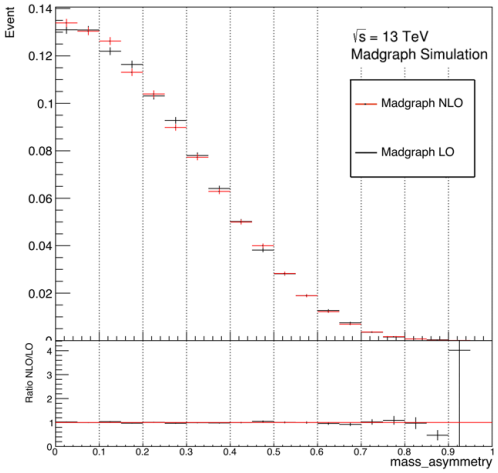

(a) A for a mass of 200 GeV

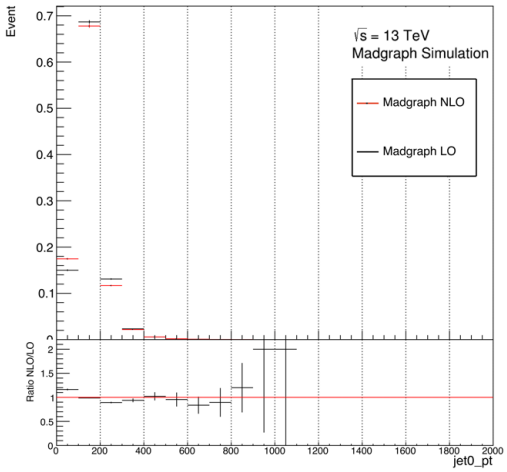

(b) A for a mass of 1 TeV

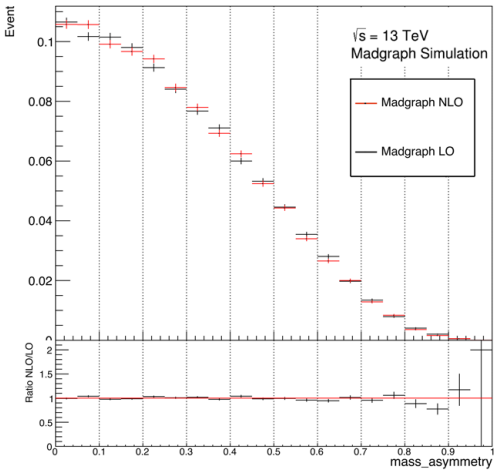

(c) p_{T} of the leading jet for a mass of 200 GeV

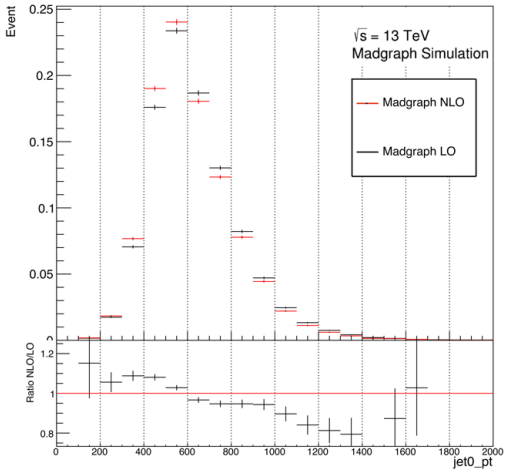

(d) p_{T} of the leading jet for a mass of 1 TeV

FIGURE 5.1 – Comparison between the LO and NLO distribution for A and p_{T} of the leading jet for a sgluon mass of 200 GeV and 1 TeV

5.3 Dataset and Event Selection

Data collected by ATLAS between 2016 and 2018 for pp collisions with an energy in the center of mass of $\sqrt{s} = 13\,\mathrm{TeV}$ are used. We choose not to use the data from 2015 in the analysis as the trigger that are used for the three other years is not available for 2015. The small increase in statistics would not justify the increase of complexity of using two triggers.

Possible triggers for the analysis were studied as the choice of the trigger can impact the signal and background efficiency. Additional cut on the trigger variable was found to be necessary to ensure that the trigger is fully efficient.

The triggers are used to preselect the event that will be used for the analysis. It will both be used for the data, the MC signal used to estimate the expected signal significance and the MC multijet background used to test the analysis method.

5.3.1 Trigger

Events registered with two different triggers were considered. The first one, called HLT_4j120, requires to 4 jets with $p_{\mathrm{T}} > 120\,\mathrm{GeV}$. The previous analysis, performed on 2015 and 2016 data, used a similar trigger : HLT_4j100. This trigger required a minimum p_{T} of $100\,\mathrm{GeV}$, allowing the analysis to efficiently probe low mass stop. To keep the amount of data register by the LHC to a reasonable level the threshold of the trigger was increased to $120\,\mathrm{GeV}$ in 2017. For consistency's sake the same threshold for the three years will be used.

The second trigger, HLT_ht1000, requires 4 jets with $HT > 1\,\mathrm{TeV}$ where HT is the sum of the p_{T} of all the jets in the events with $p_{\mathrm{T}} > 50\,\mathrm{GeV}$: $HT = \sum_{jet, p_{\mathrm{T}} > 50\,\mathrm{GeV}} p_{\mathrm{T}}$. This trigger was considered in particular for higher stop mass.

To be able to properly use a trigger one needs to be sure that it is fully efficient. To study the efficiency of a trigger, a looser trigger is needed to preselect the events that will be used for the study. The looser triggers are usually prescaled triggers, in addition to their requirements only a fraction of the events that fulfill the trigger requirement are recorded. For the events passing the looser trigger the efficiency is the number of events that passed the harder trigger divided by the total number of events. This is done as function of the variable used by the trigger, a harder cut on this variable can then be applied in the analysis to ensure a 100% efficient trigger.

The efficiency for HLT_4j120 is shown as function of the p_{T} of the fourth jet (lowest p_{T} of the 4 jets) in Figure 5.2. To study this trigger, HLT_4j45 is used to select the events. This trigger requires 4 jets with $p_{\mathrm{T}} > 45\,\mathrm{GeV}$, additionally $p_{\mathrm{T}} > 70\,\mathrm{GeV}$ is required to ensure that this trigger is 100% efficient. In Figure 5.2 (a) the efficiency of the data from 2016, 2017 and 2018 are compared. The 2016 data is slightly lower, this is probably due to a change in calibration of the jets. Figure 5.2 (b) presents the efficiency for the 3 years combined and two signal samples. Similar efficiencies are observed for data and the signal. To ensure that the HLT_4j120 is at least 95% efficient when used in the analysis a p_{T} cut of $p_{\mathrm{T}} > 140\,\mathrm{GeV}$ will be required.

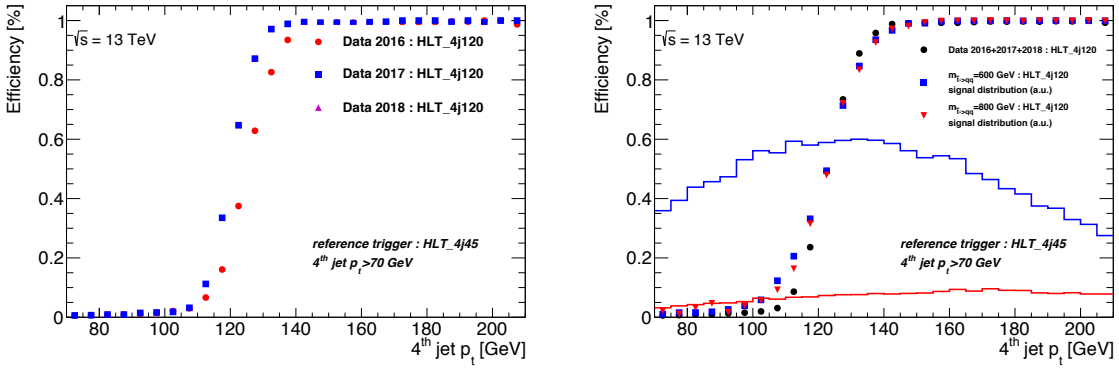

(a) (b)

FIGURE 5.2 – (a) The efficiency of the HLT_4j120 trigger in data for different years. (b) The HLT_4j120 trigger efficiency in data compared with simulated signal samples. The solid lines are the signal samples.

The efficiency for HLT_ht1000 is shown as function of the HT in Figure 5.3. In this case HLT_ht700, a trigger that requires an $HT > 700\,\mathrm{GeV}$, is used to preselect the events. An $HT > 850\,\mathrm{GeV}$ is then required to ensure that it is 100% efficient. In Figure 5.3 (a) the efficiency is compared for the three years. As for HLT_4j120 the efficiency is worse for 2016. The efficiency of the data and the signal sample are similar for HLT_ht1000 as shown in Figure 5.3 (b). To ensure

that the HLT_ht1000 at least 95% when used in the analysis an HT cut of $HT > 1080\,\text{GeV}$ will be required.

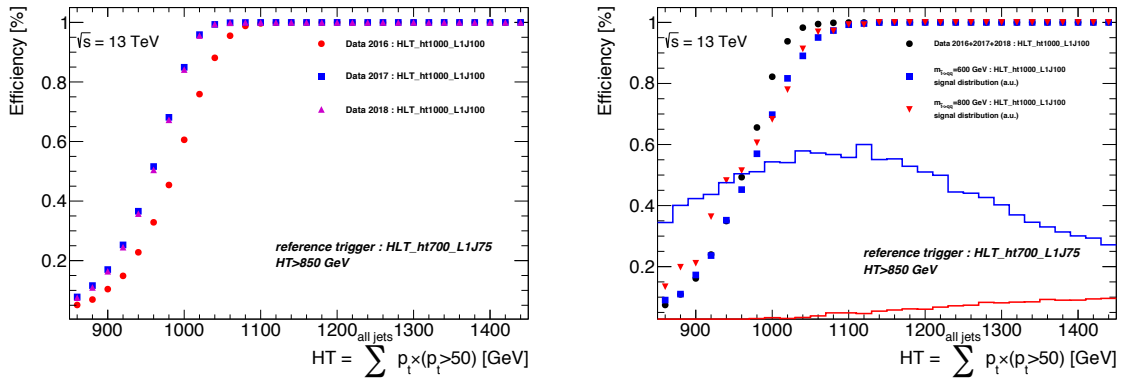

(a) (b)

FIGURE 5.3 – (a) The efficiency of the HLT_ht1000 trigger in data for different years. (b) The HLT_ht1000 trigger efficiency in data compared with simulated signal samples. The solid lines are the signale samples.

To determine which trigger should be used, the signal samples are shown in full line on Figure 5.2 (b) and 5.3 (b). The fraction of events passing the trigger is slightly larger for HLT_ht1000 but this difference tends to decrease in the signal region as shown in Figure 5.4 (a). Figure 5.4 (b) shows that HLT_ht1000 also rejects less background for larger average mass than HLT_4j120 and tend to remove the background events at low mass average that could be useful for the determination of the background from the data. For these reasons HLT_4j120 is used in the following.

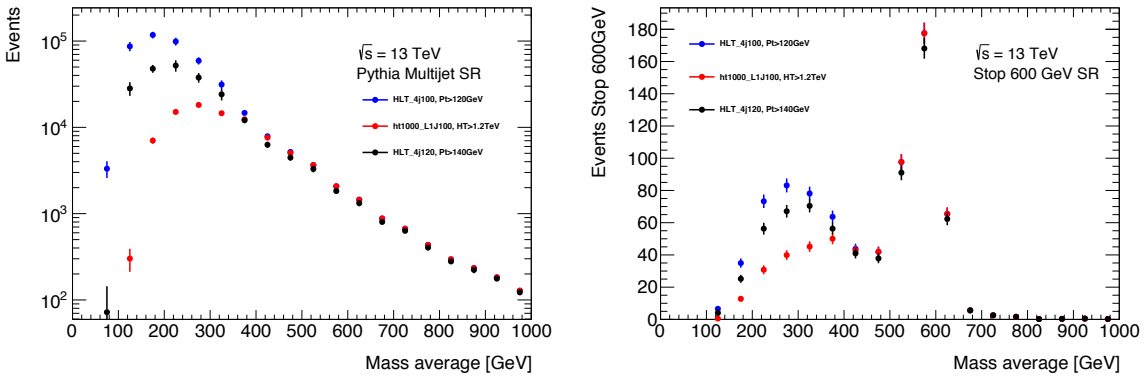

(a) (b)

FIGURE 5.4 – (a) Number of MC dijet in the SR for different the triggers as function of the averaged mass of the two reconstructed resonances. (b) Number of MC stops (m=600 GeV) in the SR for different the triggers as function of the averaged mass of the two reconstructed resonances.

In addition to the HLT_4j120 trigger and the $p_{\text{T}} > 140\,\text{GeV}$, the following event-level cuts are applied (ATLAS standard cuts) :

- A GoodRunList is required to ensure the relevant detector systems are in a good state for physics.
- Events are rejected in case of a LAr noise burst or data corruption.

- Tile corrupted events are rejected.
- Events affected by the recovery procedure for single event upsets in the SCT are rejected.
- Incomplete events (in which some detector information is missing) are rejected.
- Events are required to have a primary vertex with at least two tracks associated.

This series of cuts will be referred in the following as the preselection.

Using this preselection the number of events per accepted pb^{-1} of data should stay consistent across all years. Figure 5.5 shows the number of events in the SR per pb^{-1}. This number stays relatively constant within each year and from one year to another. A small difference can be seen between 2015, 2016 and 2017,2018. For the first two years the number of events per pb^{-1} is of the order of 70 while it is only 65 for the last two. This is consistent with the change of trigger between 2016 where HLT_4j100 was used and 2017 where HLT_4j120 was used.

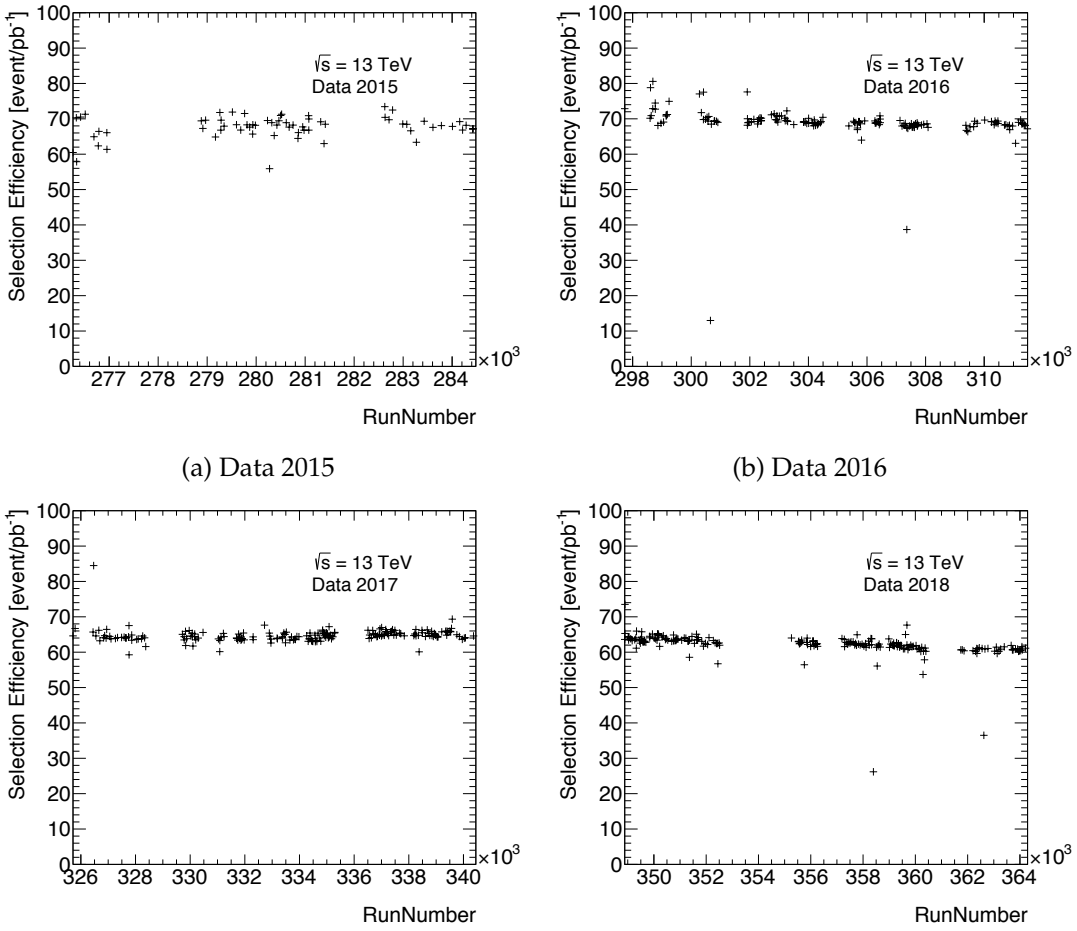

(a) Data 2015

(b) Data 2016

(c) Data 2017

(d) Data 2018

FIGURE 5.5 – Number of events in the SR of the ABCD per pb. Data from 2015 and 2016 use the HLT_4j100 trigger while 2017 and 2018 use HLT_4j120.

5.3.2 Monte Carlo samples

The dominant background for this study is the SM multijet production. To take into account the response of the detector, a Geant4 simulation of the ATLAS detector is used. To take into account the effect of the pileup, minimum bias events are generated using Pythia 8.186. The minimum bias events are then overlaid on the hard scatter event.

MC background

Background sample of multijet process are simulated using $2 \rightarrow 2$ matrix element at leading order using Pythia 8.186. The A14 tune of shower and multiple parton interactions parameters is used together with the NNPDF23LO PDF set. In total 13 samples are available, each corresponding to a different range in average dijet p_{T}. The information on the samples can be found in Table 5.3

DSID	Sample	Events	Cross section [pb]	Filter efficiency	$\sigma \times \epsilon_{filter}$[pb]
361020	Pythia8EvtGen_A14NNPDF23LO_jetjet_JZ0W	15987000.0	78420000000.	0.97565	80302080000
361021	Pythia8EvtGen_A14NNPDF23LO_jetjet_JZ1W	15987000.0	78420000000.	0.00067198	52696671.6
361022	Pythia8EvtGen_A14NNPDF23LO_jetjet_JZ2W	15987000.0	2433200000.	0.00033264	809379.648
361023	Pythia8EvtGen_A14NNPDF23LO_jetjet_JZ3W	15987000.0	26454000.	0.00031953	8452.84662
361024	Pythia8EvtGen_A14NNPDF23LO_jetjet_JZ4W	15987000.0	254630.	0.00053009	134.9768167
361025	Pythia8EvtGen_A14NNPDF23LO_jetjet_JZ5W	15987000.0	4553.5	0.00092325	4.204018875
361026	Pythia8EvtGen_A14NNPDF23LO_jetjet_JZ6W	15987000.0	257.53	0.00094016	0.2421194048
361027	Pythia8EvtGen_A14NNPDF23LO_jetjet_JZ7W	15987000.0	16.215	0.00039282	0.0063695763
361028	Pythia8EvtGen_A14NNPDF23LO_jetjet_JZ8W	15987000.0	0.62502	0.010162	0.00635145324
361029	Pythia8EvtGen_A14NNPDF23LO_jetjet_JZ9W	15987000.0	0.019639	0.012054	0.0002367285
361030	Pythia8EvtGen_A14NNPDF23LO_jetjet_JZ10W	15987000.0	0.0011962	0.0058935	0.0000070498
361031	Pythia8EvtGen_A14NNPDF23LO_jetjet_JZ11W	15987000.0	0.000042258	0.0027015	0.0000001132
361032	Pythia8EvtGen_A14NNPDF23LO_jetjet_JZ12W	15987000.0	0.0000010367	0.00042502	0.0000000004

TABLE 5.3 – Standard model multijet background used by the analysis.

The reconstruction of the resonances is run on each of the samples individually. The weight is applied to each event is defined as :

$$weight = \frac{L \times \sigma \times \epsilon_{filter}}{N_{events}} \tag{5.1}$$

where L is the integrated luminosity, σ is the cross section of the sample, ϵ_{filter} is the filter efficiency of the sample and N_{events} is the number of events in the sample.

The first three samples (361020, 361021 and 361022) have p_{T} below the trigger threshold. Since the cross sections of those samples are large compare the one of the other samples, if one of these events passes the trigger they would have a large weight and would greatly affect the output. To avoid this statistical effect, only the samples from 361023 to 361032 are used for the background.

The MC background and the data have been compared to ensure that the MC could be used to estimate the performance of the analysis. Figure 5.6 shows a comparison of the distribution of the p_{T} and η for the leading jet. A scale factor of 73% is applied to the MC to obtain the same number of events as observed in the data. An agreement of the order of 10% is observed between the data and the MC background. This discrepancy comes from the fact that multijets samples are produced at LO resulting in less jets in the final state and thus harder jets.

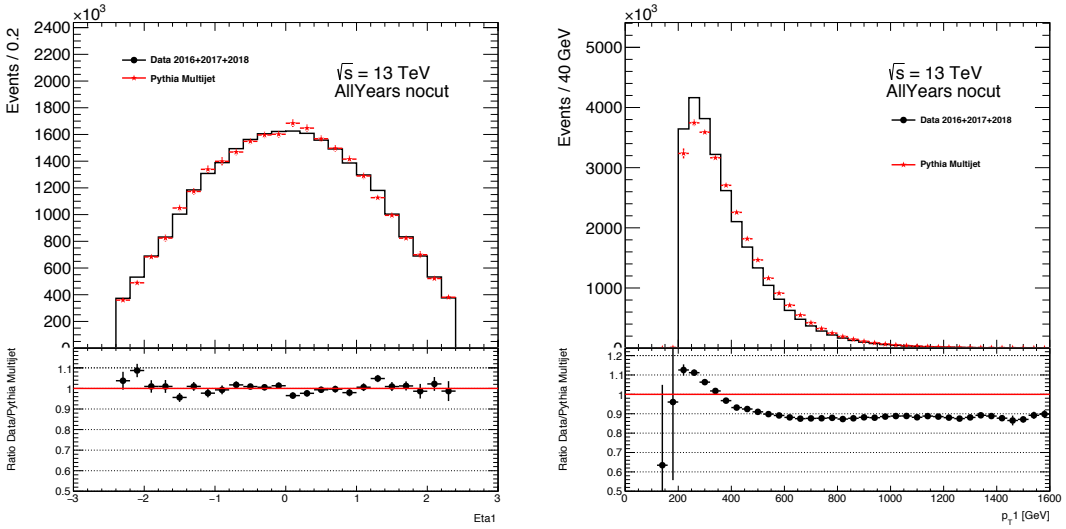

(a) (b)

FIGURE 5.6 – Comparison of the MC and the Data for the distribution of the p_{T} (b) and η (a) for the leading jet.

MC signal

For the signal samples, only RPV stop where produced. In total 13 different mass points have been considered for the stop : 300 GeV, 400 GeV, 450 GeV, 500 GeV, 550 GeV, 600 GeV, 650 GeV, 700 GeV, 750 GeV, 800 GeV, 850 GeV, 900 GeV, 1000 GeV. Two decay channels of the stop have been simulated, one into a b-quark and a light quark and one into two b quarks. The first one was used both for the inclusive search in which no requirement on the number of b quarks reconstructed in the final state was made and the 2 b-tagged search in which 2 b-quarks are required in the final state. For this analysis the jet calibration difference between b-quarks and light quarks as well as between gluon jets and quark jets plays only a minor role, justifying the use of only two samples. The second was used to investigate the possibility of performing a 4 b-tagged search.

5.4 Event topology

Once the events have been preselected, the signal events have to be separated from the background. The topology of the signal and background was studied. Since the signal final state is composed of four jets created by two resonances, different algorithms were tested to reconstruct the two stops. With the two stops reconstructed, more advanced variables can be deduced to define the signal region.

5.4.1 Preselection

The distribution of p_{T} and η of the four leading jets after preselection for the data of 2016, 2017 and 2018 and for MC signal for three different stop masses is shown in Figures 5.7 and 5.8. The index of the jets are ordered by decreasing p_{T}.

As expected, the largest the mass of the stop lead to the largest p_{T}. For a mass of $300\,\mathrm{GeV}$ there is almost no difference between the p_{T} distribution of the signal and the data, rendering any additional p_{T} cut meaningless. For larger masses on the other hand a larger difference can be observed, in particular in the distribution of the p_{T} of the fourth jet. Indeed, for the data more than 85% of the events have a fourth jet with a $p_{\mathrm{T}} < 200\,\mathrm{GeV}$, an additional cut on the p_{T} of the jets can be used to reject the background. This can be particularly useful when considering the search of high mass resonances.

The distributions also show that the pT requirements due to the trigger shape the background. As the threshold is $140\,\mathrm{GeV}$, the background is shaped like a stop of mass of $280\,\mathrm{GeV}$.

In the η distribution shown in Figure 5.8, the high mass signal jets tend to be a bit more central than the low mass one but apart from that no major difference exist between the different masses. Comparing the signal jets and the data, the signal jets tend to be more central than the one in the data. When defining the jets used in the analysis, in addition to the p_{T} requirement only jets with $|\eta| < 2.4$ will be selected. As for the p_{T}, if necessary an additional cut on the $|\eta|$ of the jets might also be used to reduce the number of background events.

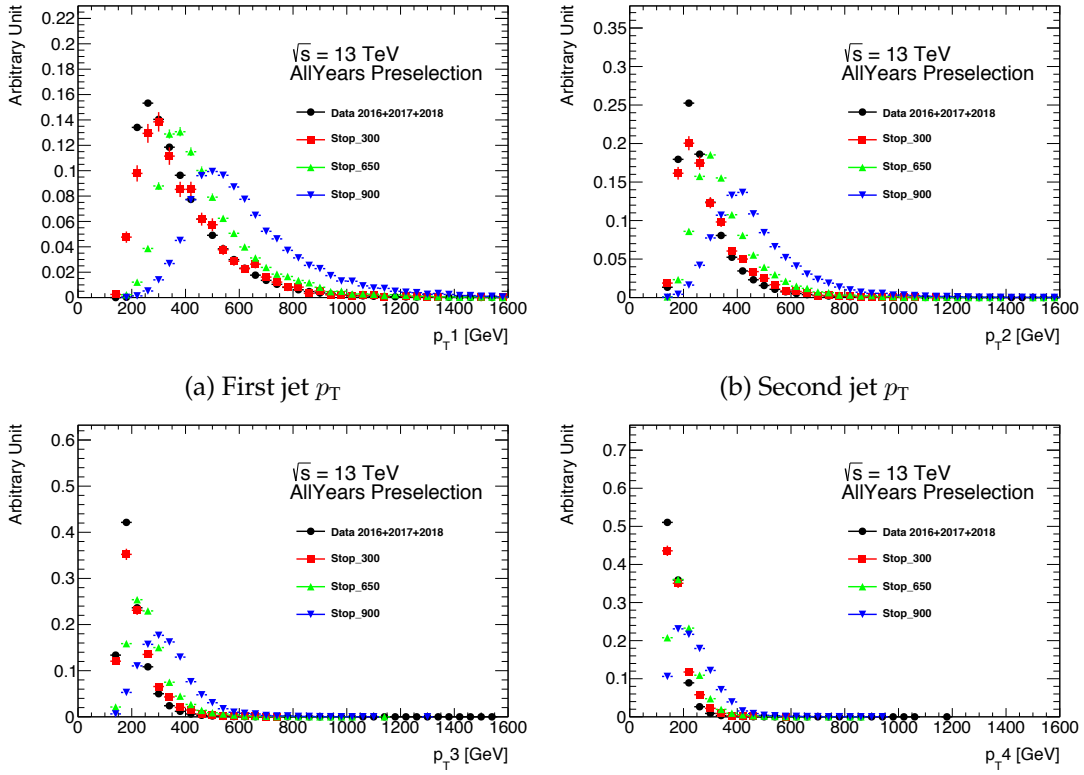

(a) First jet p_{T}

(b) Second jet p_{T}

(c) Third jet p_{T}

(d) Fourth jet p_{T}

FIGURE 5.7 – Distributions of the leading and sub-leading jet p_{T} after the preselection is applied for the data 2016+2017+2018 and the MC signal for three different masses.

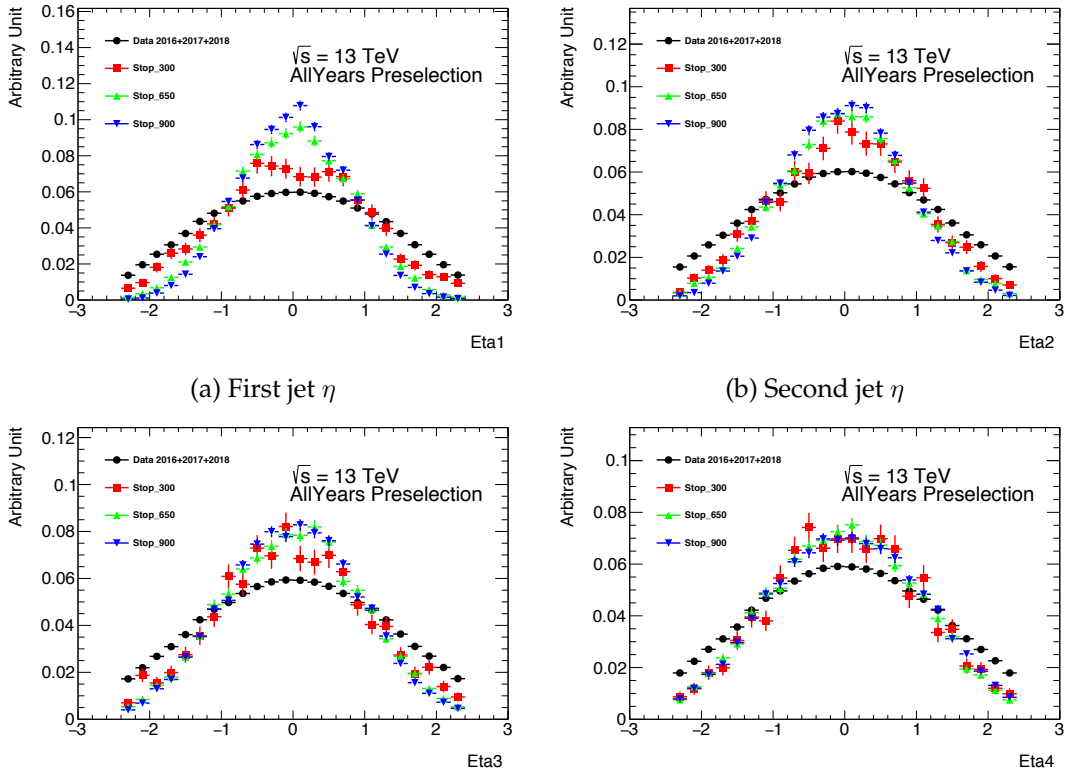

(a) First jet η

(b) Second jet η

(c) Third jet η

(d) Fourth jet η

FIGURE 5.8 – Distributions of the leading and sub-leading jet η after the preselection is applied for the data 2016+2017+2018 and the MC signal for three different masses.

5.4.2 Signal region variables

Once the events have been preselected, the two resonances have to be reconstructed. Different methods to reconstruct the resonances have been tested, they will be presented in section 5.5. Once the resonances have been reconstructed, new variables can be defined that will be used to define the signal region.

In this section all distributions will be shown using a truth pairing for the signal and a ΔR_{min} pairing for the data. The truth pairing is performed by identifying, using MC signal sample, the four truth particles that correspond to the decay product of the two truth stop. Each truth particle is associated with the closest jet with a $\Delta R < 1$. If multiple truth particles would be associated to the same jet or if not all the jets are associated with a truth particle the event is discarded. For this reason this truth matching is inefficient which leads to large errors. The pairing is then done so that the jets for which the associated truth particles correspond to the decay of one of the truth stop are paired together. The ΔR_{min} pairing used for the data is performed by comparing ΔR_{min} of the 3 possible resonance-pair in each event. The one with the smallest ΔR_{min} is then selected.

For low masses, a significant fraction of the resonances will be produced with a large transverse momentum. As a result, the decay products are expected to be close-by, but the four jets still to be resolved. The ΔR of the two resonances can be used both to reconstruct the resonances and as a discriminating variable. The total ΔR of the event, also called ΔR_{min} is defined as :

$$\Delta R_{min} = \sum_{i=1,2} |\Delta R_i - 1.0| \tag{5.2}$$

where ΔR_i is the angular distance between the two jets for the i^{th} pair and the sum is over the two pairs. The offset of -1.0 has been chosen to maximize the signal efficiency while minimizing the effects of soft jets from radiated gluons being recombined with their parent jets in multi-jet topologies.

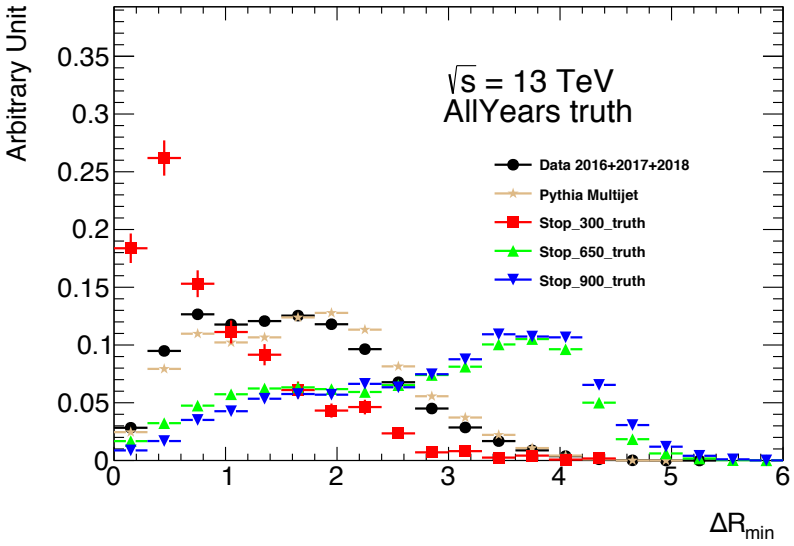

FIGURE 5.9 – Distributions of the ΔR_{min} for MC signal and data 2016, 2017 and 2018. For the MC signal a truth based paring is performed while one minimizing ΔR_{min} is used for the data.

The distribution of ΔR_{min} is shown in Figure 5.9. For low mass (lower than $400\,\mathrm{GeV}$) the truth pairs are indeed mainly at low value of ΔR_{min} while most of the background has a higher value of ΔR_{min}. On the other hand at higher mass the p_{T} of the stop are smaller and the ΔR_{min} of the truth pairs for the signal increase. An additional cut on ΔR_{min}, depending on the pairing strategy, will be used to ensure that only good resonance-pairs systems are kept.

After boosting the system formed by the resonance-pairs into its center-of-mass frame, the cosine of the angle that either of them forms with the beamline is $|\cos(\theta^*)|$. Background jets from multijet production are frequently originating from t-channel gluon exchange and are preferentially produced in the forward region, with $|\cos(\theta^*)|$ close to one. The distribution $|\cos(\theta^*)|$ is shown in Figure 5.10. For low mass signals, jets originating from the signal are instead expected to be more central and to peak at small $|\cos(\theta^*)|$ values. This can be used to separate the signal and the background. At larger signal mass the signal distribution flatten reducing the discriminating power of the variable.

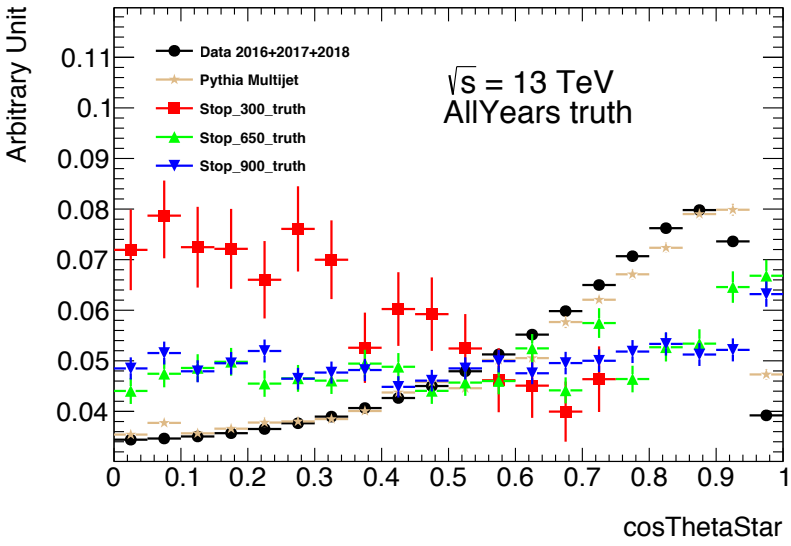

FIGURE 5.10 – Distributions of the $|\cos(\theta^*)|$ for MC signal and data 2016, 2017 and 2018. For the MC signal a truth based paring is performed while one minimizing ΔR_{min} is used for the data.

Since the two reconstructed resonances are expected to have the same masses, the mass difference is a powerful discriminant between signal and background The mass asymmetry A is defined as :

$$A = \frac{|m_1 - m_2|}{m_1 + m_2} \tag{5.3}$$

where m_1 is the invariant mass of the resonance containing the leading p_{T} jet and m_2 the invariant mass of the other resonance. The distribution of A is shown in Figure 5.11. A is close to 0 for a well reconstructed system and relatively flat for the background. No major difference is observed between different masses point.

The final discriminant used in the analysis is the average mass of the two reconstructed resonances :

$$m_{avg} = \frac{1}{2}(m_1 + m_2) \tag{5.4}$$

A peak in the m_{avg} distribution is expected at a mass corresponding to the mass of the resonance for the signal. For the background a non peaking falling distribution is expected due to the multijet process. The distribution of m_{avg} for both data and signal is shown in Figure 5.12.

For each mass hypothesis a counting experiment is performed in a window of the m_{avg} variable optimized to maximize the expected discovery significance. Depending on the method used to pair together the resonances different analysis strategies are employed.

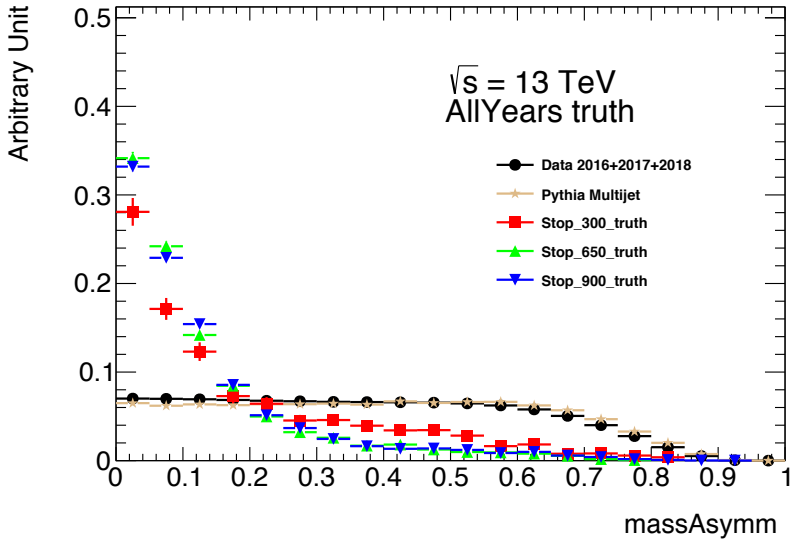

FIGURE 5.11 – Distributions of the mass asymmetry A for MC signal and data 2016, 2017 and 2018. For the MC signal a truth based paring is performed while one minimizing ΔR_{min} is used for the data.

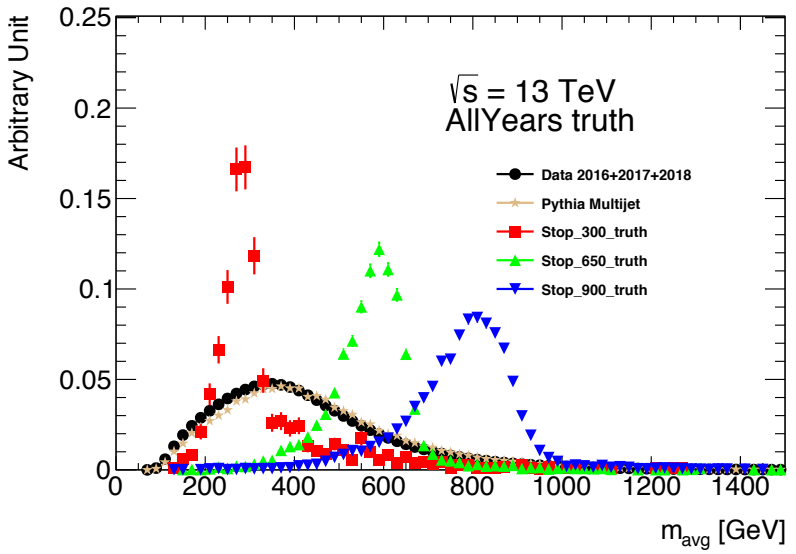

FIGURE 5.12 – Distributions of the mass average m_{avg} for MC signal and data 2016, 2017 and 2018. For the MC signal a truth based paring is performed while one minimizing ΔR_{min} is used for the data.

5.5 Pairing of the resonances

The two resonances have to be reconstructed. Only four jets are considered : the four leading jets with $p_{\mathrm{T}} > 140\,\mathrm{GeV}$ and $|\eta| < 2.4$. There are three possible pairing configurations per event. Different variables can be used to determine which of the resonance-pair is the most likely to correspond to the truth. In addition, the method used should not shape the background to look like the signal as it would decrease the ability to separate signal and background.

The signal topology can greatly depend on the mass of the resonance. For this reason two different pairing algorithms, both based on the ΔR_{min} variable will be presented. Example of other pairing algorithm that were studied will also be discussed.

5.5.1 ΔR_{min} Pairing

The pairing strategy that was employed for the analysis is the selection of the resonance-pair system with the smallest ΔR_{min}. As shown in Figure 5.9, for low signal masses due to the high p_{T} of the resonances, ΔR_{min} tends to be smaller than the background. This pairing combined with a cut on ΔR_{min} allows to reconstruct the signal and efficiently reject the background.

When using the ΔR_{min}, the signal region is defined using three cuts. First a condition on ΔR_{min} is used to reject the poorly reconstructed resonances-pair :

$$\begin{aligned} \Delta R_{min} &< -0.002 \times (m_{avg} - 225) + 0.72, m_{avg} \leq 225 \\ \Delta R_{min} &< +0.0013 \times (m_{avg} - 225) + 0.72, m_{avg} \geq 225 \end{aligned} \tag{5.5}$$

Resonances of larger masses are produced with a lower boost, and their decay products are less collimated. To compensate for the larger angular separation between the jets at high mass this requirement is scaled for the m_{avg} in the event. Then $\cos(\theta^*) < 0.3$ is required as the signal tend to have smaller value while the background peak at one. Finally, a mass asymmetry of $A < 0.06$ is required.

The distributions of the signal variables are affected by the pairing algorithm, the ones obtain after a ΔR_{min} pairing are shown in Figure 5.13.

Figure 5.14 shows the expected m_{avg} distribution for signal samples with different masses in the signal region. For all masses the distribution peaks at a mass corresponding to the mass of the resonances. At high mass, a large tail can be observed for mass lower than the expected masses. The tail are the result of bad pairing of the jets. Indeed, at higher mass the ΔR of the resonances tends to be large. Since the ΔR_{min} pairing minimizes the ΔR this will lead to a shaping of the signal toward low ΔR and low masses. This can also be observed in Figure 5.13 (a) in which the distribution of ΔR_{min} after the pairing has smaller values than for the truth at high mass.

For the larger mass signal this is problematic as the mispairing will result in a smaller signal efficiency. For example in the case of a stop with a mass of $800\,\mathrm{GeV}$ more than 60% of the events are incorrectly reconstructed. To solve this issue other pairing strategies have been studied, in particular to be used at higher masses.

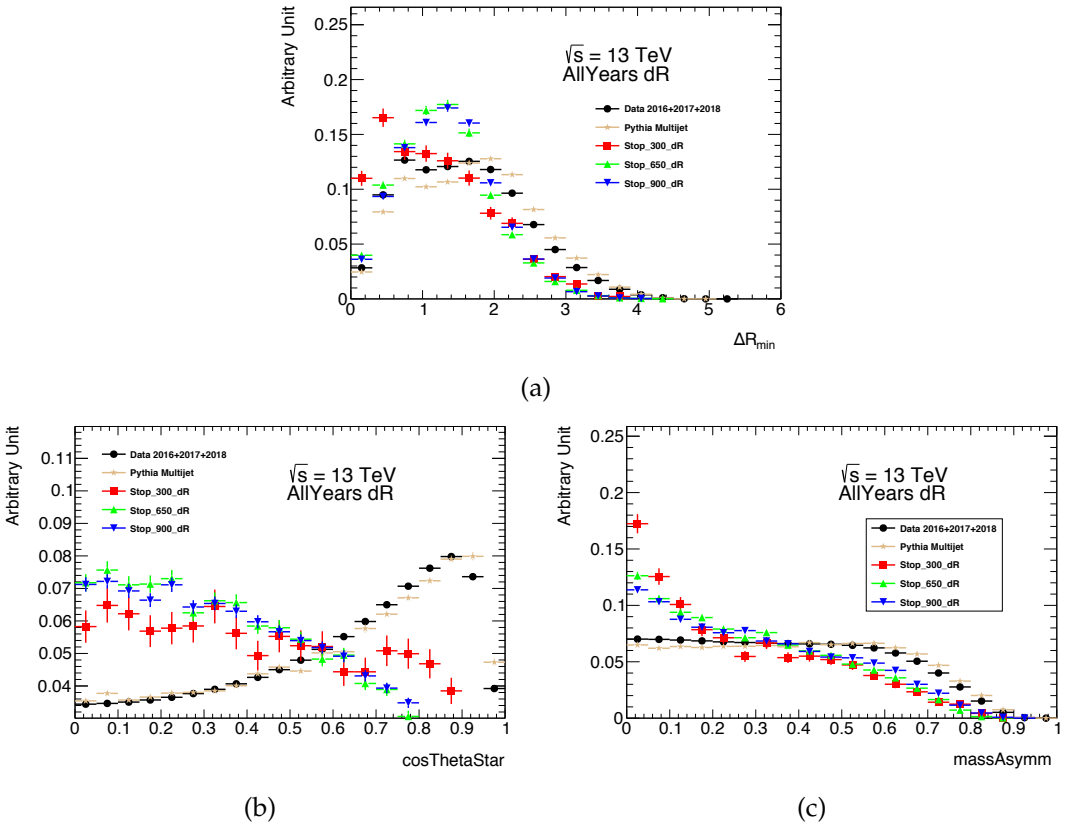

FIGURE 5.13 – Distributions of ΔR_{min} (a), $|\cos(\theta^*)|$ (b) and A (c) for MC signal and data 2016, 2017 and 2018. The ΔR_{min} pairing is used.

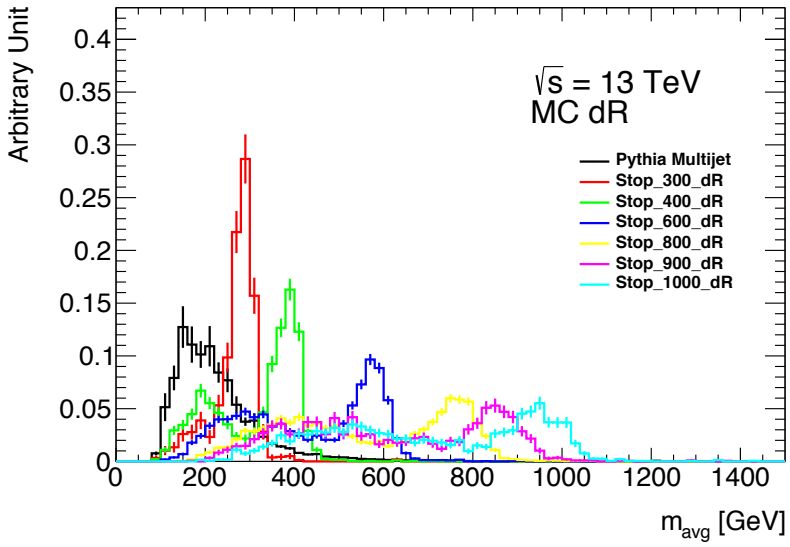

FIGURE 5.14 – Distribution of m_{avg} in the signal region for MC signal and MC background. The ΔR_{min} pairing is used.

5.5.2 ΔR_{max} Pairing

At higher mass, the ΔR of the resonances pair tend to be larger. For this reason a pairing that selects the pair with the maximum ΔR (ΔR_{max}) has also been studied. For this analysis the SR was defined as follows :

- $\Delta R_{max} < 4.4$
- $p_{\mathrm{T}4} > 180\,\mathrm{GeV}$
- $A < 0.15$

The distribution of the signal variables obtained after a ΔR_{max} pairing are shown in Figure 5.15

Figure 5.15 shows the expected m_{avg} distribution for signal samples with different masses in the signal region. At large mass the distribution of $|\cos(\theta^*)|$ is similar for both signal and background, this variable can no longer be used to discriminate the signal and the background. With this pairing method it is slightly harder to separate the signal and the background, investigation are still ongoing to determine if other signal variables could be used for the ΔR_{max} pairing.

The main advantage of this pairing method is that it allows for a better pairing of the resonances with 64% of the events in the SR correctly paired for a mass of $800\,\mathrm{GeV}$. Figure 5.16 shows the expected m_{avg} distribution for signal samples with different masses in the signal region. Compared to the large tails that were present for the larger mass sample with the ΔR_{min} pairing, the tail for the ΔR_{max} are smaller and result in a peak containing a larger fraction of the events.

The ΔR_{max} signal region has not been fully optimized yet but already achieves $\frac{signal}{\sqrt{background}}$ ratio of the same order as for the ΔR_{min} after optimization while not shaping the signal.

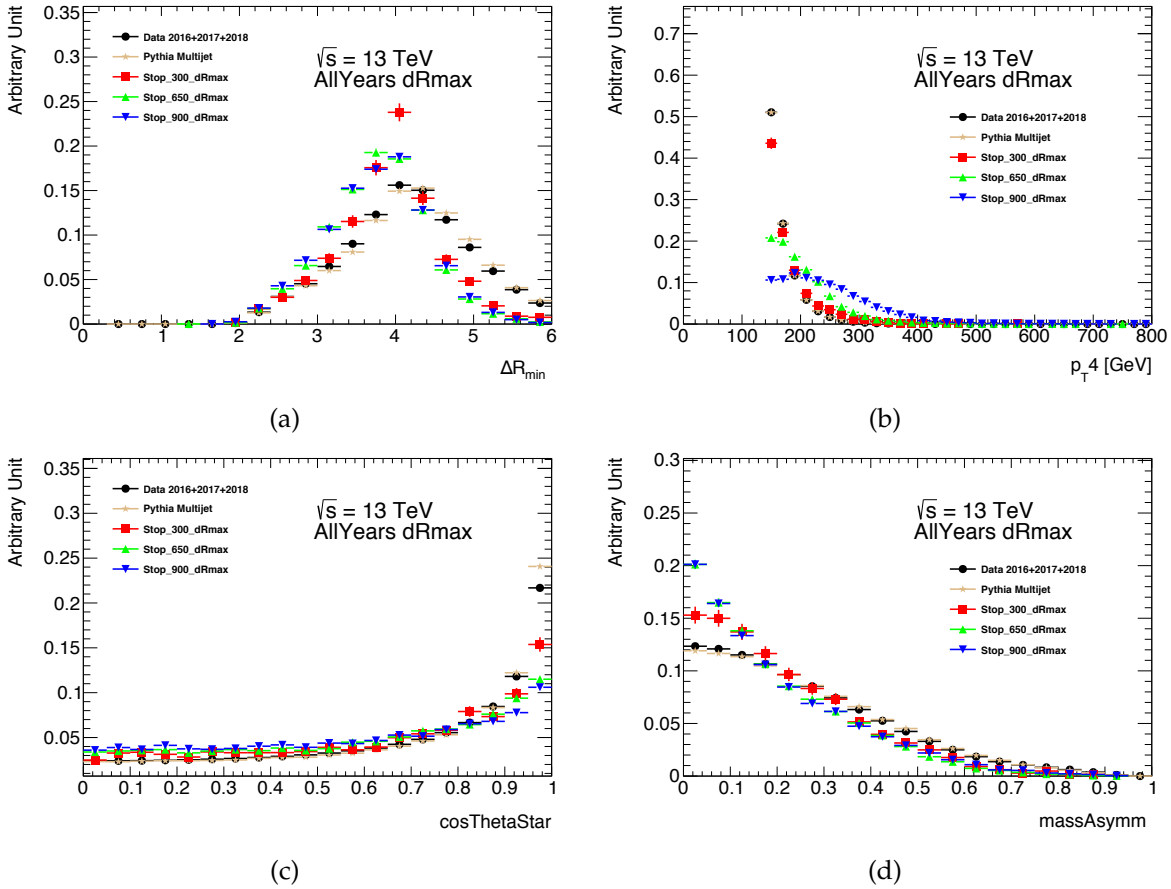

FIGURE 5.15 – Distributions of ΔR_{min} (a), $p_{\mathrm{T}4}$ (b), $|\cos(\theta^*)|$ (c) and A (d) for MC signal and data 2016, 2017 and 2018. The ΔR_{max} pairing is used.

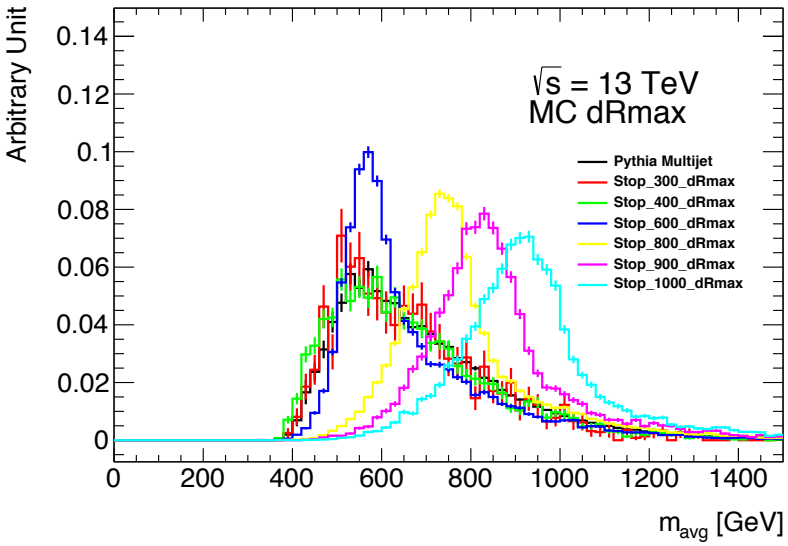

FIGURE 5.16 – Distribution of m_{avg} in the signal region for MC signal and MC background. The ΔR_{max} pairing is used.

5.6 Background estimation

The multijet background being difficult to simulate, the background will be estimated via a data driven method. In this section, two different methods will be presented. The first method called the ABCD method will be used for the estimation of the background after a ΔR_{min} pairing. For the ΔR_{max} a background fit is investigated.

5.6.1 ABCD

At low signal mass, the average mass of the resonances would correspond to the rising part of background distribution, for this reason a fit of the background cannot be used to estimate the background. The ABCD matrix method is then used instead, a schematic view of this method is shown in Figure 5.17. The data sample is split into four regions, one in which the signal selection is applied (D) and three background dominated regions (A,C and F). These regions are defined using two of the signal variables : $|\cos(\theta^*)|$ and A. For $A < 0.06$ represent the transition between the signal and the background region while for $|\cos(\theta^*)|$, 0.3 is used. If the two variables used to define these regions are uncorrelated, the background in the signal region D can be predicted from the number of events in the background dominated control region : $N_D = N_A \times \frac{N_F}{N_C}$. Two additional regions, B and E, are also defined in the $A - |\cos(\theta^*)|$ plane. The validation region (region E) is used to test the performances of the data driven method and assign an uncertainty to the background estimate. The validation region is defined with the same selection as for the signal region but the mass asymmetry requirement is changed to $0.06 < A < 0.15$

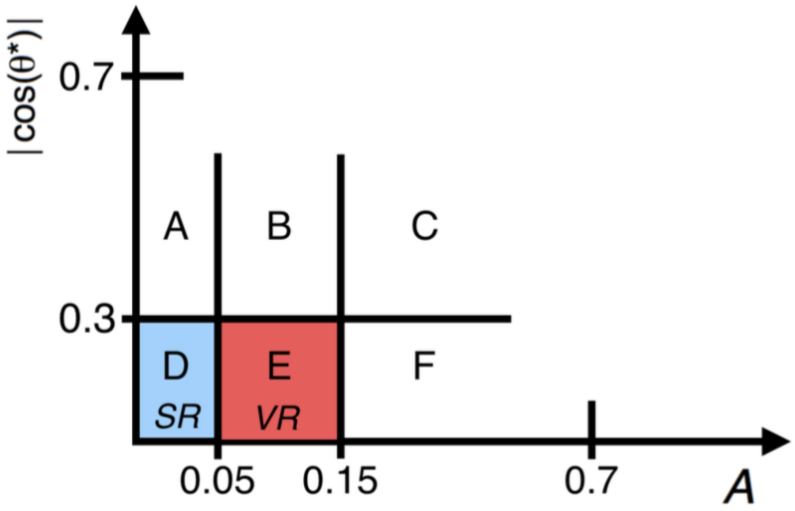

FIGURE 5.17 – Scheme of the control regions in the $|\cos(\theta^*)|$ and A plane defined to estimate the multijet background and to obtain the related uncertainty.

The correlation between the $|\cos(\theta^*)|$ and A variables has been evaluated in both data and a simulated multijet sample. The correlation of the two variables is of the order of the percent. To visualize this correlation, the bidimensional plane defined by $|\cos(\theta^*)|$ and A is shown in Figure 5.18. Each bin is normalized to the integral of events along the y-axis. A correlation between the two variables would show up in this plane as a non horizontal pattern. As long as the large values of A and $|\cos(\theta^*)|$ are removed, no correlation can be seen both for $m_{avg} > 200\,\text{GeV}$ and $m_{avg} > 1500\,\text{GeV}$.

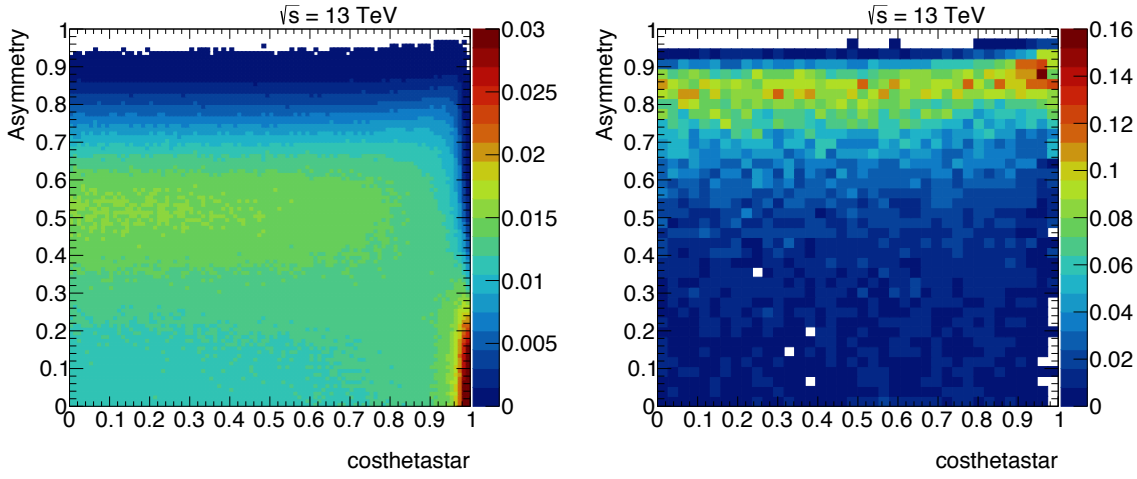

(a) (b)

FIGURE 5.18 – Distribution of events in the $|\cos(\theta^*)| - A$ plane where each bin has been scaled for the integral of events along the y-axis. The left plot is for $m_{avg} > 200\,\text{GeV}$ (a), the right plot for $m_{avg} > 1500\,\text{GeV}$ (b).

To further study its impact, the correlation has been evaluated as function of m_{avg}, in $100\,\text{GeV}$ wide slices of m_{avg}. This is presented in Figure 5.19. The nominal signal region selection is compared with a selection where the ΔR_{min} requirement is not applied, and one were the ABCD plane is restricted to $|\cos(\theta^*)| < 0.7$ and $A < 0.7$. It is visible that without requiring a maximum ΔR_{min} a strong bias appears as function of m_{avg}. This bias is strongly reduced by imposing the ΔR_{min} requirement, although a correlation can still be seen above $800\,\text{GeV}$. By further reducing the ABCD plane this effect can be reduced to masses above $1.2\,\text{TeV}$. While some non-correlation is still present at higher m_{avg} values, the large statistical uncertainty expected in the SR for such masses makes this potential bias small compared to the total uncertainty. As the statistics at larger mass increase it might become necessary to change the estimation method for large masses.

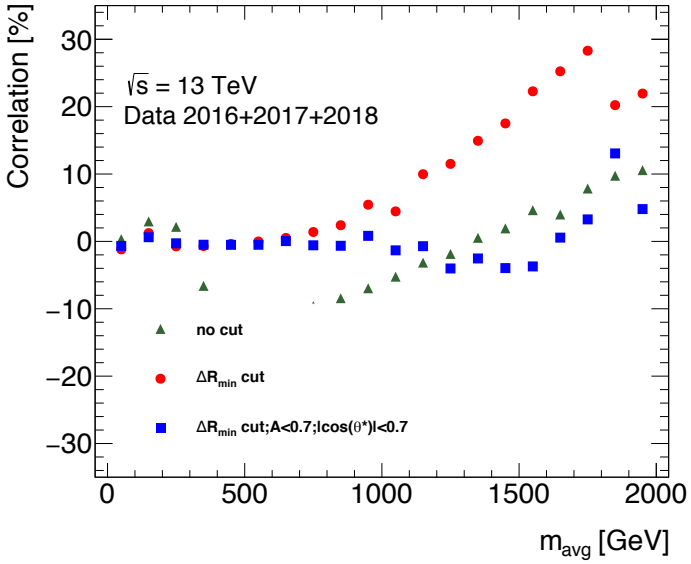

FIGURE 5.19 – Distribution of m_{avg} in the signal region for MC signal and MC background. The ΔR_{max} pairing is used.

5.6.2 Background Fit

When pairing the jets using ΔR_{max} a correlation of more than 10% between $|\cos(\theta^*)|$ and A appears, moreover $|\cos(\theta^*)|$ loses its discriminant power and is thus not useful to define the SR. For these reasons a background estimation based on a fit has been developed, this method which is independent of the simulation results in a prediction of the background. The uncertainty are two-fold : the functional form and the statistical error on the parameters. The multijet m_{avg} is fitted with the following 5 parameters function that have already been used in dijet searches [83] :

$$f(x) = p_1 \times (1-x)^{p_2} \times x^{p_3+p_4\ln(x)+p_5(\ln(x))^2} \tag{5.6}$$

where p_i are the parameters of the fit and x is defined as :

$$x = \frac{m_{avg}}{\sqrt{s}} \tag{5.7}$$

The validity of this approach has been tested using the MC multijet background samples. Even if small difference exist between the MC and the Data, the shapes are similar. If the fit performs well with the MC it should perform at least as well with the data. Figure 5.20 shows the fit the MC multijet background with Equation 5.6. A χ^2 of 93 is obtained for 65 degrees of freedom. Comparing bin per bin the value obtain with the fit and the value from the MC, they are compatible at the order of a few percents.

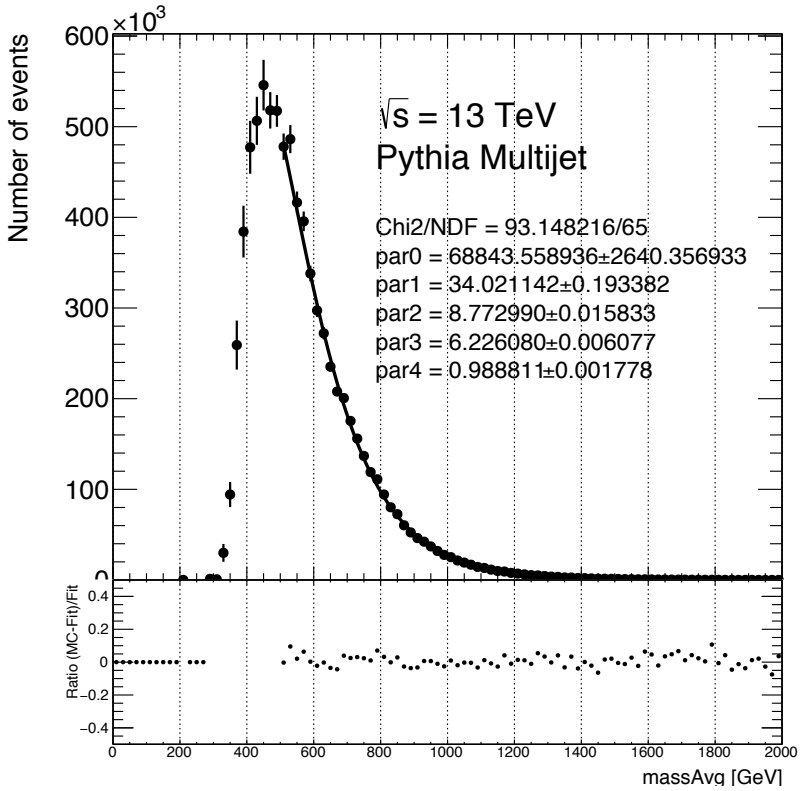

FIGURE 5.20 – Fit of the mass average of the MC multijet background with Equation 5.6. The resonance-pair is reconstructed using the ΔR_{max}.

The choice of the fitting function was tested by performing the fit with some of the parameters fixed to 0. The five parameters are necessary to correctly perform the fit on the full range

from 500 GeV to 2 TeV

To perform the analysis using background fit, a fit would be performed on the data for each mass of interest. This fit would be performed on the m_{avg} range ignoring the region were the signal would peak. The number of events predicted by the fit would then be compared with the number observed in mass range of the signal.

To be able to properly use this method, measurements need to be available for the fit on both sides of the signal mass range. This limits the mass range for which this method can be used as the background distribution peak at 450 GeV. This method is not usable for signal with a mass lower than 600 GeV. Additionally, this will limit some of the cuts that can be performed to define the SR as the position of the background peak can be affected by some cut, in particular on p_{T} and HT. For each mass point a different cut on p_{T} and HT could be optimized. This would require to perform one fit for each mass point instead of one global fit but might improve the sensibility at large masses.

5.7 Signal Region optimisation

The SR that has been presented in Section 5.5 is the result of an optimization performed to maximize the efficiency of the analysis. As ΔR_{min} will be the most useful to probe the mass range available in Run 2, its optimization is the only one that has been fully completed and that will be presented in this section.

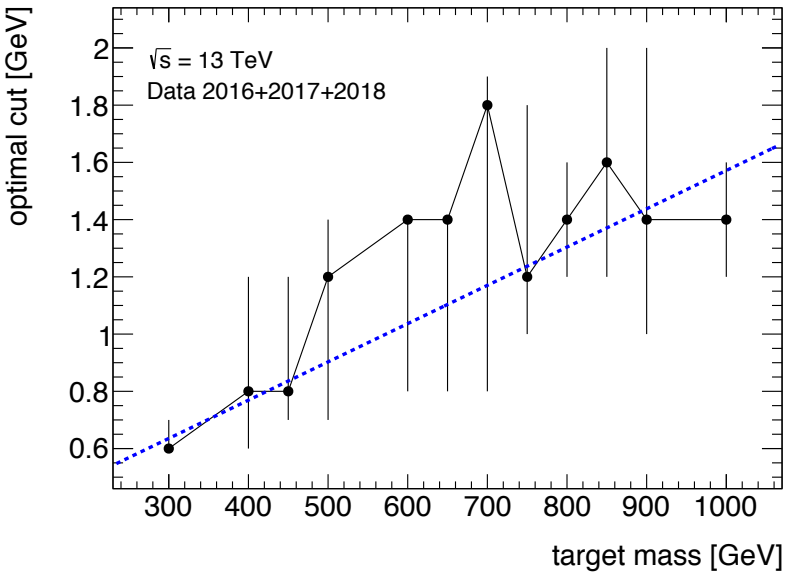

FIGURE 5.21 – Preferred value of ΔR_{min} for each stop quark mass point, derived on top of a requirement of $A < 0.06$ and $|\cos(\theta^*)| < 0.3$. The vertical line for each point represents the range of ΔR_{min} corresponding to a variation in expected significance smaller than 15% around the optimal value. The blue line indicates the results of a linear fit to the m_{avg} dependence.

For the first step of the optimization the requirement on ΔR_{min} is studied, independently for each signal mass point. For each of the masses, the data are used to estimate, using the ABCD matrix, the value of the background in the signal region. This value is compared with the expected one for the signal and the expected uncertainty to compute the significance of the signal. The value of ΔR_{min} is varied between 0 and 4 for each of these points, the value that

lead to the largest significance is considered the optimum. The value of the optimum for ΔR_{min} as function of the mass of the signal is shown in Figure 5.21.

For the optimization plot, the errors bars correspond the value of the optimized variable for which the resulting significance is less than 15% away from the optimum one. Due to this definition the error bars can be asymmetrical. This also mean that the largest the error bars on a variable the less this variable affect the analysis.

After the optimization of the ΔR_{min} for all different masses has been done, a fit is performed to determine how the requirement on ΔR_{min} varies with the m_{avg}. As the mass increase the boost of the final jets will decrease resulting in larger distances between the jets in the pairs. The low mass ($< 225\,\mathrm{GeV}$) part of the fit was already performed during the previous analysis, since no mass point lower than $300\,\mathrm{GeV}$ was available for the analysis those will be reused. A slope of 0.0013 ± 0.0002 is obtained with the fit, which correspond to the value that was presented in Section 5.5.1.

Subsequently, in order to find the optimal set of requirements, a bidimensional scan is performed varying the selection on the mass asymmetry and stop production angle. In this optimization stage all the requirements on the other variables (e.g. ΔR_{min}, jets p_{T}, ...) are kept at their nominal value. For each tested selection the background prediction is estimated with the same data-driven technique as used for the optimization of ΔR_{min}. The result of the bidimensional scan is shown for four different signal mass ($400\,\mathrm{GeV}$, $600\,\mathrm{GeV}$, $800\,\mathrm{GeV}$ and $1\,\mathrm{TeV}$) in Figure 5.22

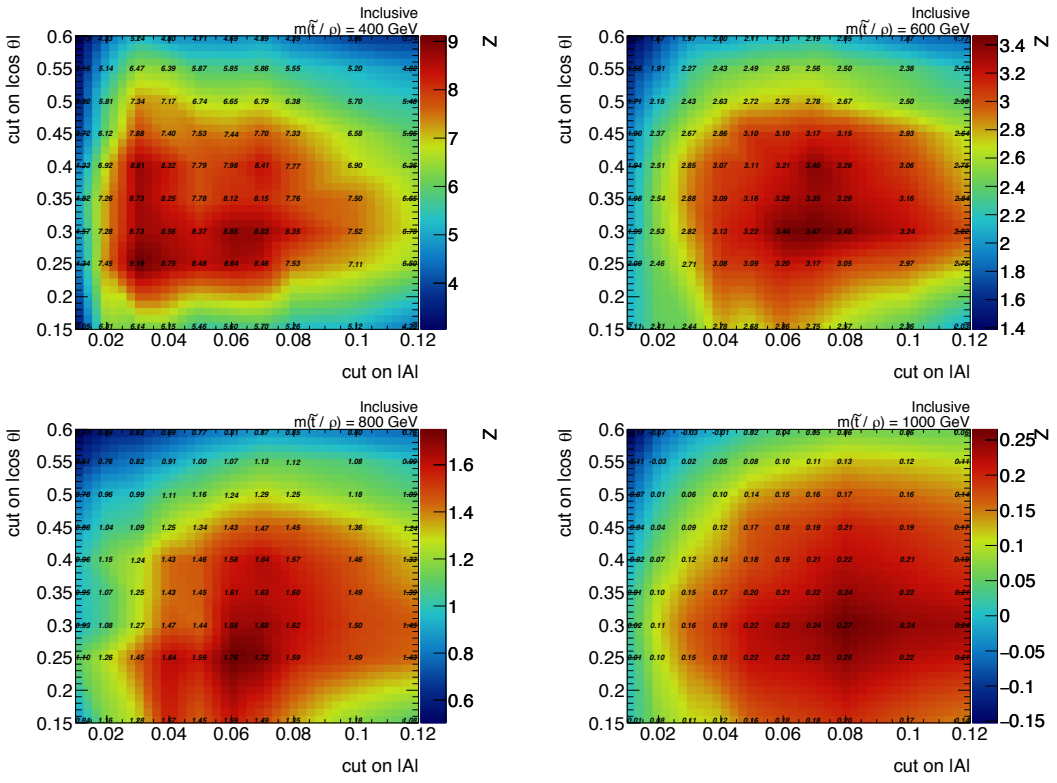

FIGURE 5.22 – Significance scan of A and $|\cos(\theta^*)|$ for several signal masses for the inclusive selection. Each plot is obtained by varying the requirement on the two variables defining the SR while keeping all the others fixed to their values at preselection.

As expected, due to the low correlation between the two variables the result obtained is similar to the one obtained with two individual monodimensional optimizations. To better

illustrate the evolution of the optimum with m_{avg}, the monodimensional optimizations are shown in Figure 5.23.

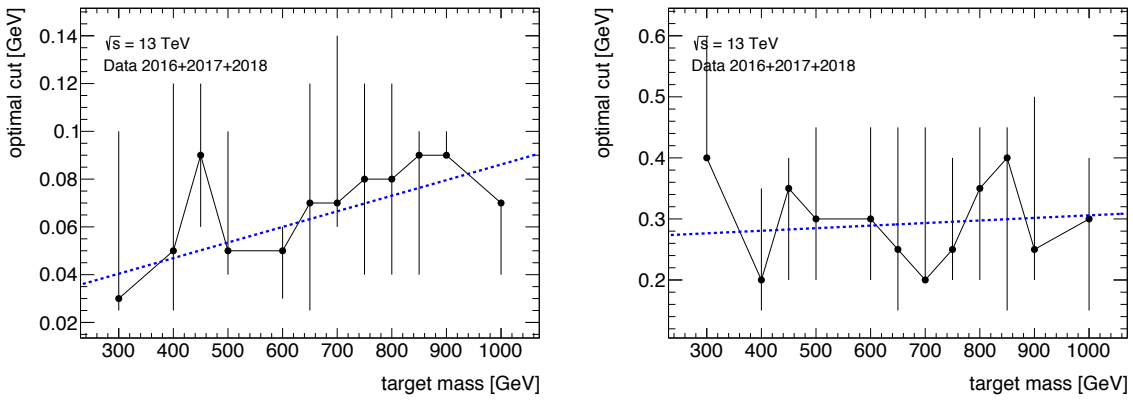

(a) (b)

FIGURE 5.23 – Preferred value of A (a) and $|\cos(\theta^*)|$ (b) for each stop quark mass point. It is derived for the inclusive selection on top of the variable ΔR_{min} requirement. The vertical line for each point represents the range of the variable corresponding to a variation in expected significance smaller than 15% around the optimal value. The blue line indicates the results of a linear fit to the m_{avg} dependence.

Small correlations between the two variable of interest and the mass average exist but since these variables are used to define the different ABCD regions they will be kept fixed. For the ABCD method, the signal region will thus be defined as A<0.06 and $|\cos(\theta^*)|$<0.3.

After optimizing the selection requirements, the final step is the optimization of the mass window used for the final counting experiment. This optimization is based on the expected discovery significance. The entire optimization procedure is repeated iteratively varying the low and high mass edge of the windows until the mass windows converge. Finally, a linear fit to the window edge locations is performed to ensure a smooth variation of the windows as a function of the top squark mass. The obtained values for the edges are finally rounded to the nearest $5\,\mathrm{GeV}$. Figure 5.24 shows the result of the mass window optimization for a selection of top squark masses.

After performing the fit the following equations are obtained for the lower and upper edges :

$$\begin{aligned} Lower\_Edge(m_{\tilde{t}}) &= -0.73(\pm 23.6) + 0.87(\pm 0.03) \times m_{\tilde{t}} \\ Upper\_Edge(m_{\tilde{t}}) &= 11.85(\pm 16.9) + 1.03(\pm 0.02) \times m_{\tilde{t}} \end{aligned} \tag{5.8}$$

For each signal mass considered, these two equation will be used to determine the window in which the counting experiment is performed.

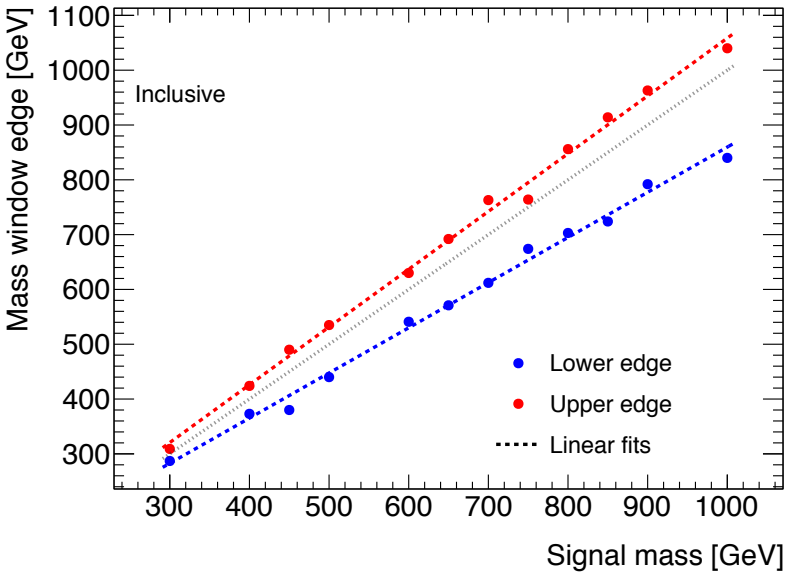

FIGURE 5.24 – Fit to the mass window edges performed after the window optimization to ensure a smooth variation with the stop mass. The fits to the upper and lower edges are indicated in red and blue respectively, while the $m_{avg} = m_{\tilde{t}}$ line is shown in grey.

5.8 Prospects

The expected significance for different mass signals has been determined. For each of the masses, the number of background events is estimated using the ABCD method. The number of events in the window for the estimated background and the signal is then computed using the window previously defined. The statistical uncertainty on the number of events is then computed for both signal and background. Finally, the systematic uncertainty corresponding to the non-closure of the ABCD is computed by comparing the number of expected events in the verification region using the ABCD with the number of events in the verification region. The results are shown in table 5.4.

$m_{\tilde{t}}$ [GeV]	window [GeV]	Exp Bkg	Stat	Syst	Exp signal	Exp stat
300	[260.27 - 320.85]	24984.2	155.642	304.987	2523.48	168.514
400	[347.27 - 423.85]	12195	105.438	176.433	3598.4	147.804
450	[390.77 - 475.35]	7988.51	84.0073	132.564	547.826	41.1125
500	[434.27 - 526.85]	5461.97	68.9927	106.332	360.823	15.6381
600	[521.27 - 629.85]	2893.78	49.7554	78.7059	247.788	7.49371
650	[564.77 - 681.35]	2255.5	43.6828	71.5036	114.286	6.35745
700	[608.27 - 732.85]	1678.03	37.4203	60.9648	64.3221	3.70901
750	[651.77 - 784.35]	1264.27	32.4835	51.7263	50.2266	2.70126
800	[695.27 - 835.85]	953.741	28.0817	43.3007	40.1534	1.22262
850	[738.77 - 887.35]	764.221	24.8396	38.1253	22.5738	1.19494
900	[782.27 - 938.85]	597.943	21.8456	32.6367	15.2926	0.813715
1000	[869.27 - 1041.85]	365.747	17.0126	23.9394	9.14368	0.443132

TABLE 5.4 – Signal efficiency and p_{T} cut efficiency for 200 GeV sgluon for LO and NLO sample.

The expected significance is computed for each mass point, this is shown in Figure 5.25. Compared with the previous analysis where masses up to $415\,\mathrm{GeV}$ were probed in the inclusive category, larger masses up to $600\,\mathrm{GeV}$ can be probed by the analysis using the data from 2016, 2017 and 2018. In addition to that a new strategy at large mass using ΔR_{max} results on the capability to probe even larger mass signals. Work is also still ongoing to extend this analysis to final states with 2 or even 4 b-tag jets.

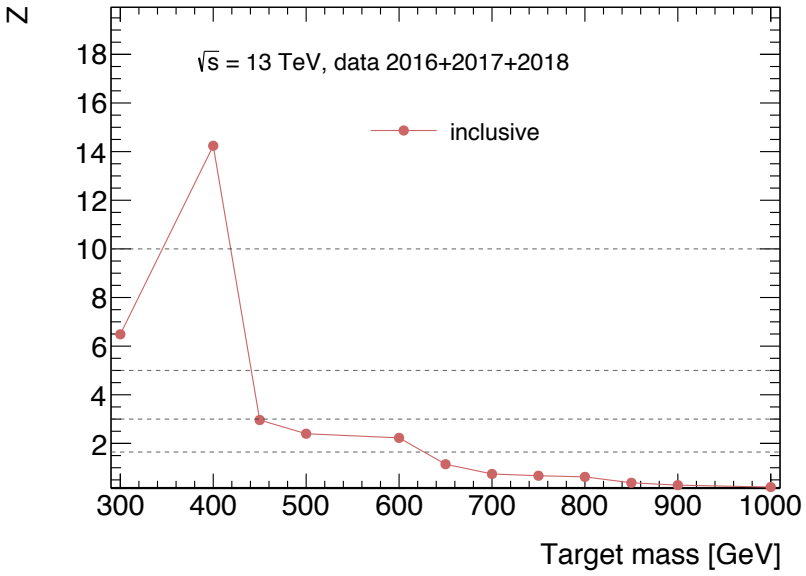

FIGURE 5.25 – Expected significance for the inclusive category as function of the signal mass.

Chapitre 6

Higgs Coupling measurement prospects at the HL-LHC

By the end of HL-LHC program the integrated luminosity measured by ATLAS and CMS will be up to $4000\,\mathrm{fb}^{-1}$. With this increase in luminosity the precise measurements of the Higgs boson and its couplings are possible. In this chapter the expected precision on the Higgs coupling measurements will be presented. I have performed this study based on the expected measurement precision at the HL-LHC.

This analysis was performed both in the Kappa and EFT framework that were presented in Section 2.1.2. SFitter was used to perform this study. SFitter can construct high-dimensional likelihood maps to determine the best fitting parameter points in a system with correlations including the treatment of theoretical errors.

6.1 SFitter

SFitter [84] is a tool that was historically developed to determine the parameters of new physics models using the measurement from "new" collider facility such as the LHC. For a given set of observables the algorithm uses Markov chains to sample the entire parameter space. A likelihood map of the parameter space can be constructed using the resulting points. Out of this map, a list of the different local maxima can be extracted.

SFitter can also be employed to estimate the error on the determination of a set of parameters. In that case one would start with a list of measurement of interest and of the different errors corresponding to these measurements. The experimental and theoretical errors are taken into account separately. First on the experimental side both statistical error and systematic error are taken into account, the statistical errors are considered uncorrelated while the systematic errors are considered fully correlated between the different measurement. These experimental error are gaussian. The second type of error are the theoretical errors. As there is no reason for why high order correction should be centered around any specific value [85]. The theoretical errors are thus not taken to be gaussian but flat. This mean that the probability any measurement does not depend on the value of the measurement as long as it is within interval defined by the theoretical error.

Toy measurements are generated taking into account the statistical, systematic and theoretical errors, including their correlations. For each of the toy measurements a likelihood map is generated and the maximum is identified, for each of the parameters of interest the value corresponding to the maximum is then determined and is often referred to as best-fit point. The errors on the parameters are then computed separately for the toys above and below the SM

expectation. On both sides the values for which $X\%$ of the toys are will be used to define the error. In the following section, 68 % (1σ) and 95 % (2σ) will be used.

6.2 Measurement

The studies are based on the estimation of errors on different Higgs cross section measurement that will be performed at the HL-LHC that were determined for the Report on the Physics at the HL-LHC [50].

This information is available as signal strength μ, which is defined as the ratio between the measure cross-section of a specifics Higgs channel and the standard model prediction for this channel :

$$\mu = \frac{\sigma_{yy\to \mathrm{H}}\ Br_{\mathrm{H}\to xx}}{\sigma^{SM}_{yy\to \mathrm{H}}\ Br^{SM}_{\mathrm{H}\to xx}} \tag{6.1}$$

The measurements for which errors on μ were available are shown in Figure 6.1, where the production sections correspond to the abbreviations defined in Section 2.

ggF :
- $\mathrm{H} \to \mathrm{ZZ}$
- $\mathrm{H} \to \mathrm{WW}$
- $\mathrm{H} \to \gamma\gamma$
- $\mathrm{H} \to \mathrm{Z}\gamma$
- $\mathrm{H} \to \tau\tau$

VBF :
- $\mathrm{H} \to \mathrm{ZZ}$
- $\mathrm{H} \to \mathrm{WW}$
- $\mathrm{H} \to \gamma\gamma$
- $\mathrm{H} \to \mathrm{Z}\gamma$
- $\mathrm{H} \to \tau\tau$
- $\mathrm{H} \to \mu^-\mu^+$

WH :
- $\mathrm{H} \to \mathrm{ZZ}$
- $\mathrm{H} \to \gamma\gamma$
- $\mathrm{H} \to \mathrm{bb}$

ZH :
- $\mathrm{H} \to \mathrm{ZZ}$
- $\mathrm{H} \to \mathrm{WW}$
- $\mathrm{H} \to \mathrm{bb}$

ttH :
- $\mathrm{H} \to \mathrm{ZZ}$
- $\mathrm{H} \to \mathrm{WW}$
- $\mathrm{H} \to \gamma\gamma$
- $\mathrm{H} \to \tau\tau$
- $\mathrm{H} \to \mathrm{bb}$
- $\mathrm{H} \to \mu^-\mu^+$

FIGURE 6.1 – List of measurement used for the Higgs couplings prospect studies.

For each of these processes five different errors were provided : the statistical error, the experimental error, the systematic error, the signal theoretical error and the background theoretical error. Since the detail of systematic uncertainty was not available they were assumed to be uncorrelated, the first three of these errors were thus implemented as uncorrelated statistical errors and the last two as theoretical errors.

Finally, correlation of all the measurements were also available and were taken into account in the determination of the couplings precision.

6.3 Coupling measurement in the Delta (Kappa) framework

Historically, new physics effects on the SM-like Higgs couplings have been parameterized using coupling modifiers. As presented in Section 2.1.2 these coupling modifiers can be expressed as Deltas. Since the measurements are presented as μ, one will first need to express μ as function of the Deltas :

$$\frac{\Gamma_{yy\to \mathrm{H}}}{\Gamma^{SM}_{yy\to \mathrm{H}}} = (1+\Delta_{yy\to \mathrm{H}})^2 \qquad Br_{\mathrm{H}\to xx} = \frac{\Gamma_{\mathrm{H}\to xx}}{\sum_i \Gamma_i} \qquad Br^{SM}_{\mathrm{H}\to xx} = \frac{\Gamma^{SM}_{\mathrm{H}\to xx}}{\sum_i \Gamma^{SM}_i}$$

$$\frac{Br_{\mathrm{H}\to xx}}{Br^{SM}_{\mathrm{H}\to xx}} = \frac{(1+\Delta_{\mathrm{H}\to xx})^2 \Gamma^{SM}_{\mathrm{H}\to xx}}{\sum_i (1+\Delta_{\mathrm{H}\to xx,i})^2 \Gamma^{SM}_i} \times \frac{\sum_i \Gamma^{SM}_i}{\Gamma^{SM}_{\mathrm{H}\to xx}} = \frac{(1+\Delta_{\mathrm{H}\to xx})^2}{\sum_i (1+\Delta_{\mathrm{H}\to xx,i})^2 Br^{SM}_i} \tag{6.2}$$

$$\mu = \frac{(1+\Delta_{yy\to \mathrm{H}})^2 (1+\Delta_{\mathrm{H}\to xx})^2}{\sum_i (1+\Delta_{\mathrm{H}\to xx,i})^2 Br^{SM}_i}$$

I have implemented the measurements, their errors and correlations in SFitter. 10000 toy measurements were produced from these measurements. For each of the toys the best fit point was determined by maximizing the likelihood thereby determining the best-fit parameter values for all Higgs couplings. In a first step the 2D distributions of the best-fit parameter values was analyzed to study correlations. Four of the correlation plots are shown in Figure 6.2. Due to the presence of the total width in μ small correlation should be observed between the different parameters. Since Hbb represent 60 % of the width of the Higgs, if Δ_b increases then Δ_X also need to increase to compensate.

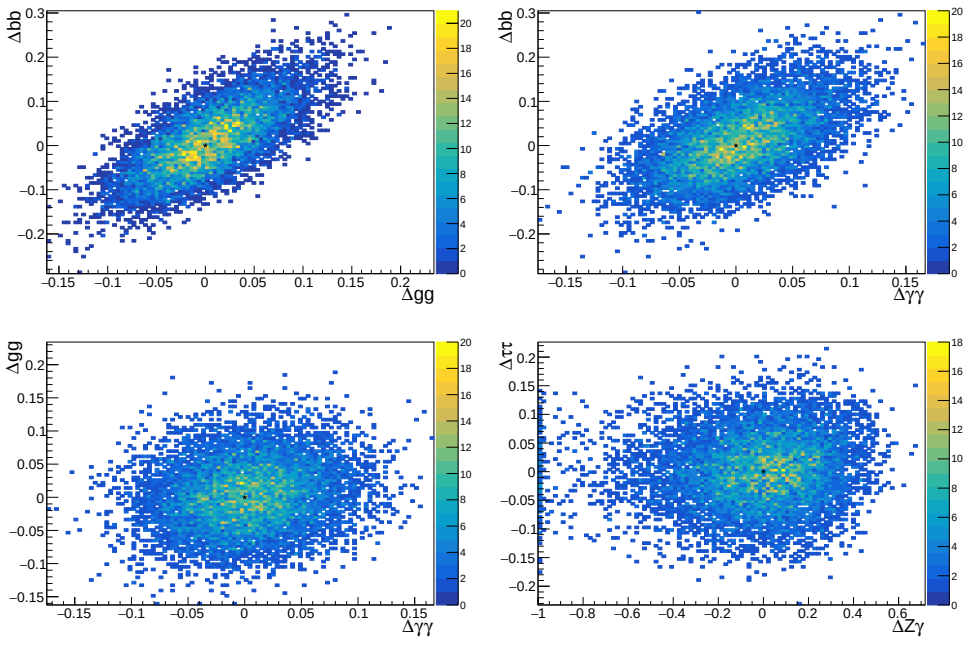

FIGURE 6.2 – Correlation between the coupling deviation.

The distributions are shown for four different couplings in Figure 6.3. As expected, all of the distributions have a gaussian shape centered on 0. A peak at -1 is observed for H $\to$ Zγ, due to the large error on this measurement the value of μ is negative for some toy which is not physical. This push the best fit point to -1 where the modified coupling is null. Using the distributions, the expected errors at the HL-LHC can be determined with different confidence level. The value corresponding to a confidence level of 68 % is represented on Figure 6.3 as two black line.

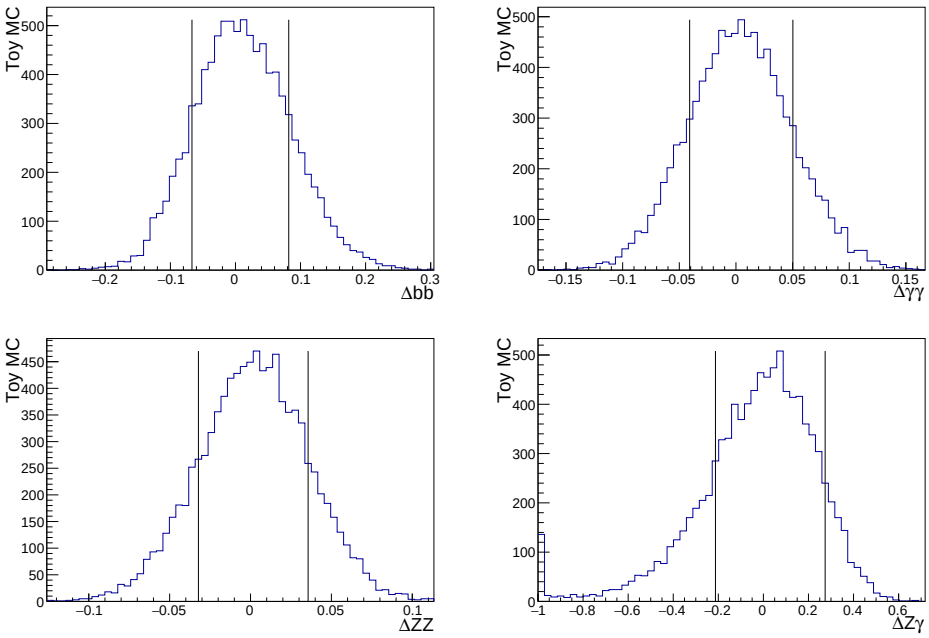

FIGURE 6.3 – Distribution of the value of four of the delta coefficients.

The result of my analysis is summarized in Figure 6.4. The red lines correspond to a confidence level (CL) of 2σ (95%) and the blue one to a confidence level of 1σ (68%) The expected value of the error for most of the coupling is of the order of 0.05 for a 68% CL. Compared to the others the error for $Z\gamma$ is relatively large, this is largely due to the fact that the branching ration of $H \longrightarrow Z\gamma$ is extremely small (almost half of $H \longrightarrow \gamma\gamma$) and further reduce by the fact that only Z-decays to leptons are considered in this analysis.

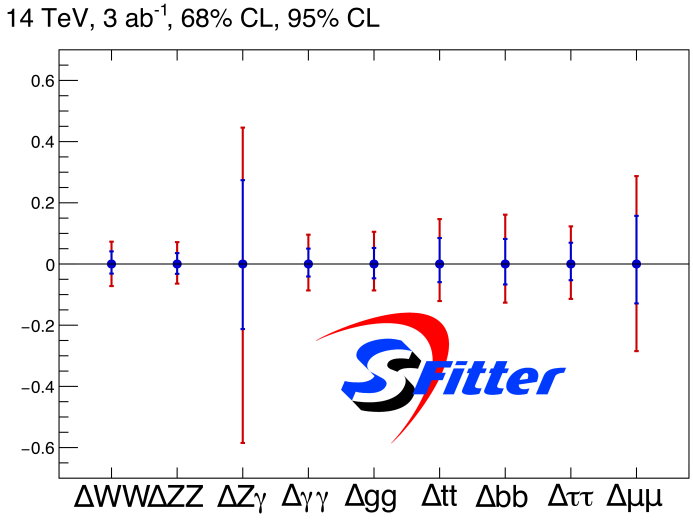

FIGURE 6.4 – Result of the analysis in term of expected uncertainty on the coupling modifier at the HL-LHC.

6.4 Coupling measurement in the EFT framework

The modification of the Higgs coupling can also be interpreted in the context of EFT. Since the SFitter framework already provides cross section and branching ratios modified by the value of the coupling constant of the different EFT operator, the implementation the μ measurement is easier in the case of EFT as no additional mathematical operations are required.

From Equations B.4 and 2.21, 10 effective HVV coupling can be derived [16] :

$$\begin{aligned}\mathcal{L}^{HVV} &= g_{\mathrm{Hgg}} H G^a_{\mu\nu} G^{a\mu\nu} + g_{\mathrm{H}\gamma\gamma} H A_{\mu\nu} A^{\mu\nu} + g^{(1)}_{\mathrm{HZ}\gamma} A_{\mu\nu} Z^\mu \partial^\nu H + g^{(2)}_{\mathrm{HZ}\gamma} H A_{\mu\nu} Z^{\mu\nu} \\ &+ g^{(1)}_{\mathrm{HZZ}} Z_{\mu\nu} Z^\mu \partial^\nu H + g^{(2)}_{\mathrm{HZZ}} H Z_{\mu\nu} Z^{\mu\nu} + g^{(3)}_{\mathrm{HZZ}} H Z_\mu Z^\mu \\ &+ g^{(1)}_{\mathrm{HWW}} (W^+_{\mu\nu} W^{-\mu} \partial^\nu H + h.c.) + g^{(2)}_{\mathrm{HWW}} H W^+_{\mu\nu} W^{-\mu\nu} + g^{(3)}_{\mathrm{HWW}} H W^+_\mu W^{-\mu}\end{aligned} \tag{6.3}$$

with the coupling depending on 6 of the Wilson coefficient :

$$\begin{aligned} g_{\mathrm{Hgg}} &= -\frac{\alpha_s}{8\pi}\frac{f_{GG} v}{\Lambda^2} & g^{(1)}_{\mathrm{HZ}\gamma} &= \frac{g M_W}{\Lambda^2}\frac{s_w (f_W - f_B)}{2c_w} \\ g_{\mathrm{H}\gamma\gamma} &= -\frac{g M_W}{\Lambda^2}\frac{s_w^2 (f_{BB} + f_{WW})}{2} & g^{(2)}_{\mathrm{HZ}\gamma} &= \frac{g M_W}{\Lambda^2}\frac{s_w (2 s_w^2 f_{BB} - 2 c_w^2 f_{WW})}{2c_w} \\ g^{(1)}_{\mathrm{HZZ}} &= \frac{g M_W}{\Lambda^2}\frac{c_w^2 f_W + s_w^2 f_B}{2c_w^2} & g^{(1)}_{\mathrm{HWW}} &= \frac{g M_W}{\Lambda^2}\frac{f_W}{2} \\ g^{(2)}_{\mathrm{HZZ}} &= -\frac{g M_W}{\Lambda^2}\frac{s_w^4 f_{BB} + c_w^4 f_{WW}}{2c_w^2} & g^{(2)}_{\mathrm{HWW}} &= -\frac{g M_W}{\Lambda^2} f_{WW} \\ g^{(3)}_{\mathrm{HZZ}} &= \frac{g M_W v^2}{\Lambda^2}\frac{f_{\phi,2}}{4c_w^2} & g^{(3)}_{\mathrm{HWW}} &= \frac{g M_W v^2}{\Lambda^2}\frac{f_{\phi,2}}{2} \end{aligned} \tag{6.4}$$

One can determine which couplings are affected by which Wilson coefficient. This is shown in Table 6.1.

	Hgg	Hγγ	HZγ	HZZ	HWW
f_{GG}	✓				
f_{BB}		✓	✓	✓	
f_{WW}		✓	✓	✓	✓
f_B			✓	✓	
f_W			✓	✓	✓
$f_{\phi,2}$				✓	✓

TABLE 6.1 – Link between the Wilson coefficient and the couplings of the Higgs boson.

In the analysis three fermionic operators will be included for the third generation as shown in Equation B.4. Out of the previously discussed operator three won't be included in the analysis : f_B, f_W and f_{WWW}. The first two do affect the coupling of the Higgs but are mostly constrained to kinematic distribution and (γ W W) and (Z W W) coupling, they are thus removed them from the fit as the list of measurement is not enough to constrain them. The third one, f_{WWW} is usually needed to fully describe anomalous triple gauge couplings in a gauge-invariant framework but since it is not constrained by Higgs coupling measurement it is also

removed from the fit. Due to their strong correlation, f_{BB} and f_{WW} are not directly implemented in SFitter but instead two dummy variable, defined as $f_{WW} + f_{BB}$ and $f_{WW} - f_{BB}$, are used.

10000 toy measurement are simulated by smearing the value of the measurement using the errors. The correlation plots can then be derived as previously, examples of four of these correlations are shown in Figure 6.5. Most of the Wilson coefficient are uncorrelated, the two exceptions are f_{WW} and f_{BB} and f_{GG} and f_t as shown in the top two plots of Figure 6.5. f_{BB} and f_{WW} are expected to be correlated, in the case of f_{GG} and f_t the correlation arise from the fact that in the SM the coupling of the Higgs to the gluons is done via quarks loop with the top quark being the dominant contribution.

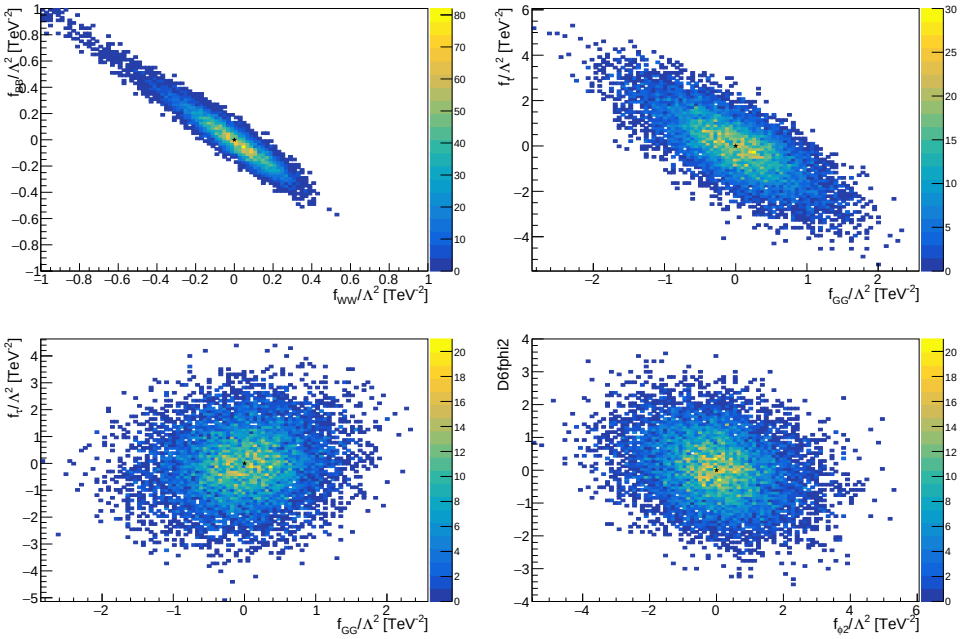

FIGURE 6.5 – Correlation between the different Wilson coefficient.

The distribution of the best-fit Wilson coefficients is shown in Figure 6.6. As expected, most of the distributions have a gaussian shape centered on 0, the standard model expectation. A slightly different shape with a second local maximum at +1.5 and -1.5 is observed for f_{WW} and f_{BB}.

The shape of the prediction for H $\rightarrow$ Zγ is not centered on the SM but follow a parabolic shape. Since this parabola pass by 0 for the SM it will also pass by 0 for another combination of Wilson coefficients, $f_{WW} = 1.5$ and $f_{BB} = -1.5$. This result in a second local maximum, with a difference in χ^2 of the order of 1. More precise measurement of HZZ, HWW and H$\gamma\gamma$ are necessary to constrain f_{WW} and f_{BB} to one maximum or the other.

The result of this analysis is presented in Figure 6.7. Constraints on the Wilson coefficient related to the coupling of the Higgs with the gauge bosons can be achieved, for f_{WW} and f_{BB} the large different between the 68% Cl and 95% CL and the asymmetry of the error in the 95% CL originate from the secondary maximum. The y axis on the right shows the scale that could be probed assuming that the coupling constant f is equal to 1. At the HL-LHC it will thus be possible to probe scales ranging from $\Lambda/\sqrt{f} = 1 - 2\,\text{TeV}$.

An improvement of the uncertainty by a factor two with respect the to the Run 1 + Run 2 precision (see Section 2.1.2) is achievable. The analysis only take into account prospect for

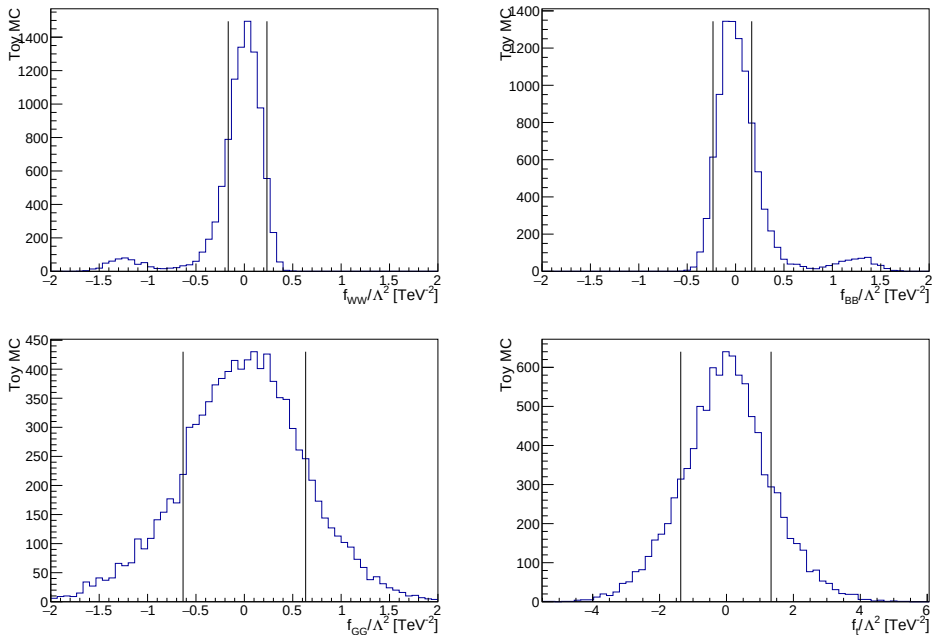

FIGURE 6.6 – Distribution of the value of four of the Wilson coefficients.

the ATLAS experiment while the Run 1 + Run 2 analysis used both ATLAS and CMS. At the HL-LHC most of the measurement uncertainty will no longer be statistically dominated but will instead be dominated by systematic and theoretical uncertainties. Compared to the Run 1 + Run 2 study, the kinematic distributions were not used in this analysis. This limit the number of Wilson coefficient that can be probed, for example no constraint could be obtained for f_W and f_B.

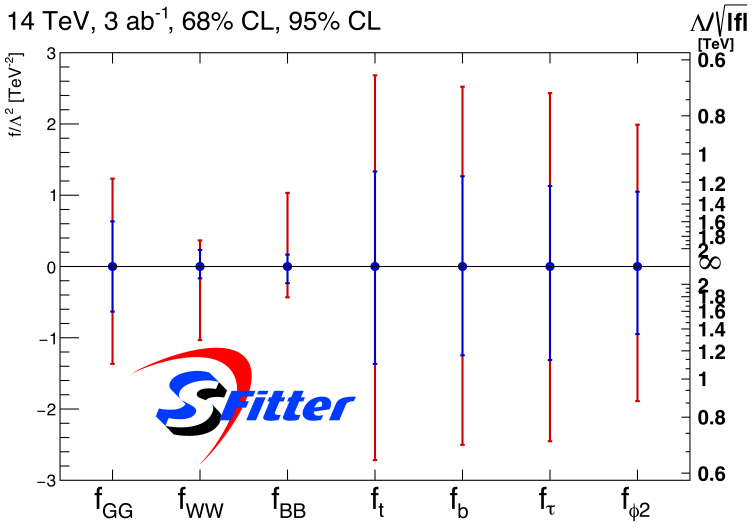

FIGURE 6.7 – Result of the analysis in term of expected uncertainty on the Wilson coefficient for the EFT.

Chapitre 7

The High Granularity timing detector Design and performance studies

In this chapter, my work on the development of the HGTD will be presented. The expected improvement of the HGTD will first be illustrated with a study I performed on the beamspot at the HL-LHC. The simulation of the HGTD that I implemented will then be presented. With this simulation I optimized the layout of the detector up to the final version that was presented in Chapter 4. Finally, using the simulation I studied the performance of the detector and the improvement to the reconstruction of the forward electrons.

7.1 Beamspot Studies

Pile-up is one of the main challenges of the HL-LHC. The average number of interactions per bunch crossing at the HL-LHC will reach $\langle\mu\rangle = 200$ and on average 1.4 vertices per millimeter, the reconstruction of the vertices will become extremely difficult for the tracking detector. The hard scatter vertex might end up being combined with close by pile-up interactions, leading to a decrease of the performance of the detector.

A way to mitigate the effect of the pileup is to exploit the time spread of the interactions during a single bunch crossing. At the LHC (and the HL-LHC) the interactions have both a spatial and the temporal distribution, with the time spread of around $180\,\mathrm{ps}$ and the spatial one of $45\,\mathrm{mm}$ ($150\,\mathrm{ps}$). Using a timing measurement with a precision of the order of $30\,\mathrm{ps}$ allows to separate interactions that occur very close in space but at different times a thus reduce the pile contamination up by a factor up to 6.

To understand precisely the effects of these conditions I have performed a study of the beamspot using a full simulation of the ATLAS detector.

7.1.1 Beamspot

At the LHC, the density of a bunch can, at the first order, be modeled with two gaussian distributions, one in the longitudinal direction and one in the transverse direction. The two bunches then cross each other in the ATLAS detector, as represented in Figure 7.1. In the nominal crossing scheme with crab-crossing, shown in Figure 7.1 (a), the two bunches will progressively overlap each other in the center of the detector [51]. As the two bunches overlap, more and more pp interactions will occur, the density of interactions as function of z being directly related to the density of protons each bunch. As the crossing is not instantaneous, all of the interactions

will take place at different times with a time range proportional to the length of the bunches ($\sim 7.5\,\mathrm{cm}$) multiply by c for a range in time of around $350\,\mathrm{ps}$.

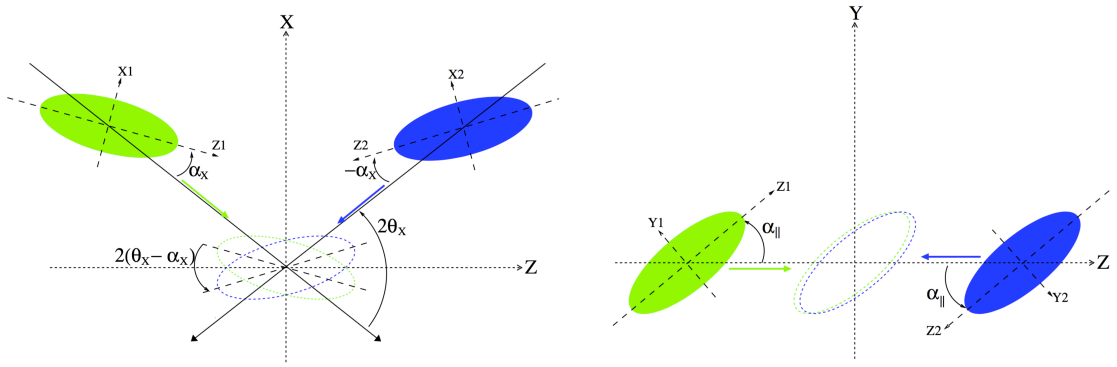

(a) (b)

FIGURE 7.1 – Sketch of the crossing of the two proton bunches in the ATLAS detector. (a) Shows the crab-crossing scheme in the crossing plane. (b) Shows the crab-kissing scheme in the transverse plane.

Due to the way the two bunches overlap, the times and positions of the interactions follow two independent gaussian distributions, the spread depending on the time spread on the interactions and on the size of the interaction region, both of these parameters are defined by the collision scheme. Four scenarios have been implemented, their different characteristics are listed in table 7.1. Three of these scenarios correspond to potential HL-LHC beam parameters : Nominal, Run-4 and 200 MHz. In addition, one scenario was defined with Crab Kissing, presented in Figure 7.1 (b) the bunches collide front to front leading to a larger spread in position of the interaction but a smaller time spread.

The Nominal and CrabKissing scenarios were used for full simulation. They both have a similar spread of the vertex position of the order of 4.5 cm.

Scenario	σ_z/c [ps]	σ_t [ps]
Nominal	150	175
Run–4	112	175
200 MHz	200	263
CrabKissing	177	29

TABLE 7.1 – The vertex spread in time and z direction, translated into time units, is shown for three HL–LHC scenarios. The fourth scenario is an example of Crab-Kissing with an angle of 50 mrad.

The distribution of the time and z of the truth vertex is shown in Figure 7.2(a) for the Nominal and Crab Kissing scenario. This illustrates the absence of correlation between the time and position of the vertices as well as the smaller time spread in the Crab Kissing scenario. The Figure 7.2(b) illustrates the time of arrival of $1\,\mathrm{TeV}$ muons in the HGTD at a radius of $200\,\mathrm{mm}$ ($|\eta| = 3.6$), the average of this distribution corresponds to the time of flight of the muons from the center of the ATLAS detector. The spread in the time of arrival corresponds to the convolution of the spread in z (which affects the time of flight) and of the spread in t. Due to this convolution the difference between the nominal and Crab Kissing scheme is less pronounced.

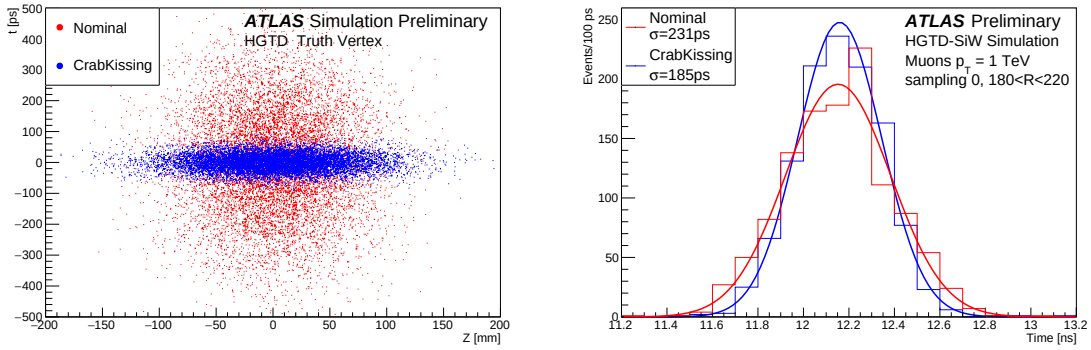

(a) (b)

FIGURE 7.2 – (a) The distribution of the beam spot for the generated time and z vertex is shown for the Nominal and CrabKissing scenarios. (b) The distribution of the arrival time for muons with a transverse momentum of $1\,\mathrm{TeV}$ is shown for the first layer of the HGTD–SiW at a radius of $200\,\mathrm{mm}$ ($|\eta| = 3.6$). The width of the distribution is the convolution of the beam-spot in z and t. Therefore, the difference between the Nominal and CrabKissing scenarios is less pronounced than in (a).

The Crab Kissing scenario was found to not be advantageous to the operation of the HGTD. It has the same spread in z as the Nominal scenario and a smaller time spread, this means that the pile-up vertex density will be similar to the nominal case but it would be more difficult to separate merged vertices using the timing information for the same timing resolution. Additionally, this scheme needs additional machine elements and therefore has been abandoned.

7.1.2 Vertex density

The spatial pileup density, i.e. the number of collisions per length unit in the z direction during a bunch crossing, is a key quantity for evaluating the performance of the HGTD. For an average of 200 collisions per bunch crossing, the expected average pile-up density is $1.6\,\mathrm{collisions/mm}$. But this average hides fluctuations that can go from $0\,\mathrm{collisions/mm}$ up $3.5\,\mathrm{collisions/mm}$ as illustrated in Figure 7.3. The local pile-up density is calculated by counting the number of collisions in a window of $\pm 3\,\mathrm{mm}$ around the hard scatter vertex then dividing this number by the size of the window. The size of the window was optimized to be large enough to avoid quantization effect but still small enough to probe the tail of the distribution.

Figure 7.3 (a) shows the difference between the pile-up density $\langle\mu\rangle = 30$, corresponding to the Run2 condition, and $\langle\mu\rangle = 200$, corresponding to the HL-LHC condition. The most probable value for the nominal HL-LHC scenario is around $1.6\,\mathrm{collisions/mm}$ as expected, 6 time higher than the Run2 case. In Figure 7.3 only $\langle\mu\rangle = 200$ was computed using a full simulation of the beam-spot interaction, the other distributions were computed using the σ_z of the beam spot as well number of collision per bunch crossing $\langle\mu\rangle$. Figure 7.3 (b) shows the local pile-up density for the HL-LHC scenarios that were presented in section 7.1.1, the main difference is the width of the beam spot, since the number of interaction is fixed to $\langle\mu\rangle = 200$ the larger the beam-spot region the smaller the pile-up density.

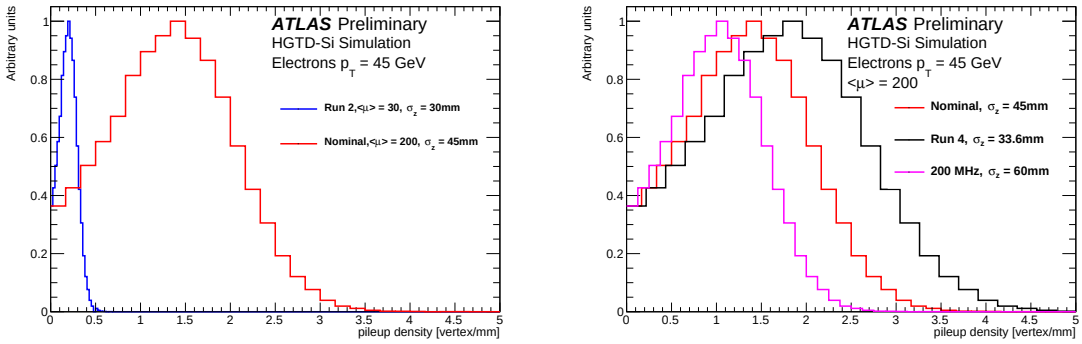

(a) (b)

FIGURE 7.3 – (a) The local pileup vertex density is shown in full simulation for the nominal HL-LHC beam-spot scenario for $\langle\mu\rangle = 30$ and $\langle\mu\rangle = 200$. The density is calculated as the number of truth vertices in a range of $\pm 3\,\mathrm{mm}$ around the signal vertex divided by the window size ($6\,\mathrm{mm}$). The simulation was performed using the nominal beam spot, the other distribution has been computed using the σ_z of the beam spot. (b) The pile-up vertex density is shown for different HL-LHC beamspot scenarios, calculated as described for (a).

Figure 7.4 shows an event display showing the time and z position of all vertices in a Zee event from full simulation with $\langle\mu\rangle = 200$. Vertices with a track in the HGTD are blue while the ones with no track in the HGTD are pink and green. Even if the detector has a relatively small coverage roughly 50% of the vertices have a track with a transverse momentum greater than $1\,\mathrm{GeV}$ in its acceptance because of its position in the forward region. The blue circle corresponds to vertices with timing information, the vertical error bars on the circle are the timing precision using all cells in the HGTD that could be associated to tracks from the vertex. In most cases the error bar is smaller than the symbol size. Figure 7.4 (b) illustrates in more detail how the HGTD can mitigate the effect of the pile-up density. The red point represents the true hard scatter interaction point where the Z is produced, the dotted line represent the reconstructed vertices. The two nearby pile-up interaction are almost at the same position in z and risk to be merged with the hard scatter interaction in the reconstructed vertex but thank to the timing information they can be disentangled.

7.2 HGTD Simulation

To be able to study the performance of the HGTD and to help with the design of the layout I developed a simulation of the detector. This simulation takes into account the readout geometry of the HGTD and the time resolution of the sensors. The readout geometry result in dead zones that will decrease the efficiency of the detector and lead to inhomogeneity. The time resolution was implemented using simulated pulses derived from testbeam studies, it will directly impact the physics performances of the detector.

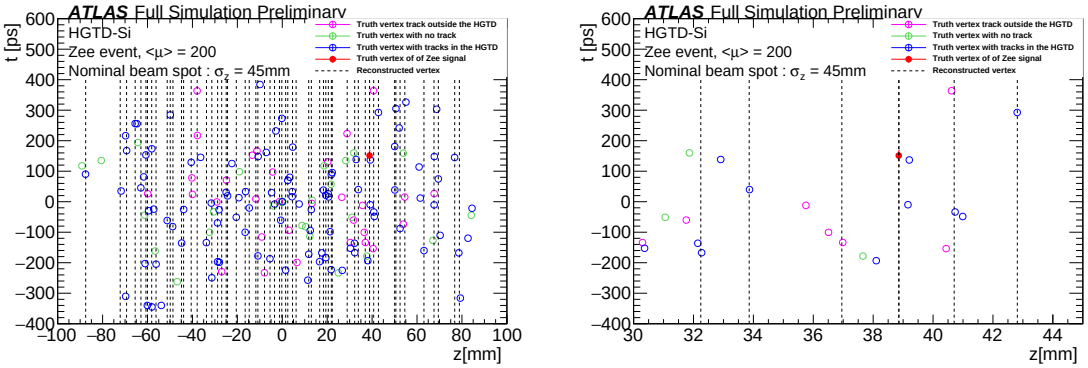

(a) (b)

FIGURE 7.4 – (a) Event display showing the time and z position of all vertices in a Zee event from the full simulation with $\langle\mu\rangle = 200$. Only tracks reconstructed with a transverse momentum greater than $1\,\mathrm{GeV}$ are used. The red circle is the truth hard-scatter vertex, the pink circles are the truth vertices with no reconstructed track in the HGTD acceptance, green circles those without accepted tracks outside the HGTD acceptance and the blue circles are the truth vertices with at least one track in the HGTD. The dotted lines are the positions of the reconstructed vertices. The error bar on the y axis is the expected precision of the vertex timing determination in the HGTD, in most cases smaller than the symbol size. (b) Zoom around the hard scatter vertex of (a).

7.2.1 Geant4 simulation

A full simulation of the HGTD with the ATLAS detector was performed using Geant4 [86] to study the performances of the HGTD. Two version of this simulation have been developed, the first one (the TP (technical Proposal) simulation) was created to be flexible and used to optimize the design of the detector, the second one (the TDR simulation) follows closely the design that was optimized with the help of the TP simulation. The TP simulation of the HGTD is composed of 4 active layers on both sides of the ATLAS detector, each of the active areas is a disc centered on the beam-pipe. The Geant4 hits in these active areas are store as LArHits with a spatial resolution of $0.5\,\mathrm{mm} \times 0.5\,\mathrm{mm}$, this granularity was initially chosen to be small enough to allow the study of different granularities. The LArHits were initially an object used to store the hits in the LAr Geant4 simulation, each of those contain a unique identifier, that is used to store its position and the time and energy of the hits. This object was chosen because of its capability to easily combine together hits in the same pad and for its ability to store times. The time of the LArHit corresponds to the time of the interaction of the particle with the active layer with respect to the time of the bunch crossing with an offset of $-11.8\,\mathrm{ns}$. This offset corresponds to the average time of flight from the nominal interaction point to the middle of the HGTD, it was chosen to obtain time with small, close to 0, numerical values to minimize the memory necessary to store them with good precision.

The layout of the HGTD in the TP simulation is shown in Figure 7.5 (a), all the volumes are implemented as discs centered on the beam-pipe with a starting radius of $50\,\mathrm{mm}$ and a maximum radius of $600\,\mathrm{mm}$. In addition, a layout including tungsten absorber, called HGTD-SiW was also developed, it is shown in Figure 7.6. The purpose of the absorber was to initiate showering inside of the HGTD, resulting in an increased energy deposit in the sensor and thus an improved time resolution. In addition, with the showering more than one hit per layer can be associated with each particle improving the time resolution per track. Due to the small performance improvements and the complexity brought by such layout the option was dropped,

in particular due to the increased radiation levels caused by of the tungsten. All the different material are stack onto each other leading to thickness of $43\,\mathrm{mm}$ ($53.5\,\mathrm{mm}$ for the HGTD-SiW case). The material used and the design of the detector have been evolving in parallel of the performance studies of the detector, which lead to the development of the TDR simulation.

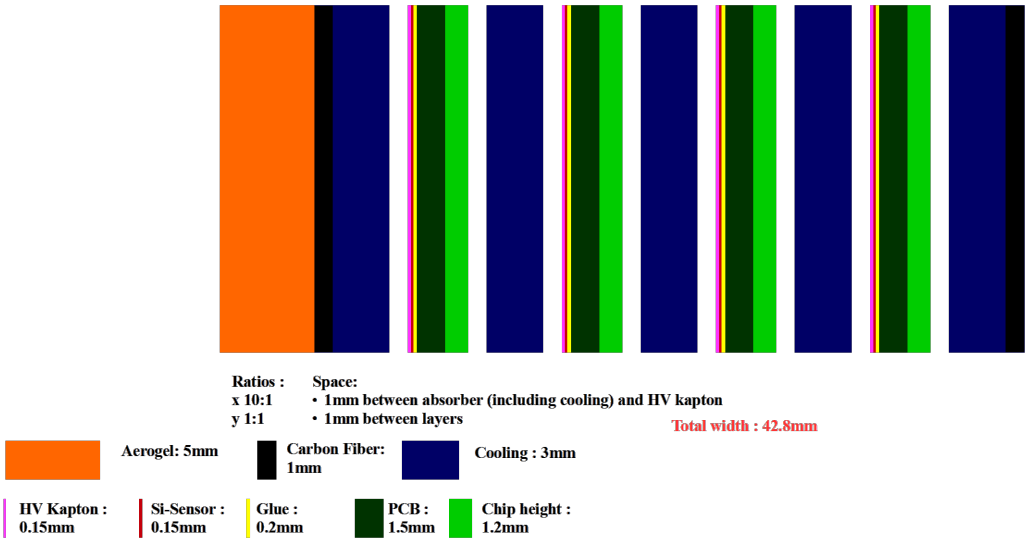

FIGURE 7.5 – The schematic view of the HGTD (TP simulation) is shown in positive-z and radius. The material used in the simulation is listed in the legend.

The TDR simulation was developed after the geometry was fixed in the Technical Proposal to be used in performances studies for the Technical Design Review. The active region is implemented as modules of $22\,\mathrm{mm} \times 40\,\mathrm{mm}$ positioned following the design of the detector, the modules are then divided in pads of either $1\,\mathrm{mm} \times 1\,\mathrm{mm}$ or $1.3\,\mathrm{mm} \times 1.3\,\mathrm{mm}$ with inter-pads dead-zones of $50\,\mu\mathrm{m}$. The different materials present in the detector have also been implemented with more precision as shown in Figure 7.7, for example the services for the different modules are not simulated as a continuous disc but as piles of strips going to the top of the rows of the modules.

7.2.2 MC samples

Single particle samples and physics samples were simulated to study the performance of the detector. To measure the effect of the pile-up on the performances, samples were produced in two configurations, $\langle\mu\rangle = 0$ and $\langle\mu\rangle = 200$, where the pile-up is simulated by adding minimum bias events on top of the $\langle\mu\rangle = 0$ event.

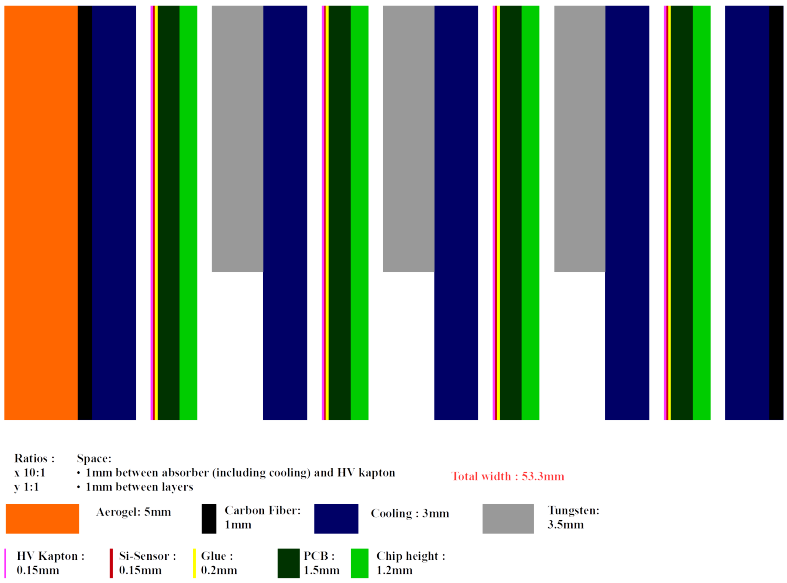

FIGURE 7.6 – Schematic view of the HGTD-SiW a variant of the HGTD in which 3 tungsten absorbers with a radiation length of 1 X_0 are added.

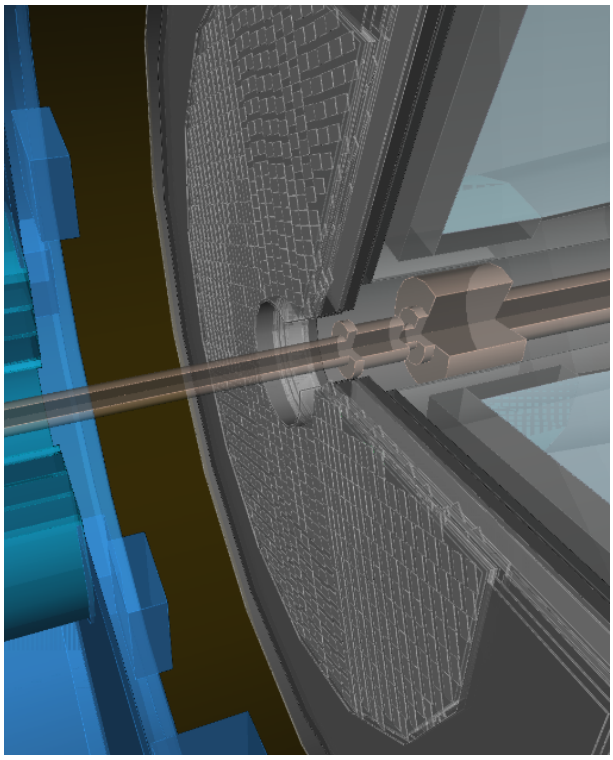

FIGURE 7.7 – Implementation of the HGTD (TDR simulation) in Geant4.

In the single particle samples, a particle is produced in the interaction region using the generator ParticleGun. The angular and momentum distribution of such particles can be defined, allowing us to limit the production to the forward region. The main purpose of the samples is to study detector level performance as well as to help understand how a certain type of particles interacts with the detector. The following single particle samples have been produced :

- Single muons, $p_{\mathrm{T}} = 45\,\mathrm{GeV}$, flat distribution in pseudo-rapidity : $2.3 < |\eta| < 4.3$.
- Single muons, $p_{\mathrm{T}} = 45\,\mathrm{GeV}$, flat distribution in polar angle : $0.03 < |\theta| < 0.18$.
- Single electrons, $p_{\mathrm{T}} = 20, 45, 100\,\mathrm{GeV}$, $2.3 < |\eta| < 4.3$.
- Single photons, $p_{\mathrm{T}} = 20, 45, 100\,\mathrm{GeV}$, $2.3 < |\eta| < 4.3$.
- Single pions, $1 < p_{\mathrm{T}} < 5\,\mathrm{GeV}$ and $p_{\mathrm{T}} = 20, 45, 100\,\mathrm{GeV}$, $2.3 < |\eta| < 4.3$.
- Single neutrino, with $\langle\mu\rangle = 200$.

The single muons sample were used to performed geometrical test on the HGTD, since at high p_{T} they are almost not affected by the magnetic field and will go straight through the detector leaving a hit in each layer. Two samples, one distributed in η and one distributed in θ were produced, the flat θ is used to obtain a distribution relatively flat in R which help the 2D visualisation of the performance. The electrons and photons were mainly used to study the response of the detector such as the number of hits created in the development of the EM shower. A momentum of $45\,\mathrm{GeV}$ was used as the nominal case for the electron as this corresponds to a Z decay. The single pions were used to study the track matching performances of the detector as most of the tracks originating from pile-up correspond to low energy pions. Finally, single neutrino event were only produced with $\langle\mu\rangle = 200$, they were used to studying the occupancy of the detector as in these events only the pile-up is present since the neutrinos does not interact with the detector.

The second type of sample that were produced are physics sample, those are based on real physics process. Among these samples I have used the $Z \to ee$ ones. The Z samples in general were used to study the lepton (electron) isolation while the $Z \to \tau\tau$ allows study of the isolation performances as function of the p_{T} of the electrons.

7.2.3 Readout geometry

The active area of the HGTD is implemented in the simulation as homogeneous disc in the TP simulation. In this version I performed the implementation of the readout geometry with a specific tool at the analysis level. This allows the simulation to stay flexible and adapt to new detector geometry without having to redo the Geant4 implementation and the full simulation each time. At the same time this tool also act as a helper to transform the hit ID stored in the LArHits into an x, y and z position. For each hit in the HGTD the tool use its coordinates to determine to which linear stave it belongs and then within this stave to which pad it belongs, the new coordinates of the hit are the coordinates of the center of the pad. If the hit is not part of any stave but corresponds to one of the inter-stave dead-zones ($1\,\mathrm{mm}$ between two stave $3\,\mathrm{mm}$ between two quadrants) it is discarded. This is no longer necessary for the TDR simulation as only the hit in the sensors are saved during the simulation.

The granularity of the first version of the Geant4 simulation is of $0.5\,\mathrm{mm} \times 0.5\,\mathrm{mm}$ so everything taken into account in the tool need to have a size multiple of $0.5\,\mathrm{mm}$. Due to this constraint the size of the pads in the simulation is of $1\,\mathrm{mm} \times 1\,\mathrm{mm}$ instead of $1.3\,\mathrm{mm} \times 1.3\,\mathrm{mm}$. Another effect of this constraint is that the fill factor, i.e. the fraction of active material in one sensor, of

the pads cannot be directly taken into account, therefore the active surface of the detector and the efficiency are overestimated. This factor is estimated to be 90% corresponding to an inter-pads dead area of $50\,\mu\mathrm{m}$. The extrapolation of the track in the HGTD can be used to determine if a hit should be rejected because of the fill factor to estimate this effect.

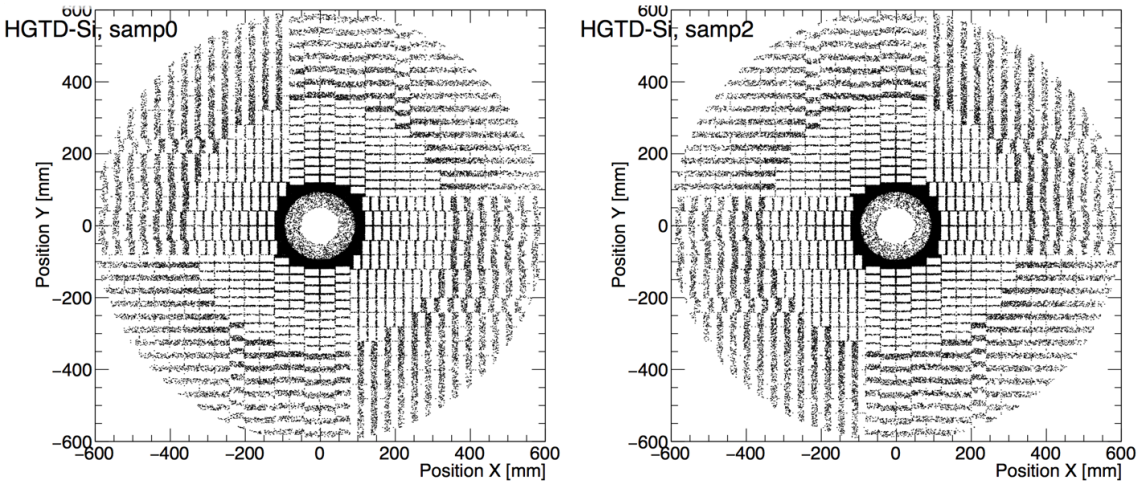

(a) (b)

FIGURE 7.8 – The uninstrumented zones implemented for the readout in the TP simulation are shown as function of the coordinates x and y for the front side of the first (a) and second (b) layers

The TP simulation is composed of 4 layers while the HGTD is composed of 2 layers with overlapping pads on both side of the cooling plate. The first two layers of the simulation are used as the two sides of the first cooling plate and the last two layers as the two sides of the second cooling plate. An additional mask is then applied to reject the hits in the inter-modules dead-zones. Figure 7.8 shows the position of all the different dead-zones in the HGTD. The figures show the symmetry that exist between the first and second layer of the HGTD as well as the change of overlap between the low and large radius (change in the size of the inter-modules dead-zones)

Finally, since the implementation of the LArHits is done as a grid following the X and Y axis, it is not possible to take directly into account the rotation of the detector without redoing a simulation with rotated LArHits. This was in a first time approximated at the track level using a bi-dimensional histogram. For each track the number of associated hits in the first two layers are added to the bin corresponding to a negative rotation of the track extrapolation position. The same operation is performed for the number of hit in the last two layers with this time a positive rotation. Once the histogram is filled, the content of each bin is divided by half the number of associated tracks to correspond to the average number of hits associated per tracks at the position of the bin. This method offer a first approximation of the performance after rotation but is very binning dependent.

For comparison, Figure 7.9 shows the position of the active are in the TDR simulation. The positioning of the module and the space between them is implemented with a greater precision and the rotation of the first and second layer can be taken into account. The studies with the TDR simulation are in agreement with results using the approximations on the TP simulation, validating the approach taken.

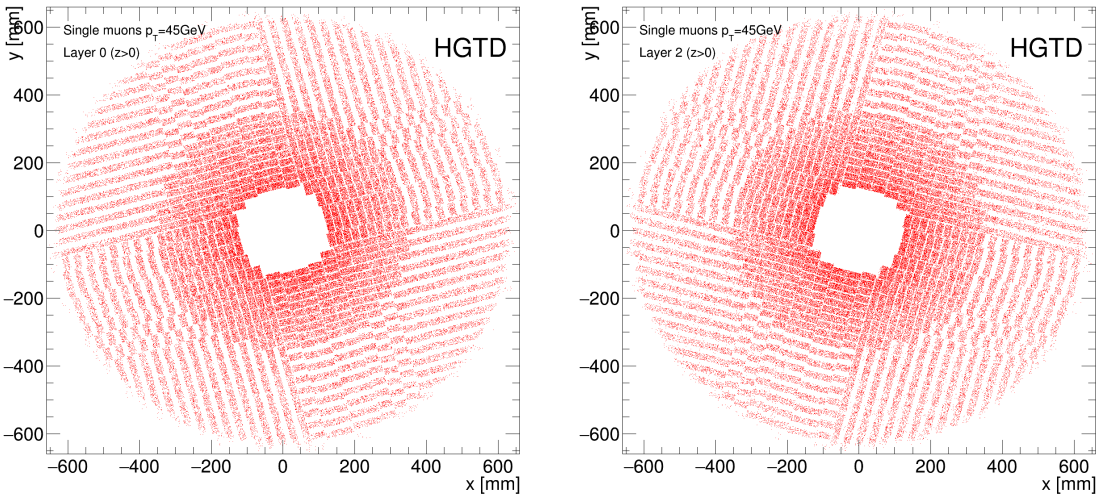

(a) (b)

FIGURE 7.9 – The active area implemented in the TDR simulation are shown as function of the coordinates x and y for the front side of the first (a) and second (b) layers

7.2.4 Simulation of the Detector Signal

The timing resolution has to be accounted for by the simulation. For this a precise understanding of the different sources of degradation of the time resolution is necessary. Two main sources are accounted for in the simulation, the resolution coming from the sensors and the resolution coming from the electronics. Since, as shown in Section 4.4 the electronics resolution comes from many different sources, its effects is accounted for with a gaussian smearing of the times. The resolution of the LGAD sensors is directly linked to the shape of the pulses which is related to the energy deposited inside the sensor. To understand the mechanism behind the pulse creation, I have performed simulations using the Weightfield2 program [87]. Weightfield2 calculates electric fields in a Silicon-Detector and then simulates the propagation and capture of the charges carriers. It can then reconstruct the pulses shape at the output of the sensor. The pulses produced this way won't be used directly in the simulation of the HGTD, but provided additional understanding on the mechanism affecting the shape of the pulses helping simulate them more efficiently in the simulation.

Once a particle cross the LGAD sensor it will create electron-hole pairs in the sensor that drift toward the cathode and anode respectively. The drift of the charges in the sensor will results in a current at the output of the sensor resulting in a pulse.

Figure 7.10 shows a pulse simulated using Weightfield2. For this simulation the doping was set to provide a gain of the order of 15 and the sensor was not irradiated, this is similar to how the sensor should be at the beginning of the life of the HGTD. The green curve is the total current created by the drift of the charges in the LGAD and the black curve is the output of the simulated electronics. The total current is the sum of the effect of the drift of the electrons (in red), of the holes (in blue) and of the gain holes (in cyan). For the total current, three regimes can be observed. Between $0\,\mathrm{ns}$ and $0.4\,\mathrm{ns}$ the pulse is rising, between $0.4\,\mathrm{ns}$ and $0.7\,\mathrm{ns}$ a slightly decreasing plateau is reached and finally between $0.7\,\mathrm{ns}$ and $1.4\,\mathrm{ns}$ the pulse is falling.

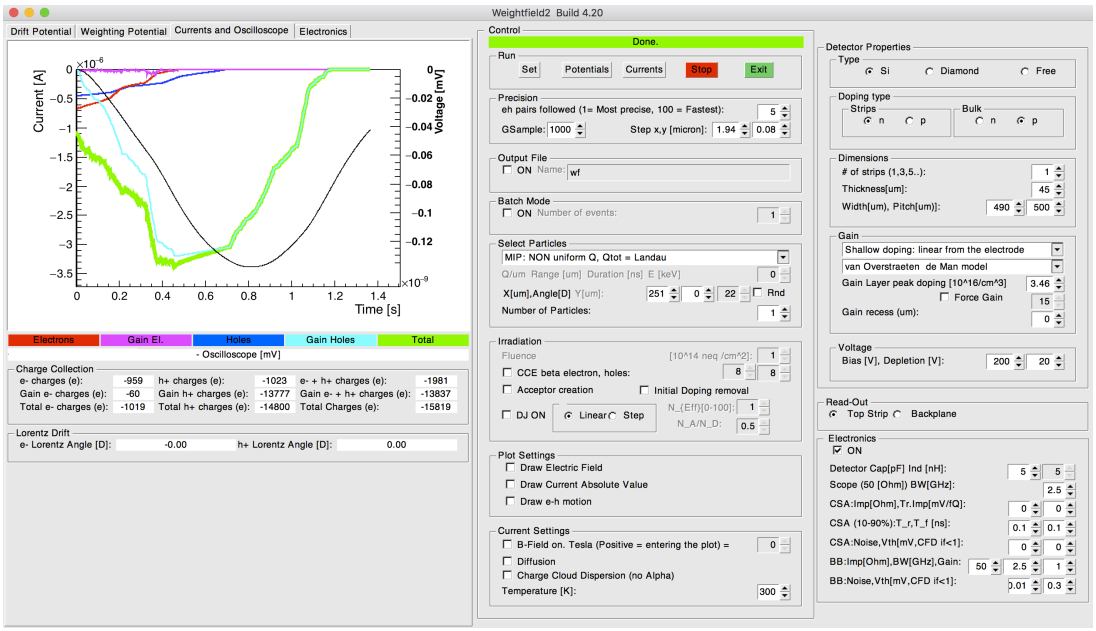

FIGURE 7.10 – LGAD pulse simulated using Weightfield2. The green curve represent the total current created by the drifting of the charges in the LGAD and the black curve represent the output of the simulated electronic. The GUI on the right shows the different option and parameters used for this simulation.

The electrons and holes are created in equal quantity initially when the particle goes through the LGAD. After reaching the cathode and anode respectively they are collected so that the total amount of drifting electrons and holes decreases. This leads to a decrease of the output current. Since the holes are drifting slower than the electrons, the holes take more time to be completely collected and thus the holes current stays above zero for longer. Before reaching the cathode the electrons go through an additional p layer which lead to a multiplication effect and the production of additional gain holes. Since a gain of a factor of 15 is achieved for each electron 15 additional gain holes will be generated, the current generated by the drift of the gain holes will dominate the total current.

The density of electrons and holes in the LGAD in the three different regime is shown in Figure 7.11. In the first regime (a) the number of gain holes increases with time as the electrons are reaching the cathode, this leads to a rise in the pulse. In the second regime (b), all the electrons have been captured so no new gain holes can be produce, stopping the rise of the pulse. Since the holes drift is slower than the electrons, there are still initial holes being collected so that the fraction of all the holes lost per unit of time is small. This lead to a small decrease of the current. Finally, in regime (c) all the initial electrons and holes have been collected and the gain holes start to be collected, the fraction of holes lost per unit of time is thus larger leading to a sharper fall of the signal.

Different slopes can be observed within in the different regimes, this is related to the inhomogeneity of the creation of the electron hole pairs in the sensor. Due to this Landau fluctuation, the density of electron-hole pairs created can change as function of y. This lead to even larger inhomogeneity once the electrons produce additional gain holes as shown in Figure 7.11 (b) where the density is high at $y = 15\,\mu\text{m}$ and low at $y = 20\,\mu\text{m}$. The inhomogeneities will change the shape of the pulse changing the time at which the pulses will cross a threshold, leading to different reconstructed times for sensors being crossed at the same time. To take this effect into account properly, I have implemented the generation of pulse shapes for each hit.

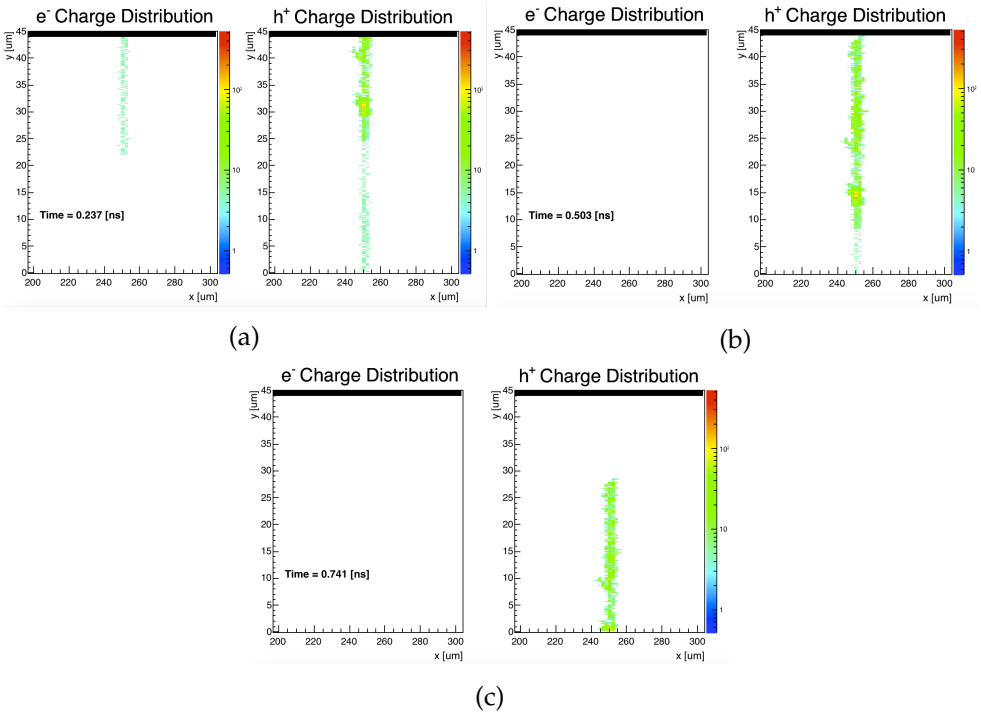

FIGURE 7.11 – Density of charges in the LGAD sensors simulated with Weighfield2 shown at three different time : (a) during the rise of the pulse, (b) during the plateau and (c) during the fall of the pulse.

7.2.5 Timing resolution

Simulated pulses are used to determine the time and energy of each pad. I used data derived from the 2016 HGTD test beam [70] to determine how best to simulate the pulses.

During the test beam $120\,\mathrm{GeV}$ pions from the SPS were used. In the setup, 3 LGAD sensors could be read by an oscilloscope in addition a Cherenkov counter with a timing resolution significantly lower than the one of the LGAD sensor. The role of this Cherenkov counter is to provide a reference for the time measure with the LGADs sensors. With the oscilloscope the pulse produced by each sensor was recorded to be analyzed offline.

From the test beam data only pulses with an energy larger than $1\,\mathrm{MIP}$ where kept. The RMS of the noise on the amplitude was estimated to be 1.5% of a MIP using the data outside the signal pulses. The pulses from the events were averaged together in bins of $25\,\mathrm{ps}$ to determine the average pulse shape. A linear interpolation with a step of $1\,\mathrm{ps}$ was then used obtain the waveform shown in Figure 7.12.

The pulse can be described with the convolution of a landau function and a gaussian function, varying only the width of gaussian function. For each hit, a 200 points pulse is computed by doing the convolution, the width of convoluted gaussian function been drawn from a gaussian distribution with a width proportional to the desired timing resolution of the pad ($25\,\mathrm{ps}$). The pulses are then normalized to the energy of the Geant4 hit. The time corresponding to the first point of the pulse is chosen to be the time of the Geant4 hit. Finally, a gaussian noise with a width equal to 1.5% of the energy of a MIP is added to the pulse. An example of the simulated pulses is shown in Figure 7.12 (b).

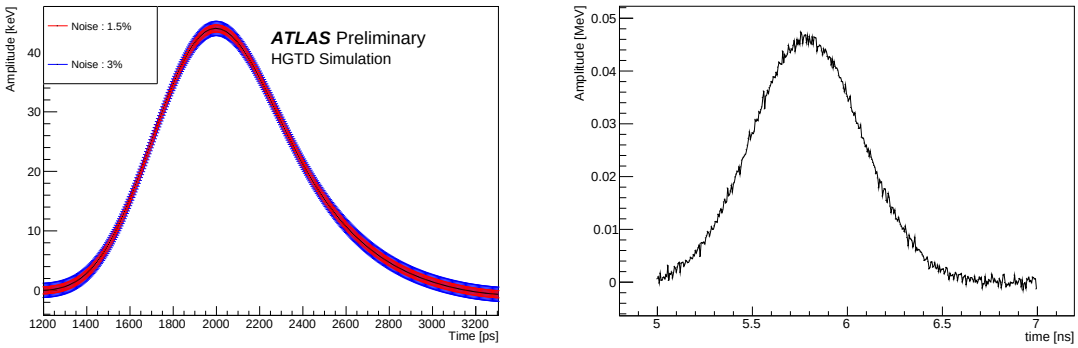

(a) (b)

FIGURE 7.12 – (a) The signal shape used in simulation, derived from testbeam data including the uncertainty on the amplitude. (b) Simulated pulse based on the convolution of a landau fonction and a gaussian function

For multiple hits in a pad, the generated pulses are summed. The new energy is the maximum of the resulting pulse. The new time will then be determined using a pseudo Constant Fraction Discriminator algorithm (see Section 4.4) : the CFD time corresponds to the time of the first point with an energy above 50% of the maximum energy. Since the time of the original hit corresponds to the first point of the pulse, this will result in a shift of $0.441\,\mathrm{ns}$ in average between the time of the hit before and after the application of this algorithm. Finally, to take into account the electronic noise the CFD time is the smeared by a gaussian with a width between $10\,\mathrm{ps}$ and $60\,\mathrm{ps}$ that depends on the radiation dose received. This models the effect of the decrease of the gain resulting larger time jitter. As shown in Figure 7.13 (a) the difference between the reconstructed time and the true time of the hits computed using this method follows a gaussian distribution with a width corresponding to the expected timing resolution.

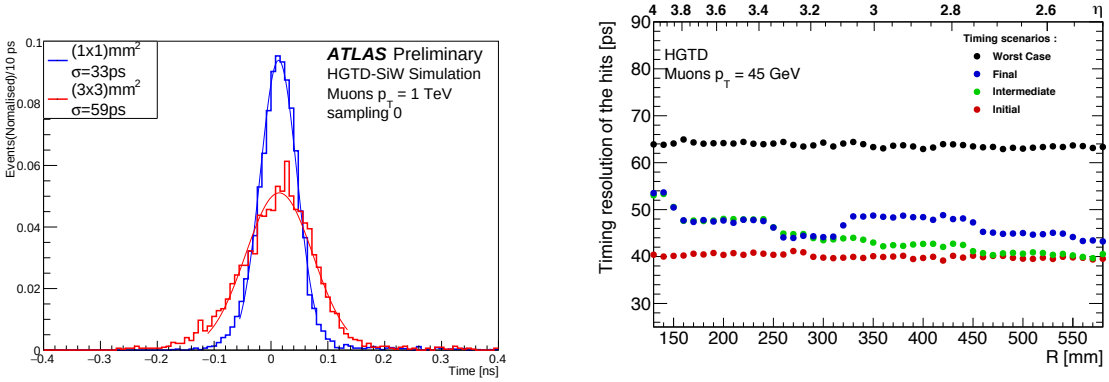

(a) (b)

FIGURE 7.13 – (a) Distribution of the difference between the reconstructed time and the true time of the hits computed using the timing resolution tool. (b) Timing resolution of the hits in the HGTD as function of the radius for different four timing scenarios.

The timing resolution of the detector and the one due to the electronics will evolved as function of the radiation dose received. The higher the dose received by the sensor the lower its gain. Since the timing resolution of the electronics is directly link to the electronic jitter. This means that for larger dose this jitter will become larger relative to the signal. To take into account this evolution in the performance studies. I implemented the possibility of choosing a

specific luminosity for the computation of the time of the hits. The algorithm first computes the dose received by the sensor as function of the radius, this evolution was obtained using FLUKA[88] calculations for two luminosity, 2000 fb^{-1} and 4000 fb^{-1} as shown Figure 7.14 (c). Since the dose evolved linearly with the luminosity an extrapolation can be performed to compute the evolution for any luminosity, taking into account the replacement of the inner ring after 2000 fb^{-1}. The dose has then been used to compute the corresponding time resolution. The gain of sensors has been measured in lab for different doses as shown in Figure 7.14 (a). The gain was combined with lab measurements of the timing resolution of the ALTIROC0 for different input gain to compute the evolution of the timing resolution as function of the dose as shown in Figure 7.14 (b).

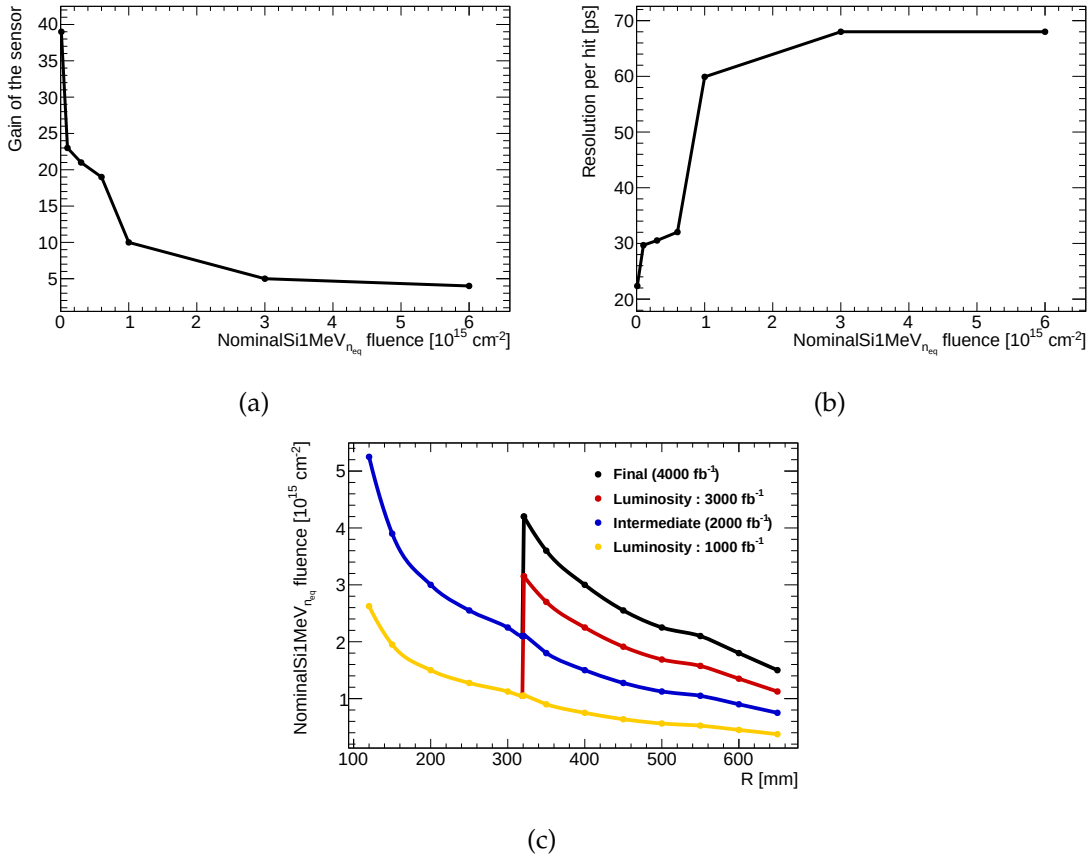

FIGURE 7.14 – (a) Evolution of the gain of the sensor as function of the dose it received used in the simulation (derived from measurement on HPK sensor). (b) Evolution of the timing resolution of the electronic associated with a sensor as function of the dose received by the sensor used in the simulation (derived from measurement on HPK sensor). (c) Dose received by the pad in the HGTD as function of the radius after a luminosity of 2000 fb^{-1} and 4000 fb^{-1} (after replacement of the inner disc) used in the simulation.

This implementation of the timing resolution is shown in Figure 7.15. The MC signal sample of single muons was used to determine the timing resolution. In the following performances plots, four timing scenarios will be used to illustrate the evolution of the performances of the HGTD with the luminosity : Initial, Intermediate pre-replacement, Intermediate post-replacement and Final. The scenarios correspond to the timing performance of the HGTD at the beginning (0 fb^{-1}), after half of the running time before (2000 fb^{-1}, Figure 7.15 (a)) and after (2001 fb^{-1}, Figure 7.15 (b)) replacement of the inner disc and at the end of the HL-LHC (4000 fb^{-1}). In older figures, the timing scenario is presented as Initial, Intermediate, Final and Worst case.

These do not take into account the luminosity and the timing resolution is directly hard-coded as function of the radius as shown in Figure 7.13 (b).

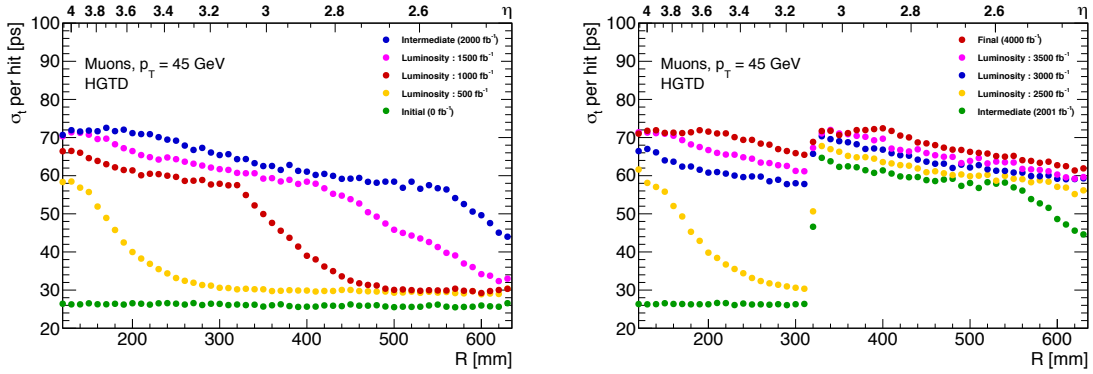

(a) (b)

FIGURE 7.15 – (a) Timing resolution of the hits in the HGTD for different luminosity before replacement of the inner disc. (b) Timing resolution of the hits in the HGTD for different luminosity after replacement of the inner disc.

The electronic will be using a fix threshold and a ToT correction to measure the time instead of a CFD (see Section 4.4.2). The readout tool provides the possibility to replace the energy stores the LArHit by the ToT. This ToT is obtain using the pulse simulated, its amplitude is multiplied by the gain corresponding to the given luminosity and radius as shown in Figure 7.15 (a) and a threshold corresponding to the energy of a MIP with a gain of four is applied.

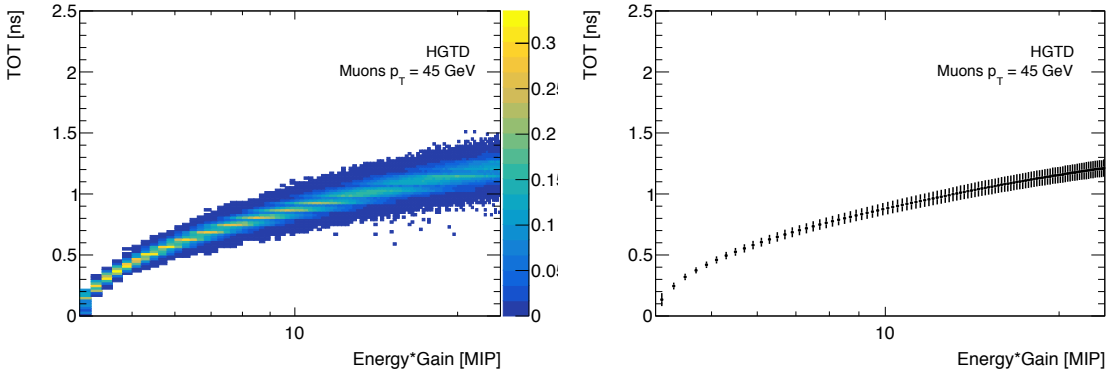

(a) (b)

FIGURE 7.16 – (a) Value of the ToT as function of energy of the corresponding hit in MIP units multiplied by the gain, the Z axis represent the fraction of event for each given energy. (b) Average value of the ToT as function of energy of the corresponding hit in MIP units multiplied by the gain, the error bars are the RMS of the distribution.

The implementation of the simulation can be improved. The current method, using a convolution of a landau and a gaussian function, reproduces the average shape of the pulse but using a variation of the width of the pulse to take into account the Landau fluctuation is not sufficient as it does not account properly for the falling pulse. As long as the pulse is used with a CFT this will not impact the time reconstructed but this might become problematic for study using the ToT. A large database of preexisting pulses could be directly used in the simulation or a function to approximate more accurately the shape of the pulse could be developed. A neural network could be used to derive such a function allowing us to simulate pulses taking into

account different parameters such as the dose, the energy and event the angle of the incoming particle.

The tools that I have developed for the readout geometry and the timing resolution were used in the studies with full and fast simulation summarized in Section 4.5.

7.3 HGTD Optimisation

The design of the HGTD have gone through multiple versions before reaching finally the one presented in Section 4.2. This section present the evolution of the geometry of the HGTD as well as the reasoning behind the different design choices. Then the optimization of the number of layers and of the overlaps between the sensors will presented.

7.3.1 Design and Geometrical efficiency

The first design of the detector was square based, the pads were put together in large square (or rectangular) modules called Active Sensor Unit (ASU). A schematic representation of the ASU is shown on Figure 7.17 (b), they are composed of a $195.5\,\mathrm{mm} \times 195.5\,\mathrm{mm}$ PCB on which are glued 4 $97\,\mathrm{mm} \times 97\,\mathrm{mm}$ silicons wafers on which are mounted the pads. The different ASU would then have been combined together to cover the surface of the detector as shown on Figure 7.17 (a).

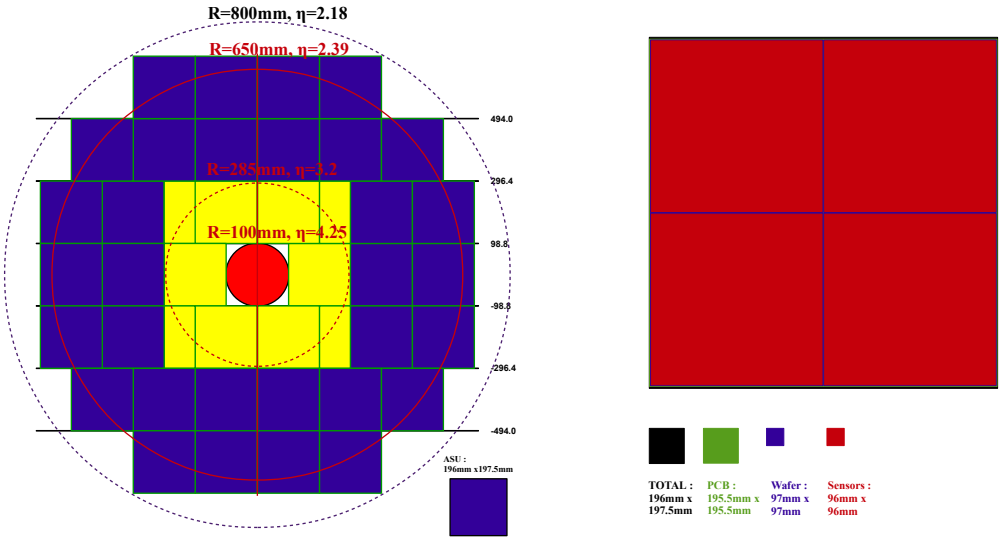

(a) (b)

FIGURE 7.17 – (a) First design of the HGTD, the square represent the different ASU. The blue one are composed of $3\,\mathrm{mm} \times 3\,\mathrm{mm}$ pads and the yellow one of $1\,\mathrm{mm} \times 1\,\mathrm{mm}$ pads. (b) Representation of the different component of an ASU, the active area is in red while the rest is inactive.

To minimize the number of pads with a double hit an occupancy (the probability of having a signal in a pad) lower than 10% was needed. Since the particle flux increase with $|\eta|$, a geometry with two different granularity was chosen at the time. At low radius (ASU represented in yellow) pads of $1\,\mathrm{mm} \times 1\,\mathrm{mm}$ are used while at large radius (ASU represented in blue) pads

of $3\,\mathrm{mm} \times 3\,\mathrm{mm}$ are used. With this design it is possible to stay below 10% occupancy while minimizing the number of pads necessary.

Four identical layers would have been built with a full coverage going from $R = 142\,\mathrm{mm}$ and $R = 640\,\mathrm{mm}$ and a partial coverage between $R = 100\,\mathrm{mm}$ and $R = 800\,\mathrm{mm}$. The 4 layers were necessary to reach the target of a timing resolution of $30\,\mathrm{ps}$ with pads of only $60\,\mathrm{ps}$ of resolution.

One important parameter when choosing a geometry is the un-instrumented zones. Figure 7.17 (b) illustrates the dead area within an ASU, the red area corresponds to the active sensor region (95% of the ASU surface) and the rest of the color corresponds to the different sources of dead area. In blue there is the $0.5\,\mathrm{mm}$ guard ring around each sensor area, in green the inter-wafer space link to the fact that the PCB on which the sensors are glued is larger than the sensors and finally in black the mechanical space between the different ASU needed for the assembly. Because of the inactive area some particle can go through the detector without leaving any signal in the detector, causing inefficiency and reducing the performance of the detector.

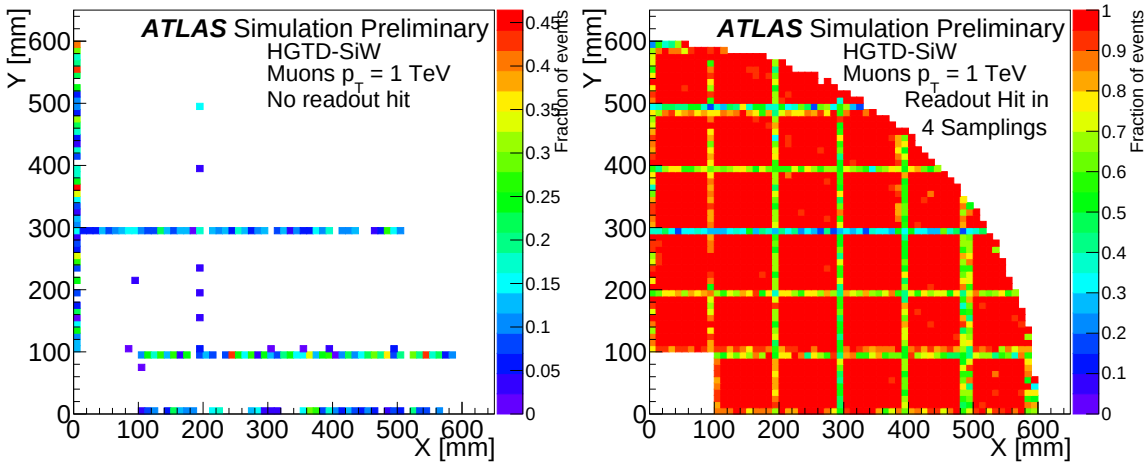

(a) (b)

FIGURE 7.18 – (a) Probability of having no readout hit in the detector as function of the X and Y position computed using $1\,\mathrm{TeV}$ muons. (b) Probability of having a readout hit in every layer of the detector as function of the X and Y position computed using $1\,\mathrm{TeV}$ muons.

The estimation of the detector inefficiency with single muons is shown in Figure 7.18. Figure 7.18 (a) shows as function of the X and Y positions of the muons in the first layer of the HGTD the fraction of events with no hits in the HGTD while the Figure 7.18 (b) shows the fraction of event with at least one hit per layer. In the Figure 7.18 (b) the red square in which 100% of the muons are associated to 4 hits corresponds to the different $96\,\mathrm{mm} \times 96\,\mathrm{mm}$ sensors area, the lines between the square correspond to the different inter-ASU and intra-ASU dead zones. Since the dead area are at the same position in all the layers of the HGTD it is possible for a muon stay in this region and leave the detector without interacting, as shown on Figure 7.18 (a) this more likely for muons that arrive in one of the horizontal dead zones since these are larger that the vertical one as shown in Figure 7.17 (b), it is also very likely for muons in the $X = 0$ or $Y = 0$ dead area. Indeed, in these cases the muons will propagate in the direction of the dead zones and will not interact with any sensor.

With this geometry 98.88% of the muons that were simulated in a flat η distribution between $|\eta| = 2.4$ and $|\eta| = 4$ have at least one hit in the HGTD and 50% of the undetected hit are link to the dead area at $X = 0$ or $Y = 0$ which are not easily avoidable.

The main problem that arises with this design is that the square based geometry does not offer enough space for the services and the cables necessary to transport the signal from the sensors to the off detector electronics. The size of the ASU were also problematic, since each ASU was effectively $200\,\mathrm{mm} \times 200\,\mathrm{mm}$ achieving a full coverage of the area between $R = 140\,\mathrm{mm}$ to $R = 640\,\mathrm{mm}$ implied wasting a lot of sensors at a radius larger than $640\,\mathrm{mm}$, increasing the cost and the size of the detector. The solution chosen to solve these problems while maintaining a good efficiency was to go from a square based detector to a linear based detector. In this second design modules of $20\,\mathrm{mm} \times 39\,\mathrm{mm}$ are put together in staves with a width of $40\,\mathrm{mm}$. With this design, the flex cables that are used to supply the power to the modules and transport the signal can be put on top of the staves and connect to all the modules in a row.

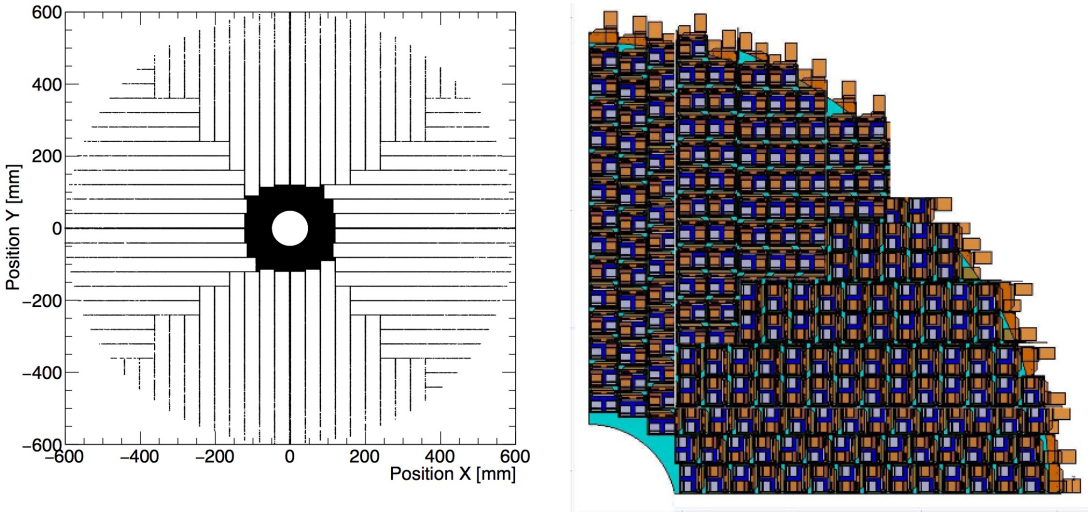

(a) (b)

FIGURE 7.19 – (a) Second iteration of the design of the HGTD (Diagonal design) the back line correspond to inactive region. (b) Position of the sensor on a quadrant of the HGTD in the Diagonal design.

The arrangement of the different staves in the HGTD, called the Diagonal design since the disposition of the staves create four diagonal line, is presented in Figure 7.19. The stave has only a width of $40\,\mathrm{mm}$ (compared to the width of 200 of the ASU) which makes it possible to fit the circle at $R = 120\,\mathrm{mm}$ efficiently. Full coverage between $150\,\mathrm{mm}$ and $640\,\mathrm{mm}$ with a 92% coverage between $120\,\mathrm{mm}$ and $150\,\mathrm{mm}$ is achievable. Similarly, since there is no major constraint on the length of the staves the radius at $R = 640\,\mathrm{mm}$ can be accommodated easily.

Signal from the modules are transfer to off-detector electronic by the flex cables that follow the direction of the staves. This defines two constraints on the geometry of the HGTD. Since the flex has to be able to connect to all the sensors in a stave, the stave should not be too long since long flex are more complicated to build. Furthermore, the longer the stave the more modules need to be put on it, as shown on Figure 7.19 (b) and since one flex is needed per module this mean that a stave too long might become too thick due to the stacking of the flex. The other constraints is the off detector electronic which is disposed homogeneously all around the HGTD. The end of the different flex cable should be as homogeneously as possible all around the outer radius of the HGTD. For this reason the geometry of Figure 7.19 (a), with staves going

both horizontally and vertically in each quadrant, was chosen instead of a geometry with all the stave going in the same direction.

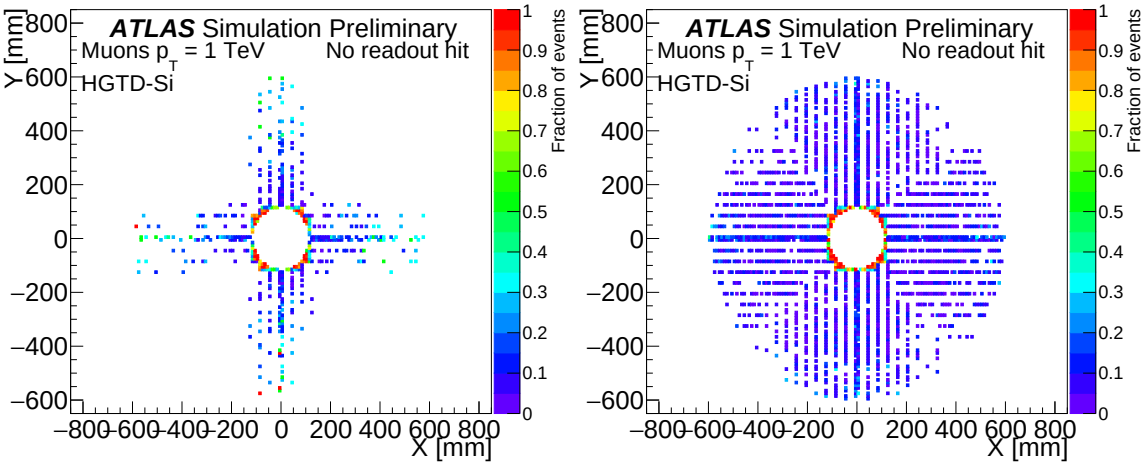

(a) (b)

FIGURE 7.20 – (a) Probability of having no readout hit in the detector as function of the X and Y position computed using 1 TeV muons in the case of the Diagonal design with four layers. (b) Probability of having a readout hit in every layer of the detector as function of the X and Y position computed using 1 TeV muons in the case of the Diagonal design with two layers.

Single Muons test were also perform to test the efficiency of this geometry as shown in Figure 7.20. In this geometry since the modules within a stave are overlapping each other the only type of dead area are the inter-stave ones and the inter-quadrant ones. The size of the dead zones are respectively of 1 mm between two staves and 3 mm between two quadrants, the real design of the detector is using two half discs separated by 3 mm instead of four quadrants but to simplify the simulation this slightly worse case with four quadrants was chosen.

Figure 7.20 (a) shows the fraction of muons crossing the detector without interacting as function of their position in the first layer of the HGTD in the case of a detector with four layers. With this design a small improvement can be observed in the number of muons detection efficiency from 98.88% up to 99.05% but similarly to the previous design the main inefficiencies are the dead zones parallel to the direction of propagation of the muons. This mean that most of the inefficiency is at X or Y close to zero.

The number of layers was changed from four to two to reduce the cost of the detector. Figure 7.20 (b) shows the same fraction as Figure 7.20 (a) in the case of two layers of active material. Because of this reduction, all the dead area became sources of inefficiency and not only the one with a value of X or Y close to zero, leading to a decrease of the muon detection efficiency from 99.05% to 98.5%.

To minimize the inefficiency in a two layer scenario the best solution is to avoid as much as possible overlapping dead area. The simplest solution to avoid this overlap was to change to a chiral design and have the two layers of the HGTD be the mirror image of one another. Three possible version of this geometry, called Helix due to the way the staves are arranged, are shown in Figure 7.21. The initial idea, called Helix 0 was to have one quadrant design with all the stave in the same direction, four of the quadrants could then be rotated and put together to cover the entire surface of the HGTD (a). If a quadrant has all its staves vertical in the first

layer then the staves of the corresponding quadrant in the second layer will be all horizontal and the geometrical efficiency will be maximum.

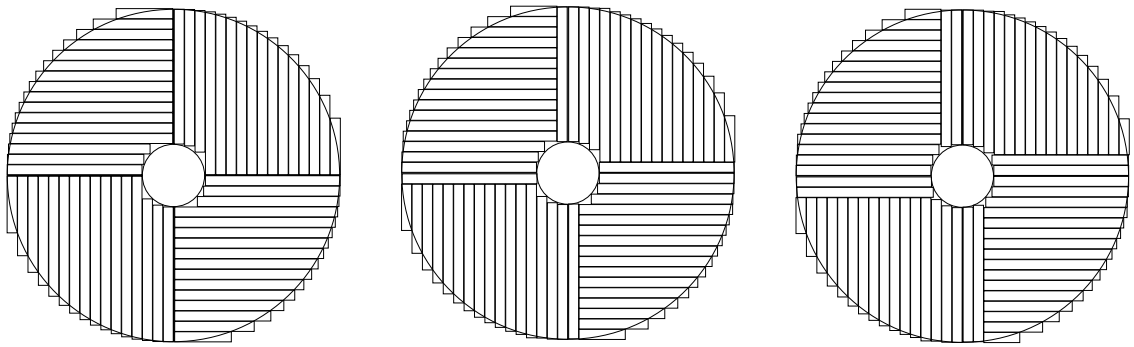

(a) (b) (c)

FIGURE 7.21 – Third iteration of the design of the HGTD (Helix design) the rectangle correspond to the different staves. (a) Helix 0 design. (b) Helix 1 design. (c) Helix 2 design.

Two other design were developed, Helix 1 (b) and Helix 2 (c), with the objective of reducing the length of the longest stave and increasing the coverage at low radius. These geometries are obtained by taking the quadrant from Helix 0 reducing the length of the stave and adding one or two extra staves perpendicular to all the other one, the number in the name of these geometries corresponds to the number of perpendicular staves. Unfortunately the geometrical efficiencies of Helix 1 and Helix 2 are a bit lower than Helix 0 since the orthogonal staves will have the same position as the staves from the second layer. This is illustrated in Figure 7.22 in which the black line corresponds to the position of the stave in the first layer and the red line corresponds to the position of the stave in the second layer for the Helix 2 geometry. In this configuration there is a total of 20 overlapping dead zones (corresponding to red line being on top of black line) compared to 4 in the Helix 0 arrangement.

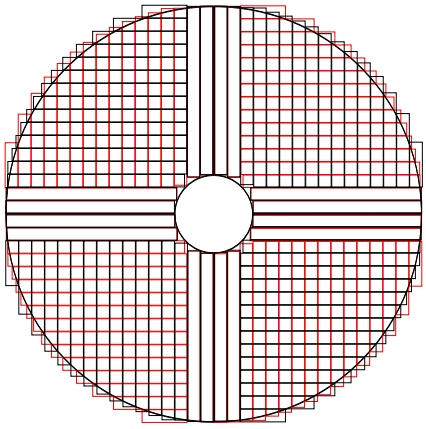

FIGURE 7.22 – Superposition of the two layer of the Helix 2 geometry. The first layer is in black and the second one is in red. Both layers are the mirror image of each other.

As for the two previous design single muon test were performed to test the efficiency of the three Helix geometry, the results are shown in Figure 7.23. The number of perpendicular staves per quadrant is directly linked to the number of dead areas. For the Helix 0 geometry shown in

Figure 7.23 (a) there are four of such dead region corresponding to the transition between the four quadrant, inefficiencies can also appear when an inter-stave region from the first cross an inter-stave region in the second layer, this happens when a red line is crossing a black line in Figure 7.22, this corresponds to the different point that appear outside the line in Figure 7.23. In Figure 7.23 (b) and (c) the number of dead area line increase which correspond to a decrease of the efficiency.

Table 7.2 shows a comparison of the different geometrical parameters and the efficiency for the Diagonal, Helix 0, Helix 1 and Helix 2 geometries. Staves cannot be too long which mean that the Helix 0 geometry cannot be used even if it provides a geometrical efficiency of 99.7%. Another parameter that has to be taken into account is the coverage at low radius, with the Helix 0 and Helix 1 geometry since most of the stave are in the same direction the coverage at low radius is not good, only 88.4% of the surface between $R = 130\,\mathrm{mm}$ and $R = 150\,\mathrm{mm}$ is covered. On the other hand the Helix 2 geometry has a better coverage of 91.8% at low radius, similar to the one obtained with the Diagonal design. The Helix 0 and Helix 1 also have another disadvantage, the end of the staves are disposed less homogeneously at the outer radius which would make the design of the off detector electronic and cable more complicated. For these reasons the Helix 2 is the preferred geometry.

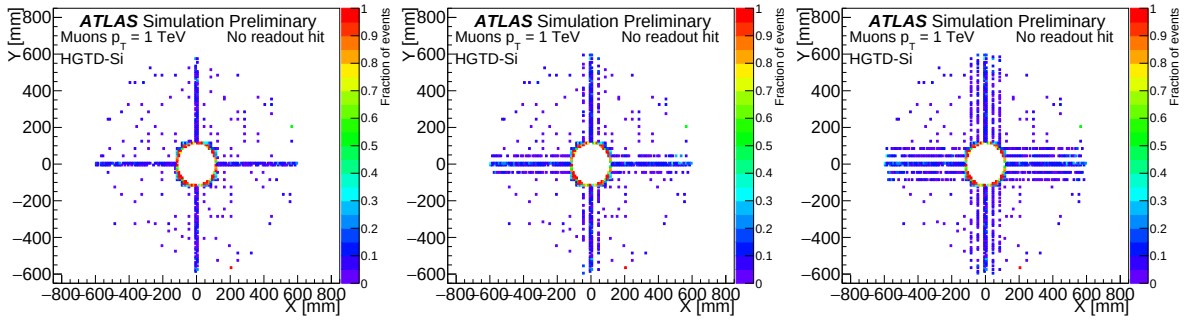

(a) (b) (c)

FIGURE 7.23 – Probability of having no readout hit in the detector as function of the X and Y position computed using 45 GeV muons in the case of the (a) Helix 0 design (b) Helix 1 design (c) Helix 2 design.

	Diagonal	Helix 0	Helix 1	Helix 2
Longest stave [mm]	524	628	587	547
Coverage [130 mm - 150 mm]	91.8%	88.4%	88.4%	91.8%
Number of staves	23	16	17	18
Geometrical efficiency	98.5%	99.7%	99.5%	98.3%

TABLE 7.2 – Summary table of the geometrical property and performances of the three Helix design.

The last change in the design of the HGTD was the introduction of a rotation of 15° of both layers in opposite direction, this is represented in Figure 7.24. This change offers two additional benefits compared to the previous geometry, first this will lead to the inter-staves dead area being at different positions in the first and second layer reducing the probability of having a particle hitting the inactive region of both layers and thus increasing the geometrical efficiency of the detector. This can be observed on Figure 7.24 (c) in which the first layer stave are represented in black and the second layer one are represented in red. The regions for which particles can go through the detector without interacting with the sensor correspond to the

intersection of the red and back point and are thus only point like compare to the linear regions of the previous geometry. The secondary and main benefit is that this geometry creates some free space in the peripheral electronics that allow us to put the tubes for the cooling system.

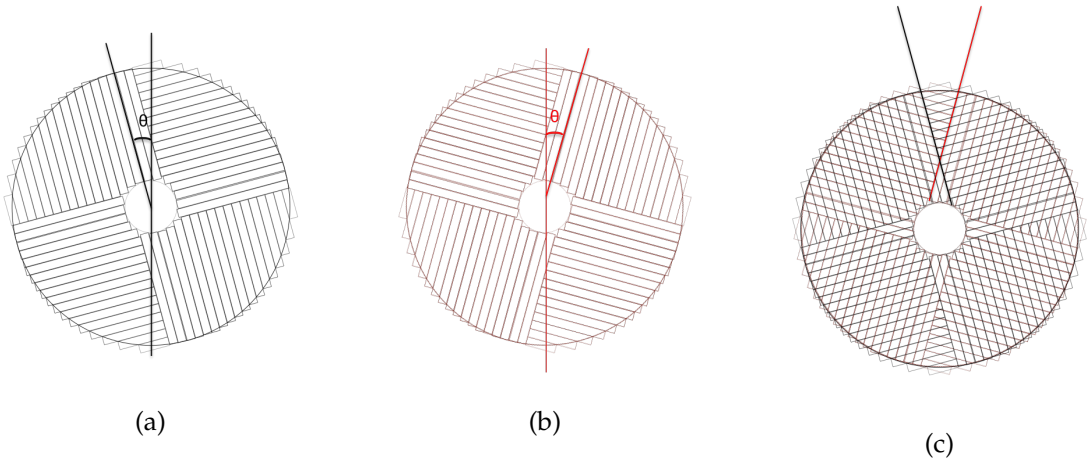

FIGURE 7.24 – The orientation of the readout rows for the first and last layer separately, and the overlay of both. Each layer is rotated in opposite directions by 15°.

In order to properly operate the detector the LGAD sensors need to be maintained at a temperature of $-30^{\circ}C$. To cool the detector different cooling loops go through each cooling plate of each half disc. The two loop in each half disc are then connected via pipes to the main cooling system of ATLAS. This connection has to be done at radius of between $700\,\mathrm{mm}$ and $900\,\mathrm{mm}$.

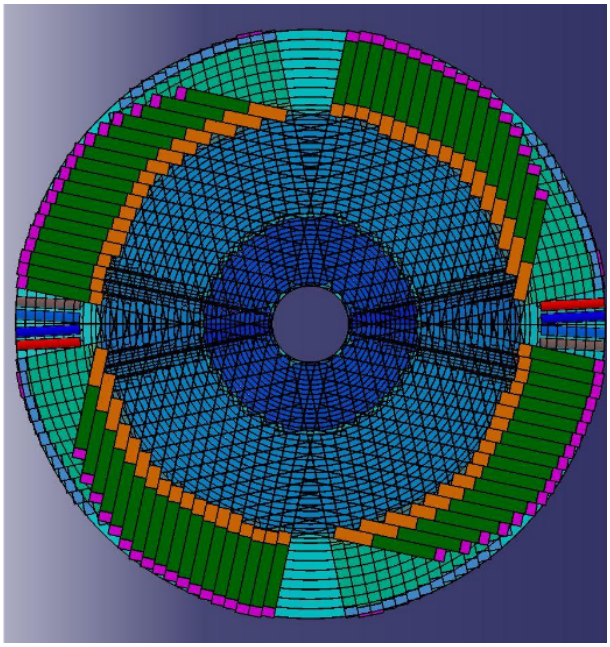

FIGURE 7.25 – Illustration of the peripheral electronic and cooling system. Since the layers are rotated in opposite directions by 15°, some space is freed to connect the HGTD cooling to the main ATLAS cooling.

The peripheral electronic is also installed at the same radius. The more flex are going out of the detector in a specific region the larger the peripheral electronic need to be. To free space for the cooling system it is thus necessary to create regions in which no stave go out of the detector,

this can be achieved by rotating the layers of the HGTD in opposite direction. This is illustrated in Figure 7.25, in this drawing the peripheral electronic is represented in green as an extension of the staves, due to the rotation four areas becomes free of electronic two of which can be used to install the cooling pipes.

The effect of the rotation angle on the performance was studied using the simulation. No effect on the average number of hits per track was observe before and after the rotation of the two layers, the rotation won't have any substantial effect on the timing resolution of the track. On the other hand the introduction of the rotation reduce the fraction of events with no hit in the detector due to uninstrumented area by a factor 3 from 0.65% of the track to 0.2% of the tracks in the inner ring (non effect is observed in the outer ring). For a rotation angle between $\theta = 10^{\circ}$ and $\theta = 20^{\circ}$ no significant differences were observed in terms of performances and efficiency. An angle of $\theta = 15^{\circ}$ was thus chosen only based mechanical criteria to ensure enough space was available for both the cooling and the electronics.

7.3.2 Number of layers

In parallel with the optimization of the design an optimization of the number of layers was also performed. After the stave design was chosen it became apparent that all the sensors could not be placed continuously on the entire length of the stave since some space was needed between two sensors to connect the electronic. To avoid creating holes in the detector it was decided to make each layer double-sided with the sensors on each side overlapping by 20% to avoid particles going through the layers without interacting. This double-sided design lead to an increase of the width of each layer. To mitigate this increase a reduction on the number of layers was necessary, but before reducing the number of layers the impact on the performances had to be derived.

In addition to the overlap of the sensor of both side of each layer the fill factor of the sensor was also taken into account in this study. The fill factor is the faction of the geometrical sensor that is active, for the LGAD sensor it is expected to be 90%, this number is mainly driven by the size of the guard ring around each pad and the inter-pad deadzone.

Figure 7.26 shows the fraction of single muons tracks with different number of hits for four different η bins. At the time of this study neither the fill factor nor the double-sided layers were implemented in the simulation. In the Geant4 simulation of the detector the position of the hits is only known with a granularity of $0.5\,\mathrm{mm}$, this granularity is too large to take into account the guard ring of the pads which is of the order of $50\,\mu\mathrm{m}$. To still be able to take these effects into account the extrapolation of the tracks is used. Using this position, the number of hits associated with the tracks was decreased or increased depending on whether the position corresponds to a dead zone or an overlap region.

Using this method while the number of hit for each track might not be correct, the distribution of the number of hit per track should. Since the extrapolation is being used only tracks associated with hit in the detector can be used, thus the fraction shown in Figure 7.26 ignores the effect of the un-instrumented zones (which correspond roughly to a 95% chance of having a hit for each layer). Due to the overlap of the sensor in each layer the number of hits can exceeded the number of layers (up to twice the number of layers).

This study was performed for different fill factors, the larger the fill factor the larger the fraction of tracks with a number of hits greater or equal to the number of layer is. A variation of the relative fraction of the different number of hits as function of η can be observed, this arises from the combination of two effects. At low η the incidence angle is large, which increase

the probability of hitting at least once the overlap region and thus populating more the case in which the number of hit is greater or equal to the number of layer. At large η the incidence angle is small, so either all the hits are in the overlap region or none are.

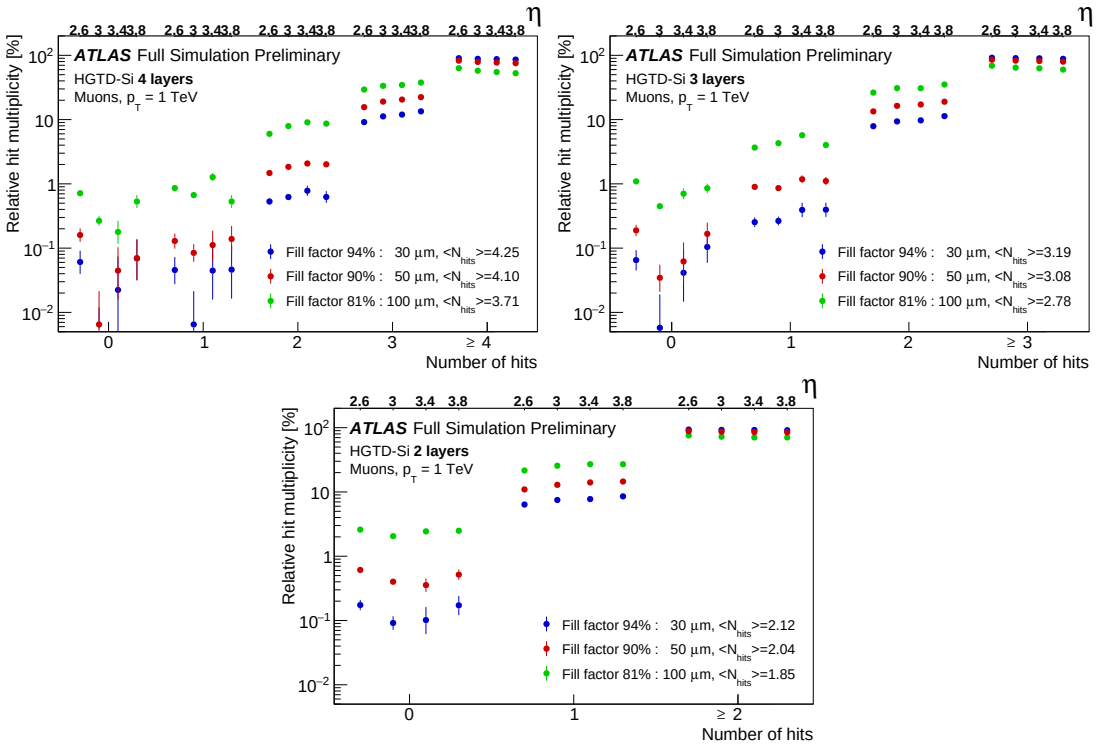

FIGURE 7.26 – Fraction of single muons tracks with N hits associated to them for the Diagonal design and (a) four layers (b) three layers (c) two layers. Normalized to the number of tracks with at least one Geant4 hit associated to them.

Table 7.3 shows the performance of detector as function of the number of layers. This table was derived for a timing resolution per pads of $60\,\mathrm{ps}$ and a fill factor of 90% using single muons tracks. As for Figure 7.26 all the number are normalized to the number of tracks with at least one hit. Due to the sensor overlap the average number of hit per track stays close to the number of layers and thus the timing resolution should be proportional to $1/\sqrt{(\text{Number of layers})}$. With four layers a resolution of the order of $30\,\mathrm{ps}$ per track can be achieved while with two layers the resolution drops to $45\,\mathrm{ps}$. If a time can be associated to the tracks, reducing the resolution does not greatly impact the physics performances. For the electrons isolation the drop from $30\,\mathrm{ps}$ to $45\,\mathrm{ps}$ was estimated to decrease the improvement brought by the HGTD by the order of 7%. A similar conclusion was reached with other performance studies. It was decided was thus decided to reduce the number of layer from four to two double-sided layers per endcap. This allows the detector to fit with the available space, reduce the detector cost with a minor impact on the physics performance.

	Two Layers	Three Layers	Four Layers
$N_{hits} \geq N_{layers}$	86%	82%	78%
$N_{hits} = 0$	0.50%	0.11%	0.07%
$< N_{hits} >$	2.04	3.08	4.1
$< \sigma_t >$	43 ps	37 ps	32 ps

TABLE 7.3 – Geometrical performances of the Diagonal design for different number of layer. The percentage are normalized to the number of tracks with at least one hit associated to them.

7.3.3 Module overlap

To minimize the inactive regions in the detector each layer of the HGTD is composed of two side with overlapping sensors as see in Figure 7.27. Each layer is composed a single cooling plate, on both side of this cooling plate modules are glued. The modules are composed of both a sensor (in red) and an ASIC (in black), with the ASIC being slightly larger that the sensor on one side to allow the connection between the ASIC and the flex cable. To ensure that no particles could go through the layer without interacting with any sensors an overlap of at least 20% between is modules is necessary at $R = 600\,\mathrm{mm}$.

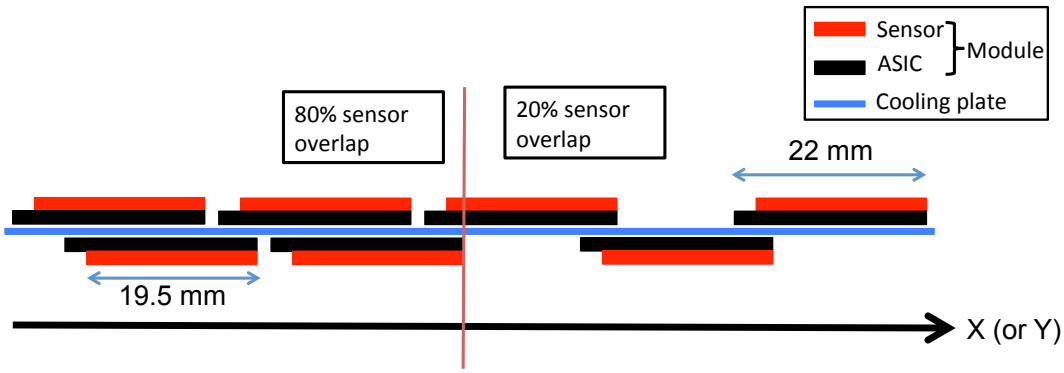

FIGURE 7.27 – The schematic drawing shows the overlap between the modules on the front and back of a cooling disc. There is a sensor overlap of 20% for $R > 320\,\mathrm{mm}$, and for $R < 320\,\mathrm{mm}$ an overlap of 80% between sensors.

The closer to the beam pipe the modules are the more irradiated they get. To mitigate this effect, a replacement of the sensor for $R < 320\,\mathrm{mm}$ at the mid-life of the detector is foreseen. Even with this replacement the timing resolution in the inner region will be substantially worse than the one in the outer region. The timing resolution of a track is inversely proportional to the square root of the number of hits associated to this track, it is thus possible to improve the resolution at low radius by increasing the number of hits. To increase the number of hits one could add an additional layer at low radius, unfortunately the limited space in which the HGTD is installed would not allow for such a layer. The solution that was chosen was to increase the overlap of the sensors within one layer. Doing so will increase on average the number of hits that will be associated with a track since two hits could be associated to the track per layer. Figure 7.28 shows the number of hits per tracks as function of the radius for different overlap scenario. For an overlap of at least 80% it is possible to achieve 3 hits per track in the inner ring of the HGTD, this overlap also has the advantages of leaving a $2\,\mathrm{mm}$ gap between two adjacent modules making the assembly of the staves simpler. For both reason an overlap of 80% was chosen to be the nominal overlap for the inner ring of the HGTD.

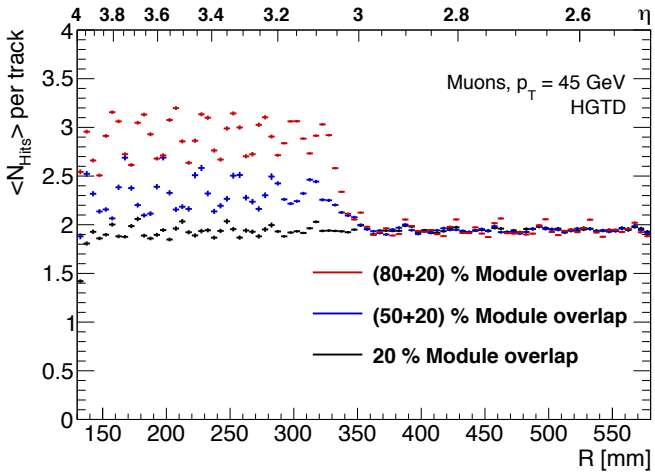

FIGURE 7.28 – Number of hits per track as function of the radius for different modules overlaps.

In Figure 7.28 an oscillation of the number of hits per track can be observed as a function of R with a periodicity of about $24\,\mathrm{mm}$. This figure was obtained with a simulation that was not using the rotation, in that case the overlap region can be at the same position in the first and second layer and thus only 2 or four hits per track will be observed. The periodicity of the oscillations corresponds to the periodicity of the placement of the modules, there are $24\,\mathrm{mm}$ between the beginning of a module and the beginning of the next one.

This figure can be compared with Figure 7.36 (a) which present the number of hits per track as function of the radius with the TDR simulation. The lower average number of hits per track comes from the addition of the inactive area within the pads and the absence of oscillation confirms that the addition of rotation decrease the RMS of the timing resolution of the tracks within the detector.

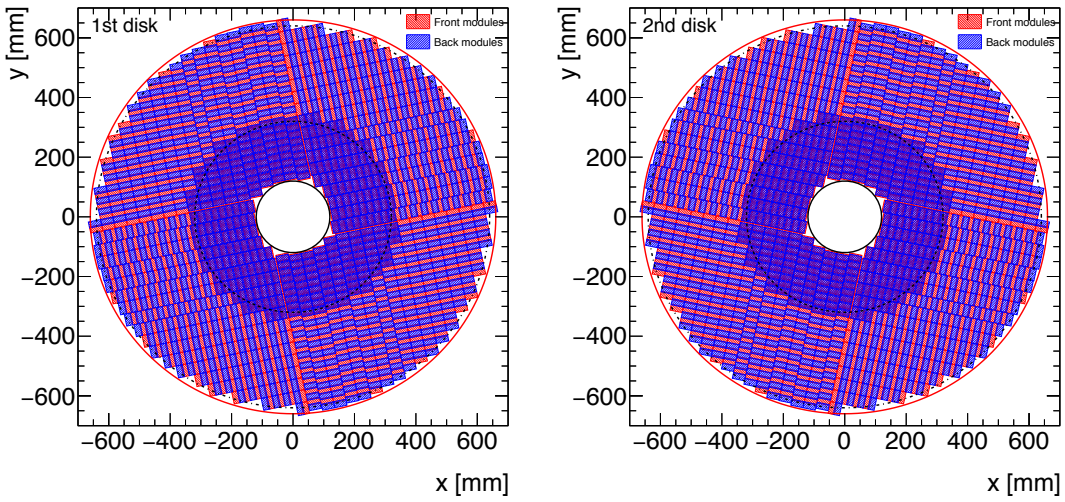

FIGURE 7.29 – Position of the front and back modules in the first (a) and second (b) layer of the HGTD.

The position of the modules on both side of the staves was chosen to maximize the performance and efficiency of the detector. In the region with 80% overlap, the back modules were not placed centered around the gap between the front modules but slightly shifted toward low

radius. This allows a reduction of the size of the gap between the start of the stave and the position of the start of the first back module, as shown in Figure 7.27, and thus decrease the inefficiency at the beginning of the staves. The starting position of the back have been determined for all possible overlaps to ensure that the back modules always overlap with the front modules by $2\,\mathrm{mm}$ on both side of the gap, this ensures no particle could go through the gap of both layers and thus crossing the layer without interacting.

Figure 7.29 represent the position of the front (in red) and back (in blue) modules within the two layers. The position of the transition between the 80% overlap region and 20% overlap region in each stave was chosen to ensure that the region $R < 320\,\mathrm{mm}$ (represented by the dotted line) had an overlap of 80%.

Due to the shift of the back modules, the transition between two different overlaps is easy to perform as shown in Figure 7.27. The position of the end of the last large (80%) overlap module (back) will always be $2\,\mathrm{mm}$ after the start of the first low (20%) overlap module (front) no matter which overlaps is considered. In that case simply changing in the periodicity of the module placement would be necessary to change the overlap.

At large radius the modules are place to maximize the coverage up to $640\,\mathrm{mm}$ (dotted line) while avoiding as much as possible to place module above $660\,\mathrm{mm}$ (red line) to keep some space between the active sensors and the electronic to allow the different connection to be performed.

New studies of the overlaps might be performed to implement a smoother transition from 80% overlap to 20% overlap. This will highly depend on the evolution of the radiation level in the HGTD region as well as on the evolution of the replacement scenario of the HGTD modules.

7.4 HGTD Performances

Using the simulation I have developed, different studies were performed to understand the behavior of the particles in the HGTD and to determine how best this detector can be used to improve the performances of the ATLAS detector. In parallel with the studies of the performance of the HGTD an optimization of the design of the detector was also performed. This section will mostly focus on my studies with electrons and muons in the HGTD.

7.4.1 Muons and Electrons in the HGTD

The first particles that were studied within the simulation of HGTD were high energy muons. Due to their high mass and long lifetime the muons will go through the entire ATLAS detector while depositing energy in their trajectories, this makes muons a good probe for geometrical effect as well as good tool to study the properties of a minimal interacting particles (MIP) in the detector. Figure 7.30 (a) show the energy deposited in the first layer of the HGTD by $45\,\mathrm{GeV}$ muons. With this spectrum it is possible to determine that the value of the MIP energy deposit in the detector is $44\,\mathrm{keV}$. The value of the MIP energy deposit is quite important to simulate the operation of the detector, the threshold the electronics used for this detector simulation is fixed at $20\,\mathrm{keV}$. This threshold will remove a large fraction of the noise in the detector while keeping most of the signal since the simulated noise is of $0.7\,\mathrm{keV}$.

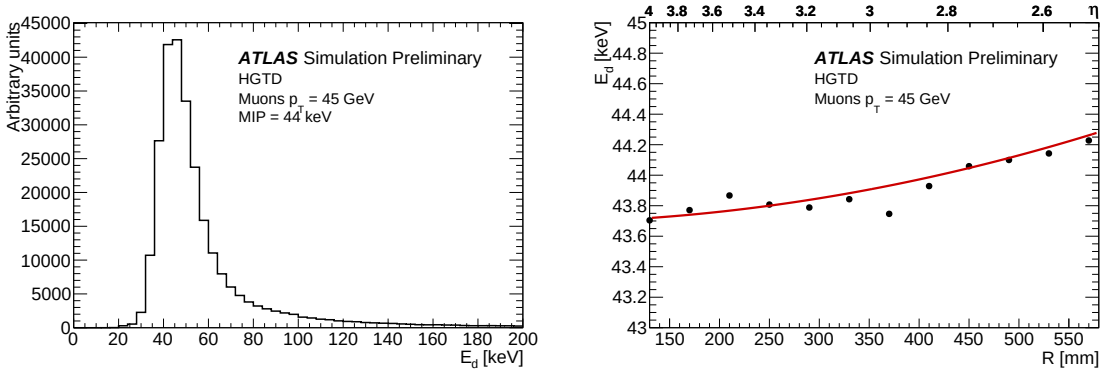

(a) (b)

FIGURE 7.30 – (a) Distribution of the energy deposited in the pads of the first layer of the HGTD by 45 GeV Muons. (b) Energy of a MIP in the HGTD as function of the radius, the red line correspond to the prediction using the variation of the amount of silicon crossed as function of the radius.

Only two criteria determine the value of the MIP energy deposition. The first one is the material used for the active region, silicon, the atomic number Z of the material being directly proportional to amount of energy loss per unit of distance for a MIP according to the "Bethe" formula[89]. The second is the thickness of the active region crossed by the particle, as a first order approximation this can be considered constant and equal to the thickness of the sensor which is 50 µm for the TDR simulation and 250 µm for the TP simulation. The total silicon thickness is 250 µm, but for an LGAD only 50 µm are active. Geant4 deposits the energy in a single hit, the noise is added based on testbeam measurements, so the absolute value of the energy deposit has no impact on the performance.

A small dependency with the radius of the sensor should also be present as at large radius the angles of the incoming particles should be larger leading to a longer path through the sensor and thus a larger energy deposit. This is shown in Figure 7.30 (b) for the first layer of the HGTD, the red line is the prediction taking into account the variation of the amount of silicon crossed as function of the incoming angle. The prediction is in good agreement with the simulation and a variation of the order of 1% can be observed between low and high radius.

Knowing the value of a MIP energy deposited in the HGTD pads, the distribution of energy deposited per hit in the HGTD can be shown using the MIP energy as a unit. The relative measurement is important to define the dynamic range for the electronics. Figure 7.31 (a) show the distribution of the energy of the most energetic hit in the last layer of the HGTD in the case of a 45 GeV electron. The dynamic range of the HGTD is between 0 and 50 MIP. This expected range should be larger than the real range, indeed since the simulation was created for a case with four layer the amount of material in the simulation is superior to the one in the current HGTD design. In simulation 4 cooling plates are used instead of 2, this decrease in material should lead to a dynamic range from 0 to 30-40 MIP.

The electronic have a dynamic range of 20 MIP, but above this range only the information on the energy will be lost. Normally the energy is used to correct the time walk effect but for hits with an energy larger than 20 MIP this is negligible, thus the limited dynamic range should not be problematic. Figure 7.31 (b) shows the distribution of the energy of the hits in the last layer of the HGTD for single 45 GeV electrons. Even if the maximum energy observed in the last layer of the HGTD is around 40 MIP, the fraction of hits with an energy larger than 10 MIP is small, so the inefficiency due to the limited dynamic range is negligible.

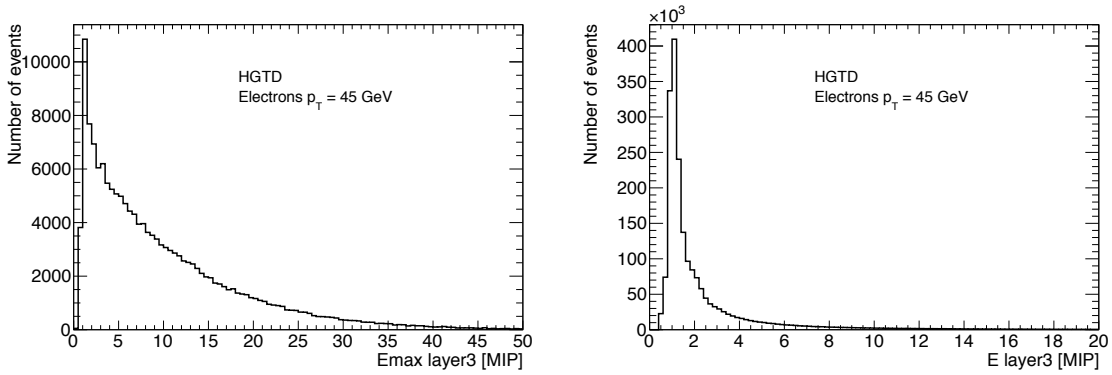

(a) (b)

FIGURE 7.31 – (a) Distribution of the energy of the most energetic hit in the last layer of the HGTD for 45 GeV electrons. The energy is presented in MIP unit. (b) Distribution of the energy of the hit in the last layer of the HGTD for 45 GeV electrons. The energy is presented in MIP units.

In Figure 7.31 (a), in addition to the main peak at 1 MIP of energy a second smaller peak is visible at an energy of 2 MIP and a third one at 3 MIP. The peaks correspond to the case when an electron (or positron) emits a photon that is converted into a electron-positron pair, if this happened in the HGTD the electron and the pair could hit the same pad causing a 3 MIP energy deposit. If only the pair coming from the converted photon hits a pad, then the energy deposited will be of 2 MIP. This demonstrates that the material inside (in the case of the 3 MIP) and before (in the case of the 2 MIP) the HGTD will tend to induce showering for the electrons. Further studies showed that 10% of the hits were part of the 2 MIP peak and 1% were part of the 3 MIP peak.

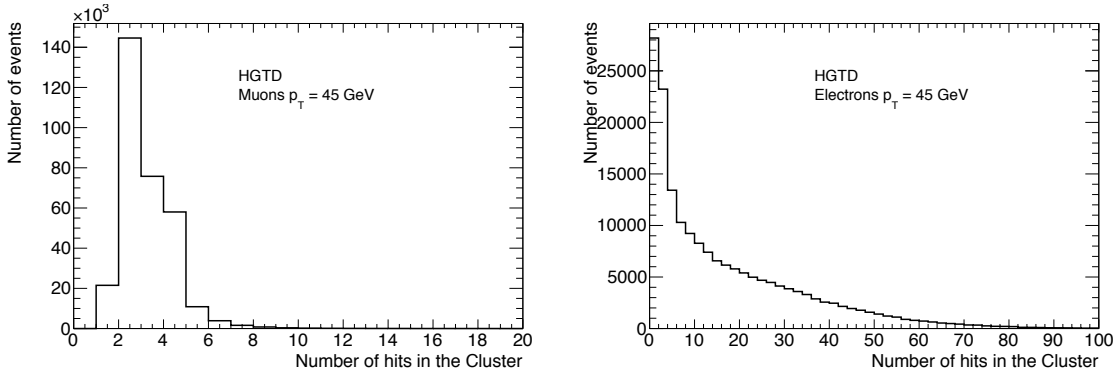

(a) (b)

FIGURE 7.32 – Number of hits associated with a muon (a) or electron (b) cluster. The cluster are define as all the hits within 30 mm of the most energetic hit.

Different particles will leads to a different number of hits in the HGTD as shown in Figure 7.32 for muons and electrons. For muons the number of hits goes in most of the case from 1 to 4. This is in good agreement with the expectation that muons should not create many secondaries in the detector and only the primary muons will interact. This lead to the muons interacting at most with one pad per layer of silicon (4 layers of silicon in total). Event with additional hit corresponds to the emission of a photon by the muon that is converted to an electron/positron pair.

Figure 7.32 (b) shows the number of hits in the HGTD for electrons. Electrons can emit photons that can then be converted to pair electrons/positrons, this lead to a larger number of hits in the electrons cluster than for the muons. This number of hit per cluster is still relatively low, reconstructing a "cluster" for the electrons is impossible in the HGTD alone.

7.4.2 Timing association

To study the association of times to tracks reconstructed with the ITk, single-pion samples ($\langle\mu\rangle = 0$, generated with a flat distribution in η and ϕ) and single-muon samples ($\langle\mu\rangle = 0$, generated with a flat distribution in θ and ϕ) were used.

In order to associate the proper timing information from the HGTD to the correct ITk track, an extrapolation is performed to determine which hits in the HGTD should be associated with the tracks. The performance of this extrapolation is directly linked to the performance of the ITk, but might also be degraded by the interaction of the particles with the materials that would create secondaries and modify the trajectories of the particles. This extrapolation uses the momentum and position of the particle associated to the track (track parameters) as well as a hypothesis on the particle nature and a map of the magnetic field in the ATLAS detector to compute the extrapolated position of the intersection of the trajectory of the particle with a given surface. 8 different surfaces are used for the HGTD, corresponding to the 4 layers of the HGTD on both sides of the ATLAS detector. To mitigate the effect of the interactions happening in the ITk, an extrapolation based on the track parameters at the last point in the tracker is used instead of one based on the track parameter at the perigee of the track. Using this extrapolation method lead to an improvement in the time association efficiency as shown in Figure 7.33 (a).

In a first approach, it is quite easy to associate hits to the tracks once the extrapolation has been performed. In each layer one could search for the closest hit to the position of the extrapolation and associate it to the track. This would work if the tracks left a hit in each layer of the HGTD, unfortunately this is not the case a track will in average only leave hits in 3 layers for a radius below $320\,\mathrm{mm}$ and 2 layers for a radius above $320\,\mathrm{mm}$. This method would lead in the layers with no hits coming from the tracks to incorrect hits being associated to the track. In a similar manner the extrapolation can fail and return an incorrect position (often because of interaction in material in front of the HGTD), this would also lead to incorrect hit being associated with the track. To avoid these misassociation only the hits in a window of $\Delta r = 1.4\,\mathrm{mm}$ around the track extrapolation position are considered.

This Δr window has been chosen to be slightly larger than the size of a pad, meaning that only the pad in which the particle is extrapolated and the adjacent one will be considered for association. The larger the window, the higher the efficiency of associating a time to the track but a larger window will also lead to pile-up hits being associated with the track, thus causing a decrease in purity. The Δr window was optimized using the evolution of the time association efficiency as function of the Δr window for single pions as shown in Figure 7.33, for $\Delta r > 1\,\mathrm{mm}$ a first plateau is reach for high p_T tracks so $\Delta r = 1.4\,\mathrm{mm}$ was chosen to be sure that for any tracks the efficiency will be in the plateau.

For a given Δr the efficiency will slightly depend on the p_T of the tracks. Figure 7.33 (b) shows the evolution of the time association efficiency as function of the Δr window on a much wider range. For high p_T tracks the maximum efficiency is reach for a window of a few centimeters so that for the tracks if they created hits in the HGTD they are at most $5\,\mathrm{cm}$ away from the extrapolation point. In the case of low p_T track is only reached for a window of $20\,\mathrm{cm}$, this is due to the fact that the angle of the multiple scattering that the pions can undergo is inversely proportional to the momentum of the track.

While the geometrical acceptance is optimized to compensate inactive zones in one layer with an active zone in another layer, the difference between track extrapolation and hit in different layers is strongly correlated. For example, the correlation of the distance between the hit and the extrapolated position in the first and last layer if of more than 70%. While the interaction between the particles and the material of the HGTD can cause some misassociation between track and the hits this effect is subdominant compared to the interaction between the particles and the material in front of the HGTD and after the last sensitive layer of the ITk.

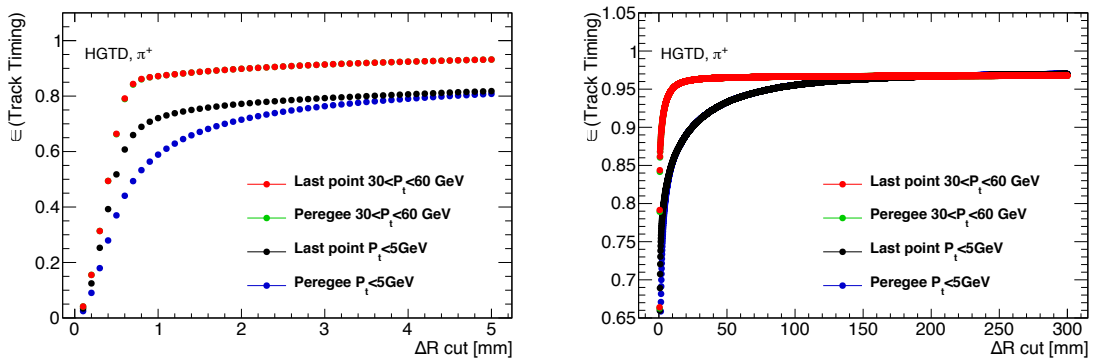

FIGURE 7.33 – Efficiencies for associating time to tracks with at least one pad in the HGTD as function of the Δr window used.

The single muons were used to test the performance of the tracks time association as function of the number of hits associated. Only the primary track, define as the one coming from primary particle with the largest reconstructed p_T, are used for this study. In Figure 7.34(a) the difference between the time of the reconstructed tracks and the truth time of the interaction is shown for different number of hits. The distributions are Gaussian with a resolution compatible with the one shown in Figure 7.13. As expected the resolution of the tracks evolves as one over the square root of the number of hits associated with the tracks.

The same study was also performed for single pions. Figure 7.34(b) shows the difference between the reconstructed time of the track and the expected one. The Gaussian core follows the expected scaling with the number of hits as for the muons. Non Gaussian tails that were not present in the muons case appear here, caused by both secondaries and poorly reconstructed time of flight at low p_T since no sagitta correction was applied. The tails are slightly asymmetric since late secondaries will tend to increase the reconstructed time.

The time association efficiency is shown Figure 7.34(c) as function of the reconstructed transverse momentum. If, instead of selecting only primary tracks the reconstructed track with the highest pT is used, the efficiency to reconstruct the correct time for the high pT pions is unchanged. Tracks with $|\eta| < 2.4$ or $|\eta| > 4.0$ are not considered in order to avoid border effects.

At the highest transverse momentum the efficiency is 90% and at the lowest momentum the efficiency is 70%. The second set of points (in red) in Figure 7.34(c) is the efficiency to associate a time within $2\sigma_{t_{reco}}$ of expected truth time. The ratio between the two efficiencies is of the order of 95%, as shown in Figure 7.34 (a) and (b) and is mostly dominated by the tail of the Gaussian distribution above 2σ.

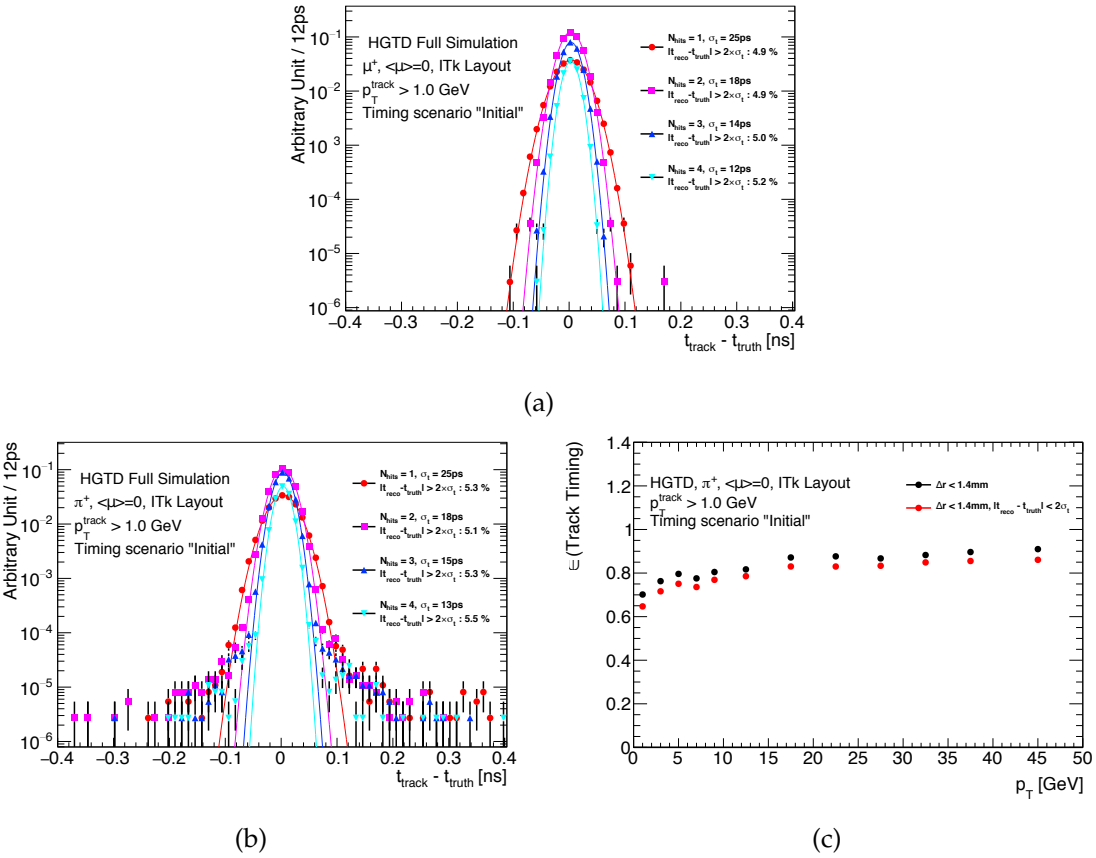

FIGURE 7.34 – The reconstructed timing resolution and efficiency are shown for different samples at $\langle\mu\rangle = 0$.

7.4.3 HGTD Track time resolution

After the hit association to the tracks, the timing resolution is studied. Single muons with a $p_{\mathrm{T}} > 45\,\mathrm{GeV}$ have been used. It is necessary to evaluate how the number of hits per track vary as function of the x and y position. Since the fluctuation of the times of the pads in each layer can be considered independent the timing resolution of the tracks will only depend on the timing resolution of the pad and the number of hits associated to a track :

$$(\sigma_T)_{track} = \frac{(\sigma_t)_{hit}}{\sqrt{N_{hits}}} \tag{7.1}$$

where σ_t correspond to the timing resolution of the pads and $\sqrt{N_{hits}}$ to the number of hits associated to the tracks. This means that the larger the number of signal hits associated to a track is the better the timing resolution is. Figure 7.35 shows the average number of hits associated per muons track in the transverse plane. Two region can be identified, an inner region ($R < 320\,\mathrm{mm}$) with a larger average number of hits per track (of the order of 3) and an outer region ($R > 320\,\mathrm{mm}$) with a smaller average number of hit per track (of the order of 2). This is due to a change of overlap between the sensor within the same layer from 80% in the inner region to 20% in the outer one, this allows a partial compensation of the faster increase of the timing resolution in the inner region due to the larger dose received. Different blue lines corresponding to regions with only one hit associated with the track can be seen, the line appear at the position of the inter-stave dead zones of the first and second layer. When two of these lines intersect a region with no hit (in pink) can be seen as the particles would at these

regions go through the detector without crossing any active region.

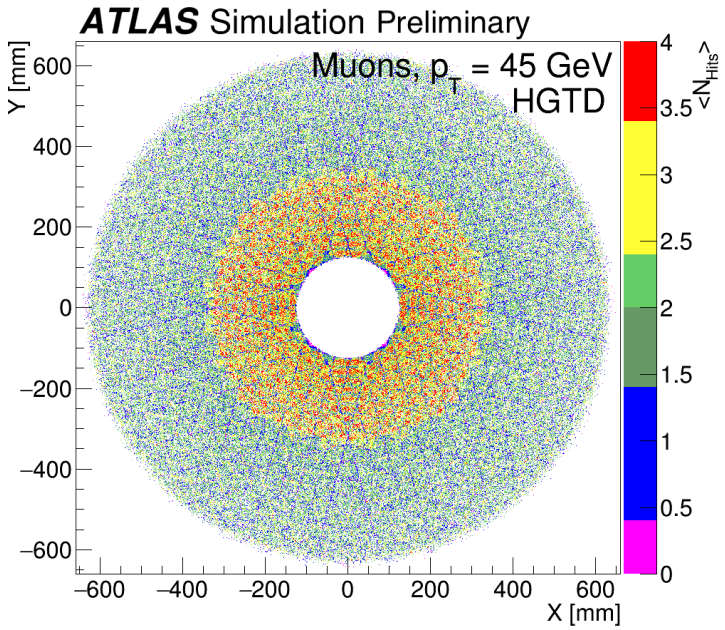

FIGURE 7.35 – The number of hits as function of the position in the HGTD is shown for the baseline layout The overlap is 80% at $R < 320\,\mathrm{mm}$ and 20% at larger radii.

The results are summarized in Table 7.4, 79% of the extrapolated muon tracks have at least two matched hits in the HGTD. For at most 2.4% of the muons, no hits are registered within the acceptance window around extrapolated position. The effect of uninstrumented zones and inactive areas on the sensor such as the guard ring and the inter-pad dead-zones are taken into account.

	$\boldsymbol{R} < 320\,\mathrm{mm}$ $(\lvert\eta\rvert > 3.1)$	$\boldsymbol{R} > 320\,\mathrm{mm}$ $(\lvert\eta\rvert < 3.1)$
$N_{\mathrm{hits}} \geq 2$	88%	72%
$N_{\mathrm{hits}} = 0$	1.6%	2.8%
$\langle N_{\mathrm{hits}} \rangle$	2.7	1.9

TABLE 7.4 – The percentage of tracks with at least two hits, the percentage of tracks escaping undetected and the average number of hits for muons with a p_{T} of $45\,\mathrm{GeV}$ are shown for the baseline detector layout. The values include the effect of non-instrumented zones, inter-pad dead-zones and guard ring as well as the track-matching efficiency.

Figure 7.36 (b) shows the resolution of the muon tracks as function of the radius of their extrapolation in the first layer of the HGTD. This plot was obtain by drawing for each bin the distribution of the difference between the reconstructed time of the track and the true time of the track, the RMS of these gaussian distribution were then taken as the timing resolution of the tracks. This can be compared to the average number of hits associated per tracks shown in Figure 7.36 (a), the region with the smaller timing resolution corresponds to the region with a larger number of hits per track. The number of hits that can be associated per track (and by extension the number of layer) will define the performance of the detector.

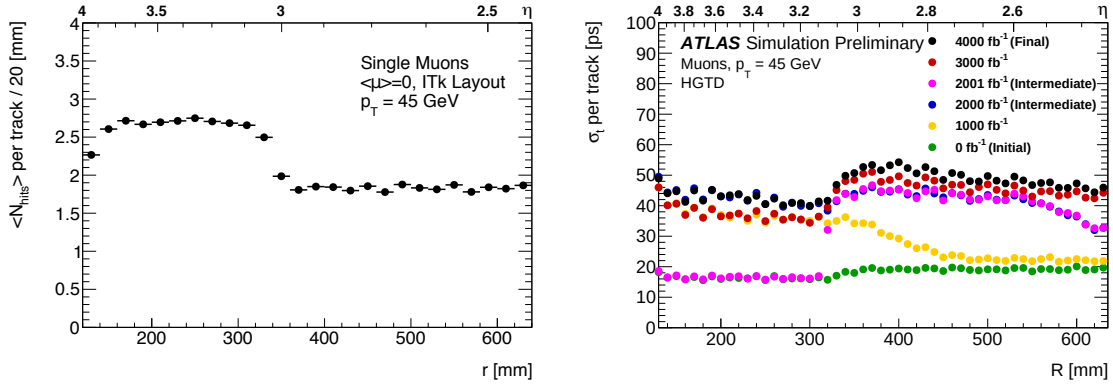

(a) (b)

FIGURE 7.36 – (a) The average hit multiplicity as function of the radius (and pseudo-rapidity) is shown for the baseline HGTD layout of 80/20% overlap below/above 320 mm. (b) Timing resolution of simulated muons tracks in the HGTD as function of the radius for different timing scenarios.

7.4.4 HGTD Time calibration

To operate a timing detector a precise calibration of the different channel is necessary. The timing information is obtained via a master clock that is then distributed through the flex to the ASICs. Any temporal or spatial variation of the times distributed from the clock would result in a decrease of the timing performance of the detector. Since the LGAD sensors have a timing resolution of 20 ps the contribution from the electronic and the clock to the time resolution should be kept smaller, for example for the clock it should be kept lower than 10 ps over the entire detector. Different effect can contribute to the timing resolution of the clock :

- The detector geometry and alignment.
- The time of flight of the particle to the detector.
- The propagation of the time to the electronic and to the channels.
- The noise in the cables.
- The variation of temperature in the detector.

To perform this calibration a solution would be to use the distribution of the times of all the hits in each pad. The distributions for pads at three different radii are shown in Figure 7.37. These distribution shows a gaussian core derived from the time dispersion of the LHC collision ($\sim$250 ps) with a tail corresponding to either low momentum particles trapped in the magnetic field, particle with long lifetime or back scattering particles produced through the interaction of particles with the material after the HGTD. With at least 10000 hits per pad it is possible to fit this gaussian core to determine with a precision of a few ps the reconstructed time of the interaction for that pad. With fewer events, as shown in Figure 7.37 (c), the fit is no longer reliable. This would translate into 10^5 (10^6) events to be recorded at inner (larger) radius. The integration time to reach a sufficient statistic will then depend on the data taking rate, assuming a 1 MHz rate 22 s would be needed to reach the target on the entire range of the detector (0.45 s at low radius). Depending on the effect that want to be calibrated all the pads connected to the same ASIC could be combined together to reduce the integration time need by a factor 225 (down to 100 ms). After integration, the reference time of the ASIC can be extracted. By subtraction this reference time to the times of the measured hits all the contribution to the timing resolution of the clock with a period larger than the integration period are removed.

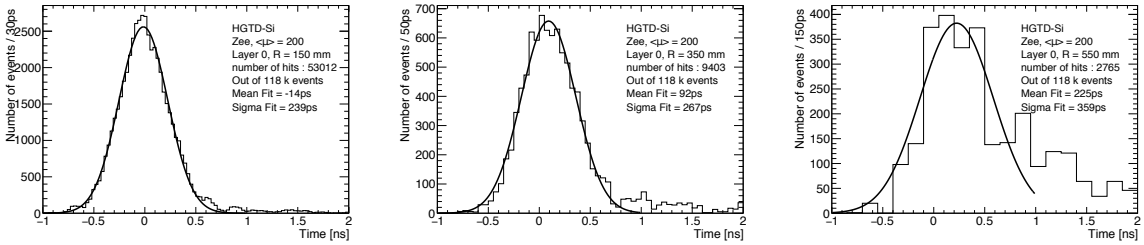

(a) (b) (c)

FIGURE 7.37 – Time of hits distribution at (a) $150\,\mathrm{mm}$, (b) $350\,\mathrm{mm}$ and (c) $550\,\mathrm{mm}$ using a Z to ee sample of 118 000 events. The hits or 9 cells are used to increase the statistics. The small bias of the t0 comes from the time reconstruction method used.

More advance studies are currently in progress to try to simulate all the different effects contributing clock time resolution to identify if a more performant algorithm could be developed for the calibration of the time.

7.4.5 HGTD Lepton Performance

In order to understand the performances of the detector, studies of the effect of the HGTD on the reconstruction of different object in the ATLAS detector where performed. In this section, studies of how the electron isolation efficiency is improved by the HGTD are presented based on the full simulation of the HGTD in Geant4. For leptons, it is important to know if they originate from the hard scatter event or if they are the result of a decay, a conversion or a fake. The lepton isolation is a key ingredient to this identification. A lepton is defined as isolated if there is no other track with a $p_{\mathrm{T}} > 1\,\mathrm{GeV}$ in a region of $\Delta R < 0.2$ around the main lepton track. The hard scatter electrons are in general well isolated while the others are not.

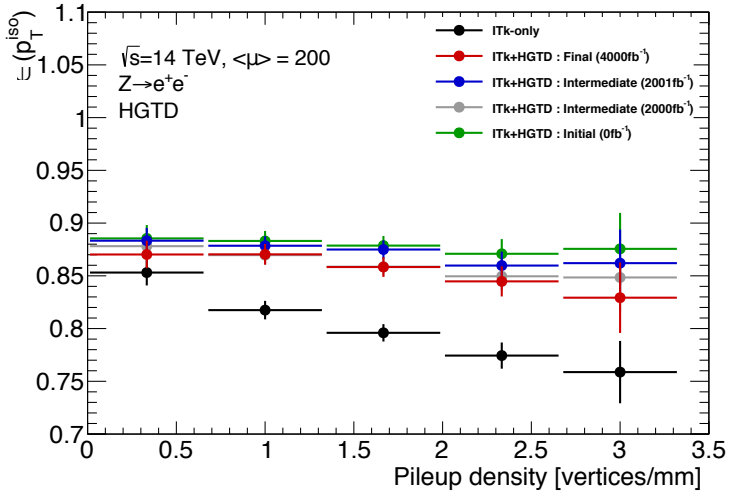

FIGURE 7.38 – Selection efficiency for the electron isolation criteria as a function of the pileup density using the ITk and ITk + HGTD for different timing resolutions.

The HGTD is used to assign a time to leptons in the forward region. This information can be exploited to reject tracks which come from other interactions but are spatially close to the energy deposits in the calorimeter and/or the track associated to the lepton. With this rejection, the isolation of the electrons can remain high even in high pile-up environment.

Figure 7.38 show the efficiency of tagging a hard scatter electrons as isolated for different timing scenarios. This efficiency was computed using Z boson production followed by a decay to a pair of electrons. Only events with an electron of more than $20\,\mathrm{GeV}$ passing the Forward Medium criteria [58] in the acceptance of the HGTD are selected, keeping only those matched with a truth electron with a $p_{\mathrm{T}} > 20\,\mathrm{GeV}$ in a cone of $\Delta R < 0.2$. The electron track is defined as the track closest to the electron cluster having a ratio of transverse track momentum to transverse cluster energy greater than 0.1. The correct electron track is selected in 95% of the cases. All the other tracks with a $p_{\mathrm{T}} > 1\,\mathrm{GeV}$ in a region of $\Delta R < 0.2$ around the electron track are also associated to the electron.

The HGTD is then used to associate a time to each track. The tracks are extrapolated to the HGTD surfaces using the last measured point in the ITk. The closest HGTD hit in a window of $3.5\,\mathrm{mm}$ between the extrapolated position and the hit position is associated to the track. The window is larger for electrons than for pions and muons to account for Bremsstrahlung in the material between the last ITk measurement and the first sensitive layer of the HGTD. The times of all the hits associated to the track are then corrected to take into account the time of flight and averaged together to compute the time of the tracks. The time of the non-electron tracks are then compare with the time of electron one. If the difference between these tracks is more than twice the quadratic sum of the timing resolution of both tracks, the track is discarded. Once this rejection have taken place the efficiency of the Lepton Isolation is computed as the fraction of electrons with only one tracks divided by the number of electrons with at least one track.

The two main effects responsible for the loss of the efficiency of the Lepton Isolation are the pile-up contamination and the early emission of a photon by the electrons. As shown on Figure 7.38 without the HGTD the efficiency decrease sharply when the pile-up vertex density increase, indeed the higher this density is the higher is the probability of a tracks coming for pile-up vertices to end up close to the electrons. With the use of the HGTD it is possible to use the timing information to reject some of these tracks and thus making the dependency on the local pileup density smaller.

In addition to this study, the rejection of non-isolated track should have also been studied. Unfortunately no simulated dataset were available to perform such a study. To ensure the coherence of the presented result the type of particle corresponding to the track removed by the HGTD was studied.

When an electron emits an early photon its conversion can create additional tracks close to the electrons, this effect cannot be mitigated at the detector level and create an upper limit on the efficiency achievable for the lepton isolation. Figure 7.39, show the different type of particles contributing to the lepton isolation inefficiency as function of the local pile up density for 3 different versions of the ITk. This was obtained by using the information from the truth particle associated with the tracks close to the electron tracks when one was available.

Four types of contamination of the electrons are presented, Leptonic which mostly corresponds to electrons created by conversion of a photon emitted by the primary electrons, Hadronic which correspond mostly to track coming from pile-up vertices, Leptonic+Hadronic in which there are both contamination from electrons and hadrons and unknown which correspond to track with no truth particle associated.

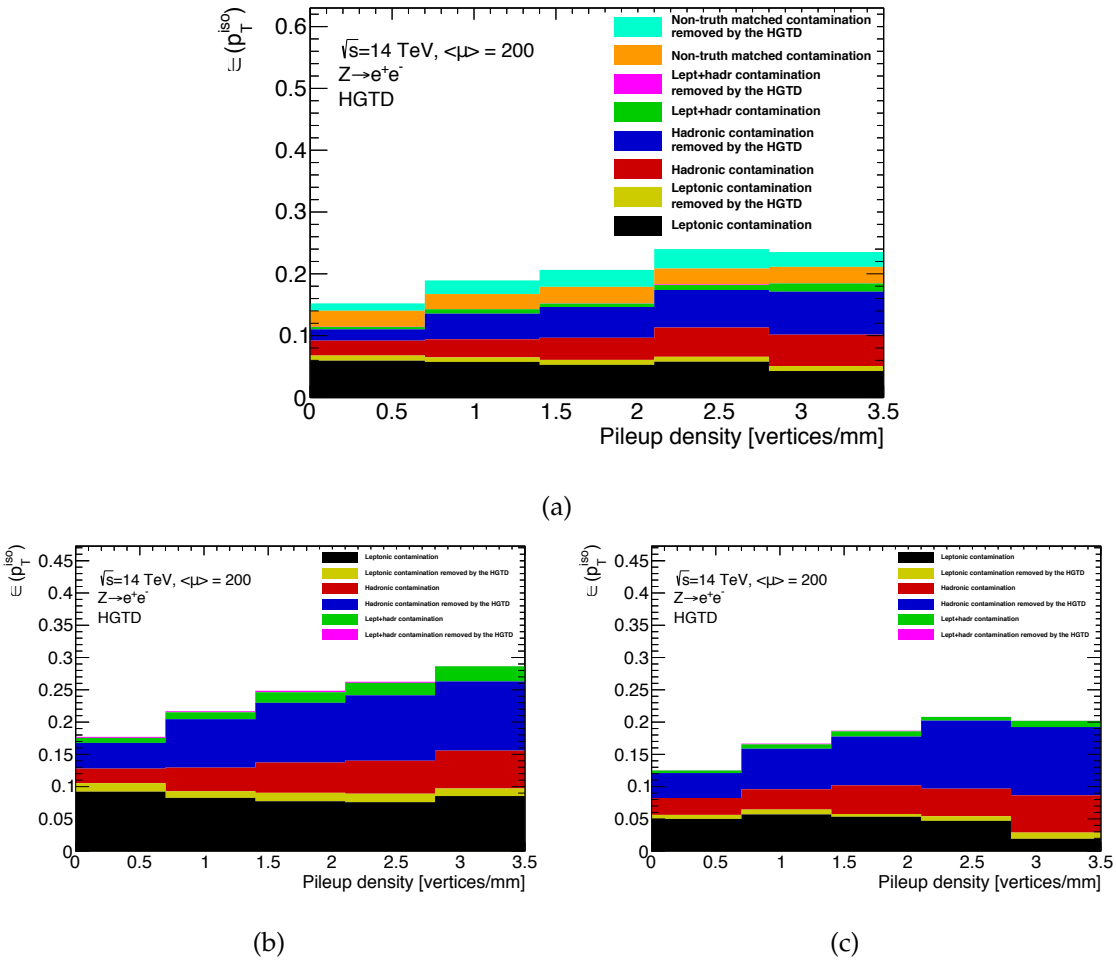

FIGURE 7.39 – Fraction of electrons lost because of the different type of contamination. Figure (a) correspond to ITk step 3, Figure (b) correspond to ITk step 2.2 and Figure (c) correspond to ITk step 1.6.

The black fraction corresponds to Leptonic contamination that is not remove by the HGTD. The increase of this fraction between ITk 1.6 (c) and ITk 2.2 (b) is consistent with the increase of material in the simulation of the ITk. For ITk 2.2 at most a Lepton Isolation efficiency if 90% can be achieved. The blue and red represent respectively the hadronic contamination removed and not removed by the HGTD, more than 60% of the hadronic contamination can be removed by the HGTD improving greatly the efficiency.

Only 10% of leptonic contamination is removed by the HGTD, most of this contamination should originate from early showering of the electrons and should thus be in time with the electron. This appears to be consistent with the efficiency of the timing association being of the order of 90%. This also confirms that mostly out of time tracks are rejected, the addition of the time selection of the track used for the isolation should only affect the isolated electron selection efficiency without decreasing the rejection of non-isolated electrons.

7.4.6 Other performance studies

The simulation presented in Section 7.2 and the detector level performances studies shown in Section 7.4 were reused by other groups for performance studies.

This included all the work on jets that was presented in Section 4.5.1. This study did not use the full simulation of the HGTD but instead preferred, for simplicity sakes, to use a full simulation of the ATLAS detector without the HGTD. The timing information was then implemented by smearing the times of the tracks with a gaussian distribution with a width corresponding to the resolutions shown in Figure 7.36.

Finally, the full simulation was used in the study of the performances of the HGTD as a luminometer shown in section 4.5.3.

Chapitre 8

Conclusion

In this thesis I presented three different topics of research.

I prepared the search of pair produced colored particles in the ATLAS detector using data recorded in 2016, 2017 and 2018. No significant difference were observed between MC sgluon sample produced using LO and NLO after applying the analysis requirements. To determine how to best pair the jets in the final state to reconstruct the two pair produced colored resonances, I studied the topology of pair produced stops decaying via RPV. At low mass, the stop tends to decay into two close-by jets. This proximity can be used to efficiently reconstructed the resonances. At higher mass, the distance between the jets tend to be larger. This leads to large inefficiency in the reconstruction at large mass. I developed a new pairing maximizing the distance between the jets belonging to the same pair. For each of the pairing algorithm I developed a data based background estimation. For the low mass case, an ABCD matrix is used to estimate the background while at larger mass a fit of the background distribution provides a robust estimate of the background. I optimized the requirement used for the ABCD matrix with a data based method as well as the one for the fit. With the analysis stops with a mass up to $600\,\mathrm{GeV}$ can be probed, extending the mass range explored by $150\,\mathrm{GeV}$.

The extension of this analysis to final states with 2 b-tags and even 4b-tags will need to be performed in the future for both pairing methods. For these channels larger masses can be probed due to the lower background but the estimation of the background is more complicated. In the future, the increase of the luminosity at the HL-LHC will allow us to probe larger mass (up to $850\,\mathrm{GeV}$) for the stop but tighter trigger threshold will be used.

I studied the prospects for the Higgs coupling extraction at the HL-LHC using SFitter. The studies were performed using both the Delta and EFT framework and were based on expected uncertainty on the signal strength. An improvement of the uncertainty on the EFT by a factor of the order of two with respect to the Run 1 + Run 2 precision has been shown to be achievable.

The study was performed without kinematic distributions, limiting the number of Wilson coefficients that can be constrained. As certain Wilson coefficients are momentum dependent, the currently estimated precision is a lower bound on what can be achieved at the HL-LHC.

I have contributed to the optimization of the HGTD. To understand how a timing detector can improve the performance of the ATLAS detector, a study of the beam spot at the HL-LHC was performed. I developed the simulation of the readout geometry of the detector and developed the timing simulation of the sensor plus electronics system based on testbeam data and specialized sensor simulation studies (weightfield). This simulation was used by myself as a baseline to study the design and the performance of the detector. I optimized the layout of the detector, maximizing its efficiency and performance. I studied the geometrical efficiency, the timing resolution per track, the efficiency of associating correct times to the tracks. These studies showed that the time association efficiency is limited by the amount of materiel between the

ITk and HGTD due to the effect of multiple scattering. Finally, I determined the improvement that timing information can bring to the isolation of forward electrons. An improvement of the lepton isolation efficiency by 10% was observed.

As the design of the HGTD becomes more detailed, the implementation of the simulation will also need to evolve. A more precise version of the geometrical simulation has been developed. The implementation of more sophisticated algorithms for the association of time to the objects reconstructed will also be necessary. The current algorithm used from this association is cut based, tests of more advanced χ^2 based algorithm are ongoing. Ultimately the performance of this detector will be limited by the amount of material between the HGTD and the tracker.

CMS will also install a MIP timing detector for the HL-LHC. It will be composed of a single layer in the barrel using crystal tiles and discs in the forward region using LGAD. The limited number of layer might result in a lower efficiency and time resolution but their full coverage will provide timing information for all the reconstructed object.

On a longer time scale, timing detector will be an important ingredient for future detectors. Timing information can help with the object reconstruction and the combination of the information of the different sub-detectors. The 5D particle flow of the HGTD-SiW studied in simulation gives a first idea on the power of the approach.

Annexe A

The High Granularity timing detector with tungsten absorbers

Along with the development of the initial design of the HGTD an option using tungsten absorber was proposed. This design, called HGTD-SiW consisted of four layers of silicon interleaved with three layers of tungsten, each corresponding to a radiation length of 1 X_0. These tungsten absorbers would have been installed in the $|\eta|$ region between 2.4 to 3.2. The initial purpose of this design was to reach good timing resolution if a good enough gain could not be achieved using LGAD sensors. In that case, the showering induce by the absorber would have created secondaries that would increase the energy deposit in the pads resulting in a larger signal and thus a better timing resolution. Additionally, the showering of the primary particles in the detector could have been used for particle identification and would have resulted in more than 4 hits being associated to each particle resulting in extremely good timing resolution. This design has been evaluated in terms of performance but was eventually dropped because of moderate performance improvement but strong constraints on the detector requirement (radiation levels, space needed, more complex electronics, ...).

Most of the component use in simulation of this option are identical to the one used in the TP version, the main difference being the $3 \times 3.5\,\mathrm{mm}$ of tungsten. This extra material bring the thickness of the detector from $42.8\,\mathrm{mm}$ to $53.3\,\mathrm{mm}$. This option was dropped before the decision of using 2 layers with modules on both side of the cooling plate, as a consequence all the Figures that will be presented in the next paragraph have been created using a simulation of the HGTD with 4 layers and no module overlap.

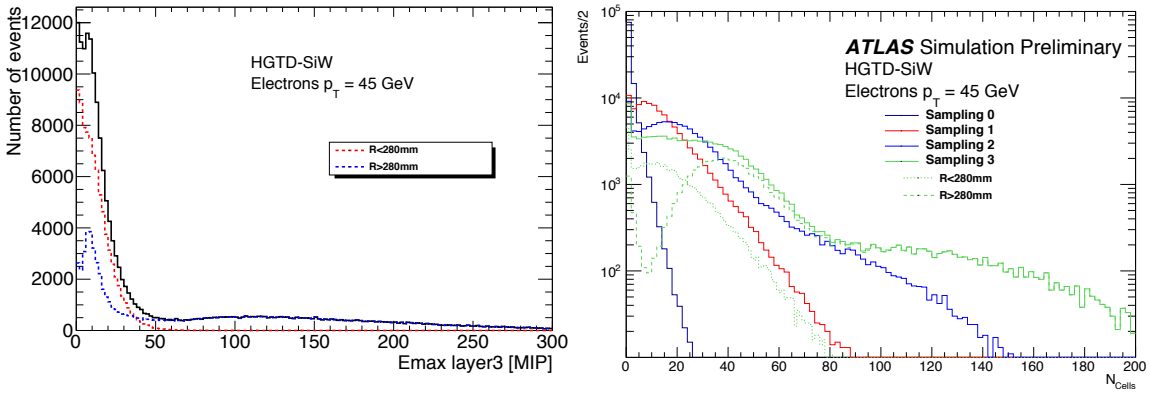

(a) (b)

FIGURE A.1 – (a) Distribution of the maximum energy in MIP units deposited in a pad in the last layer of the HGTD-SiW. (b) Distribution of the number of pads hit for the different layers of the HGTD-SiW.

The presence of tungsten in the detector will cause some showering to start in the HGTD, this showering can provide some additional gain for the detector and allow the use of clustering algorithm in the HGTD. Figure A.1 show the maximum energy deposited in layer 3 by electrons as well as the number of hits in the different layer of the HGTD. The two Figures are to be compared with the one presented in Section 7.4.1. The energy distribution shown in Figure A.1 (a) can be separated into 2 distributions, one for the electrons with $R > 280\,\mathrm{mm}$ which corresponds to the electrons going through the tungsten absorber and one for the electrons with $R < 280\,\mathrm{mm}$. With no tungsten the most probable is 1 MIP and the range goes from 0 to 50 MIPs while in the case of tungsten absorber the peak is at 10 MIPs and the range goes from 0 to 300 MIPs. This shows that the effect of the tungsten absorbers is equivalent to an additional gain of 10.

Figure A.1 (b) shows the distribution of the numbers of hits in each layer of the HGTD-SiW for single electrons of $45\,\mathrm{GeV}$. For the last layer the distribution is separated into two, one corresponding to the no tungsten region and one corresponding to the absorber region. The number of hits per layers increase with the number of layers due to the development of the electromagnetic shower in the HGTD, this showering could be exploited to improve greatly the timing resolution of the HGTD, instead of associating 4 hits per tracks more could be associated because of the shower. Since the timing resolution in proportional to the $\frac{1}{\sqrt{N_{hits}}}$, the more hit associated to a single track the more precise the timing measurement.

A similar effect can be observed for jets. For hadronic particles, the interaction length λ (9.95 cm) is 28 time smaller than the radiation length X_0 (0.35 cm) for electromagnetic particles. This would lead to a smaller shower development but would still result in an increase in the number of hits and a reduction of the timing resolution by a factor 2. Unfortunately this showering would occur both for the primary particles and the pile-up one, resulting in an increase of the radiation dose received by the sensor resulting in a faster decrease of performance.

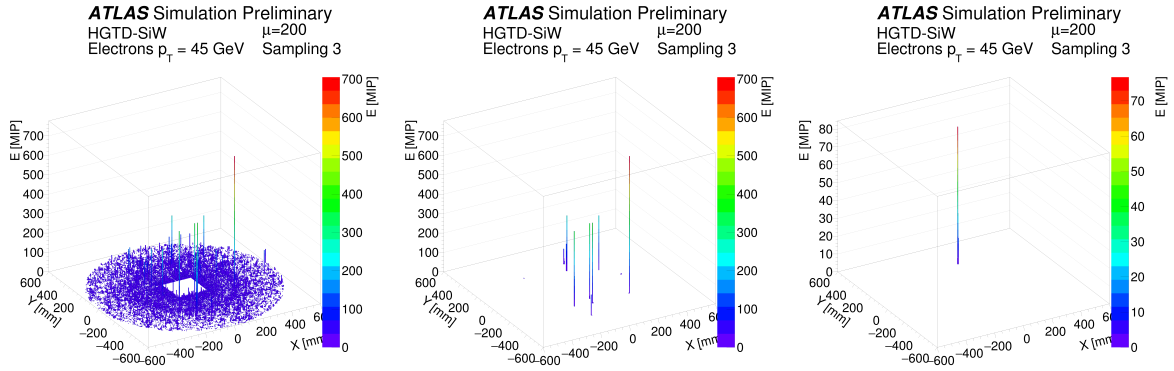

(a) (b) (c)

FIGURE A.2 – (a) The energy deposited in the HGTD-SiW sampling 3 is shown for an ATLAS simulation of an electron with a transverse momentum of $45\,\mathrm{GeV}$ and 200 events of pile-up. (b) The energy deposited in the HGTD-SiW sampling 3 is shown for an ATLAS simulation of an electron with a transverse momentum of $45\,\mathrm{GeV}$ and 200 events of pile-up for the 10 most energetic clusters in an intermediate step of the 5 dimensional electron reconstruction. (c) The energy deposited in the HGTD-SiW sampling 3 is shown for an ATLAS simulation of an electron with a transverse momentum of $45\,\mathrm{GeV}$ and 200 events of pile-up after the final step of the 5D (time, energy, three-dimensional positions of energy deposit) electron reconstruction.

The shower development in the HGTD was used to create an algorithm to reconstruct electrons using only the HGTD and no external information. The different steps of this algorithm are illustrated in Figure A.2. First the Figure A.2 (a) shows the energy in all the pads of the last layer of the HGTD. To determine which of these hits correspond to the electron all hits are clustered into $15\,\mathrm{mm}$ circular cluster in the last layer, this cluster size was chosen to correspond to 3 times the average radius of a cluster and 1.5 time the Moliére radius of tungsten. A cluster is computed for every single hits in the last layer, overlapping cluster are then removed keeping only the most energetic one. Finally, out of the remaining cluster only the ten most energetic are considered as electrons candidates, the larger the number of candidate the more efficient the algorithm becomes but this also lead to an increase of the fake rate. The cluster remaining after this selection are shown in Figure A.2 (b). To determine if the cluster was created by electron or by pile up an object called tracklet is used, the tracklet represents small track computed inside the HGTD. Since the electron showering should start in the HGTD, a single hit can be identified as the start of the shower in the first layer, tracklet are then computed as all the hits in a straight line between the hits in the last layer and the start of the cluster in the first layer, a time is associated to each tracklet by averaging the time of all the hits associated with it. All the tracklet with a time more than 2σ away from the time of the cluster are rejected. A cluster is identified as coming from an electron if it has more than 5 tracklets, in average more than 2 hits per tracklet and more than 60% of the total energy of the cluster inside the tracklets. Using this method 80% of the electrons are correctly reconstructed and only 5% of pile up clusters are misidentified. Figure A.2 (c) show the remaining electron after the application of the cuts.

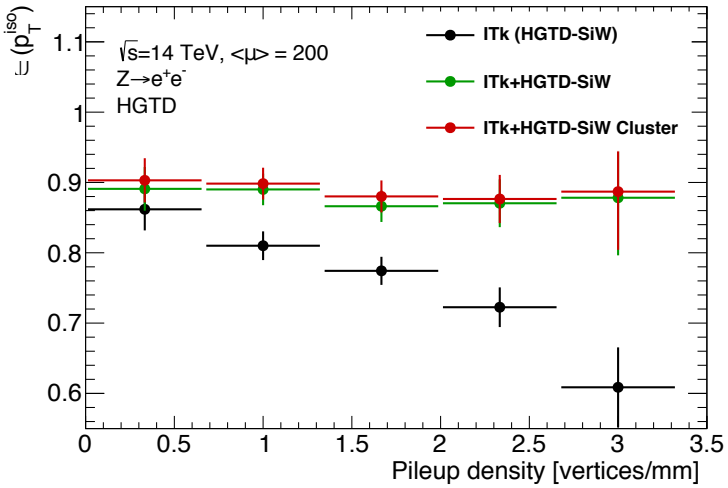

FIGURE A.3 – Selection efficiency for the electron isolation criteria as a function of the pileup density using the ITk and ITk + HGTD-SiW with and without the clustering algorithm for the Initial Timing scenario.

Once these clusters have been created, they can be used to improve the performance of the detector. For example, it is possible to compute the time of the electrons with a precision of the order of $5\,\mathrm{ps}$ by averaging the times of all the tracklet within the cluster. This can improve the lepton Isolation efficiency, indeed in the method presented in section 7.4.5 the time of reference is the time of the lepton track with a timing resolution of the order of $28\,\mathrm{ps}$ so with a 2σ cut taking into account the timing resolution of the track and of the Lepton Track we can reject all the track with a time distant of more than $79\,\mathrm{ps}$ ($2 \times \sqrt{28^2 + 28^2}$) from the lepton track time. In the case of the cluster, since the resolution on the electrons time is good we can reject all the track with a time distant of more than $57\,\mathrm{ps}$ ($2 \times \sqrt{28^2 + 5^2}$) from the cluster time. The Lepton Isolation efficiency is shown in Figure A.3 for the Initial Timing scenario. This method improves

the lepton isolation efficiency by only 1%. Indeed, this method can improve the reconstruction of the time of the electrons but the time of the extra tracks close to the electrons is still computed using one to four points limiting the impact of the improved reconstruction. Additionally, it was also shown that after a timing resolution reached $40\,\mathrm{ps}$ reducing it further does not improve much the lepton isolation.

Small improvement were also observed in studies with jets. At the time due to the complexity of creating, installing and operating the HGTD with the addition of tungsten absorber and the small improvement in terms of performances it was decided to abandon this option.

Annexe B

Résumé

B.1 Contexte phénoménologique

B.1.1 Modèle Standard de la physique des particules

Le Modèle Standard (MS) de la physique des particules est un modèle qui a été développé durant la seconde moitié du 20ème siècle. Il s'agit d'une théorie quantique des champs qui décrit les particules élémentaires et leurs interactions. Ce dernier a été précisément testé durant les cinquante dernières d'années et a réussi expliquer avec succès les données obtenues expérimentalement. La dernière particule à avoir été prédite par ce modèle est le Boson de Higgs. Il fut observé au LHC par les expériences ATLAS et CMS en 2012, soit plus ou moins 55 ans après sa prédiction. Le MS décrit trois des quatre interactions fondamentales :

- L'interaction électromagnétique, responsable de l'interaction entre particules chargées.
- L'interaction faible, qui est reliée à la désintégration du neutron et au courant faible.
- L'interaction forte, qui agit sur les quarks et les confinent ensemble pour former des hadrons.

Les particules du MS peuvent être séparées en deux catégories. Les fermions, qui ont un spin demi-entier et qui constituent les briques de construction de la matière. Les bosons, qui eux ont un spin entier et qui sont les médiateurs des interactions fondamentales précédemment évoquées. Toutes ces particules sont représentées dans la Figure B.1, les différentes boites correspondent aux différentes interactions. Chacune de ces particules élémentaires dispose d'une antiparticule avec la même masse et spin mais des charges électriques et de couleurs opposés.

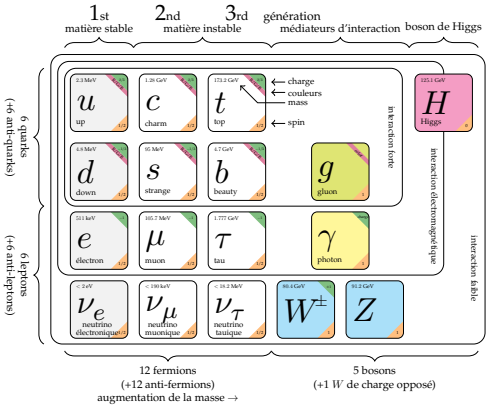

FIGURE B.1 – Contenu en particules du Modèle standard

Pour expliquer les masses des particules du MS le mécanisme de Brout-Englert-Higgs a été introduit. Ce dernier permet par l'ajout d'un champ supplémentaires de faire apparaître des termes de masse dans le Lagrangien du modèle standard et donner naissance à une particule supplémentaire, le boson de Higgs. Ce boson peut être produit lors d'une collision proton-proton par l'interaction de quarks et de gluons. Il va ensuite se désintégrer en différentes particules du MS. Le couplage du boson de Higgs aux particules du MS est directement proportionnel à leur masses de ce fait le plus massif une particule sera le plus probable sera la désintégration du boson de Higgs en cette dernière.

La mesure de ces différentes désintégrations est centrale car elle nous permet d'avoir accès aux couplages du boson de Higgs avec les particules du MS. Leur étude permet d'une part de comprendre les propriétés du boson de Higgs et d'autre part de chercher l'existence de nouvelle physique. En effet si de nouvelles particules existent et se couplent au boson de Higgs, elles risquent de modifier les modes de production et de désintégration du boson de Higgs.

B.1.2 Physique au delà du modèle Standard

Malgré toutes ses réussites, il subsiste des observations qui ne peuvent pas être expliquées par le MS. On peut citer par exemple l'absence d'unification des différentes forces à grande échelle d'énergie comme c'est déjà le cas pour les interactions faible et électromagnétique. Le problème de hiérarchie, lié à la large différence d'échelle entre les interactions gravitationnelle et faible (l'interaction faible est 10^{24} fois plus forte que l'interaction gravitationnelle). Cette large différence d'échelle peut avoir un effet sur les corrections radiatives de la masse du boson de Higgs qui peuvent devenir extrêmement larges à haute échelle d'énergie. On peut finalement ajouter que le MS ne dispose pas de candidat pour la matière noire et ne permet pas d'expliquer l'asymétrie matière-antimatière dans notre univers.

Parmi les différentes théories au-delà du MS qui permet de résoudre ces limitations une est particulièrement attractive, il s'agit de la SuperSymétrie (SUSY). Cette théorie consiste en l'ajout d'une symétrie supplémentaire entre les bosons et les fermions. On va associer à chaque degré de liberté fermionique un dégré de liberté bosonique et à chaque degré de liberté bosonique un degré de liberté fermionique. Du fait de cette symétrie, les particules et leurs partenaires supersymétriques devraient avoir la même masse, ce qui est en contradiction avec les observations. Cette symétrie doit donc être brisée, ce qui amène les masses des particules supersymétriques à être plus élevées que celles de leurs partenaires.

Un des problèmes de la SUSY est qu'elle peut amener à des interactions qui violent la conservation des nombres B et L. Cela peut amener à la désintégration du proton sur des échelles de temps relativement courtes alors que sa durée de vie a été mesurée comme étant plus grande que $10^{29} - 10^{33}$ années. Pour empêcher cela une symétrie supplémentaire, appelée la R-parité doit être ajoutée. Elle correspond à un nouveau nombre quantique : $R = (-1)^{3(B-L)+2s}$ qui sera égal à 1 pour les particules du MS et -1 pour les particules supersymétriques. La conservation de ce nombre va donc interdire les interactions amenant a la désintégration du proton.

En partant du modèle standard on construit dans le cadre de la supersymétrie son extension minimale, le MSSM (Minimal Supersymmetric extension to the Standard Model). La liste des particules le composant est représentée dans la Table B.1. Dans ce modèle, il existe un mélange entre les gauginos électrofaible neutre ($\widetilde{W}^3$ and $\widetilde{B}_\mu$) et les higgsinos neutre ($\widetilde{H}_u^0$ and $\widetilde{H}_d^0$) créant quatre neutralinos : $\widetilde{\chi}_1^0$, $\widetilde{\chi}_2^0$, $\widetilde{\chi}_3^0$ et $\widetilde{\chi}_4^0$. De même, le gaugino électrofaible chargé ($\widetilde{W}^\pm$) et le higgsino chargé ($\widetilde{H}_u^+$ et $\widetilde{H}_d^-$) se mélangent pour créer deux charginos : $\widetilde{\chi}_1^\pm$, $\widetilde{\chi}_2^\pm$.

Noms	Champ MS	superpartenaire	SU(3)	SU(2)	U(1)
quark, squarks, (3 families)	$(u_L d_L)$	$(\widetilde{u}_L \widetilde{d}_L)$	3	2	$\frac{1}{6}$
	u_R	$\widetilde{u}_R$	$\overline{3}$	1	$-\frac{2}{3}$
	d_R	$\widetilde{d}_R$	$\overline{3}$	1	$\frac{1}{3}$
leptons, slepton, (3 families)	$(\nu_L e_L)$	$(\widetilde{\nu}_L \widetilde{e}_L)$	1	2	$-\frac{1}{2}$
	e_R	$\widetilde{e}_R$	1	1	1
higgs, higgsino	$(H_u^+ H_u^0)$	$(\widetilde{H}_u^+ \widetilde{H}_u^0)$	1	2	$\frac{1}{2}$
	$(H_d^0 H_d^-)$	$(\widetilde{H}_d^0 \widetilde{H}_d^-)$	1	2	$-\frac{1}{2}$
gluons, gluinos	g	$\widetilde{g}$	8	1	0
W boson, winos	$W^\pm, W^3$	$\widetilde{W}^\pm, \widetilde{W}^3$	0	3	0
B boson, bino	B_μ	$\widetilde{B}_\mu$	0	1	0

TABLE B.1 – Contenue en particule du MSSM

B.2 L'expérience ATLAS, le LHC et leurs améliorations

B.2.1 Le Grand Collisionneur de Hadrons

Le Grand Collisionneur de Hadrons (LHC) est un accélérateur de particules de 27 km de long. Ce collisionneur a été conçu pour enregistrer des collisions pp avec une énergie dans le centre de masse de $\sqrt{s} = 14\,\text{TeV}$, des collisions plomb-plomb et proton-plomb peuvent également être faites pour étudier le plasma de quarks et de gluons. Le projet LHC fut approuvé en 1994, sa construction a ensuite commencé en 2000 au CERN dans l'ancien tunnel du Grand Collisionneur électron-positron (LEP). Depuis 2010 le LHC enregistre des données, les objectifs principaux de ce programme sont la découverte du boson de Higgs, ce qu'il accomplit en 2012, l'étude du MS et la recherche de nouvelle physique au-delà du MS.

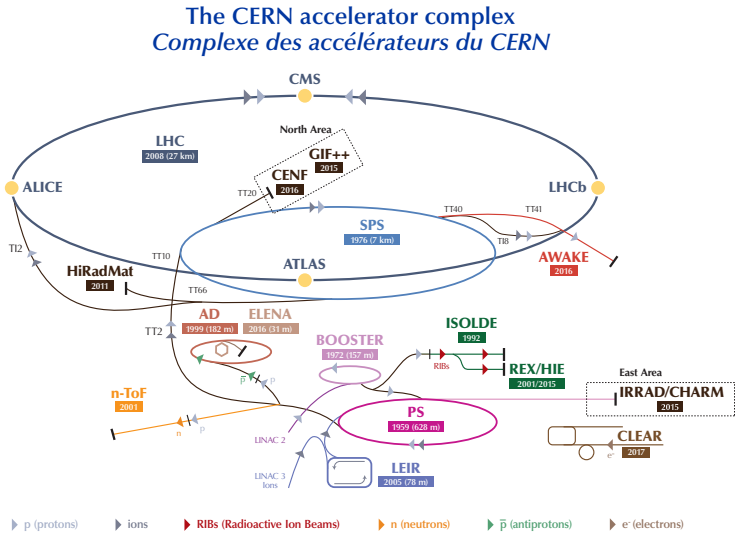

FIGURE B.2 – La chaine d'accélération du LHC.

Le LHC est la dernière étape dans la chaîne d'accélération installée au CERN comme on peut le voir Figure B.2. En effet pour accélérer des particules, des protons en l'occurrence, ces dernières doivent passer par une série d'accélérateurs qui vont chacun augmenter un peu plus l'énergie des protons. Un champ magnétique est appliqué aux particules pour les forcer à maintenir une orbite circulaire, en un point de cette orbite les particules sont soumis à un fort champ électrique qui va permettre leur accélérations

Les protons dans l'accélérateur sont groupés par paquets, chaque paquet contenant au alentour de 1.15×10^{11} protons. Chacun de ces paquets est séparé du suivant par $25\,\mathrm{ns}$, soit la période de collision de l'accélérateur. Du fait de la grande quantité de protons présents dans chaque paquet, la probabilité d'interaction de deux protons lors d'une collision peut être relativement élevée et amener à plusieurs interactions par croisement de faisceau. Ce phénomène est connu sous le nom d'empilement, et correspond aux interactions supplémentaires qui ont lieu en même temps que l'interaction d'intérêt.

Les collisions de particules ont lieu en quatre points le long de l'accélérateur. A chacun de ces point de collision correspond une expérience différente : ATLAS, CMS, LHCb et ALICE. Les études présentées dans cette thèse concernent l'expérience ATLAS.

B.2.2 L'Expérience ATLAS

ATLAS (A Thoroidal LHC Apparatus) est une expérience généraliste avec un programme de physique centré sur la mesure des propriétés du Boson de Higgs et la recherche de nouvelle physique. Une vue schématique d'ATLAS et ce ses sous composants est montrée Figure B.3.

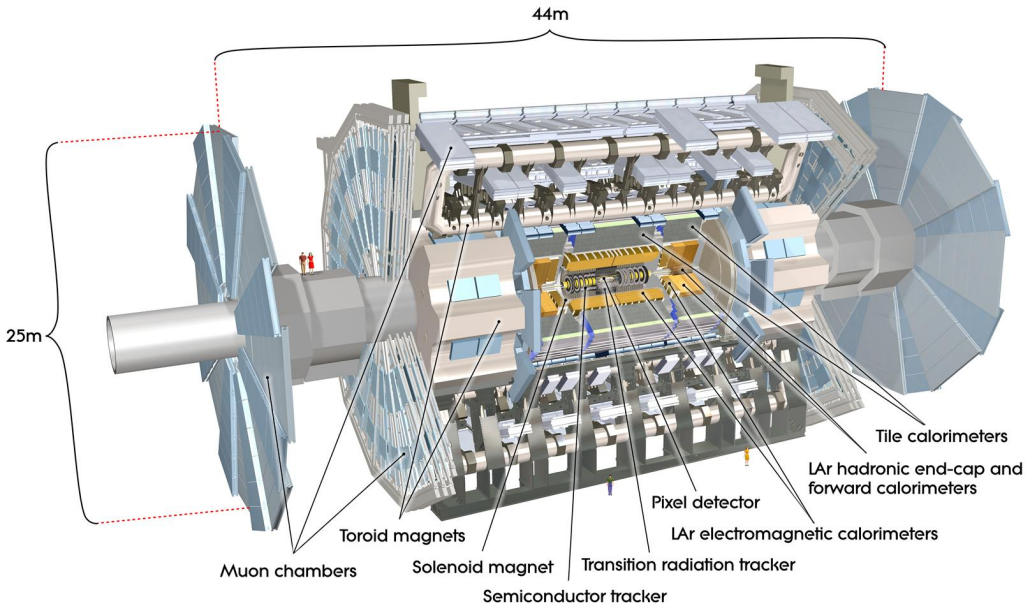

FIGURE B.3 – Vue schématique du détecteur ATLAS.

Ce dernier est composé de différents sous-détecteurs :

- Le Détecteur Interne. Composé de plusieurs trajectographes fortement segmentés, il va ainsi permettre de reconstruire la trajectoire et l'impulsion des particules chargées qui le traversent. Pour déterminer la valeur de cette dernière on utilise la mesure de la courbure des trajectoires dans le champ magnétique. La deuxième fonction de ce détecteur est l'identification des points d'interaction primaires et secondaires et de séparer les interactions d'empilement des interactions de signal.
- Les Calorimètres. Il s'agit d'une combinaison de matériaux actifs et passifs qui vont induire la création de gerbe au passage des particules, permettant la mesure de l'énergie de ces dernières. Ils sont composés de deux parties, un calorimètre électromagnétique, placé en premier qui mesure entièrement l'énergie des électrons et des photons et d'un calorimètre hadronique placé après qui mesurera l'énergie restante des hadrons le traversant et les arrêtent.
- Le Spectromètre à Muons. Placé à la périphérie du détecteur, il est également constitué de trajectographes moins segmentés que le Détecteur Interne. La combinaison des informations provenant de ces deux détecteurs permet la reconstruction des muons.

Une fois que les signaux provenant des différents sous-détecteurs ont été collectés, des algorithmes sont appliqués pour pouvoir reconstruire les différents objets physiques. Chaque type de particule va laisser un signal spécifique dans chacun des sous-détecteurs, en combinant l'ensemble des informations de ces derniers il est donc possible de reconstruire la nature de la particule à l'origine de ces signaux. Cette étape est extrêmement importante car les analyses de physique vont ensuite se baser sur les différents objets reconstruits pour définir leur séparation du signal et du bruit de fond.

B.2.3 Les Améliorations du LHC et d'ATLAS

Le Grand Collisionneur de Hadrons à Haute luminosité (HL-LHC) est la seconde phase du programme du LHC, son commencement est prévu pour début 2026. Le principal objectif du HL-LHC est l'augmentation de la luminosité instantanée de $1.5 \times 10^{34}\mathrm{cm}^{-2}\,\mathrm{s}^{-1}$ jusqu'a $7.5 \times 10^{34}\mathrm{cm}^{-2}\,\mathrm{s}^{-1}$. Cette luminosité étant liée aux paramètres de l'accélérateur est directement proportionnelle au nombre d'événements observés, une augmentation de cette dernière permet donc d'augmenter la statistique disponible pour les analyses de physique et d'améliorer leurs performances. Les plans pour les améliorations du LHC sont présentées en Figure B.4.

Pour l'accélérateur, les améliorations consistent principalement en l'installation d'aimants plus puissants. Il sera ainsi possible d'obtenir des paquets de protons plus petits mais contenant plus de protons, augmentant de ce fait la densité de protons dans les paquets. Cette augmentation de la densité résultera en une chance accrue d'interaction entre les protons lors des collisions et donc à une plus grande luminosité. Malheureusement cette augmentation de la luminosité se transcrit aussi sous forme d'une augmentation de l'empilement et de l'irradiation des détecteurs, ce qui conduira à d'une baisse de performance. Pour compenser ces effets une amélioration des différents détecteurs est également prévue.

L'objectif principal des améliorations d'ATLAS est de maintenir des performances au moins aussi bonnes que celles obtenues au LHC et si cela s'avère possible d'améliorer celles-ci.

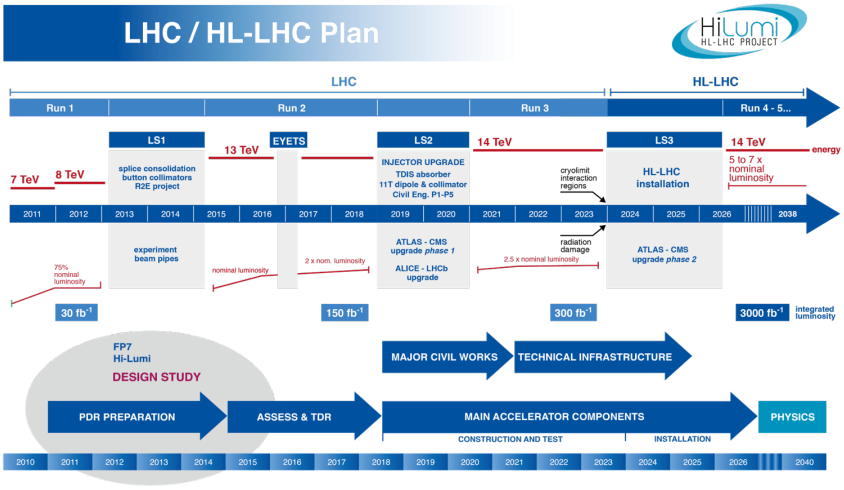

FIGURE B.4 – Plan pour l'amelioration du LHC vers le HL-LHC.

L'amélioration principale prévue est de remplacer l'actuel détecteur interne par le nouveau trajectographe Interne (ITk). Ce nouveau détecteur sera constitué uniquement de capteurs en silicium permettant une meilleure résistance aux radiations. La segmentation sera améliorée d'un facteur passant de $50\,\mu\text{m} \times 250\,\mu\text{m}$ à $50\,\mu\text{m} \times 50\,\mu\text{m}$ pour les couches les plus internes, cela permettra d'améliorer la résolution spatiale du détecteur et de pouvoir ainsi plus facilement séparer les particules provenant de l'interaction principale de l'empilement. Finalement pour améliorer les performances vers l'avant, la couverture qui va actuellement jusqu'à $|\eta| = 2.5$ sera étendue jusqu'à $|\eta| = 4$.

En plus des améliorations du trajectographe, l'électronique du calorimètre sera remplacé pour le HL-LHC ce qui permettra ainsi d'améliorer sa segmentation de lecture. Finalement, pour réduire les effets de l'empilement et améliorer les performances du détecteur ATLAS vers l'avant, un nouveau détecteur de temps appelé le HGTD sera installé pour le HL-LHC, ce dernier sera présenté plus en détail dans la Section B.5.

B.3 Recherche de la supersymétrie avec violation de la R-parité

B.3.1 Signature complètement hadronique avec quatre jets dans l'état final

Au LHC, la recherche de nouvelle physique dans des états finaux complètement hadronique et sans énergie transverse manquante ou lepton s'avère être extrêmement difficile du fait de la large section efficace de production des processus multijet. Il est donc important d'étudier cette région de l'espace des phases étant donné qu'elle est ignorée par la plupart des analyses SUSY standards. Cette thèse présente l'étude de la signature de quatre jets dans l'état final, formant deux résonances.

Les Sgluons sont les partenaires scalaires des gluinos dans le MRSSM. Ces particules se couplent aux quarks via des boucles de gluinos et de squarks et se couplent aux gluons via des boucles de squarks comme montré sur la Figure B.5 (a). Ces particules pourraient être produites en paire au LHC, chacun des sgluons se désintègrerait ensuite en une paire de quarks ou de gluons amenant ainsi un état final avec quatre jets sans énergie transverse manquante.

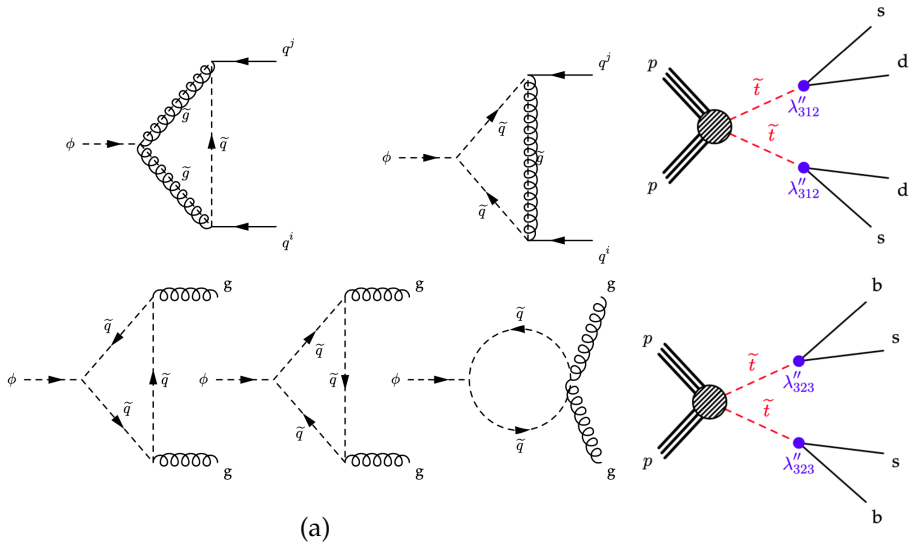

FIGURE B.5 – (a) Désintégration des sgluons. (b) Désintégration des stop.

Des signatures comprenant quatre jets peuvent aussi se trouver dans la SUSY sans ajouter de particule supplémentaire. Par exemple la R-Parité, si violée, permet l'écriture d'interaction supersymetrique de la forme :

$$W_{RPV} = \frac{1}{2}\lambda_{ijk} L_i L_j E^c_k + \lambda'_{ijk} L_i \overline{Q}_j \overline{D}_k + \frac{1}{2}\lambda''_{ijk} \overline{U}_i \overline{D}_j \overline{D}_k + \mu_i H_u L_i \tag{B.1}$$

Dans le modèle qui nous intéresse, λ''_{ijk} est non nul pour $j \neq k$, dans ce cas la sparticule initial se désintégrera en deux quarks différents. Au LHC, des stops pourraient être produits par paires durant les collisions. Ces stops pourraient ensuite se désintégrer via des couplages violant la R-Parité en deux jets, donnant naissance à des états finaux avec quatre jets comme illustrés Figure B.5 (b).

Les états finaux de ces deux signatures étant relativement similaires, ils peuvent tous les deux être recherchés dans la même analyse. Pour la simplicité des simulations, des stops violant la R-Parité ont été utilisés pour l'analyse mais les résultats sont aisément réinterprétables dans le cadre des sgluons.

B.3.2 Topologie des événements

Pour sélectionner les événements nous intéressant, j'ai déterminé le filtre à événements du système de déclenchement le plus adapté. Il s'agit du HLT_4j120, pour ce filtre au moins quatre jets avec un p_{T} de plus de $120\,\mathrm{GeV}$ sont nécessaires. La valeur de la coupure en p_{T} du filtre a été imposée pour limiter le taux d'événements enregistrés par ce filtre, de ce fait il impactera fortement l'efficacité de l'analyse pour les faibles masses de stop. En plus de ce filtre une coupure sur le p_{T} minimum des jets à $140\,\mathrm{GeV}$ est imposée, celle-ci assure une efficacité complète du filtre.

Comme expliqué précédemment, les signaux considérés sont composé de deux résonances identiques produites en paire se désintégrant en paires de jet. L'état final se compose donc de quatre jets. Pour reconstruire les événements, les quatre jets de plus haut p_{T} dans l'état sont sélectionnés. A partir de ces quatre jets, deux paires de jet doivent être reconstruites, chacune

de ces paires correspondant à une des résonances. Pour ce faire différents algorithmes d'appariement peuvent être utilisés.

Une fois ces paires reconstruits différentes variables sont déduites pour permettre de séparer le signal et le bruit de fond. Ces variables sont :

1. ΔR_{min} : La somme des distances entre les deux jets de chaque paires.
2. $|\cos(\theta^*)|$: L'angle de production de la paire.
3. $A = \frac{m_1 - m_2}{m_1 + m_2}$: L'asymétrie de masse entre les deux resonances.

Les distributions de ces variables en utilisant les informations des vraies distributions sont présentées en Figure B.6.

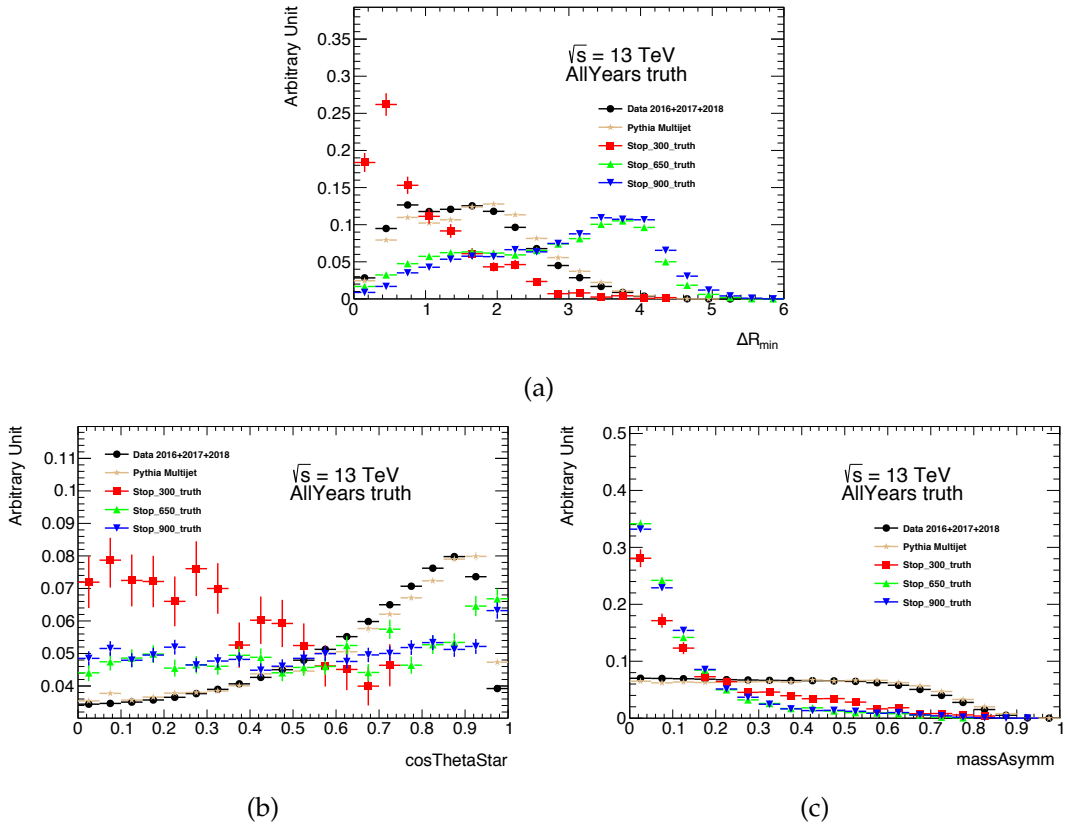

(a)

(b)

(c)

FIGURE B.6 – Distribution de ΔR_{min} (a), $|\cos(\theta^*)|$ (b) et A (c) pour le signal Monte Carlo et les donnée 2016, 2017 et 2018. L'appariement en ΔR_{min} est utilisé pour les donnée.

Différentes méthodes d'appariement peuvent être utilisées, la première qui était utilisé pour l'itération précédente de cette analyse est l'appariement en ΔR_{min}. L'idée derrière cette méthode est de sélectionner le système de paires minimisant la valeur de ΔR_{min}. A faible masses les stops émis ont une grande impulsion, de ce fait l'angle entre les deux jets résultant de sa désintégration devrait être petit. En plus de cette méthode une coupure additionnelle sur ΔR_{min} est appliquée permettant de grandement réduire le bruit de fond pour lequel ΔR_{min} tend à être plus large.

Cette méthode perd par contre en efficacité pour de plus grandes masses où l'impulsion des stops est plus faible. D'autres méthodes ont donc été testées pour les masses plus élevées, l'une d'entre elle consiste à choisir la paire qui maximise ΔR_{max} au lieu de celle qui la minimise. Cette méthodologie a l'avantage d'augmenter l'efficacité de l'appariement comparé à la

méthode précédente, par contre elle tend à diminuer la séparation entre le bruit de fond et le signal.

B.3.3 Perspective

Une fois les paires reconstitués et les variables déterminées, une estimation du bruit de fond effectué dans la région du signal pour être comparé au nombre d'événements mesuré à celui attendu. Pour ce faire on utilise habituellement la simulation Monte Carlo des processus de bruit de fond mais malheureusement le bruit de fond multijet est compliqué à simuler précisément. On utilisera donc des méthodes se basant sur les données pour estimer ce bruit de fond.

La première méthode appelée méthode ABCD, consiste a séparer les événements en quatre régions en utilisant deux variables ($|\cos(\theta^*)|$ et A). Une de ces régions contiendra le signal (C) tandis que les quatre autres contiendront uniquement du bruit de fond (ABD). A condition que les deux variables soient bien indépendantes, le nombre d'événements de bruit de fond dans la région de signal peut s'obtenir grace à :$N_C = N_A \times \frac{N_D}{N_B}$.

Cette méthode fonctionne pour l'appariement en ΔR_{min} mais pas pour celui en ΔR_{max} pour lequel $|\cos(\theta^*)|$ et A sont corrélés. On utilisera donc pour ces dernières une régression du bruit de fond qui est extrapolée dans la région de masse considérée pour le signal en question. En général cette méthode est plus appropriée pour les larges masses ou l'extrapolation est plus aisé à effectuer et ou des corrélations commencent à apparaitre entre $|\cos(\theta^*)|$ et A.

Ces méthodes ont ainsi été optimisée pour maximiser la significance du signal grâce aux échantillons Monte Carlo. La significance attendue a été calculée pour chaque point de masse dans le cadre de l'appariement en ΔR_{min} comme montré sur la Figure B.7. Comparé à l'analyse précédente ou des masses jusqu'à $415\,\mathrm{GeV}$ ont été rejetées, cette nouvelle analyse devrait pouvoir augmenter cette limite jusqu'à $600\,\mathrm{GeV}$ en utilisant les données de 2016, 2017 et 2018.

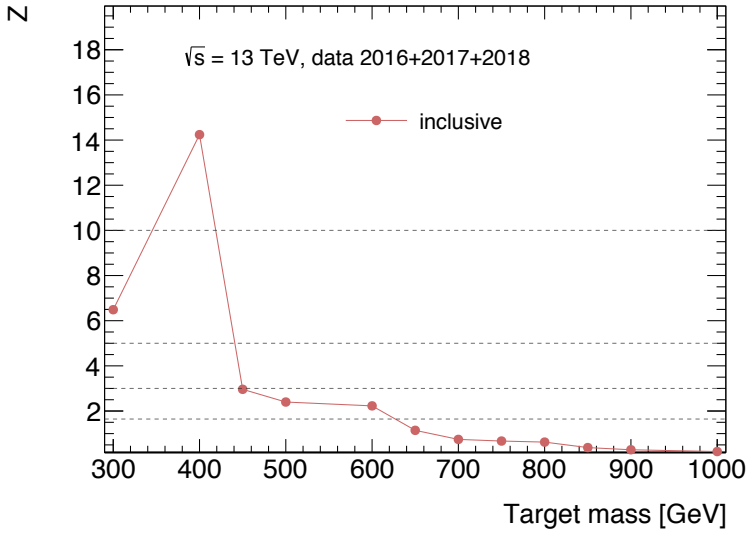

FIGURE B.7 – Significance attendue pour la catégorie inclusive en fonction de la masse du stop.

B.4 Prospective de mesure des couplages du boson de Higgs au HL-LHC

D'ici la fin du HL-LHC, la luminosité intégrée mesurée par ATLAS et CMS aura atteint $4000\,\mathrm{fb}^{-1}$. Avec une telle augmentation de la luminosité une mesure précise des différents couplages du boson de Higgs devrait être possible. J'ai donc préformé une étude de la précision attendue pour la mesure de ces couplages au HL-LHC à l'aide de SFitter. Cette étude basée sur les estimations des erreurs sur les mesures de sections efficaces du Higgs qui seront effectuées au HL-LHC tel que déterminées dans le "Report on the Physics at the HL-LHC".

SFitter est un outil qui a été historiquement développé pour déterminer les paramètres de modèles de nouvelle physique en utilisant les mesures provenant de "nouveaux" collisionneurs comme le LHC. Pour un jeu donné d'observables, l'algorithme utilise des chaines de Markov pour échantillonner l'espace des paramètres. Une carte de probabilité de l'espace des paramètres est ensuite construite en utilisant les points ainsi obtenus. Les maximums locaux de cette carte sont ensuite extraits. SFitter peux aussi être utilisé pour estimer les erreurs sur la détermination d'un jeu de paramètres. Dans ce cas on utilise une liste de mesure d'intérêt et les erreurs correspondantes. De nouveaux jeux de mesures simulés peuvent ensuite être déterminés en utilisant ces erreurs. Pour chaque jeu simulé la valeur la plus probable des paramètres est déterminées, on obtient ensuite l'erreur sur ces paramètres en utilisant la dispersion de leurs valeurs.

Pour étudier les couplages plusieurs approches sont possibles. La première est l'utilisation des Delta, on définit des modificateurs de couplage appelés kappa définis pour chaque couplage du Higgs tel que :

$$g_{xxH} \equiv g_x = \kappa_x g_x^{SM} = (1 + \Delta_x) g_x^{SM} \tag{B.2}$$

En utilisant ce formalisme on peut déterminer la valeur de Δ correspondant aux mesures disponibles, $\Delta = 0$ correspondant au MS. La Figure B.8 présente les erreurs sur la détermination des Δ au Run1 pour ATLAS et CMS (a) et les erreurs attendues que j'ai calculé pour le HL-LHC pour ATLAS seul (b). Une large amélioration au HL-LHC est visible comme attendue.

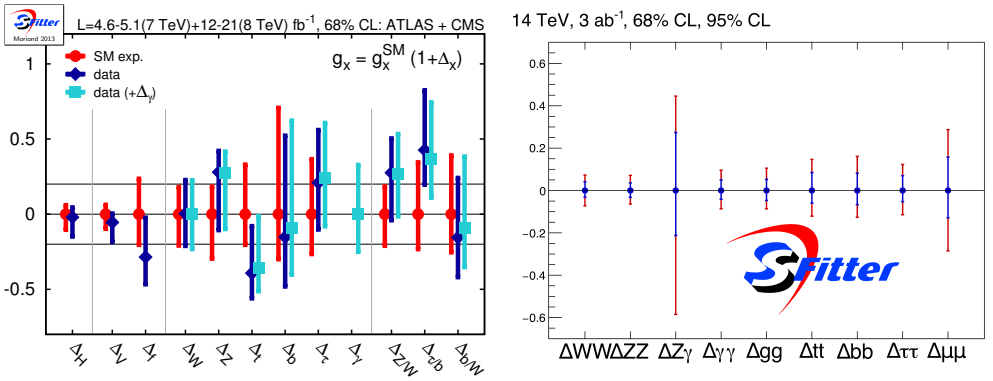

(a) (b)

FIGURE B.8 – (a) Limite sur les modificateurs de couplage sous forme de Δ pour ATLAS et CMS présenté aux conférence d'hiver 2013 à Moriond et Aspen. (b) Résultat de mon étude sur les incertitudes attendues sur les modificateurs de couplage Δ avec ATLAS au HL-LHC.

L'autre approche pour étudier les déviation des couplages est celle des Théories Effectives des Champs (EFT). En faisant l'hypothèse que les nouveaux états qui pourraient affecter les couplages du Higgs appartiennent à $SU(2)$, ces nouveaux états peuvent être pris en compte

grâce à une EFT. Cette approche est valable tant que l'échelle d'énergie à laquelle ces nouveaux états se trouvent (noté Λ) n'est pas accessible au LHC. On obtient ainsi un Lagrangien effectif combinant le Lagrangien du MS avec un Lagrangien de dimension 6 invariant sous $SU(2)_I \times U(1)_Y$:

$$\mathcal{L}_{eff} = \mathcal{L}_{SM} + \sum_x \frac{f_x}{\Lambda^2}\mathcal{O}_x + ... \tag{B.3}$$

où $\mathcal{O}_x$ est un opérateur et f est une constante de couplage aussi appelé coefficient de Wilson. Il existe en tout 59 opérateurs de dimension 6 indépendants. En imposant l'invariance selon C et P et en négligeant tous les opérateurs qui ne sont pas contraints par les mesures des couplages Higgs au LHC, on obtient le Lagrangien effectif suivant :

$$\begin{aligned} Lagr_{eff} = & \frac{-\alpha_s}{8\pi}\frac{f_{GG}}{\Lambda^2}\mathcal{O}_{GG} + \frac{f_{BB}}{\Lambda^2}\mathcal{O}_{BB} + \frac{f_{WW}}{\Lambda^2}\mathcal{O}_{WW} + \frac{f_B}{\Lambda^2}\mathcal{O}_B + \frac{f_{WWW}}{\Lambda^2}\mathcal{O}_{WWW} \\ & + \frac{f_{\phi 2}}{\Lambda^2}\mathcal{O}_{\phi 2} + \frac{f_{\phi 3}}{\Lambda^2}\mathcal{O}_{\phi 3} + \frac{f_\tau m_\tau}{\nu\Lambda^2}\mathcal{O}_{e\phi,33} + \frac{f_b m_b}{\nu\Lambda^2}\mathcal{O}_{d\phi,33} + \frac{f_t m_t}{\nu\Lambda^2}\mathcal{O}_{u\phi,33} \\ & + invisible\ decay \end{aligned} \tag{B.4}$$

Le résultat d'une analyse utilisant une EFT avec les données de ATLAS et CMS pour le Run1+Run2 est montré en Figure B.9 (a). Les erreurs que j'ai calculé pour ATLAS à la fin du HL-LHC sont présentées en Figure B.9 (b), une amélioration d'un facteur 2 est observée. C'est légèrement inférieur à ce qui est attendu, cela correspond au fait que les mesures au HL-LHC ne seront plus dominées par les effets statistiques et que les effets systématique et théoriques affecteront aussi les erreurs.

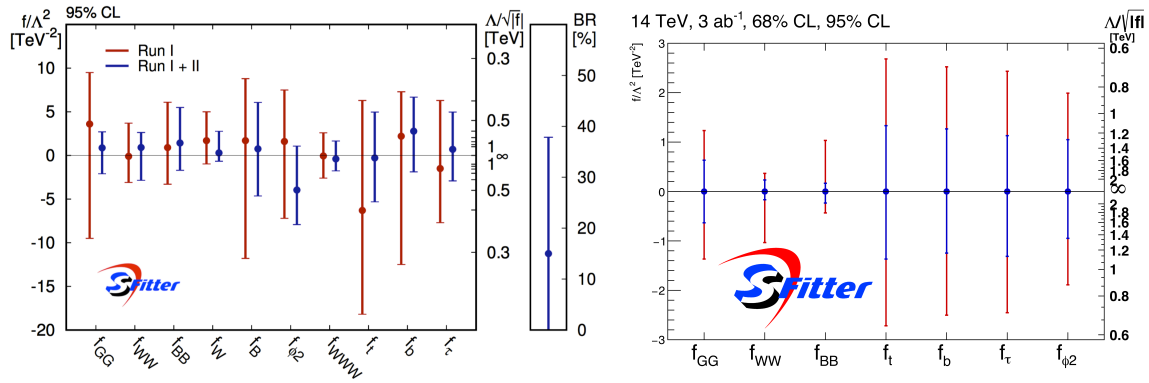

(a) (b)

FIGURE B.9 – (a) Limites sur les coefficients de Wilson obtenus au Run1 (en rouge) et au Run1+Run2 (en bleu) pour ATLAS et CMS. (b) Résultat de mon étude sur les incertitudes attendues sur les coefficients de Wilson avec ATLAS au HL-LHC.

B.5 Le Détecteur de temps fortement segmenté

B.5.1 Le HGTD

Au HL-LHC, du fait de l'augmentation de la luminosité l'empilement va également augmenter Etant donné que la taille longitudinale du faisceau restera similaire, cela se traduira par une densité d'interaction d'empilement plus élevé. Cette haute densité peut avoir des effets sur la reconstruction des événements dans ATLAS. En effet si la distance entre une interaction de signal et une interaction d'empilement est inférieure à la résolution du trajectographe, ces deux interactions seront reconstruites comme n'en étant qu'une seule et les objets de signal risquent donc d'être contaminés par l'empilement. Ceci est particulièrement vrai vers l'avant du détecteur où la résolution du trajectographe est moins bonne, de l'ordre du millimètre.

Pour remédier à ce problème l'installation d'un détecteur de temps vers l'avant à été prévue, il s'agit du Détecteur de temps fortement segmenté (HGTD). Le concept de ce détecteur est que si on est capable de reconstruire précisément le temps des différentes interactions, on pourra utiliser cette information supplémentaire qui est décorrélée de la position pour séparer les interactions et ainsi supprimer la contamination liée à l'empilement. De manière plus générale, l'objectif de ce détecteur est ainsi d'améliorer les performances d'ATLAS dans la région vers l'avant de telle sorte qu'elles soient comparables à celles de la région centrale.

Ce nouveau détecteur sera installé durant l'arrêt du LHC avant le debut du HL-LHC, devant le bouchon d'ATLAS comme indiqué sur la Figure B.10. Pour chaque bouchon deux couches de détecteurs au silicium double face seront installées. L'objectif de ce détecteur est d'atteindre une résolution de $30\,\mathrm{ps}$ pour les traces vers l'avant. Pour ce faire, une résolution d'au moins $50\,\mathrm{ps}$ par pixel doit être atteinte. Ces résolutions peuvent être atteintes en utilisant des détecteurs à avalanche de faible gain (LGAD), ce nouveau type de pixel fonctionne comme une jonction PN à laquelle on aurait ajouté une couche P supplémentaire, cela induit des gerbes électromagnétiques dans le pixel resultant en un signal plus grand. Ce signal plus large permet ensuite d'obtenir une meilleure résolution temporelle.

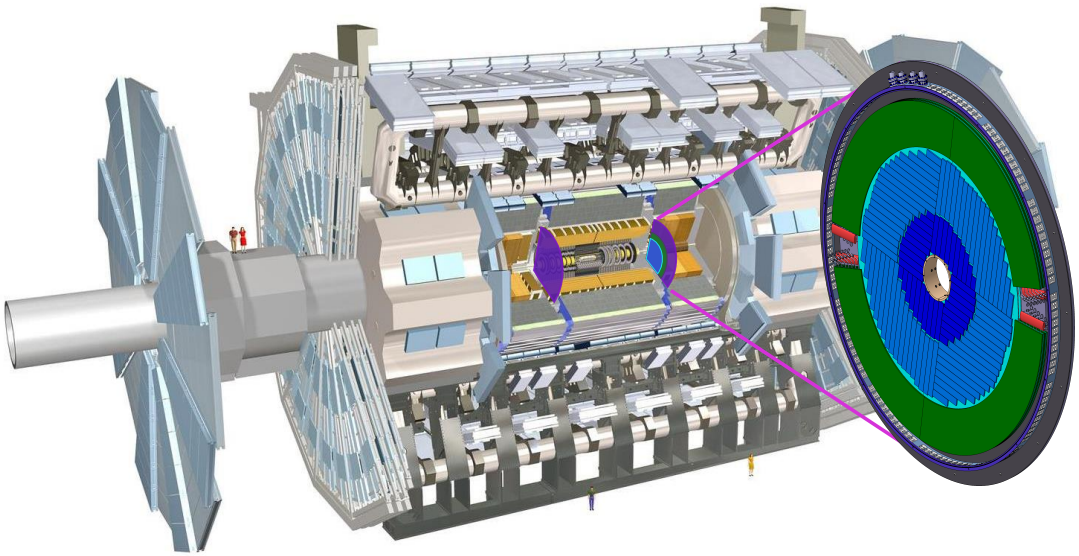

FIGURE B.10 – Position du HGTD dans ATLAS.

B.5.2 Simulation du HGTD

Pour pouvoir étudier les performances de ce nouveau détecteur, il a été nécessaire d'en développer une simulation. Cette simulation se doit de prendre en compte la géométrie du détecteur et la résolution en temps des pixels, en effet ces deux paramètres vont directement affecter l'efficacité du détecteur ainsi que sa résolution. Une simulation complète du HGTD à l'intérieur d'ATLAS à été effectuée dans Geant4.

Pour permettre une optimisation de la géométrie du détecteur, la partie active du détecteur à été simulée dans un premier temps comme deux disques complets de silicium. La géométrie était ensuite implémentée à posteriori sous forme de masque supprimant les coups ne correspondant pas à une partie active du détecteur. La position des coups après application de ce masque pour les faces avant des deux layer est montrée Figure B.11. Une fois la géométrie definitive déterminée grace à ces masques, une implementation plus précise de la géométrie ou chaque élément est présent a été développé.

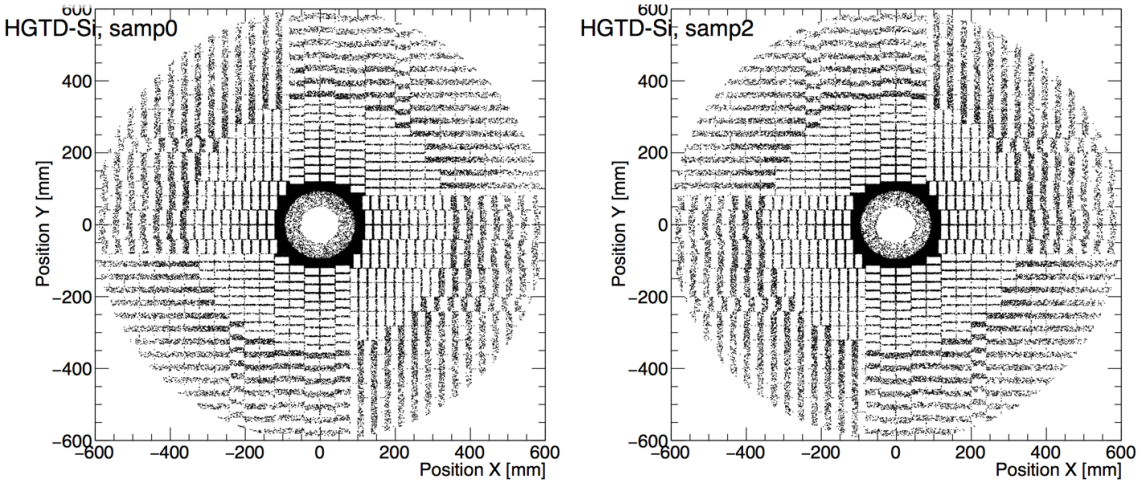

(a) (b)

FIGURE B.11 – Zones non-instrumenté pour la lecture du HGTD dans la simulation pour les face avant du la première (a) et deuxième couche (b).

La simulation de la résolution en temps des pixels se base sur des connaissances acquises via des tests faisceau et des simulations des LGADs. Au lieu de simplement tirer des temps suivant une distribution gaussienne autour du temps attendu des coups, une simulation des processus liés au pixels et à l'électronique est effectuée pour plus de precision.

Grâce à un très grand catalogue de signaux issus des tests faisceau j'ai pu obtenir un signal modèle, Pour chaque coup on va donc générer un signal en modifiant légèrement ce signal modèle. Ce nouveau signal va être utilisé pour calculer l'énergie et le temps du coups via un algorithme de discriminateur à fraction constante similaire à ce qui pourrait être utilisé dans l'électronique. Cet algorithme permet donc de prendre en compte les différents effets pouvant dégrader la résolution et en particulier de simuler correctement le cas ou plusieurs coups arrivent simultanément dans le même pixel.

B.5.3 Etude et optimisation des performances HGTD

Grace à la simulation que j'ai ainsi développé j'ai pu étudier et optimiser les performances du détecteur. Il existe deux principaux critères influant sur les performances du détecteur : l'efficacité, à savoir la fraction de particules traversant le détecteur en déposant un signal et la résolution en temps des traces associées au détecteur, cette dernière affectant directement l'impact du HGTD sur les performance d'ATLAS.

Pour optimiser l'efficacité du détecteur une série de géométries à été développée, de plus en plus réaliste et cherchant à chaque fois à maximiser l'efficacité. La principale source d'inefficacité sont les recouvrements entre zones non instrumentées dans les deux couches. Pour minimiser cet effet, j'ai montré qu'une symétrie miroir entre les deux couches réduisait le recouvrement de ces zones. De manière plus générale, plus la position des modules dans les deux couches est décorrélée meilleure est l'efficacité. J'ai ainsi également montré que l'ajout d'une rotation entre les deux couches permet d'augmenter encore plus l'efficacité.

Pour la résolution en temps du détecteur deux critères entrent en ligne de compte, la résolution intrinsèque des pixels et de l'électronique ainsi que le nombre de coups associés à chaque trace. La résolution intrinsèque peut être affectée entre autres par la dose d'irradiation reçue par les pixels, plus celle-ci est grande plus leurs gains sont dégradés ce qui détériore leurs résolutions. Le nombre de coups par trace sera quant à lui directement impacté par la géométrie du détecteur, j'ai donc optimisé cette dernière pour maximiser les performances. Plus on est proche du faisceau de particules plus la dose reçue sera élevé, pour compenser cela j'ai fait en sorte que l'on obtienne 3 coups par traces à petit rayon ($R < 320\,\mathrm{mm}$) et deux à rayon plus grand. Pour ce faire on utilise le fait que le détecteur est composé de couches double face avec des pixels de chaque côté. Ces pixels se recouvrent en temps normal de 20%. Pour éviter les inefficacités, j'ai montré qu'en augmentant ce recouvrement à 80% on peut obtenir en moyenne trois coups dans deux couches.

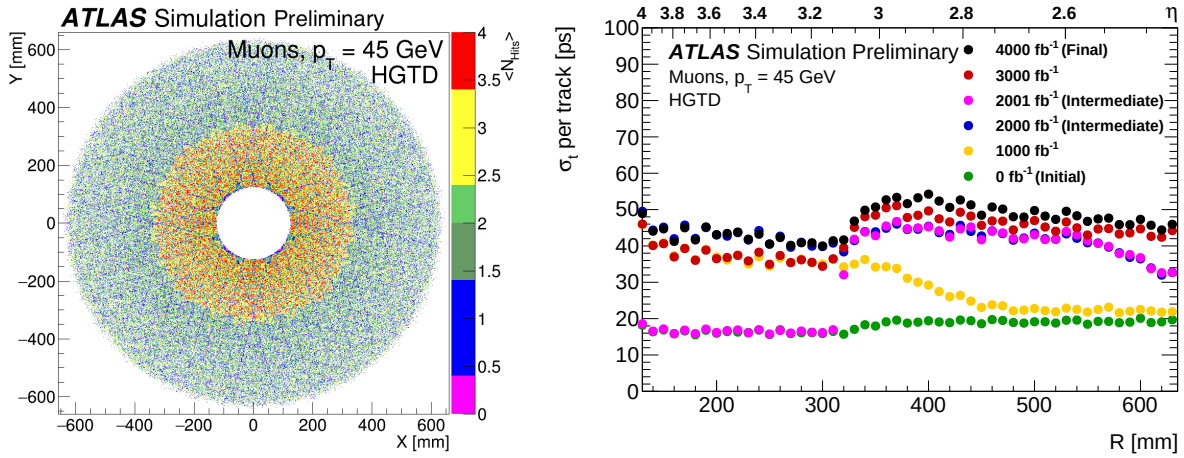

(a) (b)

FIGURE B.12 – (a) Nombre de coups par trace en fonction de la position dans le HGTD pour un recouvrement de 80% pour $R < 320\,\mathrm{mm}$ et 20% pour les rayons plus large. (b) Resolution en temps de muons simulé à travers le HGTD en fonction du rayon pour différents scenarii d'irradiation.

J'ai implémenté cette géométrie dans la simulation, la Figure B.12 (a) illustre le nombre de coups par trace que l'on peut obtenir pour des muons de haut p_{T}. On peut voir que au centre ce nombre est en moyenne de trois, avec des zones à deux et à quatre coups tandis quelle est de deux à plus large rayon. La résolution en temps résultant par trace est montrée en Figure B.12 (b) pour différents scenarii d'irradiation. Il est important de noter qu'un remplacement des pixels à faible rayon ($R < 320\,\mathrm{mm}$) est prévue après la moitié de la vie du détecteur. Sans ce remplacement la dose à laquelle les pixels centraux serait soumis deviendrait trop importante et il cesserait de fonctionner. Cela peut se voir sur la Figure B.12 (b) par le retour à une résolution de $20\,\mathrm{ps}$ pour $R < 320\,\mathrm{mm}$ dans le scenario intermédiaire post-remplacement ($2001\,\mathrm{fb}^{-1}$). On peut voir que l'on arrive ainsi à maintenir une résolution inférieure à $50\,\mathrm{ps}$ sur toute la vie du détecteur.

Ces études sur la résolution en temps ont été effectuées en utilisant des muons de haut p_{T} car l'efficacité d'association de ces traces de muons à leurs coups dans le détecteur est proche de 100%. On peut ainsi avec ces particules étudier l'efficacité géométrique du détecteur sans avoir à prendre en compte l'efficacité d'association entre une trace et ces coups. J'ai étudié cette association sans empilement à l'aide de pions de p_{T} différent. Pour un p_{T} supérieur à $20\,\mathrm{GeV}$ une efficacité de l'ordre de 90% est observée alors que pour des p_{T} inférieur à $1\,\mathrm{GeV}$ la résolution est de l'ordre de 70%. Cette perte d'efficacité est principalement due à la présence divers matériaux entre le trajectographe et le HGTD. Ce dernier va causer des diffusions multiples Coulombienne pour les particules le traversant avec un angle inversement proportionnel à l'impulsion de ces particules. La position des coups dans les HGTD peut ainsi se retrouver éloigné de la position de l'extrapolation de la trace correspondante, diminuant l'efficacité de l'association Des efforts au niveau de la trajectographie sont actuellement en cours pour réduire cet effet, mais il risque quand même de limiter les performances du HGTD.

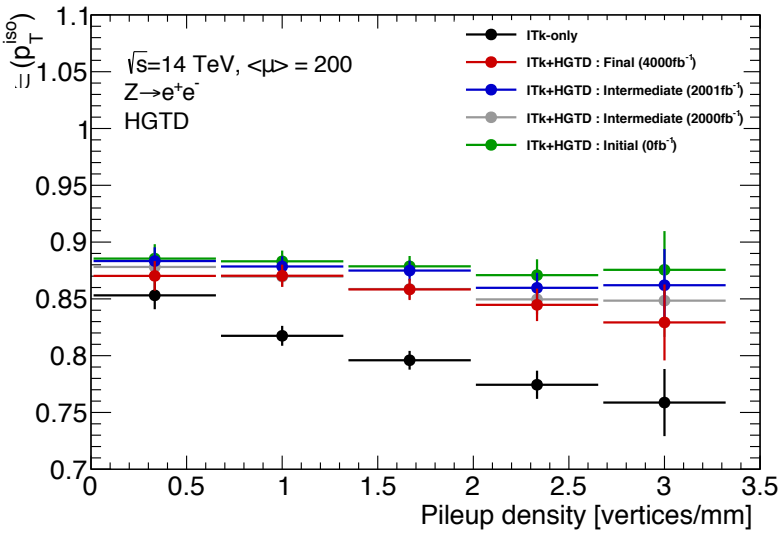

FIGURE B.13 – Efficacité de selection pour le critère d'isolation des électrons en fonction de la densité locale d'empilement pour l'ITk et l'ITk et le HGTD.

Pour terminer j'ai également utilisé la simulation que j'ai développée pour tester les performances en termes de physique du HGTD, en particulier pour l'isolation des électrons. L'isolation des électrons est un ingrédient clé de l'identification de ces derniers. Pour s'assurer qu'ils proviennent bien de l'interaction d'intérêt et non d'un faux, d'une désintégration ou d'une conversion, on impose qu'il ne doit pas y avoir d'autre trace provenant de l'interaction primaire à proximité de celle de d'électrons avec un $p_{\mathrm{T}} > 1\,\mathrm{GeV}$ dans un cône de $\Delta R < 0.2$. Cette méthode est très efficace en absence d'empilement mais quand celui-ci est trop important, des traces provenant de l'empilement peuvent se retrouver à proximité de celles d'électrons réduisant l'efficacité d'identification des électrons. C'est ce qu'on peut voir sur la Figure B.13 à travers les points noirs, plus la densité locale d'empilement augmente plus l'efficacité de l'isolation pour les vrais électrons diminue.

On peut remédier à cet effet en utilisant l'information en temps du HGTD. Si on demande aux traces proches de d'électrons d'être également compatibles en temps avec ce dernier on va pouvoir se débarrasser de la contamination en trace d'empilement. Comme on peut le voir sur la Figure B.13 on va ainsi pouvoir obtenir une efficacité quasiment indépendante de la densité d'empilement. Cette amélioration de l'ordre de 10% de l'efficacité de l'isolation vers l'avant pourra affecter différentes analyses de physique, telles que par exemple la mesure de l'angle de mixage faible, qui utilise des électrons vers l'avant.

Bibliography

[1] M. Tanabashi et al. "Review of Particle Physics". In: *Phys. Rev.* D98.3 (2018), p. 030001. DOI: 10.1103/PhysRevD.98.030001.

[2] Michael E. Peskin and Daniel V. Schroeder. *An Introduction to quantum field theory*. Reading, USA: Addison-Wesley, 1995. ISBN: 9780201503975, 0201503972. URL: http://www.slac.stanford.edu/~mpeskin/QFT.html.

[3] Georges Aad et al. "Observation of a new particle in the search for the Standard Model Higgs boson with the ATLAS detector at the LHC". In: *Phys. Lett.* B716 (2012), pp. 1–29. DOI: 10.1016/j.physletb.2012.08.020. arXiv: 1207.7214 [hep-ex].

[4] Steven Weinberg. "A Model of Leptons". In: *Phys. Rev. Lett.* 19 (21 1967), pp. 1264–1266. DOI: 10.1103/PhysRevLett.19.1264. URL: https://link.aps.org/doi/10.1103/PhysRevLett.19.1264.

[5] Abdus Salam and John Clive Ward. "Weak and electromagnetic interactions". In: *Nuovo Cim.* 11 (1959), pp. 568–577. DOI: 10.1007/BF02726525.

[6] F. Englert and R. Brout. "Broken Symmetry and the Mass of Gauge Vector Mesons". In: *Phys. Rev. Lett.* 13 (9 1964), pp. 321–323. DOI: 10.1103/PhysRevLett.13.321. URL: https://link.aps.org/doi/10.1103/PhysRevLett.13.321.

[7] Peter W. Higgs. "Broken Symmetries and the Masses of Gauge Bosons". In: *Phys. Rev. Lett.* 13 (16 1964), pp. 508–509. DOI: 10.1103/PhysRevLett.13.508. URL: https://link.aps.org/doi/10.1103/PhysRevLett.13.508.

[8] M. Cepeda et al. "Higgs Physics at the HL-LHC and HE-LHC". In: (2019). arXiv: 1902.00134 [hep-ph].

[9] D. de Florian et al. "Handbook of LHC Higgs Cross Sections: 4. Deciphering the Nature of the Higgs Sector". In: (2016). DOI: 10.23731/CYRM-2017-002. arXiv: 1610.07922 [hep-ph].

[10] A. David et al. "LHC HXSWG interim recommendations to explore the coupling structure of a Higgs-like particle". In: (2012). arXiv: 1209.0040 [hep-ph].

[11] Remi Lafaye et al. "Measuring the Higgs Sector". In: *JHEP* 08 (2009), p. 009. DOI: 10.1088/1126-6708/2009/08/009. arXiv: 0904.3866 [hep-ph].

[12] David López-Val, Tilman Plehn, and Michael Rauch. "Measuring extended Higgs sectors as a consistent free couplings model". In: *JHEP* 10 (2013), p. 134. DOI: 10.1007/JHEP10(2013)134. arXiv: 1308.1979 [hep-ph].

[13] Anke Biekötter, Tyler Corbett, and Tilman Plehn. "The Gauge-Higgs Legacy of the LHC Run II". In: *SciPost Phys.* 6 (2019), p. 064. DOI: 10.21468/SciPostPhys.6.6.064. arXiv: 1812.07587 [hep-ph].

[14] Ilaria Brivio and Michael Trott. "The Standard Model as an Effective Field Theory". In: *Phys. Rept.* 793 (2019), pp. 1–98. DOI: 10.1016/j.physrep.2018.11.002. arXiv: 1706.08945 [hep-ph].

[15] B. Grzadkowski et al. "Dimension-Six Terms in the Standard Model Lagrangian". In: *JHEP* 10 (2010), p. 085. DOI: 10.1007/JHEP10(2010)085. arXiv: 1008.4884 [hep-ph].

[16] Tyler Corbett et al. "Constraining anomalous Higgs interactions". In: *Phys. Rev.* D86 (2012), p. 075013. DOI: 10.1103/PhysRevD.86.075013. arXiv: 1207.1344 [hep-ph].

[17] "The matter-antimatter asymmetry problem". In: (2014). URL: http://cds.cern.ch/record/1998489.

[18] Stephen P. Martin. "A Supersymmetry primer". In: (1997). [Adv. Ser. Direct. High Energy Phys.18,1(1998)], pp. 1–98. DOI: 10.1142/9789812839657_0001,10.1142/9789814307505_0001. arXiv: hep-ph/9709356 [hep-ph].

[19] Abdelhak Djouadi. "The Anatomy of electro-weak symmetry breaking. II. The Higgs bosons in the minimal supersymmetric model". In: *Phys. Rept.* 459 (2008), pp. 1–241. DOI: 10.1016/j.physrep.2007.10.005. arXiv: hep-ph/0503173 [hep-ph].

[20] D. I. Kazakov. "Beyond the standard model: In search of supersymmetry". In: *2000 European School of high-energy physics, Caramulo, Portugal, 20 Aug-2 Sep 2000: Proceedings*. 2000, pp. 125–199. arXiv: hep-ph/0012288 [hep-ph].

[21] Rabindra N. Mohapatra. "Supersymmetry and R-parity: an Overview". In: *Phys. Scripta* 90 (2015), p. 088004. DOI: 10.1088/0031-8949/90/8/088004. arXiv: 1503.06478 [hep-ph].

[22] Ian J. R. Aitchison. "Supersymmetry and the MSSM: An Elementary introduction". In: (2005). arXiv: hep-ph/0505105 [hep-ph].

[23] Georges Aad et al. "Summary of the ATLAS experiment's sensitivity to supersymmetry after LHC Run 1 - interpreted in the phenomenological MSSM". In: *JHEP* 10 (2015), p. 134. DOI: 10.1007/JHEP10(2015)134. arXiv: 1508.06608 [hep-ex].

[24] Graham D. Kribs, Erich Poppitz, and Neal Weiner. "Flavor in supersymmetry with an extended R-symmetry". In: *Phys. Rev.* D78 (2008), p. 055010. DOI: 10.1103/PhysRevD.78.055010. arXiv: 0712.2039 [hep-ph].

[25] Tilman Plehn and Tim M. P. Tait. "Seeking Sgluons". In: *J. Phys.* G36 (2009), p. 075001. DOI: 10.1088/0954-3899/36/7/075001. arXiv: 0810.3919 [hep-ph].

[26] S. Y. Choi et al. "Color-Octet Scalars of N=2 Supersymmetry at the LHC". In: *Phys. Lett.* B672 (2009), pp. 246–252. DOI: 10.1016/j.physletb.2009.01.040. arXiv: 0812.3586 [hep-ph].

[27] Jared A. Evans and Yevgeny Kats. "LHC Coverage of RPV MSSM with Light Stops". In: *JHEP* 04 (2013), p. 028. DOI: 10.1007/JHEP04(2013)028. arXiv: 1209.0764 [hep-ph].

[28] B. C. Allanach, A. Dedes, and Herbert K. Dreiner. "Bounds on R-parity violating couplings at the weak scale and at the GUT scale". In: *Phys. Rev.* D60 (1999), p. 075014. DOI: 10.1103/PhysRevD.60.075014. arXiv: hep-ph/9906209 [hep-ph].

[29] Morad Aaboud et al. "A search for pair-produced resonances in four-jet final states at $\sqrt{s} = 13$ TeV with the ATLAS detector". In: *Eur. Phys. J.* C78.3 (2018), p. 250. DOI: 10.1140/epjc/s10052-018-5693-4. arXiv: 1710.07171 [hep-ex].

[30] Albert M Sirunyan et al. "Search for pair-produced resonances decaying to quark pairs in proton-proton collisions at $\sqrt{s} = 13$ TeV". In: *Phys. Rev.* D98.11 (2018), p. 112014. DOI: 10.1103/PhysRevD.98.112014. arXiv: 1808.03124 [hep-ex].

[31] Apollinari G. et al. *High-Luminosity Large Hadron Collider (HL-LHC): Technical Design Report V. 0.1*. CERN Yellow Reports: Monographs. Geneva: CERN, 2017. DOI: 10.23731/CYRM-2017-004. URL: https://cds.cern.ch/record/2284929.

[32] Esma Mobs. "The CERN accelerator complex - August 2018. Complexe des accélérateurs du CERN - Août 2018". In: (2018). General Photo. URL: http://cds.cern.ch/record/2636343.

[33] Oliver S. Bruning et al. "LHC Design Report Vol.1: The LHC Main Ring". In: (2004).

[34] *ATLAS Luminosity Public Results Run1*. URL: https://twiki.cern.ch/twiki/bin/view/AtlasPublic/LuminosityPublicResults.

[35] *ATLAS Luminosity Public Results Run2*. URL: https://twiki.cern.ch/twiki/bin/view/AtlasPublic/LuminosityPublicResultsRun2.

[36] G. Aad et al. "The ATLAS Experiment at the CERN Large Hadron Collider". In: *JINST* 3 (2008), S08003. DOI: 10.1088/1748-0221/3/08/S08003.

[37] S. Chatrchyan et al. "The CMS Experiment at the CERN LHC". In: *JINST* 3 (2008), S08004. DOI: 10.1088/1748-0221/3/08/S08004.

[38] A. Augusto Alves Jr. et al. "The LHCb Detector at the LHC". In: *JINST* 3 (2008), S08005. DOI: 10.1088/1748-0221/3/08/S08005.

[39] K. Aamodt et al. "The ALICE experiment at the CERN LHC". In: *JINST* 3 (2008), S08002. DOI: 10.1088/1748-0221/3/08/S08002.

[40] O. Adriani et al. "The LHCf detector at the CERN Large Hadron Collider". In: *JINST* 3 (2008), S08006. DOI: 10.1088/1748-0221/3/08/S08006.

[41] G. Latino. "The TOTEM Experiment at the LHC". In: *QCD and high energy interactions. Proceedings, 44th Rencontres de Moriond, La Thuile, Italy, March 14-21, 2009*. 2009, pp. 357–360. arXiv: 0905.2936 [hep-ex].

[42] J. L. Pinfold. "The MoEDAL Experiment at the LHC - a New Light on the Terascale Frontier". In: *J. Phys. Conf. Ser.* 631.1 (2015), p. 012014. DOI: 10.1088/1742-6596/631/1/012014.

[43] G. Aad et al. "The ATLAS Inner Detector commissioning and calibration". In: *Eur. Phys. J.* C70 (2010), pp. 787–821. DOI: 10.1140/epjc/s10052-010-1366-7. arXiv: 1004.5293 [physics.ins-det].

[44] M Capeans et al. *ATLAS Insertable B-Layer Technical Design Report*. Tech. rep. CERN-LHCC-2010-013. ATLAS-TDR-19. 2010. URL: https://cds.cern.ch/record/1291633.

[45] *ATLAS liquid-argon calorimeter: Technical Design Report*. Technical Design Report ATLAS. Geneva: CERN, 1996. URL: https://cds.cern.ch/record/331061.

[46] *ATLAS tile calorimeter: Technical Design Report*. Technical Design Report ATLAS. Geneva: CERN, 1996. URL: https://cds.cern.ch/record/331062.

[47] *ATLAS muon spectrometer: Technical Design Report*. Technical Design Report ATLAS. Geneva: CERN, 1997. URL: https://cds.cern.ch/record/331068.

[48] Aranzazu Ruiz-Martinez and ATLAS Collaboration. *The Run-2 ATLAS Trigger System*. Tech. rep. ATL-DAQ-PROC-2016-003. Geneva: CERN, 2016. DOI: 10.1088/1742-6596/762/1/012003. URL: https://cds.cern.ch/record/2133909.

[49] *High Luminosity Project Schedule*. URL: https://project-hl-lhc-industry.web.cern.ch/content/project-schedule.

[50] *Report on the Physics at the HL-LHC and Perspectives for the HE-LHC*. Tech. rep. arXiv:1902.10229. Presented at The HL/HE-LHC Physics Workshop: final jamboree, 1 March 2019. Geneva: CERN, 2019. URL: https://cds.cern.ch/record/2651134.

[51] Stéphane Fartoukh. "Pile up management at the high-luminosity LHC and introduction to the crab-kissing concept". In: *Phys. Rev. ST Accel. Beams* 17.11 (2014), p. 111001. DOI: 10.1103/PhysRevSTAB.17.111001.

[52] ATLAS Collaboration. *Technical Design Report for the ATLAS Inner Tracker Pixel Detector*. Tech. rep. CERN-LHCC-2017-021. ATLAS-TDR-030. Geneva: CERN, 2017. URL: https://cds.cern.ch/record/2285585.

[53] ATLAS Collaboration. *Technical Design Report for the ATLAS Inner Tracker Strip Detector*. Tech. rep. CERN-LHCC-2017-005. ATLAS-TDR-025. Geneva: CERN, 2017. URL: https://cds.cern.ch/record/2257755.

[54] ATLAS Collaboration. *Technical Proposal: A High-Granularity Timing Detector for the ATLAS Phase-II Upgrade*. Tech. rep. CERN-LHCC-2018-023. LHCC-P-012. Geneva: CERN, 2018. URL: https://cds.cern.ch/record/2623663.

[55] ATLAS Collaboration. *Technical Design Report for the Phase-II Upgrade of the ATLAS LAr Calorimeter*. Tech. rep. CERN-LHCC-2017-018. ATLAS-TDR-027. Geneva: CERN, 2017. URL: https://cds.cern.ch/record/2285582.

[56] M. Aaboud et al. "Performance of the ATLAS Track Reconstruction Algorithms in Dense Environments in LHC Run 2". In: *Eur. Phys. J.* C77.10 (2017), p. 673. DOI: 10.1140/epjc/s10052-017-5225-7. arXiv: 1704.07983 [hep-ex].

[57] Morad Aaboud et al. "Reconstruction of primary vertices at the ATLAS experiment in Run 1 proton-proton collisions at the LHC". In: *Eur. Phys. J.* C77.5 (2017), p. 332. DOI: 10.1140/epjc/s10052-017-4887-5. arXiv: 1611.10235 [physics.ins-det].

[58] Georges Aad et al. "Electron reconstruction and identification efficiency measurements with the ATLAS detector using the 2011 LHC proton-proton collision data". In: *Eur. Phys. J.* C74.7 (2014), p. 2941. DOI: 10.1140/epjc/s10052-014-2941-0. arXiv: 1404.2240 [hep-ex].

[59] Morad Aaboud et al. "Measurement of the photon identification efficiencies with the ATLAS detector using LHC Run-1 data". In: *Eur. Phys. J.* C76.12 (2016), p. 666. DOI: 10.1140/epjc/s10052-016-4507-9. arXiv: 1606.01813 [hep-ex].

[60] Georges Aad et al. "Muon reconstruction performance of the ATLAS detector in proton-proton collision data at $\sqrt{s}$ =13 TeV". In: *Eur. Phys. J.* C76.5 (2016), p. 292. DOI: 10.1140/epjc/s10052-016-4120-y. arXiv: 1603.05598 [hep-ex].

[61] W Lampl et al. *Calorimeter Clustering Algorithms: Description and Performance*. Tech. rep. ATL-LARG-PUB-2008-002. ATL-COM-LARG-2008-003. Geneva: CERN, 2008. URL: https://cds.cern.ch/record/1099735.

[62] Matteo Cacciari, Gavin P. Salam, and Gregory Soyez. "The anti-k_t jet clustering algorithm". In: *JHEP* 04 (2008), p. 063. DOI: 10.1088/1126-6708/2008/04/063. arXiv: 0802.1189 [hep-ph].

[63] Ariel Schwartzman. "Jet energy calibration at the LHC". In: *Int. J. Mod. Phys.* A30.31 (2015), p. 1546002. DOI: 10.1142/S0217751X15460021. arXiv: 1509.05459 [hep-ex].

[64] *Optimisation and performance studies of the ATLAS b-tagging algorithms for the 2017-18 LHC run*. Tech. rep. ATL-PHYS-PUB-2017-013. Geneva: CERN, 2017. URL: https://cds.cern.ch/record/2273281.

[65] G. Pellegrini et al. "Technology developments and first measurements of Low Gain Avalanche Detectors (LGAD) for high energy physics applications". In: *Nucl. Instrum. Meth.* A765 (2014), pp. 12 –16. DOI: 10.1016/j.nima.2014.06.008.

[66] *HGTD Public Plots*. URL: https://twiki.cern.ch/twiki/bin/view/AtlasPublic/LArHGTDPublicPlots.

[67] RD50 collaboration. URL: https://rd50.web.cern.ch/rd50.

[68] Hartmut F. W. Sadrozinski, Abraham Seiden, and Nicolò Cartiglia. "4D tracking with ultra-fast silicon detectors". In: *Rept. Prog. Phys.* 81.2 (2018), p. 026101. DOI: 10.1088/1361-6633/aa94d3. arXiv: 1704.08666 [physics.ins-det].

[69] G. Kramberger et al. "Radiation Hardness of Thin Low Gain Avalanche Detectors". In: *Nucl. Instrum. Meth.* A891 (2018), pp. 68–77. DOI: 10.1016/j.nima.2018.02.018. arXiv: 1711.06003 [physics.ins-det].

[70] C. Allaire et al. "Beam test measurements of Low Gain Avalanche Detector single pads and arrays for the ATLAS High Granularity Timing Detector". In: *JINST* 13.06 (2018), P06017. DOI: 10.1088/1748-0221/13/06/P06017. arXiv: 1804.00622 [physics.ins-det].

[71] *Expected Performance of the ATLAS Inner Tracker at the High-Luminosity LHC*. Tech. rep. ATL-PHYS-PUB-2016-025. Geneva: CERN, 2016. URL: https://cds.cern.ch/record/2222304.

[72] *Tagging and suppression of pileup jets with the ATLAS detector*. Tech. rep. ATLAS-CONF-2014-018. Geneva: CERN, 2014. URL: https://cds.cern.ch/record/1700870.

[73] Georges Aad et al. "Observation and measurement of Higgs boson decays to WW* with the ATLAS detector". In: *Phys. Rev.* D92.1 (2015), p. 012006. DOI: 10.1103/PhysRevD.92.012006. arXiv: 1412.2641 [hep-ex].

[74] Paul Adrien Maurice Dirac. "Quantised singularities in the electromagnetic field," in: *Proc. Roy. Soc. Lond.* A133.821 (1931), pp. 60–72. DOI: 10.1098/rspa.1931.0130.

[75] Gerard 't Hooft. "Magnetic Monopoles in Unified Gauge Theories". In: *Nucl. Phys.* B79 (1974). [,291(1974)], pp. 276–284. DOI: 10.1016/0550-3213(74)90486-6.

[76] Y. M. Cho, Kyungtae Kimm, and J. H. Yoon. "Mass of the Electroweak Monopole". In: *Mod. Phys. Lett.* A31.09 (2016), p. 1650053. DOI: 10.1142/S021773231650053X. arXiv: 1212.3885 [hep-ph].

[77] ATLAS Collaboration. "Search for magnetic monopoles and stable particles with high electric charges in 8 TeV *pp* collisions with the ATLAS detector". In: *Phys. Rev.* D93.5 (2016), p. 052009. DOI: 10.1103/PhysRevD.93.052009. URL: https://link.aps.org/doi/10.1103/PhysRevD.93.052009.

[78] ATLAS Collaboration. "Luminosity determination in pp collisions at $\sqrt{s}$ = 8 TeV using the ATLAS detector at the LHC". In: *Eur. Phys. J.* C76.12 (2016), p. 653. DOI: 10.1140/epjc/s10052-016-4466-1. arXiv: 1608.03953 [hep-ex].

[79] Dorival Goncalves-Netto et al. "Sgluon Pair Production to Next-to-Leading Order". In: *Phys. Rev.* D85 (2012), p. 114024. DOI: 10.1103/PhysRevD.85.114024. arXiv: 1203.6358 [hep-ph].

[80] J. Alwall et al. "The automated computation of tree-level and next-to-leading order differential cross sections, and their matching to parton shower simulations". In: *JHEP* 07 (2014), p. 079. DOI: 10.1007/JHEP07(2014)079. arXiv: 1405.0301 [hep-ph].

[81] Torbjörn Sjöstrand et al. "An Introduction to PYTHIA 8.2". In: *Comput. Phys. Commun.* 191 (2015), pp. 159–177. DOI: 10.1016/j.cpc.2015.01.024. arXiv: 1410.3012 [hep-ph].

[82] Céline Degrande et al. "Automated next-to-leading order predictions for new physics at the LHC: the case of colored scalar pair production". In: *Phys. Rev.* D91.9 (2015), p. 094005. DOI: 10.1103/PhysRevD.91.094005. arXiv: 1412.5589 [hep-ph].

[83] *Dijet resonance searches with the ATLAS detector at 14 TeV LHC*. Tech. rep. ATL-PHYS-PUB-2015-004. Geneva: CERN, 2015. URL: https://cds.cern.ch/record/2002136.

[84] Remi Lafaye et al. "Measuring Supersymmetry". In: *Eur. Phys. J.* C54 (2008), pp. 617–644. DOI: 10.1140/epjc/s10052-008-0548-z. arXiv: 0709.3985 [hep-ph].

[85] J. Charles et al. "Bayesian statistics at work: The Troublesome extraction of the CKM phase alpha". In: (2006). arXiv: hep-ph/0607246 [hep-ph].

[86] S. Agostinelli et al. "GEANT4: A Simulation toolkit". In: *Nucl. Instrum. Meth.* A506 (2003), pp. 250–303. DOI: 10.1016/S0168-9002(03)01368-8.

[87] Francesca Cenna et al. "Weightfield2: A fast simulator for silicon and diamond solid state detector". In: *Nuclear Instruments and Methods in Physics Research Section A: Accelerators, Spectrometers, Detectors and Associated Equipment* 796 (2015). Proceedings of the 10th International Conference on Radiation Effects on Semiconductor Materials Detectors and Devices, pp. 149 –153. ISSN: 0168-9002. DOI: https://doi.org/10.1016/j.nima.2015.04.015. URL: http://www.sciencedirect.com/science/article/pii/S0168900215004842.

[88] Giuseppe Battistoni et al. "Overview of the FLUKA code". In: *Annals of Nuclear Energy* 82 (2015). Joint International Conference on Supercomputing in Nuclear Applications and Monte Carlo 2013, SNA + MC 2013. Pluri- and Trans-disciplinarity, Towards New Modeling and Numerical Simulation Paradigms, pp. 10 –18. ISSN: 0306-4549. DOI: https://doi.org/10.1016/j.anucene.2014.11.007. URL: http://www.sciencedirect.com/science/article/pii/S0306454914005878.

[89] H. Bethe. "Zur Theorie des Durchgangs schneller Korpuskularstrahlen durch Materie". In: *Annalen der Physik* 397 (1930), pp. 325–400. DOI: 10.1002/andp.19303970303.

université PARIS-SACLAY | ÉCOLE DOCTORALE PHENIICS

Titre : ATLAS : Recherche de la Supersymétrie et optimisation du Détecteur de temps fortement segmenté

Mots clés : ATLAS; SUSY; RPV; Higgs; HGTD; HL-LHC; Détecteur de Temps

Résumé : Le Modèle Standard de la physique des particules a jusqu'alors extremement bien reussi à decrire les particules elementaires et leurs interactions. Malgre cela, il demeure toujours des questions ouvertes. La possibilite de repondre à ces questions grace la Supersymetrie est actuellement à l'etude dans les collisions proton-proton à 13 TeV dans le cadre de l'experience ATLAS au LHC.
Cette thèse presente la recherche de la production de paires de particules colorees dans ATLAS, ces dernières se desintegrant en paires de jets. Pour ce faire, les donnees de 2016, 2017 et 2018 ont ete utilisees. De telles particules echappent aux recherches standards de la Supersymetrie du fait de l'absence d'energie transverse manquante dans l'etat final. Deux signatures furent considerees, la desintegration de stops via des couplages violant la R-parite et la production de sgluon, le partenaire scalaire du gluino. En l'absence de signal, une amelioration de 200 GeV sur la masse maximum exclue est attendue. Le HL-LHC augmentera la luminosite integree delivree afin de nous permettre de rechercher des particules plus massives et d'ameliorer les mesures de precision du Modèle Standard. La luminosite instantanee augmentera d'un facteur 5 et une luminosite integree de 4000 fb^{-1} devrait pouvoir etre atteinte à la fin du LHC en 2037.
Cette thèse presente egalement une etude des perspectives de mesure des couplages du Higgs au HL-LHC effectuee à l'aide de SFitter. Il est demontre que dans le cadre des Delta et d'une EFT, l'augmentation de la luminosite genère une amelioration de la precision de la mesure des couplages.
Finalement, le Detecteur de temps fortement segmente, qui sera installe dans ATLAS au HL-LHC, est presente. La simulation de ce detecteur a ete developpee pour prendre en compte la resolution temporelle du detecteur et fut utilisee pour optimiser sa geometrie. Les performances de ce detecteur ont ete etudiees, plus de 80 % des traces ont leurs temps correctement associe avec une resolution de 20 ps avant irradiation de 50 ps après. En utilisant les informations temporelles, l'isolation des electrons peut etre amelioree de 10 %.

Title : ATLAS : Search for Supersymmetry and optimization of the High Granularity timing detector

Keywords : ATLAS; SUSY; RPV; Higgs; HGTD; HL-LHC; Timing Detector

Abstract : The Standard Model of particle physics has been extremely successful in describing the elementary particles and their interactions. Nevertheless, there are open questions that are left unanswered. Whether supersymmetry can provide answers to some of these is being studied in 13 TeV proton-proton collisions in the ATLAS experiment at the LHC. In this thesis a search for pair produced colored particles in ATLAS decaying into pairs of jets using data from 2016, 2017 and 2018 is presented. Such particles would escape standard Supersymmetry searches due to the absence of missing transverse energy in the final state. Stops decaying via a R-parity violating coupling and sgluon, scalar partners of the gluino, were considered. In the absence of a signal, an improvement of 200 GeV on the limit on the stop mass is expected.
The HL-LHC will increase the integrated luminosity delivered to probe even higher mass ranges as well as improving the precision of Standard model measurements. The instantaneous luminosity will be increased by a factor 5 and an integrated luminosity of 4000 fb^{-1} should be reached by the end of the LHC in 2037.
A study of the Higgs coupling measurement prospects at the HL-LHC using SFitter is performed. Using the Delta and EFT framework shows that the increase in luminosity will result in a significant improvement of the precision of the measurement of the couplings.
The High granularity timing detector detector will be installed in ATLAS for the HL-LHC. A simulation of the detector that takes into account the timing resolution was developed and used to optimize its layout. The detector performance was studied. More than 80 % of the tracks have their time correctly reconstructed with a resolution of 20 ps before irradiation and 50 ps after. Using the timing information, the electron isolation efficiency is improved by 10 %.

Université Paris-Saclay
Espace Technologique / Immeuble Discovery
Route de l'Orme aux Merisiers RD 128 / 91190 Saint-Aubin, France